



**This electronic thesis or dissertation has been
downloaded from Explore Bristol Research,
<http://research-information.bristol.ac.uk>**

Author:

White, Sam R

Title:

Robotic Manipulators & Advanced Emerging Technologies

The future of nuclear waste processing

General rights

Access to the thesis is subject to the Creative Commons Attribution - NonCommercial-No Derivatives 4.0 International Public License. A copy of this may be found at <https://creativecommons.org/licenses/by-nc-nd/4.0/legalcode>. This license sets out your rights and the restrictions that apply to your access to the thesis so it is important you read this before proceeding.

Take down policy

Some pages of this thesis may have been removed for copyright restrictions prior to having it been deposited in Explore Bristol Research. However, if you have discovered material within the thesis that you consider to be unlawful e.g. breaches of copyright (either yours or that of a third party) or any other law, including but not limited to those relating to patent, trademark, confidentiality, data protection, obscenity, defamation, libel, then please contact collections-metadata@bristol.ac.uk and include the following information in your message:

- Your contact details
- Bibliographic details for the item, including a URL
- An outline nature of the complaint

Your claim will be investigated and, where appropriate, the item in question will be removed from public view as soon as possible.

Robotic Manipulators & Advanced Emerging Technologies

The future of nuclear waste processing

By

SAMUEL RENWICK WHITE



Department of Physics
UNIVERSITY OF BRISTOL

A dissertation submitted to the University of Bristol in accordance with the requirements of the degree of DOCTOR OF PHILOSOPHY in the Faculty of Physics.

JUNE 2022

Word count: Approx 55,000

To my supportive family Mum, Dad, Ben, Grandpa, Granny and Grandma for being behind me
on every step of this journey.

In memory of Frederick John White.

ABSTRACT

There is a growing global demand for safe, environmentally conscious, and long-term radioactive waste disposal solutions. Owing to the potentially deleterious effects of waste evolution during containment, there are strict guidelines and waste packaging specifications which must be adhered to, including rigorous documentation of waste inventories. This mandates a detailed characterisation of waste materials prior to packaging. Waste must be characterised in terms of its material, chemical and radiometric properties. Currently, this characterisation is a highly dangerous and labour intensive process which puts workers at risk. In addition, frequent estimations are made on waste items on the basis of ex-situ sub-samples. These not only sacrifice accuracy in characterisation, but also introduce lengthy time delays into the process.

The primary objective of this thesis was to explore the use of robotic systems and other advanced emerging technologies that could be integrated and then implemented to resolve these challenges, fully autonomously and without human intervention. Ultimately, any integrated technology must fulfil a requirement to facilitate, accurate, in-situ characterisation of individual waste objects, while improving worker safety, increasing characterisation accuracy and streamlining an otherwise time consuming process. Hence, the research and development of a prototype fully-autonomous, robotic waste sorting system which can fulfil each of these aforementioned objectives is detailed. The fully-autonomous components were delivered by a variety of robotic manipulator systems integrated with sensory hardware for both manipulation and characterisation. For object manipulations, depth vision cameras were used to intelligently deliver the robotic end-effector to relevant locations to enable grasping. To provide short distance stand-off characterisation of the waste objects, a variety of sensors were integrated onto robotic arms, including micro gamma-spectrometers, Laser Raman Spectroscopy probes and a portable X-ray Fluorescence (XRF) device. These were able to classify the material and radiometric composition of waste objects. AI algorithms were frequently employed to assist all processes.

Following a progressive development sequence, robotic integration of each individual characterisation system is demonstrated in its own chapter. From the technology development demonstrated in this thesis, it may be concluded that a fully integrated robotic system may be deployable as part of an integrated waste sorting and segregation solution which could autonomously handle, measure and determine long-term disposal routes for mixed assorted nuclear wastes.

AUTHOR'S DECLARATION

I declare that the work in this dissertation was carried out in accordance with the requirements of the University's Regulations and Code of Practice for Research Degree Programmes and that it has not been submitted for any other academic award. Except where indicated by specific reference in the text, the work is the candidate's own work. Work done in collaboration with, or with the assistance of, others, is indicated as such. Any views expressed in the dissertation are those of the author.

SIGNED: DATE:

ACKNOWLEDGEMENTS

Thank you to both my supervisors Tom Scott and David Megson-Smith for their continued support and enthusiasm throughout my PhD project. Without you, this project would not have been possible. To Guido Hermann who supervised my project for the first year, setting a direction for research. Thank you Peter Martin, for the breakfast discussions and technical input. To John Dilworth for his mentorship and innovative robotic concepts. Thank you also to the team at KUKA, in particular Alan Oakley and Dave Burns for their interest and guidance on all things robotics. To Karen Aplin and David Cussans for their insights and support during the APM process. In addition, to Max Youngman, with whom I commenced robotic waste drum inspection project with during my undergraduate project, it was these early ideas which have progressed into my PhD project.

I would like to thank the University of Bristol and the Engineering and Physical Sciences Research Council (EPSRC) for their support and funding. I would like to acknowledge and thank the National Centre for Nuclear Robotics (NCNR) EP/R02572X/1 for having me as an affiliated student and also the Robotics and AI in Nuclear (RAIN) EP/W001128/1 consortium for letting me enjoy their regular events, workshops and seminars. Being involved with such amazing projects has helped me to learn and develop as a researcher.

To Kamran Ahmad and Luke Dubono from ImiTec Ltd. for their technical support in the early stages of the project. Yannick Verbelen for help on all things electronic, Dean Connor on all things radiation detection, Jonny Teague for PhD guidance, Matthew Ryan-Tucker for his programming expertise, Kaiqiang Zhang for his early PGR mentorship, Kieran Wood for his inputs on reconstruction algorithms, Suresh Kaluvan and Chris Hutson for advising on a wide variety of topics.

To the team in the physics workshop, Adrian Crimp, Bart Dworzanski who made and assisted in the development of numerous components, essential for my project. In addition, John Nicholson for his technical guidance and support. Thank you to my father, Philip White, for transforming many of my 3D print and paper designs into metal finished products. The NNUF hot robotics team, Sabrina Shirazi and Sofia Leadbetter, who have facilitated the use of a significant amount of robotic and sensory equipment during this project. To Andrew Hughes, for his assistance with robot deliveries and facilitating research at Fenswood Farm.

Thank you to everyone at the IAC who has made the University a welcoming and supportive environment. In particular Antonis Banos, Haris Parasklouvalis, Lingteng Kong, Euan Connolly, Erin Holland and Dimitris Samaras. Last, but by no means least, thank you to my Engineering colleagues, Alison Ponche, Duanqi Zhao, Diego Navarro, Pedro Simplicio and Erwin Jose Lopez Pulgarin, for the lunchtime conversations in the early days of the PhD and continued friendship.

I owe it to you all.

PUBLICATIONS AND PRESENTATIONS

Publications

S.R. White, D.A. Megson-Smith, S. Kaluvan, D.Burns & T.B. Scott, "Using Robotic Manipulators for Radioactive Waste Inspection", Waste Management Symposia, 2020.

C. Hutson, A. Banos, D.T. Connor, K. Zhang, S. Kaluvan, **S.R. White**, Y. Verbelen, M.G. Ryan-Tucker, J. Knighton, K. Wood, D.A. Megson-Smith, E.I. Holland, P.G. Martin & T.B. Scott, "Development of Robotic Inspection Systems for In-situ Characterisation Prior to Decommissioning", Waste Management Symposia, 2020.

S.R. White, D.A. Megson-Smith, K. Zhang, D.T. Connor, P.G. Martin, C. Hutson, G. Hermann, J. Dilworth & T.B. Scott, "Radiation Mapping and Laser Profiling Using a Robotic Manipulator", Front. Robot. AI, 26 November 2020.

S.R. White, K.T. Wood, P.G. Martin, D.T. Connor, T.B. Scott & D.A. Megson-Smith, Radioactive Source Localisation via Projective Linear Reconstruction. Sensors 2021, 21, 807.

S.R. White, D.A. Megson-Smith, S. Kaluvan & T.B. Scott, "Demonstration of a Prototype Autonomous Sort and Segregation System", Waste Management Symposia, 2021.

S.R. White, D.T. Connor, D.A. Megson-Smith, S. Kaluvan & T.B. Scott, "A Radiometric Classification Technique for Nuclear Waste Objects", Waste Management Symposia, 2022.

E.L. Connolly, **S.R. White**, D.T. Connor & P.G. Martin, "Revolutionising Detection Systems For Intercepting The Illicit Transportation Of Radioactive Materials Concealed Within Shipping Containers", Proceedings of the INMM & ESARDA Joint Virtual Annual Meeting, 2021.

S.R. White, P.G. Martin, D.A. Megson-Smith & T.B. Scott, "Application of automated and robotically deployed in-situ X-ray fluorescence analysis for nuclear waste management.", Journal of Field Robotics, accepted.

Presentations

NCNR Big Meet - Presented progress on robotic radiation mapping system, April 2019.

Waste Management Symposia 2020 - Presented research on robotic vision-based object targeted radiation mapping, March 2020.

RAIN Webinar - Presented research on Projective Linear Reconstruction of radioactive sources for the RAIN Webinar, June 2020.

Waste Management Symposia 2021 - Presented research on weighing objects using a robotic manipulator, March 2021.

Robot Lab Live - Presented a live robotic system demonstration about a KUKA LBR iiwa mounted on a Superdroid HD2. System was able to radiation map walls and surfaces to identify radioactive sources, June 2021.

Waste Management Symposia 2022 - Presented research on activity calculation, March 2022.

Faculty of Engineering Research Showcase - Presented PhD research as part of the event at the University of Bristol, May 2021.

Posters

Waste Management Symposia 2020 - **S.R. White**, D. Burns, D.A. Megson-Smith & T.B. Scott, "An Autonomous Nuclear Waste Sorting and Segregation System", March 2020.

Waste Management Symposia 2022 - **S.R. White**, D.A. Megson-Smith & T.B. Scott, "Radiation Mapping with Robotic Manipulators", March 2022.

PRIZES AND AWARDS

This PhD research received the following award:

Worthfulship Company of Scientific Instrument Makers - Post Graduate Scholarship

TABLE OF CONTENTS

	Page
List of Tables	xvii
List of Figures	xix
1 Introduction	1
1.1 Introduction	2
1.1.1 Radiation	2
1.1.2 Nuclear Fission	4
1.2 Nuclear Waste	5
1.2.1 Radioactive Waste Lifecycle	5
1.3 An Opportunity for Robotics	14
1.3.1 Robotics for Sort and Segregation	16
2 Theory of Robotic Techniques and Characterisation	19
2.1 Introduction	20
2.1.1 State of the Art Waste Sorting Systems	20
2.1.2 Theory Workflow	22
2.2 Robotics	23
2.2.1 Robotic Manipulator Fundamentals	24
2.2.2 Workspaces	27
2.2.3 Robotic working envelopes	29
2.2.4 Programmatic Control	29
2.2.5 Force Sensitive Robotic Manipulators	30
2.3 Robot Sensor Integration	31
2.3.1 3D Visualisation Methods	31
2.3.2 Pixel Space to Robot Space	32
2.4 Grasping Methodology	33
2.5 Radiometric Characterisation	36
2.5.1 Gamma Radiation Detection	37
2.5.2 Detection	39

TABLE OF CONTENTS

2.5.3	Practical Radiation Detection	40
2.5.4	Gamma Spectroscopy	43
2.5.5	Currently Deployable Devices	43
2.5.6	Radiometric characterisation summary	45
2.6	Material Characterisation	45
2.6.1	X-ray Fluorescence	46
2.6.2	Laser Raman Spectroscopy	48
2.7	Summary	50
3	Radiation Surveying using Robotic Manipulators	53
3.1	Introduction	54
3.2	Methods	56
3.2.1	Radioactive Sources	56
3.2.2	Sensor selection	57
3.2.3	Collimator	58
3.2.4	Robot Sensor Integration	58
3.2.5	Visualisation	61
3.2.6	Spectral Windowing and Dose Rate Conversion	61
3.3	Experimental Scenario Setup	62
3.3.1	Radiation Survey and Laser Profiling	63
3.4	Results and Discussion	64
3.4.1	Scenario 1	64
3.4.2	Scenario 2	65
3.4.3	Scenario 3	66
3.4.4	Scenario 4	67
3.5	Conclusions	69
4	Radiation Survey Optimisation	71
4.1	Introduction	71
4.2	Method	73
4.2.1	Radiation Mapping System	73
4.2.2	Radiation Mapping Algorithms	74
4.2.3	Algorithm Testing	82
4.3	Results and Discussion	84
4.3.1	Simulated Results	84
4.3.2	Live Experimentation	88
4.3.3	Applicability to waste sorting	90
4.4	Conclusion	91

5	Algorithms for Accurate Radioactive Source Localisation	93
5.1	Introduction	94
5.2	Methods	98
5.2.1	Radiation Survey Data as a Linear Problem	98
5.2.2	General Linear Problem	99
5.2.3	Algebraic Reconstruction Techniques	99
5.2.4	Kaczmarz Method	99
5.2.5	Implementation of Kaczmarz for Radioactive Source Localisation	100
5.2.6	Detector Response Function	100
5.2.7	Fitting the Detector Response Function	102
5.2.8	PLR Algorithm	103
5.2.9	Experimental Scenarios	104
5.3	Results and Discussion	104
5.3.1	Scenario 1 - Two sources	104
5.3.2	Scenario 2 - Four lower activity sources	105
5.3.3	Scenario 3 - Proximity limit	106
5.3.4	Scenario 4 - Mixed source strengths	107
5.3.5	Quantitative Measurement of PLR	108
5.4	Conclusion	109
6	Robotic Material Characterisation with XRF	111
6.1	Introduction	112
6.2	Method	114
6.2.1	X-ray Characterisation	114
6.2.2	Robotic Integration	115
6.2.3	Assessing the Quality of Elemental Analysis Results	118
6.2.4	Assorted Object Assay	118
6.2.5	Exterior Drum Scanning	121
6.3	Results and Discussion	123
6.3.1	Concentration Calibration	123
6.3.2	Positioning Accuracy Verification	124
6.3.3	Assorted Object Scanning for Sorting and Segregation	124
6.3.4	Drum Surface Scanning	127
6.4	Conclusions and Future Work	129
7	Robotic Material Characterisation with Raman Spectroscopy	131
7.1	Introduction	132
7.2	Method	133
7.2.1	Raman Spectroscopy System	134

TABLE OF CONTENTS

7.2.2	Robotic Raman Data Collection	134
7.2.3	AI Based Vision Scanning	135
7.2.4	Experimental Setup	143
7.3	Results and Discussion	147
7.3.1	Proof of Concept Test Scenarios	147
7.3.2	Sorting and Segregation Scenarios	149
7.4	Conclusion	156
8	Confirmatory Classification Techniques	159
8.1	Introduction	160
8.2	Activity determination	162
8.2.1	Activity determination methods	162
8.2.2	Activity determination results and discussion	170
8.3	Robotic article mass determination	177
8.3.1	Testing Weighing Algorithm	180
8.3.2	Robotic article mass determination results and discussion	181
8.3.3	Discussion of in-situ weighing	187
8.4	Conclusions	188
9	Conclusions and Future Work	191
9.1	Chapter Conclusions	191
9.2	Future Work: Towards a Prototype System	194
9.2.1	3D Photogrammetry Survey	198
9.2.2	Robotic Radiation Survey	198
9.2.3	Robotic Separation of Waste	198
9.2.4	Robotic XRF Survey	198
9.2.5	Robotic Raman Survey	199
9.2.6	Robotic Grasping of waste articles	199
9.2.7	Confirmatory Classification Techniques	199
9.2.8	Determine Waste Stream	200
9.2.9	Optimised Packaging	200
9.2.10	Radiation Damage Resolution	200
9.3	Alternative Implementations	200
	Bibliography	203

LIST OF TABLES

TABLE	Page
1.1 Current, future arisings and lifetime total expected volumes of different nuclear waste categories. All values are a direct reproduction from the Nuclear Decommissioning Authority report [52]. * <i>This negative value reflects the future conditioning of waste volumes.</i>	10
2.1 Summary of the key features in the selection of scintillator detector materials. The £ symbols represent relative crystal costings with £ representing the cheapest systems and £££ the most expensive.	45
3.1 Puck types and placements relative to the robot base coordinates for each scenario.	64
4.1 Puck types and placements relative to the robot base coordinates for each scenario.	84
4.2 Comparison of simulated optimisation algorithms for identifying the location of a single radioactive source across a millimetre search space.	85
4.3 Comparison of simulated optimisation algorithms for identifying the location of the strongest radioactive source of two, across a millimetre search space.	86
4.4 Comparison of simulated optimisation algorithms for identifying the location of the strongest radioactive source of seven, across a millimetre search space.	87
4.5 Comparison of simulated optimisation algorithms for identifying the location of any of the radioactive sources of seven, across a millimetre search space.	88
4.6 Comparison of live optimisation algorithms for identifying the location of a single radioactive source, across a millimetre search space.	89
4.7 Comparison of live optimisation algorithms for identifying the location of any of the radioactive sources of two, across a millimetre search space.	89
4.8 Comparison of live optimisation algorithms for identifying the location of any of the radioactive sources of 7, across a millimetre search space.	90
5.1 Puck types and placements relative to the robot base coordinates.	104
5.2 The standard deviations of the fitted Gaussians as in Figure 5.10.	108
8.1 Results of the trial activity calculation experiments.	175

LIST OF FIGURES

FIGURE	Page
1.1 Example nuclear fission of U-235.	4
1.2 Photograph of Sellafield site taken August 2021.	6
1.3 Photograph of the Trawsfynydd ILW Store, taken from [62]. Locally mined slate was used on the exterior of the building to improve the aesthetics and support the local economy.	11
1.4 A photograph of the retrieval operation inside the Berkeley vaults [67]. A wide variety of wastes can be seen, including pipework, PPE and construction rubble.	12
1.5 Artists impression of the proposed GDF. Image taken from [70]. The spacing of waste volumes is partly constrained by rock strength, heat generation and criticality risk.	13
1.6 Photograph of a KUKA KR150 robotic manipulator.	15
1.7 Illustration detailing the progressive use of robotic systems within nuclear waste processing.	17
2.1 Robotic systems used for the BEP project. Taken from [90].	21
2.2 Photograph of the KUKA KR150 ('Betty') used for experimentation. Overlaid are the axis numbers and positions.	25
2.3 Photograph of the KUKA LBR iiwa ('Alfie') used for experimentation. Overlaid are the axis numbers and positions.	25
2.4 DH joint configuration diagram example for a 6 axis robot.	27
2.5 Robot tool implementation. Image taken from KUKA System Software 8.3 Operating and Programming Instructions for System Integrator's [76].	28
2.6 Working envelopes of (a) the KUKA KR150 and (b) the LBR. Taken from KUKA AG [76].	29
2.7 Representation of the PTP, LIN and CIRC motions used in robotics programming. The black line indicates the robot path between programmed positions.	30
2.8 Example of photogrammetry. Left shows a RGB image of a model robotic arm. Right shows a depth camera interpretation of the same scene.	32
2.9 Example of an affine transformation.	33
2.10 Experimental setup showing the robotic grasping system in position to grasp an assortment of objects.	34

LIST OF FIGURES

2.11	(a) shows the RGB colour image of 3 distinct blocks ready to be grasped. (b) shows the depth image of (a). (c) shows the object identification thresholded image. (d) highlights the contour analysis which gives rise to the grasping angle chosen by the robotic system.	35
2.12	Top left shows a colour image of an exemplar waste sorting scenario. Bottom left shows an example ‘grasping image of the same scene. Right shows the robotic system grasping a tin can.	36
2.13	Diagrammatic representation of Compton scattering.	38
2.14	Dominant gamma-photon interaction regions with respect to energy. Adapted from [115].	39
2.15	Diagrammatic representation of the mechanism used by Ion chambers, Proportional counters and Geiger-Muller tubes.	41
2.16	Diagrammatic representation of the mechanism behind scintillator detectors.	42
2.17	Diagrammatic representation of the mechanism behind semiconductor type detectors	43
2.18	XRF of an argon atom, depicting the release of X-ray induced k_{α} and k_{β} characteristic X-rays. Image inspired by [152].	47
2.19	Principles of scattering events, showing how LRS can be used to detect PVC. Image inspired by [164].	49
3.1	Diagram showing the internal construction of the radioactive source pucks. The relative gamma-ray solid angle which reaching the collimated detector is pictorially represented [180].	57
3.2	Left: Computer image of the designed collimator for robotic radiation mapping. Right: Cross section of the collimator.	58
3.3	Photograph of the developed radiation mapping system on an industrial robot arm.	59
3.4	Flowchart detailing the information and control flow algorithm controlling the robotic radiation mapping system.	60
3.5	Diagrammatic representation of a raster scan path.	61
3.6	Graph showing the calibration method used by Connor et al. to determine the dose rate conversion factor [182]. RP 5 and LRP 10 are labels for the two different sources used within Connor et al.’s research.	62
3.7	3D model and overlaid radiation map generated from a robot scan above two Cs-137 sources 30 cm apart. Left to right the source activity is 30 kBq and 36 kBq, respectively. The colour represents the gamma radiation counts in counts per second for a given 2×2 mm pixel.	64
3.8	3D model and overlaid radiation map generated from a robot scan above 2 Cs-137 sources directly adjacent to each other. Left to right the source activity is 30 kBq and 36 kBq, respectively. The colour represents the gamma radiation counts in counts per second for a given 2×2 mm pixel.	65

3.9	3D model and overlaid radiation map generated from a robot scan above 2 Cs-137 sources directly adjacent, from a second angle to aid visual clarity of the distinguished pucks. Left to right the source activity is 30 kBq and 36 kBq, respectively. The colour represents the gamma radiation counts in counts per second for a given 2×2 mm pixel.	66
3.10	3D model and overlaid radiation map generated from a robot scan above 2 Cs-137 sources 1 cm apart. Left to right the source activity is 30 kBq and 36 kBq, respectively. The colour represents the gamma radiation counts in counts per second for a given 2×2 mm pixel.	66
3.11	3D model and overlaid radiation map generated from a robot scan completed at a 1 cm standoff above 2 Cs-137 sources 1 cm apart. Left to right the measured source surface dose rates are $4.5 \mu\text{Svh}^{-1}$ Pitchblende, $7.5 \mu\text{Svh}^{-1}$ Cs-137, $10 \mu\text{Svh}^{-1}$ Cs-137 and $4.3 \mu\text{Svh}^{-1}$, respectively. The colour represents the gamma radiation counts in counts per second for a given 2×2 mm pixel.	68
3.12	3D model and overlaid radiation map generated from a robot scan completed at a 1 cm standoff above 2 Cs-137 sources 1 cm apart. Left to right the measured source surface dose rates are $4.5 \mu\text{Svh}^{-1}$ Pitchblende, $7.5 \mu\text{Svh}^{-1}$ Cs-137, $10 \mu\text{Svh}^{-1}$ Cs-137 and $4.3 \mu\text{Svh}^{-1}$ Pitchblende, respectively. The colour represents the Cs-137 gamma radiation dose rate for a given 2×2 mm pixel.	68
4.1	Photograph of the developed radiation mapping system on a KUKA LBR MED.	73
4.2	An example of the evaluation positioning for a brute force optimisation technique when applied across a radiation field containing 2 sources.	74
4.3	An example of the evaluation positioning for a particle swarm optimisation technique when applied across a radiation field containing 2 sources. The progression of evaluation positions tried is shown across iteration one (a), five (b) and ten (c) for a ten iteration procedure containing 20 particles.	77
4.4	An example of the evaluation positioning for a SHGO optimisation technique when applied across a radiation field containing 2 sources.	78
4.5	An example of the evaluation positioning for a basin hopping optimisation technique when applied across a radiation field containing 2 sources.	79
4.6	An example of the evaluation positioning for a differential evolution optimisation technique when applied across a radiation field containing 2 sources.	80
4.7	An example of the evaluation positioning for a dual annealing optimisation technique when applied across a radiation field containing 2 sources.	82
5.1	Diagrammatic representation of the isotropic emission of radiation and consequent reduction in gamma-photon flux as detector position moves.	95
5.2	Desplitting of a Magnox fuel rod and subsequent FED materials generated. Adapted from [205].	95

LIST OF FIGURES

5.3 Photograph of FED in a Magnox waste vault. Taken from [204]. 96

5.4 Photograph of the KUKA KR 150 system used, with a set of four sealed sources arranged on a table top. Inset - a detailed schematic of the detector and collimator setup.101

5.5 Quadrant cross-section of the as measured Detector Response Function (left) and the fitted model Detector Response Function (right). On the left-hand image, a model detector crystal (collimator and aluminium case not shown) is superimposed to highlight the experimental method. The detector crystal is outlined as an oblong shape with finite volume, although the algorithm assumed a perfect point, and all distances and angles are measured relative to the centre of the crystal. 103

5.6 The results from scenario 1 - using two similar sources. After processing with (a) simple interpolation, and (b) the PLR algorithm. The scan used a 1 cm resolution. The dashed white circles represent the true location of the source pucks. 105

5.7 The results from scenario 2 - four lower activity sources. After processing with (a) simple interpolation, and (b) the PLR algorithm. The scan used a 2 cm resolution. The dashed white circles represent the true location of the source pucks. 106

5.8 The results from scenario 3 - proximity limit. After processing with (a) simple interpolation, and (b) the PLR algorithm. The scan used a 1 cm resolution. The dashed white circles represent the true location of the source pucks. 106

5.9 The results from scenario 4 - mixed source strengths. After processing with (a) simple interpolation, and (b) the PLR algorithm. The scan used a 1 cm resolution. The dashed white circles represent the true location of the source pucks. 107

5.10 Comparison of 1D transects through the interpolated raw measurements (Raw Data) against the best solution estimated by the linear reconstruction technique (PLR data). Best fit Gaussian distributions have been fitted to both to enable a quantitative resolution assessment to be made. 108

6.1 Customisable sensor rack used within this chapter. Attached is the Vanta and the RealSense L515. 116

6.2 Schematic flowchart illustrating the platforms configuration and workflow, including details of the application-specific user parameters necessary to undertake each scanning scenario. 117

6.3 Photograph of the vision-based scanning system in progress; showing the assorted objects on the scan surface, the KUKA LBR iiwa, Intel® RealSense™ L515 and Olympus Vanta™. 120

6.4 Photograph of the depth sensor based positioning experiment. (a) shows the robot in the predefined ‘camera pose’. This identifies the cylindrical object on the table. An affine transformation is then used to guide the robot to the object. (b) when the robot is in position, the laser may be used to measure the accuracy of the transformation. . 121

6.5	Photograph of the drum setup, detailing the positions of the copper tape, CsCl doped paint, undoped paint, aluminium sheet and stainless steel disc.	122
6.6	Concentration profile of the pXRF line scan over a linear transect of the CsCl doped paint. Left to right, the mass of dopant added to the paint was 0.0 g, 0.5 g, 1.0 g, 1.5 g, 2.0 g, 2.5g, 3.0g. The colourful line is an interpolated concentration wt% for Cl along the transect. The black squares represent the results of the laboratory EDS testing, with associated error.	123
6.7	Results of the vision-based autonomous robotic XRF mapping of system identified objects of interest for the metallic block experiment. (a) shows the experimental setup. (b-d) show the elemental concentrations of (b) Cu, (c) Si and (d) Al.	125
6.8	Results of the vision-based autonomous robotic XRF mapping of system identified objects of interest, as shown in Figure 6.3. (a) initial colour image from the RealSense™ L515 camera, (b) depth image of (a). The red box in (a) and (b) indicates the region which is displayed in the sub-figures, showing the single element XRF maps of: (c) Fe, (d) Cu, (e) Ca and (f) Zn.	126
6.9	3D surface concentration maps of the 200 L drum. (a) LE, (b) Ca (identifying the paint), (c) Cl (CsCl doped paint), (d) Al (identifying the aluminium sheet), (e) Cr (identifying the stainless steel), (f) Cu (identifying the copper tape).	128
7.1	Robotic Raman inspection system setup.	134
7.2	Example of the K-means clustering process.	136
7.3	Demonstration of k-means clustering technique. Circled is the ‘knee’ identified by the knee method.	137
7.4	Colour identification of Raman scan locations. (a) shows the initial colour figure, (b) shows the identified colours using the methods outlined and their locations, (c) shows the depth camera image and (d) shows one cutdown colour representation.	138
7.5	An example of progressive erosion of a square, illustrating how the algorithm reduces the surface area of shapes.	139
7.6	Raman auto-focusing system methodology in progress.	140
7.7	Autonomous filing system used to catalogue Raman data.	141
7.8	GUI developed for the robotic Raman system.	143
7.9	Stand-off Raman probe attached to KUKA KR150.	144
7.10	Experimental positioning of the 11 ‘mystery’ powders.	145
7.11	KUKA KR150 powder scanning in progress.	145
7.12	Setup of the sorting and segregation applicable test scenario. Shown are the nitrile glove, pliers, Rubik’s cube and electrical wiring.	146
7.13	Experimental Raman spectra collected for the concrete sample, alongside the matched calibration spectra. 99.8% match determined.	147

LIST OF FIGURES

7.14	Experimental Raman spectra collected for the iron oxide sample, alongside the matched calibration spectra. 97.6% match determined.	148
7.15	Experimental Raman spectra collected for the CsCl sample, alongside the matched calibration spectra. 86.9% match determined.	149
7.16	(a) shows a colour photograph taken by the robotic system. (b) shows the objects identified by the system.	150
7.17	Experimental Raman spectra collected for the electrical cabling, alongside the matched calibration spectra. 99.67% match determined.	151
7.18	Experimental Raman spectra collected for the nitrile gloves, alongside the matched calibration spectra. 99.97% match determined.	152
7.19	Experimental Raman spectra collected for an orange rubics cube piece alongside the matched calibration spectra. 99.05% match determined.	153
7.20	Experimental Raman spectra collected for the red rubber on the pliers, alongside the matched calibration spectra. 99.71% match determined.	154
7.21	Experimental Raman spectra collected for the black rubber on the pliers, alongside the matched calibration spectra. 99.84% match determined.	155
7.22	Experimental Raman spectra collected for the nitrile gloves, alongside the matched calibration spectra. 99.91% match determined.	155
8.1	Diagrammatic representation of the geometric response of a radiation detector.	162
8.2	Diagrammatic representation of the geometric response of a radiation detector.	163
8.3	Example Co-60 spectrum.	165
8.4	Co-60 spectrum showing the baseline fitting procedure diagrammatically.	166
8.5	Processing workflow for the autonomous geometric efficiency calculation. (a) Shows the photograph of the object in front of the depth camera. (b) Shows the unprocessed depth image. (c) Shows the processed depth image. (d) Shows the point samples to be input into the MC geometric efficiency code.	168
8.6	Photograph showing the radioactive source pucks used. Left shows the individual puck. Right shows the puck attached to the aluminium block.	170
8.7	Energy calibration graph.	170
8.8	Graph of gamma-photon energy vs intrinsic efficiency.	171
8.9	Depth images taken on the Intel RealSense D435 camera. Left, shows an example of a matt finish 'wooden block'. Right, shows the reflective 'metallic block' surface.	172
8.10	Left, shows a colour image of the scanned object. Right, shows an overlaid depth image of the detected object.	173
8.11	Graph showing the effect of shape area and stand-off distance on geometric efficiency error.	174
8.12	Force diagram explaining how torque can be applied about a pivot point.	177
8.13	Photograph of the robot in the weighing pose. Labelled are the robot axes.	178

8.14	Reference torque measurement recorded at axis 2 for 100 iterations. Error bars are omitted for clarity of visualisation.	179
8.15	Results of 50 iterations of the weighing algorithm with a 2.003 ± 0.001 kg mass and no gripper. Error bars calculated as ± 50 g.	181
8.16	Results of 30 iterations of the mean averaged weighing algorithm with a 2.003 ± 0.001 kg mass and no gripper. Error bars calculated as ± 20 g.	182
8.17	Results of 30 iterations of the mean averaged weighing algorithm with a 0.110 ± 0.001 kg mass and attached gripper. Error bars calculated as ± 2 g.	183
8.18	Results of 30 iterations of the mean averaged weighing algorithm with a 0.128 ± 0.001 kg wooden block and attached gripper. Error bars calculated as ± 20 g.	184
8.19	Results of 30 iterations of the mean averaged weighing algorithm with a 2.011 ± 0.001 kg mass and attached gripper.	185
8.20	Results of 10 iterations of the mean averaged weighing algorithm with a 2.660 ± 0.001 kg mass and attached gripper.	186
8.21	Results of 9 iterations of the mean averaged weighing algorithm with a 6.498 ± 0.001 kg mass and attached gripper.	187
9.1	System design of complete working system.	197

INTRODUCTION

Nuclear power is a reliable, low carbon energy source, which is likely to play a prominent role in the global pursuit of reducing the effects of climate change [1]. Ignoring the carbon dioxide released attributable to plant construction, fuel extraction and transportation; nuclear power is almost entirely carbon neutral [1]. It is dependable and able to produce energy regardless of environmental factors, unlike wind and solar energy [2]. To support this, in the last decade an increasing number of nuclear reactors around the world are entering their power generating phase of operations, with around 50 currently under construction [3]. However, public perception of nuclear power has been negatively affected following accidents such as Three Mile Island, Chernobyl and Fukushima [4]. Such accidents have resulted in the wide-scale release of radioactive material, leading to contamination of surrounding areas [5]. A further area of public concern, is the generation of long-lived hazardous wastes which contain ionising radiation, resulting as a bi-product of nuclear energy production [6, 7]. If these wastes are not managed in a sustainable and responsible way, they pose significant risks to biological life [8]. Hence, there is a growing global demand for safe, environmentally conscious, and long-term radioactive waste disposal solutions. Owing to the potentially deleterious effects of mixed assorted wastes in storage, there are strict guidelines and waste packaging specifications which must be adhered to [9]. These have been put in place to prevent adverse chemical reactions which may lead to serious consequences for wastes in storage. Such measures include rigorous documentation of inventories, mandating detailed characterisation of waste materials prior to packaging [10].

It is anticipated, that a robotic solution could be developed to sort and manage nuclear waste, autonomously and in-situ [11]. Robotic systems could be used to augment and eventually replace the human workforce, delivering a step change in characterisation accuracy, safety and waste

throughput. The overarching purpose of this thesis is to explore such systems and technology, ultimately demonstrating their functionality and use in applicable environments. Initially, this first chapter seeks to examine the challenges presented by nuclear waste, by exploring the entire nuclear waste lifecycle. Once the challenge is clearly identified, robotic systems may be developed to offer a partial or full technical solution.

The following chapter is based on the methods, results and discussion presented within the following previously published, peer-reviewed articles:

S.R. White, D.T. Connor, D.A. Megson-Smith, S Kaluvan and T.B. Scott, "A Radiometric Classification Technique for Nuclear Waste Objects", Waste Management Symposia, 2022.

1.1 Introduction

1.1.1 Radiation

Crucial to the underlying principles of nuclear power generation and the hazards associated with the bi-product wastes, is radiation. The term 'radiation' is defined as the transmission of energy through space or a medium, as a wave formation [12]. Light and sound are examples of radiation; with light propagated by photons in the form of electromagnetic (EM) radiation and sound as part of an acoustic wave propagated through a medium via a compression/decompression [12]. In this work, radiation will refer specifically to ionising radiation. Ionising radiation manifests itself, by definition, as high energy electromagnetic waves or particles that are capable of ionising incident materials [13]. This occurs via interactions which may remove electrons and/or break chemical bonds [13]. Ionising radiation at high intensities is known to have a significant impact on biological life, as when these ionising interactions occur with DNA within cells, induced structural changes have the potential to cause cancer or genetic damage [14]. Hence it is imperative to limit human contact with ionising radiation to reduce these risks.

There are five primary types of ionising radiation: alpha, beta, gamma, X-ray and neutron [15]. **Alpha radiation** is the emission of a particle consisting of two neutrons and two protons from an unstable nucleus, known as an alpha particle [15]. The relatively strong charge and mass of alpha particles, compared to other sources of ionising radiation, mean that they react strongly with matter [16]. Alpha particles are only able to travel a few centimetres in air, and are stopped by human skin. However, if an alpha emitting radiation source is ingested, it is incredibly damaging to the human body [8], so it is crucial that alpha contaminated materials are dealt with carefully and contained appropriately. This is typically quite simple owing to their low penetrating power. The chemical equation for an alpha release is given in e.q. 1.1. **Beta**

radiation is the emission of a positron/electron from a nucleus. Containing a weaker charge than alpha radiation, beta particles have a reduced ionisation effect, but can travel a few metres in air and are stopped by a few millimetres of aluminium sheet [17]. Similarly to alpha radiation, beta radiation particles can be easily contained, due to their relatively low penetrating power. An example beta decay chemical equation is given in e.q. 1.2. **Gamma radiation** is a high energy electromagnetic (EM) wave. They are photonic in nature, weakly interacting and can therefore travel large distances, stopped only by dense or sufficiently thick materials, such as centimetres of lead or metres of concrete [18]. While they are more weakly interacting than alpha particles, this penetration power makes them difficult to contain. Therefore, they should be handled carefully or remotely. An example equation of a gamma-photon release is given in e.q. 1.3. **X-rays** are similar to gamma-photons, but are lower energy EM waves and typically originate from electron deceleration. However, there is an overlap with the energy range of X-ray and gamma radiation on the EM spectrum [19]. This means detection in the region remains the same, with the technicality of emission separating the two forms of radiation. Finally, **neutron radiation** is the release of a neutron by an atom. This can occur spontaneously, via induced fission events, or from the interaction of an alpha particle with a nucleus [19]. Neutrons interact with materials and can make them radioactive (activated) following neutron capture, as described by e.q. 1.4. Neutrons are the only form of radiation capable of inducing radioactivity. This is a result of the neutron capture process creating an unstable activation product, which subsequently decays via alpha, beta, gamma or even neutron radiation [20]. They are highly penetrating to most materials, but are stopped by mediums containing large hydrogen concentrations, such as water or concrete.



Radioactivity is measured in terms of ‘activity’, which quantifies the number of releases which occur within a given time period. The SI units refer to activity in becquerels (Bq), which records disintegration’s per second. Radioactive releases are stochastic, meaning they can be statistically

derived, but not predicted exactly. Radioactivity for a given radioisotope is measured using a decay rate, as described by e.q. 1.5.

$$(1.5) \quad A = \frac{\Delta N}{\Delta t}$$

Where A is the radioactivity, N is the number of nuclei and t represents the time.

1.1.2 Nuclear Fission

Civil nuclear power depends on the process of nuclear fission to release atomic energy in a controlled way [21]. Certain ‘fissile’ atoms can be split apart by an impinging low energy, thermal neutron [21]. The neutron is absorbed into the fissile nucleus causing it to destabilise and split into 2 daughter nuclei and releasing energy in the form of heat, radiation and 2-3 neutrons a high proportion of the time [21]. It is these additional neutrons that may proceed to cause the fission of further fissile atoms. The released thermal energy may then be harnessed by more conventional power generation mechanisms to produce energy [21]. If left uncontrolled, a cascading fission chain can in turn lead to a runaway reaction, as is the case with a nuclear weapon. However, in nuclear reactors, neutron absorbing control rods are used to limit the neutron flux in the core, thereby ensuring this does not happen [22]. A diagram of nuclear fission is included in Figure 1.1.

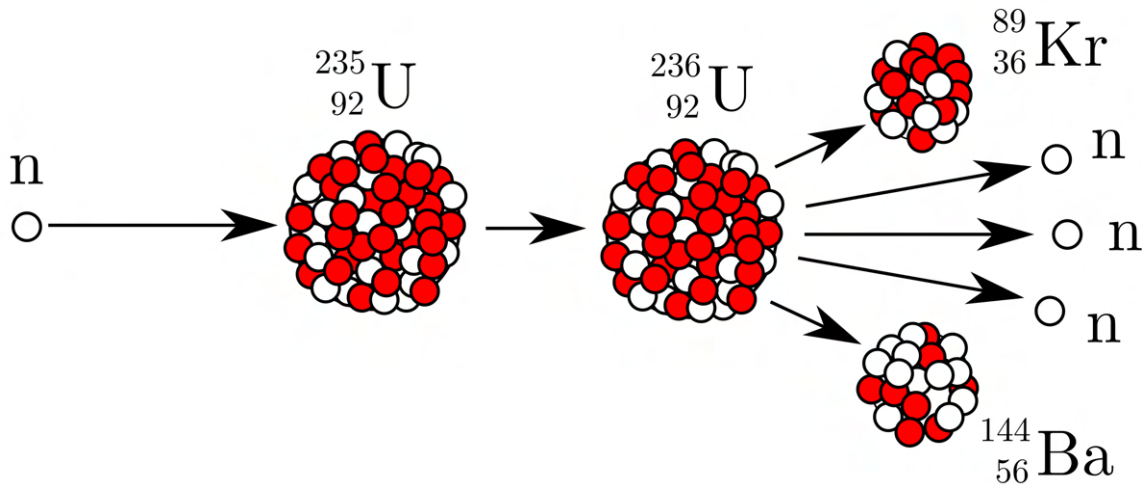


Figure 1.1: Example nuclear fission of U-235.

The neutrons released by the fission process can induce radioactivity in the reactors surrounding constituent materials via neutron activation. A prominent example of this is the production of Cobalt-60 (Co-60), from Co-59. Co-59 is found in certain steel alloys within the plant and neutron capture produces Co-60, which is unstable and decays via gamma radiation [23].

In addition to neutron activated materials, some of the produced daughter nuclei, termed fission products, are also radioactive. Some examples include Strontium-90 (Sr-90) and Caesium-137 (Cs-137) [24], in addition to Kr-89 and Ba-144, as shown in Figure 1.1. Indeed a wide spectrum of fission products can and do form during fission. Radioactive fission products can cause contamination within other components of the power plant [25] and are contained within the fuel when it is eventually extracted [26]. Therefore, both neutron activation and fission product formation mean that great care must be taken in waste management, decommissioning, de-fueling and other clean-up activities associated with nuclear power. This is what constitutes the majority of nuclear waste from civil nuclear power plants.

1.2 Nuclear Waste

It is evident that nuclear waste is produced as a bi-product of nuclear power generation. While power generation represents a large proportion of waste arrisals, radwaste may also be produced by other means. Such routes include scientific research [27], nuclear weapons [28], medicine [27] and even oil extraction [29]. Ultimately, this waste must be disposed of responsibly, something for which the International Atomic Energy Authority (IAEA) provides guidance for [30]. This guidance is described as part of the radioactive waste lifecycle.

1.2.1 Radioactive Waste Lifecycle

The radioactive waste lifecycle traces radioactive waste from generation to final disposal. It is important to understand these processes at a high level, to provide a comprehensive overview of the problems and challenges associated with each step. Broadly, the process is structured as follows [30], [31].

1. Planning and preparation
2. Waste generation or retrieval
3. Sorting and segregation
4. Size reduction
5. Decontamination
6. Treatment
7. Conditioning
8. Interim storage

9. Disposal

In the UK, the government organisation Sellafield Ltd. is the countries primary waste management facility at Seascale in Cumbria; storing, conditioning, processing and packaging a wide variety of nuclear wastes [32]. A photograph of the Sellafield site from August 2021 is shown in Figure 1.2, depicting its varied skyline with many different facilities packed onto a relatively small 5 km² parcel of land.



Figure 1.2: Photograph of Sellafield site taken August 2021.

1.2.1.1 Planning and Preparation

The early planning and preparation process involves discussion with the waste management company and the waste producer. In the case of the UK, UK Radioactive Waste Inventory (UKRWI), managed by the Nuclear Decommissioning Authority (NDA), represents the ‘management company’ and the ‘waste producers’ are Site Licence Companies (SLCs). SLCs are companies licensed to handle and use radioactive materials. These discussions help waste management to understand quantities and characterisations of the waste destined for storage [31]. This means identifying the activity of and quantity of radioactive species, enabling assessment of storage and handling risks and consequently providing a storage cost estimation [30]. For new waste generation, this process is more refined, as there is ability to analyse waste production routes, leading to known quantities and profiles of waste. Hence, optimal waste management and characterisation processes may be

designed in advance [30]. However, for historic ‘legacy’ wastes, this may not be possible, due to poor record keeping. Instead, scoping processes can be used to generate the strongest possible evidence for waste production, and therefore estimate the quantities of radionuclides present [30]. Characterisation can then be centred around missing information about wastes.

1.2.1.2 Waste Generation or Retrieval

With a potential storage route envisaged, waste may be generated and retrieved. Nuclear waste is generated throughout the lifetime of a nuclear power plant, from operation to decommissioning. As discussed, operating nuclear reactors generate significant volumes of nuclear waste. The highest activity of this waste comes from the fuel used to power the reactor [33]. Fuel typically consists of uranium, plutonium or rarely thorium; the fuel is isotopically enriched and facilitates the fission process in the reactor [33]. Eventually, they require replacing and the ‘spent’ fuel rods are removed from the reactor. In general spent fuel rods are highly radioactive, requiring extensive shielding, with waste management typically involving managed storage for years or even decades before further processing is conducted [33].

When a reactor reaches its end of life stage, the decommissioning process begins after its final defuelling. The reactor is dismantled and ideally the site can eventually become re-purposed. During the decommissioning process significant volumes of waste are produced. More modern reactor designs, such as the current Generation IV fleet, have post-closure, expedited decommissioning and waste-minimisation as central aspects to their design [34]. However, legacy reactors, such as the UK’s Magnox fleet, have and continue to produce, a large volume of nuclear waste awaiting long-term storage and final disposal [35]. The NDA are seeking to dismantle facilities and decontaminate sites as soon as reasonably practicable, moving radioactive and hazardous wastes generated in the decommissioning process into safe storage [36]. The current preference is to enter a programme of ‘continuous decommissioning’, with remediation deferrals made only where there is a significant safety benefit achieved by not leaving sites or facilities in a state of managed stasis (care and maintenance), for example to reduce radiation hazard through radioactive decay [36].

The activities of the UK in the 1940’s and early 1950’s pioneered the global nuclear revolution. The world’s first commercial nuclear power reactor at Calder Hall in 1956 was a landmark achievement [37]. Such programmes were initiated by the drive for ‘energy too cheap to meter’, alongside the simultaneous production of plutonium (Pu), for the UK’s nuclear weapons programme [38]. However, despite this huge technological achievement in such a short space of time, there was not any substantial consideration of the arising wastes, or any planning and preparation procedures. This has resulted in significant volumes of legacy radioactive wastes which are poorly documented [39]. This waste inventory is further compounded by the waste

arisings associated with current and future reactor operations, fuel reprocessing and decommissioning activities. Similar problems can be found in other early nuclear superpowers, including the United States [40], Russia [41] and France [42]. Consequently, there are substantial volumes of assorted wastes; much of which is held in underground storage ‘vaults’ and/or sealed drums awaiting sorting, conditioning and consigning to final disposal [43].

1.2.1.3 Sorting and Segregation

It is crucial to understand, to a high-level of compositional accuracy, the individual contents of mixed nuclear wastes in order to facilitate the consigning of the items to different appropriate waste-streams. Efficient and correct sorting is important to protect against expensive wrongful assignments of material, especially materials that have recycle value or could behave problematically in stored wastes [9, 44].

Waste stream identification can be resolved by the process of sorting and segregation [30]. Here, waste items are characterised both in terms of their radiometric and material properties in preparation for subsequent handling and processing activities. Assessments of the waste are made on the basis of the waste classifications and Waste Acceptance Criteria (WAC) guidance [30]. In the UK, waste classes, broadly, are categorised on the basis of radioactivity per unit mass [45]. In addition to the radiometric regulations determining waste classification, each waste item must be assessed on material characteristics, as defined by the WAC. Evolution of waste packages in storage is inevitable, as radioisotopes decay, but principally as species and compounds react over time. Components of the waste matrix may degrade and generate adverse compounds such as uranium hydride (UH_3) [46], voluminous metal oxides, or expansive gases following the degradation of materials [47]. Material assessments reduce the risks associated with adverse reactions taking place within individual waste containers, helping to ensure that a high package structural integrity is maintained in storage and that each waste packages has a well detailed material inventory [31]. The NDA and its subsidiary Radioactive Waste Management Ltd. (RWM) provides guidance detailing chemicals and compounds which must not be mixed and provides specifications for packaged wastes [9]. Avoidance of potentially problematic mixes through accurate characterisation during sorting and segregation reduces or even removes such problems arising in storage and disposal.

The general guidance from the IAEA states that waste should be classified into distinct waste classes [30]. In the UK nuclear waste is arranged into 5 classes: Very Low Level Waste low volume (VLLW, low volume), Very Low Level Waste high volume (VLLW, high Volume), Low Level Waste(LLW), Intermediate Level Waste (ILW) and High Level Waste (HLW) [48].

Very Low Level Waste

Very Low Level Waste (VLLW) is the least dangerous category and can safely be disposed of via municipal, commercial or industrial waste streams [49]. It is a subcategory of LLW, which itself is divided into two further subcategories: low and high volume. Low volume VLLW, are wastes of less than 0.1 m³, containing less than 400 kBq of total activity. For high volume VLLW, more than 0.1 m³ is permitted, with a total activity of 4 kBqkg⁻¹, or 40 kBqkg⁻¹ if the waste contains exclusively tritium. The primary reason for the volume discrepancy is to place measures on the volumes of VLLW that can be deposited at individual landfill sites.

Low Level Waste

Low Level Waste (LLW) may be defined as waste which does not exceed 4 MBqkg⁻¹ of alpha or 12 MBqkg⁻¹ of beta/gamma activity [49]. Operational examples of LLW include plastics and metallic objects such as tools [50], which may have come into contact with radioactive emitters and are thus contaminated. Decommissioning examples comprise typically of contaminated rubble and soils derived from plant closure activities [50]. Currently, it costs £7.5k to store a cubic metre of LLW [51] and there is an estimated future arising of 1.48 million cubic metres of LLW waste awaiting disposal in the UK alone [52].

Intermediate Level Waste

Intermediate Level Waste (ILW) is defined as waste which exceeds the upper level of LLW class, but is not heat generating [53]. Typical constituents of ILW are reactor components and graphite used as neutron moderators [54]. Currently, it costs £50k, to store a cubic metre of ILW [11]. Whilst ILW does not account for the same volume of waste as LLW, there is nonetheless substantial volumes. For example, there is an estimated 99,000 tonnes of irradiated graphite [55] destined for ILW waste storage, equating to approximately 136,000 m³ [56]. Some 247,000 m³ ILW is anticipated in total [52].

High Level Waste

High Level Waste (HLW), carries the same Bqg⁻¹ as ILW, but is additionally heat generating [57]. HLW represents 95% of waste inventories total radioactivity, but less than 5% of the total volume. Broadly, it is produced spent fuel used in a reactor, or waste produced from the reprocessing of nuclear fuel [58]. Spent fuel typically consists of uranium, or plutonium; having been enriched to sustain the fission process [33].

The total and predicted future volumes of each waste class is summarised in Table 1.1. The volume is very substantial and highlights the scale of the UK's nuclear waste management challenge.

Waste Category	Volume (m ³)		
	Reported (as of 1 April 2019)	Estimated Future Arisings	Lifetime Total
HLW (>10 Gbq/kg)	2,150	-760*	1,390
ILW(<10 GBq/kg)	102,000	145,000	247,000
LLW (<12 MBq/kg)	27,400	1,450,000	1,480,000
VLLW (<100 kBq/kg)	1,040	2,830,000	2,830,000
Total	133,000	4,420,000	4,560,000

Table 1.1: Current, future arisings and lifetime total expected volumes of different nuclear waste categories. All values are a direct reproduction from the Nuclear Decommissioning Authority report [52]. * *This negative value reflects the future conditioning of waste volumes.*

1.2.1.4 Waste Processing

Arising nuclear wastes are subject to a number of processing steps to ensure conformity for on-wards storage and eventually disposal. The flow-sheet followed for processing will vary depending on the waste being handled, and accounting for its material make-up as well as activity. There are however, some universally in-common processing steps, which are covered herein. The processing steps are not presented in any particular order.

Size Reduction

Wastes are size reduced (compacted) to ensure they meet the further treatment and packaging requirements. In addition, this can help to reduce waste volumes as far as reasonably practicable, thus reducing storage costs [31].

Decontamination

Decontamination may then be required to remove radionuclides to reduce activity and ensure waste meets the WAC guidelines satisfactorily [31]. For example, chemical decontamination may be applied to segmented components to dissolve contaminants contained within outer coating layers [59].

Waste Treatment

Waste ‘treatments’ are then applied to alter their characteristics, to enable them to meet the requirements of the subsequent management, for example recycling and disposal [31]. Examples include the incineration of certain solid wastes and the evaporation of liquid wastes.

Waste Conditioning

Conditioning and immobilisation is then used to physically or chemically fix wasteforms enabling their prolonged safe storage and transport [31]. Examples include the grouting of metallic ILW wastes produced by cladding decanning during Magnox fuel reprocessing [60]. These metallic

wastes typically contain assorted Magnox cladding swarf that for many decades were ‘fixed’ by grouting them into 500 L stainless steel drums, using a specific grout mix, including Old Portland Cement (OPC) and Blast Furnace Slag (BFS) [61].

1.2.1.5 Waste Storage

Once packaged in suitable containers wastes may be stored for long (multi-decade periods) in maintained and shielded waste storage facilities. ‘Storage’ is different from ‘disposal’, as in disposal waste should not be retrieved [31]. In essence, it is accepted practice to store wastes until an appropriate long-term disposal route becomes available. An example of a ‘modern’ intermediate waste store is the Trawsfynydd ILW Store, photographed in Figure 1.3.



Figure 1.3: Photograph of the Trawsfynydd ILW Store, taken from [62]. Locally mined slate was used on the exterior of the building to improve the aesthetics and support the local economy.

The 500 L drum has been widely utilised for the packaging and interim storage of conditioned Low Heat Generating Wastes (LHGW) and will be one of the primary waste containers stacked within a future Geological Disposal Facility (GDF) within a transport ‘stillage’ (of four such containers) [63]. A large inventory of waste from thousands of wastestreams has already been packaged into 500 L drums [64]. However, the degradation of the integrity of such waste containers prior to our current understanding of wasteform evolution is of particular concern. This waste, much of which has been packaged for decades, lacks detailed records and must be re-characterised for safety and

assurance reasons [64]. This is a further justification of the importance of accurate waste assay.

Waste assay and package assurance are both crucial steps in ensuring compliance with the eventual WAC on material entering the facility. It is therefore of paramount importance that a suitable suite of automated characterisation tools are developed to ensure that waste packages meet these demands [65].

A large volume of legacy nuclear waste is contained within Active Waste Vaults (AWV), such as the Berkeley vaults in Gloucestershire, UK or the numerous vaults present at each Manox and AGR station. As discussed, in the early development of the nuclear industry, little regard was given to nuclear waste and its long-term consequences. In the case of the Berkeley vaults, the majority of this active waste came from the former Berkeley nuclear power plant, which was decommissioned around 30 years ago [66]. The waste is currently being extracted by robotic systems, as shown in Figure 1.4, to be packaged and relocated in an Interim Storage Facility (ISF) [67]. ISFs are intended to be a short-term storage solution of approximately 100 years [68], for waste until a GDF becomes available [31].



Figure 1.4: A photograph of the retrieval operation inside the Berkeley vaults [67]. A wide variety of wastes can be seen, including pipework, PPE and construction rubble.

1.2.1.6 Waste Disposal

The final destination of the UK's nuclear waste inventory is a Geological Disposal Facility (GDF) [69]. Figure 1.5 shows an artists impression of a UK-based GDF. The multitude of waste packages,

of various different designs containing material derived from across the entire UK nuclear estate, will eventually be stored hundreds of meters underground in a GDF. Once inside the GDF, radioactive waste can decay naturally, over very long geological timescales, without reaching the surface and causing any detrimental effects to the surface biosphere [69]. Currently, in the UK, an appropriate site is being sought via a process of community volunteerism to host the GDF. This is very important, as not only must the geology meet certain criteria and no structural weaknesses e.g. faults, but it must also be accepted and supported by a host population for >100 years. At the time of writing, working groups in Theddlethorpe, Lincolnshire, UK, are currently investigating the possibility of hosting a GDF [69].

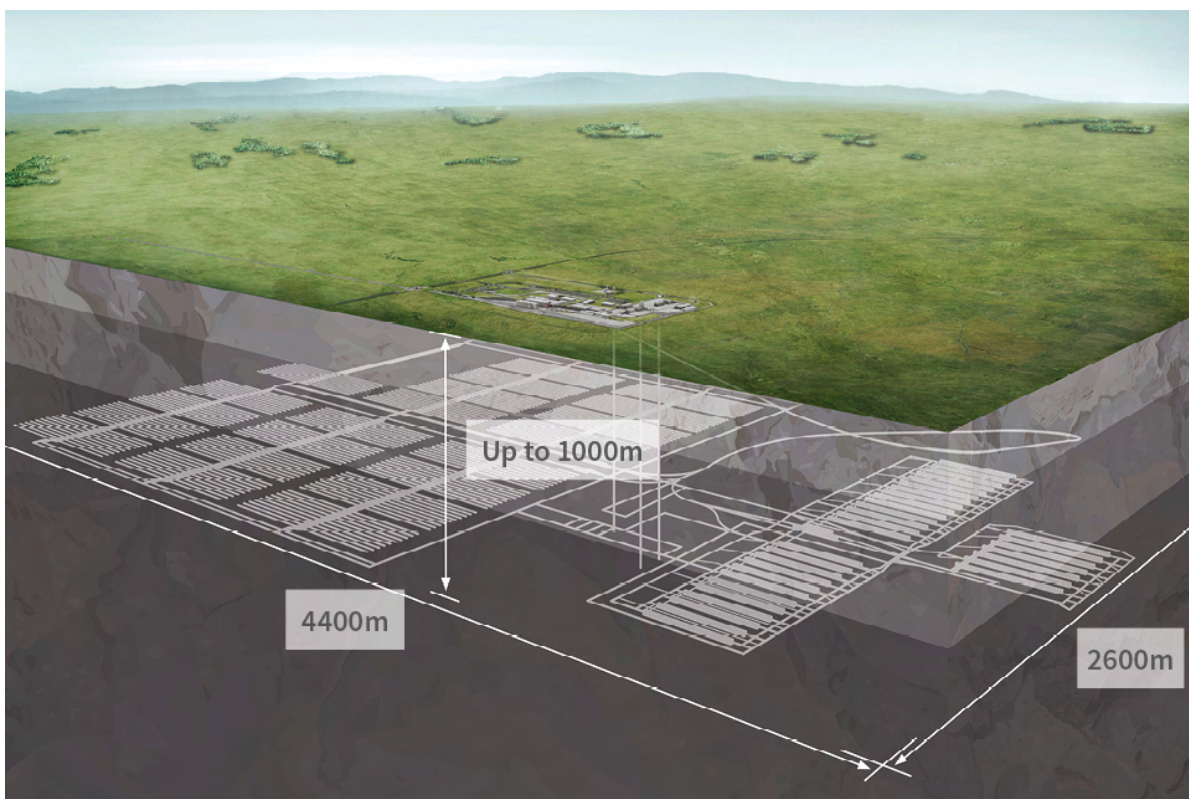


Figure 1.5: Artists impression of the proposed GDF. Image taken from [70]. The spacing of waste volumes is partly constrained by rock strength, heat generation and criticality risk.

The UK also has a low level waste repository (LLWR) near the village of Drigg in Cumbria [71]. LLWR is a surface disposal facility for LLW and some forms of old ILW. By comparison to a GDF which may still be decades away for the UK, the LLWR has been in operation since 1959 [71]. It provides a viable and cost-effective disposal solution for these lower activity, lower hazard wastes [71]. Given the huge cost difference between consigning waste to a GDF versus the LLWR, it is hugely important that waste materials are accurately sorted and segregated to avoid wrongful consignment for disposal. This is an issue that could needlessly cost the UK taxpayer many £Bn

if not suitably addressed.

Nuclear waste is by no means a UK-centric problem, across the globe there is some 6,317,000 m³ of nuclear waste awaiting a long-term storage or disposal solution [72]. This volume is set to increase substantially over the coming decades, partly driven by the global de-carbonisation agenda. Hence, there is a global requirement for long term disposal. A growing number of older reactors are currently at, or in the very near future, entering the decommissioning stage of their lifetime. These reactors will join the near 200 which are already shut down globally [73], with the majority awaiting decommissioning and dismantling. Accordingly, there is a potential technology export opportunity for the UK. Because our nation is arguably the first to make a concerted effort on reactor decommissioning, any useful technologies developed for the processing and separation of assorted wastes in the UK, will likely have excellent export potential to countries yet to address their own decommissioning challenges.

1.3 An Opportunity for Robotics

Owing to the hazardous materials routinely identified in nuclear waste - and the shear volumes involved, it would be prudent to resolve the waste sorting and characterisation dilemmas without human involvement. This represents an opportunity for the application of remote or robotic systems to handle the tasks. There are numerous robotic systems already available off-the-shelf, that the nuclear decommissioning and waste management sectors could exploit. One viable option, is the application of robotic manipulators. These arm-like robotic systems, as photographed in Figure 1.6, could, in effect, replace and enhance human interventions in the radioactive waste lifecycle. Over the past decades, robotic manipulators have become commonplace in manufacturing and are extensively used across industrial sectors from aircraft manufacturing [74] to cake decorating [75]. Such robotic systems are currently replacing and augmenting the human workforce. A number of commercially available robotic arms exist, such as those produced by KUKA [76], FANUC [77], ABB [78] and Kinova [79]; demonstrating high levels of repeatability and sub-millimetre positional accuracy. This makes them excellent platforms for tasks involving repeated motions and precise positioning. Robotic manipulators are also routinely used in hazardous environments, such as paint workshops [80] and bomb disposal [81]. Crucially, they have demonstrated a capability of tolerating radioactive environments. A recent example is the work of Zhang et al. who demonstrated the radiation tolerance of a KUKA LBR iiwa R800 robotic manipulator, showing it operated functionally in front of a 20 TBq Co-60 source until a dose rate of 164.55 Gy was received over a period of 16.8 h [82]. Reportedly, damage to one of the joints optical encoders caused the system to fail, as the system could no longer localise its joint space positioning [82]. It has been proposed that damage to radiation exposure limited components, such as optical equipment, could be replaced after a certain operational life has

expired [83], allowing for the system to be continually used. The received dose of 164.55 Gy is equivalent to 8250 workers maximum permitted dose for an entire year, in the UK, making a robotic manipulator an attractive option for nuclear waste sorting.



Figure 1.6: Photograph of a KUKA KR150 robotic manipulator.

It is recognised that robotic systems could be implemented at all stages of the nuclear waste life-cycle. However, it is the proposition of this thesis that within the area of sorting and segregation that the greatest step change in performance could be delivered. Current sort and segregation operations use largely manual, labour intensive, human-led processes, with workers handling wastes with air-fed suits and other personal protective equipment (PPE) [11]. Geiger-Muller (GM) tubes are used to approximate the radioactivity levels of waste and samples are sent off-site for ex-situ laboratory analysis [11]. Sub-sample laboratory analysis takes time and adds cost and risk related to handling and transport. Hence, conducting more analysis in-situ is seen as highly desirable for reducing or removing programme delays introduced by ex-situ lab analysis. However, the uncertainties surrounding these processes can lead to significant human error and consequently excessive conservatism are placed on measurements and operator decisions. These uncertainties

often lead to lower level wasteforms being packaged in higher activity containers, resulting in significant cost increases¹. These activities introduce numerous hazards due to the necessity of the close proximity of the workforce to sources of ionising radiation. Therefore, a system capable of accurately and autonomously consigning waste objects to appropriate wastestreams could introduce tremendous financial and safety benefits.

1.3.1 Robotics for Sort and Segregation

Robotics in the nuclear sector could deliver dramatic cost savings. The primary reason is that there is currently a substantial cost involved with sending people into radioactive environments. They must be provided with personal protective equipment and be supported by a health physics monitoring team. This means in some scenarios, a single person goes into an active environment, with a support team of as many as 10 people. Such costs are substantial. The expectation for robotics in nuclear, is that by removing humans from the active environment and letting robotic solutions take over, these costs could be saved. Therefore, costs are reduced because there are not so many people required to complete the cleanup operations. In addition, a robotic system delivered correctly has a higher efficiency and throughput than an equivalent person. A robot can operate for 24 hours a day, 52 weeks per year without rest. This, is in combination with the fact a robot can take on the order of 10000 times more radiation than a human being. However, this remains a grand vision for nuclear robotics. Pragmatically, at the moment robotics technology is not well enough developed to deliver significant costs savings, because the reliability, repeatability and resolution of fault scenarios are current limitations. This is why there is a need for research and development. In the future, it is anticipated robotics could operate with human supervision on a ratio that is a few human supervisors to one robot. This would add a redundancy in fault scenario detection, ensuring the safety of the system. Subsequently, such technology could be developed further towards a one-to-one relationship between robot and supervisor. Ultimately, a situation may be reached where one human supervisor and several robotic systems are all working simultaneously. The supervisor only taking control of the robots when one of them starts to develop a fault scenario that it cannot be fixed on its own. The concept of this is illustrated in Figure 1.7.

¹There is a significant fiscal disparity for waste storage between waste categories, as discussed in section 1.5, VLLW costs £1k per cubic metre, LLW costs £7.5k per cubic metre and ILW costs £50k per cubic metre.

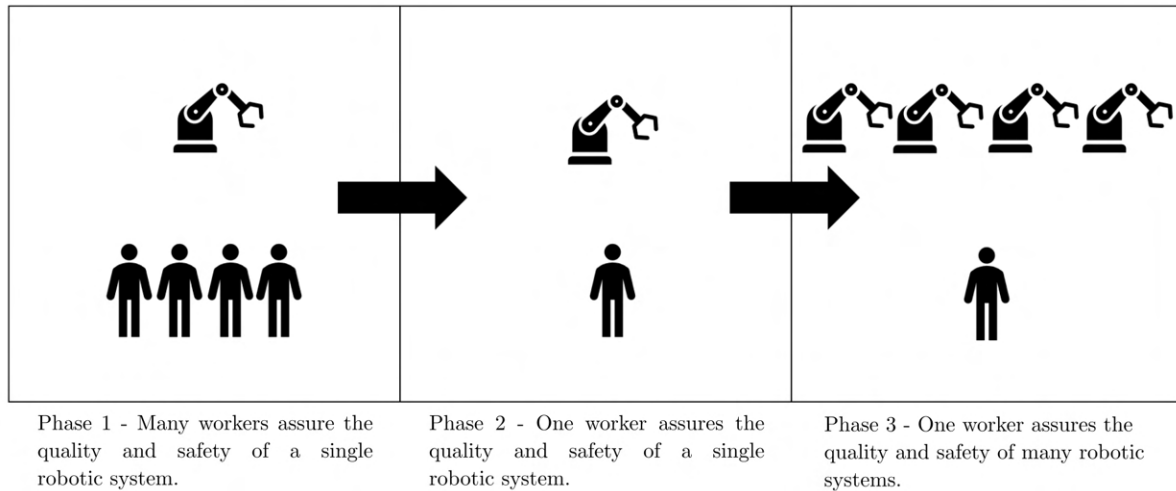


Figure 1.7: Illustration detailing the progressive use of robotic systems within nuclear waste processing.

Conceptually, robotic manipulators could be used to accelerate and improve the sorting and segregation process. They are routinely used for grasping and manipulating objects [84]. In this way, they could be applied to autonomously grasp waste objects, manipulate them and place them into storage. More powerfully, it is conceivable to imagine, a suite of sensory techniques which could be carefully selected to accurately determine both material and chemical characteristics. Thus, an integrated robotic system could autonomously delivering the requirements of waste classification and the WAC. The ultimate goal of this PhD project is to develop the technology in terms of automation and sensory integration of Commercially available Off The Shelf (COTS) components, to pave the way towards autonomous nuclear waste sorting. Each chapter offers a progression of integrated technology which could be applied to the problem of waste sorting. Ultimately, these components comprise of an end to end solution for characterising waste both in terms of their material, radiometric and mass properties, facilitating waste stream identification for long-term containment.

THEORY OF ROBOTIC TECHNIQUES AND CHARACTERISATION

Chapter 1 highlighted the challenges of nuclear waste sorting and segregation, documenting the requirements for long-term waste disposal. A fully-autonomous, robotic system is sought to deliver a step-change in characterisation accuracy and safety, while accelerating an otherwise time-consuming, labour intensive, manual process. The development of such a system, requires a capability to both characterise and handle nuclear waste articles. This chapter seeks to explore the fundamentals of the techniques required for fulfilling an in-situ, fully autonomous waste sorting and segregation solution. As an initial point of reference, it is important to discuss ‘the state of the art’ in the waste sorting sector. Hence, some of the key developments in the robotic waste sorting space will be covered in this chapter. The majority of literature focuses on municipal waste stream recycling, which has some of the major challenges, but reduced regulation and accuracy requirements associated with it. However, one identified system pertains to nuclear waste sorting - though not fully-autonomous, it still faces some of the challenges associated with radioactive waste sorting, such as accurate waste stream identification and radiation tolerance issues. All have made important developments in the field which must be explored, although have technical shortcomings which must be addressed within this thesis. Primarily, these shortfalls centre on careful automated processing, without contamination spread and highly accurate characterisation. For an autonomous radioactive waste sorting system to fulfill these requirements, handling and grasping of objects will doubtless be essential. Modern robotic techniques are apt for such processing and could therefore feature heavily within nuclear waste sorting and segregation. Therefore, the basic underlying theory of robotic manipulator and control is examined, as an integral component of this thesis. These robotic systems can be augmented with the application of vision and photogrammetry techniques, which are employed to facilitate robotic sensing and grasping operations. Hence, fundamental photogrammetric tech-

niques are addressed, supporting a grasping methodology. Further to this, such systems could support the integration of sensors apt to characterise waste in-situ. Therefore, characterisation and detector technology which could be robotically deployed may be useful. It is evident that both radiometric and material identification will be crucial. Hence, the science of radiation detection methods will be discussed in detail. Following this, material analysis methods will be covered, focusing on X-ray Fluorescence (XRF) and Laser Raman Spectroscopy (LRS). These were chosen as emerging systems and devices available for robotic deployment, enabling the development of a robotic, in-situ and autonomous characterisation toolkit.

The following chapter is based on the methods, results and discussion presented within the following previously published, peer-reviewed articles:

S.R. White, D.A. Megson-Smith, K. Zhang, D.T. Connor, P.G. Martin, C. Hutson, G. Hermann, J. Dilworth, T.B. Scott, "Radiation Mapping and Laser Profiling Using a Robotic Manipulator", *Front. Robot. AI*, 26 November 2020.

S.R. White, P.G. Martin, D.A. Megson-smith and T.B. Scott, "Application of automated and robotically deployed in-situ X-ray fluorescence analysis for nuclear waste management.", *Journal of Field Robotics*, accepted.

2.1 Introduction

2.1.1 State of the Art Waste Sorting Systems

It should be recognised that there are a number of commercial waste sorting systems that are currently available. These exist primarily outside of the nuclear sector, where autonomous systems are commonly used to sort mixed wastes [85]. Prominent examples include those in the recycling industry where separation of plastics is essential to the sorting process. There are a wide variety of techniques to separate individual plastic types. These include thermal-adhesion sorting, float-sink sorting, dry zig-zag sorting, electrostatic sorting, froth flotation sorting [86]. Such implementations would be inappropriate for radioactive waste streams owing to use of air streams and motions required, leading to a high potential for contamination spread. The mechanism for physical radwaste processing should be slower, more precise and not spread contamination.

In academic research settings, waste sorting is currently being thoroughly investigated. Stollo et al. presented an AI based approach to household waste sorting [87]. Demonstrated was a robotic

arm based system with waste fed by a conveyor. Sensing was achieved using a combination of a near infrared camera and RGB camera. The team were able to successfully distinguish between 7 different materials and remove them from the conveyor. Such a system may be complementary, but not complete for nuclear waste sorting and segregation owing to the potential of misclassification, something which is acceptable for municipal waste, but would not meet the stringent acceptance criteria mandated for a nuclear system.

More applicable to the nuclear waste sorting problem, is the Box Encapsulation Plant (BEP) at Sellafield Ltd. which is being designed to receive, process and package legacy ILW remotely using KUKA robotic manipulators [88]. The work is manifesting itself as a series of experimental trials to show that waste can be processed using robotic systems. Trial work has sought to demonstrate the use of a combination of both “pre-programmed” fully-autonomous and teleoperation modes of operation. A wide variety of robotic tooling is shown to perform a range of tasks including grasping, bolt removal and spraying tasks. Success of initial trials has proved robotic manipulators and associated technologies are viable for nuclear waste processing [89]. Figure 2.1 shows the BEP robot system.

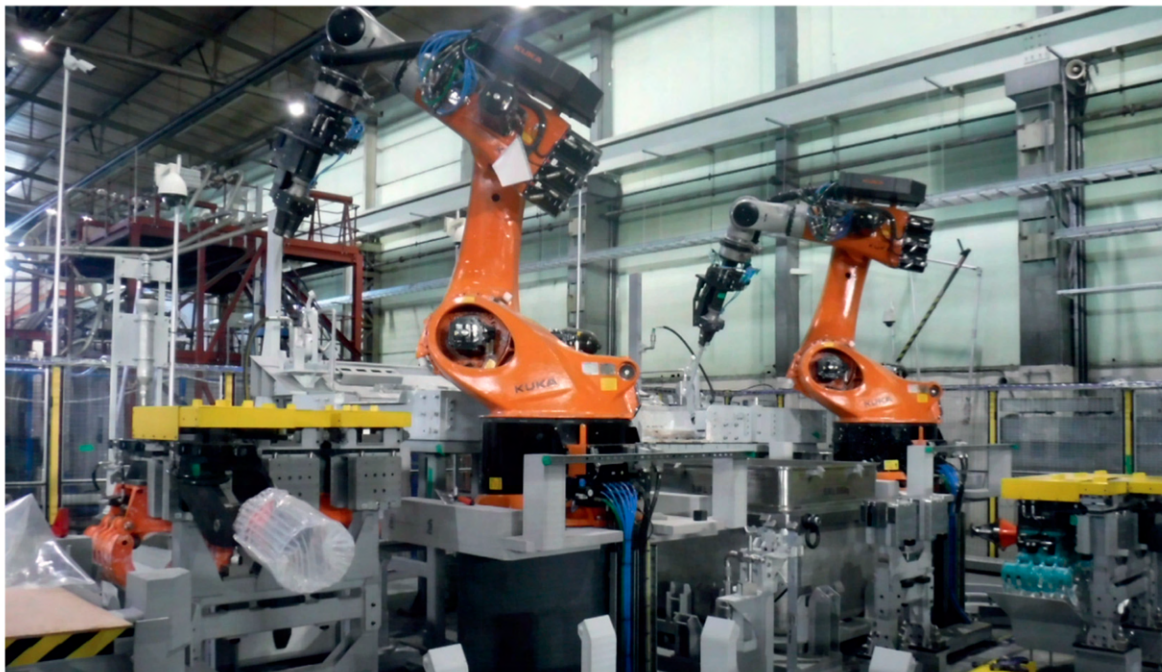


Figure 2.1: Robotic systems used for the BEP project. Taken from [90].

BEP represents a pioneering radioactive waste sorting and handling system. However, it does not offer the solution desired from this work. While the waste is sorted robotically, much of it is not completed autonomously, depending on teleoperation, prior information of waste and visual

inspections [88].

2.1.2 Theory Workflow

The process of sorting and segregating nuclear waste can be broken down into two major classification objectives: radiometric and non-radiometric categorisation. At a high level, the UK's nuclear waste classification guidance distinguishes waste inventories in terms of activity per unit mass [91]. This directs objects towards the appropriate waste stream, classifying waste on the basis of radioactivity. Evidently, lower activity wastes containing fewer hazardous materials are easier to sort. Such wastes could be sorted in municipal waste sorting and recycling routes. Higher level wastes pose an increased environmental and societal risk, requiring GDF disposal for millennia. Therefore, additional care must be taken in ensuring the long-term safety of waste packaging and contents, thus avoiding the deleterious effects of waste evolution discussed in chapter 1. The solution is to clearly identify and fingerprint all material and chemical contents of each waste package. This way chemical reactions and other post-storage side-effects can be analysed such that stored wastes do not exhibit negative evolutionary behaviours.

It is envisaged, a robotic manipulator based system could analyse assorted waste objects on a sorting table. This analysis would characterise waste objects in terms of radioactivity and material composition, before subsequent disposal routes and mechanisms may be determined. Chapter 1 noted remote and robotic systems are ripe to be exploited in hazardous environments such as nuclear waste sorting. Robotic manipulators serve a dual purpose within this research. Firstly, they act as the carrier platform for in-situ sensing and characterisation tasks prior to waste sorting. This means that robotically deployed sensors can be used to provide an overview of the radiometric, material and physical form of waste objects. Secondly, they can be used for handling and manipulation objectives, removing wastes and directing them to their long-term disposal route.

Robots are commonly used to complete motions and 'pick and place' operations in structured environments. In manufacturing they will routinely move components between locations, following pre-programmed paths. A comprehensive introduction to robotic systems, namely robotic manipulators is provided in section 2.2. However, in a sorting and segregation scenario, wastes are likely to be distributed randomly across a defined sorting area. In such an unstructured environment, the use of robotic systems requires additional perceptive technologies. These technologies can enable the robot to understand its environment dynamically, exhibiting a degree of intelligence by making sensory input based decisions. One such perceptive technology robotic systems can be augmented with are depth cameras, providing the robotic system with a 3 dimensional interpretation of its surroundings. This vision based feedback enables robots to move within unstructured environments, directing precision motions. Such techniques are employed extensively within this

thesis and therefore the principles of depth cameras and dynamic robotic motion are explored within section 2.3 and 2.4.

Alongside vision-based perceptive technologies, robotic systems can also be augmented with characterisation based sensory techniques. Integration of radiation detectors can be used to provide robotic systems with a radiometric categorisation capability. These may be used to determine the radioisotope, which provides additional information on waste package contents. A detailed comprehension of radiometric sensing technologies may be found in section 2.5. Ostensibly, non-radioactive materials would be undetectable using radiometric techniques. Accordingly, material categorisation techniques must be used to identify the metals, chemicals and compounds, present within nuclear waste. The aim of this is to ensure the structural integrity of each waste package is maintained, by not introducing problematic materials which may react or corrode inducing volume expansions of waste in containment [9]. There are a number of techniques which could be used to facilitate these waste characterisation requirements. Crucially, any chosen technology must be remotely deployable on a robotic manipulator platform. Selected for this work were X-ray Fluorescence (XRF) and Laser Raman Spectroscopy (LRS). The justifications of these choices and theoretical understanding is given in section 2.6.

2.2 Robotics

Robotic systems could represent a very powerful solution to many problems within the nuclear industry. They are spatially precise and repeatable platforms. As chapter 1 showed, they have also been demonstrated to have high radiation tolerances [82]. This means operable in environments which are considered too dangerous or undesirable to send humans, as is the case for many nuclear and/or radiological scenarios. Sensors integrated on robotic manipulators could take advantage of this, providing the ability to remotely inspect environments, or in the case of this work, assorted wastes. This could facilitate the detailed and high fidelity characterisation of wasteforms in advance of handling. As already identified, such handling could also be achieved by a robotic manipulator system with an attached gripper.

This section seeks to provide a basic understanding of robotic manipulator functionality and control. The two robotic manipulators discussed within this thesis, are the KUKA KRC2 KR150 and the KUKA LBR iiwa/MED¹. The KR150, photographed in Figure 2.2, is an industrial specification manipulator, with a 150 kg payload capability and a 2.7 m reach. The LBR, photographed in Figure 2.3, is a collaborative (see section 2.2.5) manipulator, with 14 kg payload capabilities and 0.82 m reaches.

¹The ‘iiwa’ and the ‘MED’ are different robotic arms, but their kinematic functionality and control methodology is exactly the same. These arms will be referred to as simply the ‘LBR’ herein.

2.2.1 Robotic Manipulator Fundamentals

At a fundamental level, robotic manipulators have rigid 'links' which are connected serially together by rotational axis joints. Examples of rotational axis joint positionings for the KR150 and LBR arms are given in Figures 2.2 and 2.3. They have a mobility capability which is described by 'degrees of freedom'. Degrees of motion for robotic manipulators may broadly be separated into two classes, translational and rotational envelopes. These are presented as follows:

- Translational envelope (Cartesian positioning)
 1. Motion in cartesian x axis
 2. Motion in cartesian y axis
 3. Motion in cartesian z axis
- Rotational envelope (Tait-Bryan Angles)
 1. Rotation about the x axis
 2. Rotation about the y axis
 3. Rotation about the z axis

This means that a 6 DoF robotic end-effector has the capability to reach any combination of position and rotational orientation within its working envelope. A 7 DoF robotic arm has the additional capability of reaching the positions of the 6 DoF case, but in more than one possible orientation. This capability is often referred to as an 'elbow roll' [92] and can increase flexibility for arms required to work in confined spaces.

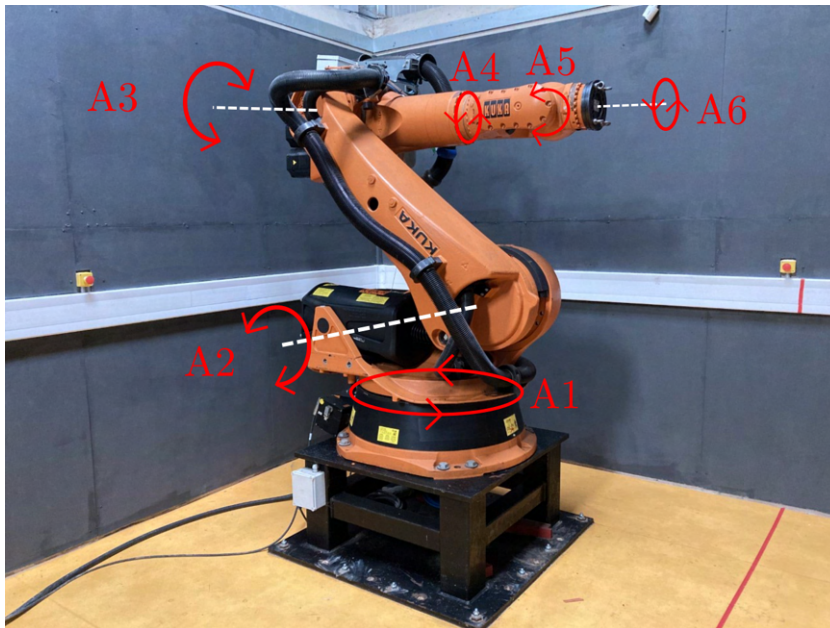


Figure 2.2: Photograph of the KUKA KR150 ('Betty') used for experimentation. Overlaid are the axis numbers and positions.

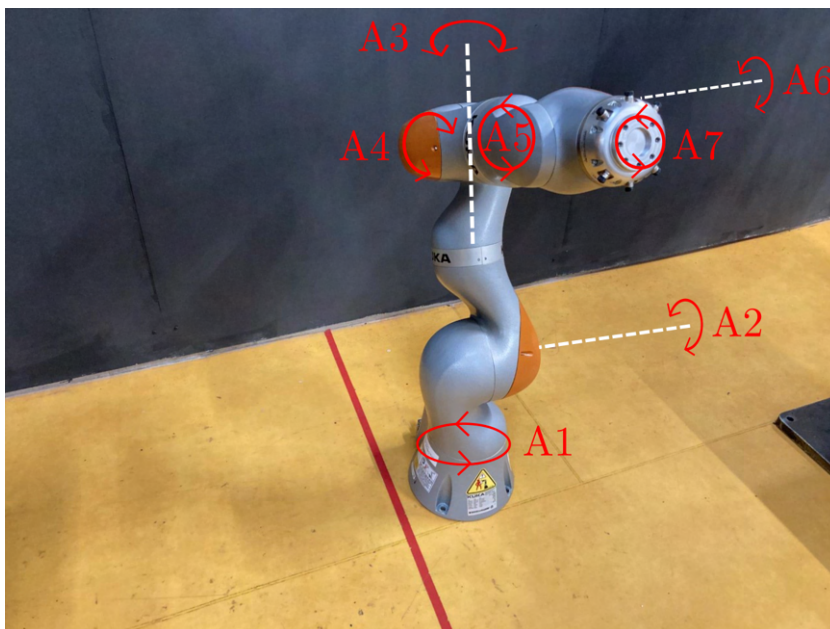


Figure 2.3: Photograph of the KUKA LBR iiwa ('Alfie') used for experimentation. Overlaid are the axis numbers and positions.

2.2.1.1 Robot Kinematics

Robot kinematics are the cornerstone of robot manipulator control. Each rotational joint on a robotic manipulator is a key feature of the kinematic chain required to action the aforementioned degrees of freedom. Forward kinematics take the rotational joint angles and determine the end-effector positioning. Hence, they define how the joints of the robot should be orientated to achieve axis based motions. The basis is grounded in mathematical transformations, whereby known joint angles and link lengths, determine the cartesian co-ordinates of the end of the robot arm.

The Denavit-Hartenberg (DH) approach is one of the most commonly applied forward kinematics methodologies [93], so that will be discussed here. Each joint has an associated axis which is defined as follows:

1. Z axis (Z_i), is defined as the axis of rotation of a joint (i).
2. X axis (X_i) is defined as the axis at the common normal between Z_{i-1} and Z_i .
3. Y axis (Y_i) is defined as the normal to the X and Z axis.

An example of DH co-ordinates and robotic joint connections for a 6-axis robot are shown in Figure 2.4. Such diagrams are commonly used to help understand robotic joint configurations. Transformations may be defined with additional information including four additional parameters. These parameters are d , the distance between Z_{i-1} along the common normal, θ , the angular difference between X_{i-1} and X_i , r the length of the common normal, α the angular difference between Z_{i-1} and Z_i . Therefore the i^{th} joint has the transformation T_i which applies to it, as given in equation 2.1 [94].

$$(2.1) \quad T_i = \begin{bmatrix} \cos(\theta) & -\sin(\theta)\cos(\alpha) & \sin(\theta)\sin(\alpha) & r\cos(\theta) \\ \sin(\theta) & \cos(\theta)\cos(\alpha) & -\cos(\theta)\sin(\alpha) & r\sin(\theta) \\ 0 & \sin(\alpha) & \cos(\alpha) & d \\ 0 & 0 & 0 & 1 \end{bmatrix}$$

To determine the final position of the end effector, a linear combination of transformations must be computed, as ΠT_i . The final matrix gives the rotational components of the end effector in the top left 3x3 matrix and the position in the top right hand 1x3 matrix.

Inverse kinematics are used to compute joint angles required to determine the end-effector positionings. For a 6 DoF robotic system, this can theoretically be computed analytically, however it is not possible at this time, owing to the non-linearity of the equations involved [95]. Instead, numerical methods, such as the Newton-Raphson method are used [96]. In the 7 DoF case, there

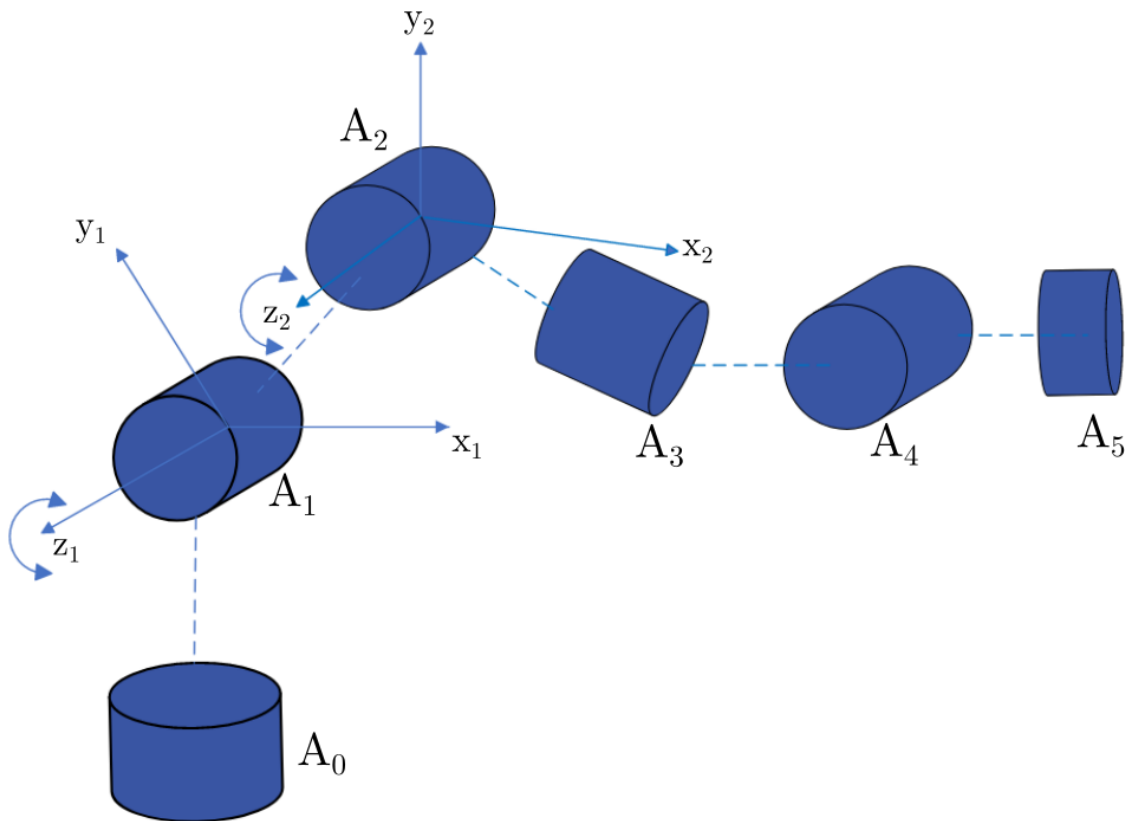


Figure 2.4: DH joint configuration diagram example for a 6 axis robot.

is no analytical solution, because there are in effect an infinite solutions for each end-effector positioning. Hence, numerical methods and optimisation procedures are invoked to determine solutions.

For all robotic applications detailed in this thesis, the standard KUKA kinematic control software was used. Hence, a comprehensive understanding of the inverse kinematics is not necessary, but is included for completeness.

2.2.2 Workspaces

Robotic control systems operate in different ‘workspaces’, which define programmatic control systems. The 3 workspaces used in this thesis are ‘joint space’, ‘cartesian space’ and ‘tool space’.

2.2.2.1 Joint Space

The simplest control mode for robotic manipulators is joint space, this is where the user defines the angles at which each robotic joint should be positioned. In a program, several joint positions

may be defined and the robot can move between each one. This is most commonly used to instruct the robot of a start position, or where the user wishes to define the precise pose of an arm.

2.2.2.2 Cartesian Space

Cartesian space is where the robot responds to positions in terms of a defined X, Y, Z co-ordinate base. The classic cartesian space is known as the 'world base', and is defined where the centre (0, 0, 0) position is at the centre of the robot base. The user may redefine the base, as appropriate for the given application through use of rotational and translational transformations. For example, if the workspace was a flat sloped surface, it may be helpful to define one co-ordinate axis along the slope.

2.2.2.3 Tool Space

In tool space, the co-ordinate base extends from the end of the 'tool' you are using. Tool space is useful where robot motions are required relative to the tool. In this way, cartesian motions are relative to the end of the tool, but more usefully, so are rotations. This means that any rotation in the Tait-Byran angles A, B, C are set relative to the end of the tool piece. Figure 2.5 shows the tool space transform. This may be an arc-welding tool, gripper or a sensor are augmented onto the end-effector of the robotic manipulator.

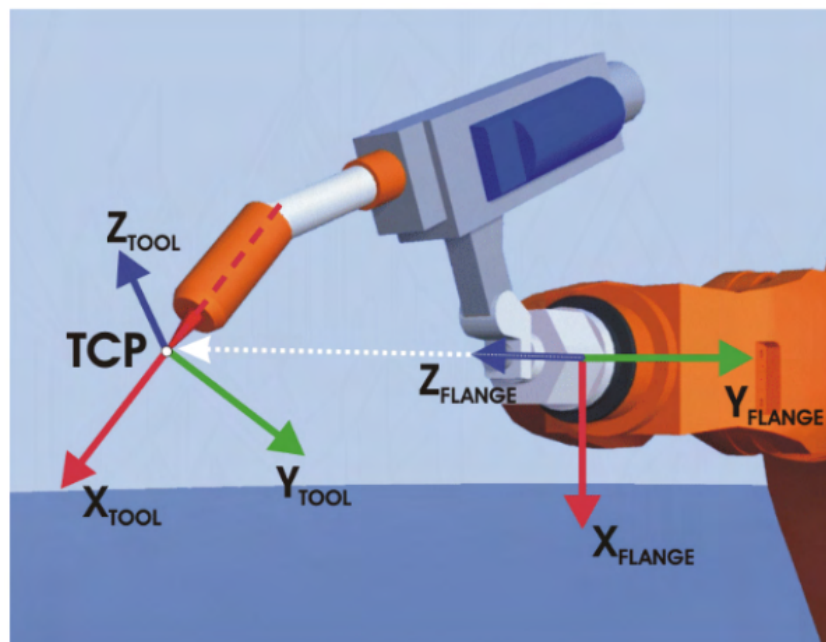


Figure 2.5: Robot tool implementation. Image taken from KUKA System Software 8.3 Operating and Programming Instructions for System Integrator's [76].

2.2.3 Robotic working envelopes

The constraints implemented by the fixed joints of a traditional robotic manipulator system mean there are limitations to the robot workspace. These constraints are known as the robotic working envelope, a feature that is important to be aware of ahead of programming. Figure 2.6 (a) and (b), show the working envelope of the KR150 and the LBR respectively.

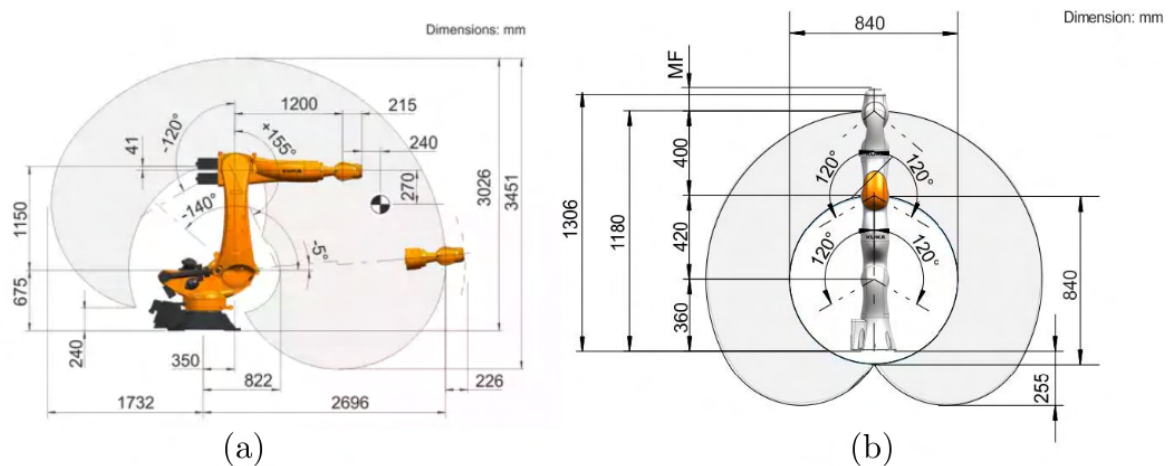


Figure 2.6: Working envelopes of (a) the KUKA KR150 and (b) the LBR. Taken from KUKA AG [76].

Ostensibly, it is important to ensure all robotic procedures are carried out within the workspace.

2.2.4 Programmatic Control

The aforementioned spatial configurations for positioning of robotic systems are designated by physical constraints, but also robotic programmatic control software. Control systems vary between robotic equipment, but the key principles remain the same.

On an industrial KUKA KRC2 robotic manipulator, such as the KR150, this control and positional feedback can be accomplished through the KSS KRC2 control software and Robotic Sensor Interface (RSI) packages. Programming is completed using the KUKA Robot Language (KRL). There are three main programming commands used in KRL, consisting of: point-to-point (PTP), linear motion (LIN) and circular (CIRC). PTP processes motions in joint space, taking the path of least resistance from one joint configuration to another. LIN performs linear motions on the end-effector within the cartesian framework. CIRC motions draw arcs, as defined by 3 co-ordinate positions: start, auxillary and end. Figure 2.7 represents these motions pictorially.

For use on the KUKA LBR, control can be accomplished via the KUKA Sunrise Toolbox (KST)

and positional information can be retrieved via a direct communication over a server connection. The same direct motions (PTP, LIN and CIRC) can be accomplished on the LBR system. Off-the-shelf, the KST uses JAVA to receive commands. However, for the research in this thesis, a PythonTM wrapper developed by Safeea [97] was used, delivering the same functionality as the KRL software.

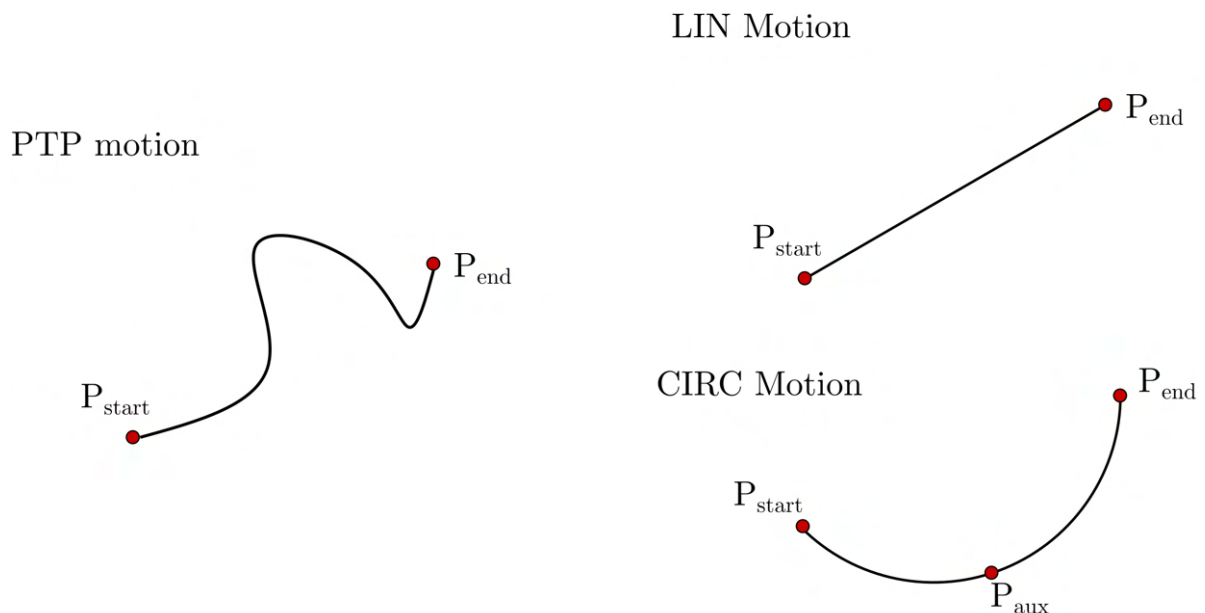


Figure 2.7: Representation of the PTP, LIN and CIRC motions used in robotics programming. The black line indicates the robot path between programmed positions.

2.2.5 Force Sensitive Robotic Manipulators

Recent trends towards the goal of industry 4.0 - the fourth industrial revolution, have led to the development of force sensitive, collaborative robotic manipulators, or so called ‘cobots’. These robot arms are designed to be inherently human-safe, detecting their surroundings and ensuring they do not harm human collaborators [98]. However, there is a recognisable use case for them within hazardous environments, minimising collisional impacts and thus reducing potential damage or contamination. In addition, it is theoretically possible to make in-situ mass measurements, through analysis of the force feedback (see chapter 8).

The force-torque sensing capability on the KUKA LBR arms is to within $\pm 2\%$ of the maximum torque [99]. This is possible, due to the force torque sensors which are located next to the gear box of each robotic joint. The precise details of the sensor are commercially protected, hence cannot be discussed further here.

2.3 Robot Sensor Integration

Robotic systems are frequently designed to make repeatable motions. In such robotic implementations, robots know the precise locations of tools and workpieces. For example a robotic welding system will be able to take an attached welding tool and weld objects on known paths. The objects are typically clamped in place, so the robot can perform the weld blind to external factors. This is fine in structured environments, such as production lines, but is undesirable for unstructured waste sorting applications. Waste is expected to arrive as an unstructured collection of objects, where the robot must identify objects, blind to any priori information.

The aforementioned robotic controls can be used to respond to sensor data. This robot-sensor fusion can be used to design more intelligent, autonomous systems. A prominent example of this, is the use of vision feedback to direct robotic systems to new locations. This vision feedback reduces the need for the robot to have tools and workpieces placed in pre-defined locations, giving robotic systems the ability to identify and locate such objects autonomously.

2.3.1 3D Visualisation Methods

3D visualisation methods represent a powerful sensory input for a robot-sensor fusion application. If implemented intelligently, visual feedback can be used by a robotic system to understand an unstructured environment. Algorithms and software can interpret such visualisations and subsequently direct robotic systems to appropriate locations, as required by the application. Such visualisation methodologies are explained in this section.

2.3.1.1 Photogrammetry Techniques

Photogrammetry is the process of creating software based 3D surface models from camera and positional data. It can be used to acquire depth images, which provide a 3D representation of a scene along with colour image information, in terms of pixels with Red Green Blue (RGB) additive colour model values. Therefore, depth images provide RGBD (Red Green Blue Depth) data, for each pixel. These can be used to generate a 3D representation of a photograph. There are two main varieties of depth camera which will be used in this thesis; stereo vision and LiDAR cameras.

2.3.1.2 Stereo Cameras

Stereo cameras attempt to mimic the depth perception of human eyes. By taking two images a fixed width apart, triangulation techniques can be used to resolve the distance to pixels across camera images [100]. A cutting-edge COTS example is the RealSense™ D435 stereo camera [101]. It is used within this thesis to generate 3D reconstructions of objects. An example of a depth image and corresponding RGB image is shown in Figure 2.8.



Figure 2.8: Example of photogrammetry. Left shows a RGB image of a model robotic arm. Right shows a depth camera interpretation of the same scene.

It is difficult to convey photogrammetry techniques on a 2D page. However, in software, it is possible to rotate the frame, revealing a clear 3D shape.

2.3.1.3 LiDAR Cameras

LiDAR cameras incorporate a camera as well as using the same principles as Time of Flight (ToF) laser ranging sensors. They send out pulses of collimated laser light and the time from the transmission of each pulse to receiving a return signal after reflecting off a surface is recorded. This enables the distance to the reflecting surface to be measured. The key difference is that with a LiDAR camera, it is simultaneously sending and receiving millions of signals every second, allowing for a pixel based collection of numerous distance measurements across a surface. This allows for the depth image to be reconstructed [102].

The Intel RealSense™ L515 was used in this work to collect RGBD photos, in a field of view of 70 deg x 55 deg [102]. Intel RealSense™ cameras are factory calibrated, hence it is unnecessary to calibrate them.

2.3.2 Pixel Space to Robot Space

Essential to dynamic robotics, in which the robot is not pre-programmed to move to specified locations, is the ability to use sensory feedback to direct robot positionings. Required, is an ability to convert from the camera resolved ‘pixel-space’ into robot-space. In essence, this is a capability to transform pixel numbers to the co-ordinate space of the robotic system. This allows for camera images to be processed, pixel co-ordinates defined and subsequent robot motions to be performed. One possible solution are affine transformations. Affine transformations are mathematical transforms which preserve colinearity [103]. Colinearity means that points

which were aligned before the transform are still aligned following the transform [103]. Affine transformations are linear combinations of rotations, translations, scaling and shears. In addition, the scaling of the points remains the same. An example of an affine transformation is shown in Fig 2.9.

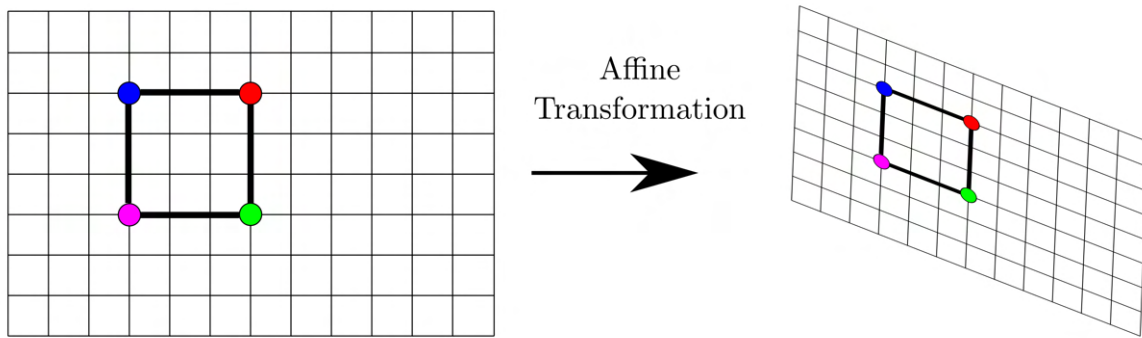


Figure 2.9: Example of an affine transformation.

Robotic manipulators can exploit affine transformations to convert camera defined pixel-space to robot-space. On a practical basis, for a 2D implementation, this can be achieved by identifying three, co-ordinate positions on an image, and relating them to a physical set of robotic co-ordinates. The transformation matrix can then be calculated and pixel-space to robot-space transforms can be computed for all co-ordinates. An affine transformation was available within the openCV libraries [104]. This was used to fulfill the pixel to robot space transformations required as part of this thesis.

When a depth camera is implemented into the system, depth measurements are connected to each pixel. These measurements can be implemented into the robotic positioning to ensure the robotic system moves to the correct location in 3D space.

2.4 Grasping Methodology

Robotic grasping in unstructured environments is a prominent component of modern robotics research. Frequently, photogrammetric techniques are used to guide robots to objects and positions to make robotic grasps [84], [105]. An implementation of such a photogrammetry based robotic guidance methodology was designed as a control mechanism for this thesis. This was accomplished for the KUKA LBR robotic manipulators, operating in a floor mounted orientation. The defined work area was setup on the floor in front of the arm, as pictured in Fig 2.10. A Blue Robotics Newton gripper [106] was selected as a gripper, due to its waterproofing, giving it the capability to be washed down for decontamination purposes. This was mounted to the end-effector

of the LBR. A RealSense™ L515 was attached to a mounting plate on the end-effector, enabling depth images to be taken to inform robotic positioning. An example of a robotic grasp is discussed to explain the methodology.

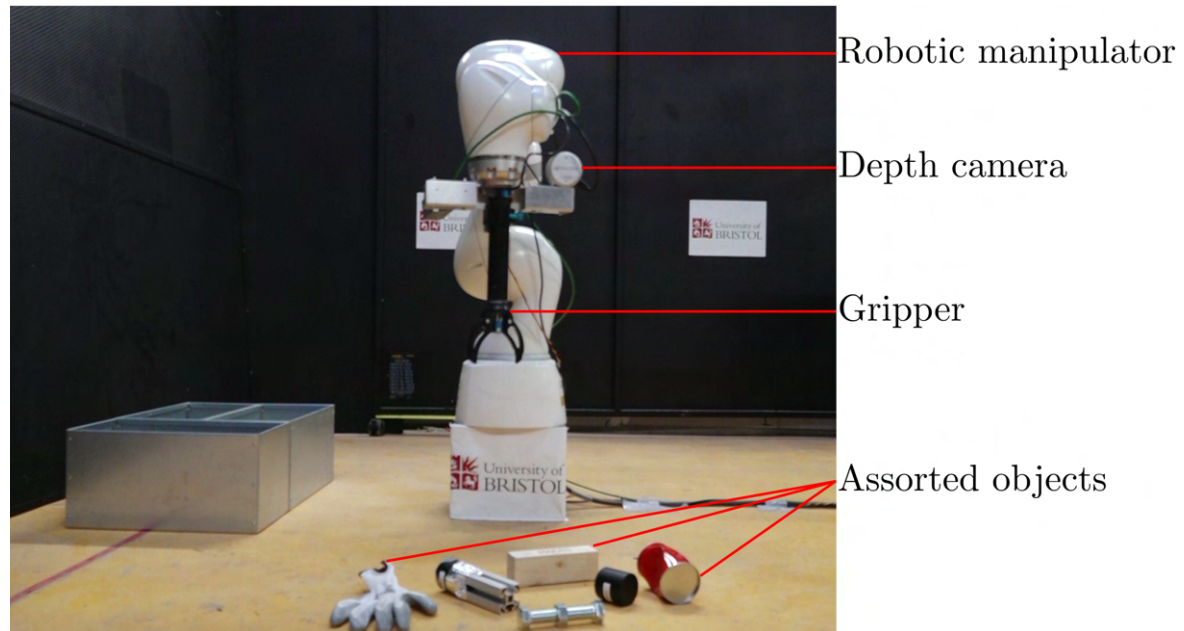


Figure 2.10: Experimental setup showing the robotic grasping system in position to grasp an assortment of objects.

Initially, a depth image is taken from a known robotic joint configuration, in which the camera is directed towards the workspace area. This configuration is known as the ‘camera pose’. An example colour image from the camera pose is shown in Figure 2.11(a), showing 3 similarly sized blocks laid on the workspace. The collected depth image is smoothed using a Gaussian filtering technique. This resulting image is known as the ‘object image’ and an example of this is shown in Figure 2.11(b). Next, using a thresholding technique, objects below a certain height are subtracted from the object image. Effectively, this removes contributions from camera depth noise and the object surface. The resultant image may be known as the ‘grasping image’, an example is shown in Figure 2.11(c).

This simplified grasping image contains the data needed to orient the arm and attached gripper to an appropriate top-down grasping pose. The grasping image has highlighted objects. A contour analysis technique allows the continuous boundary points to be identified, effectively defining the perimeter of each shape. Contour analysis is a common implementation used for object identification techniques [107]. In essence, the contour analysis returns a series of co-ordinate points across the image frame. These points can be used to fit a minimum area bounding rectangle, which encompass the shapes. This was implemented using openCV’s contouring tools [104]. The

result can be seen in Figure 2.11(d), where one of the rectangular shapes is clearly highlighted.

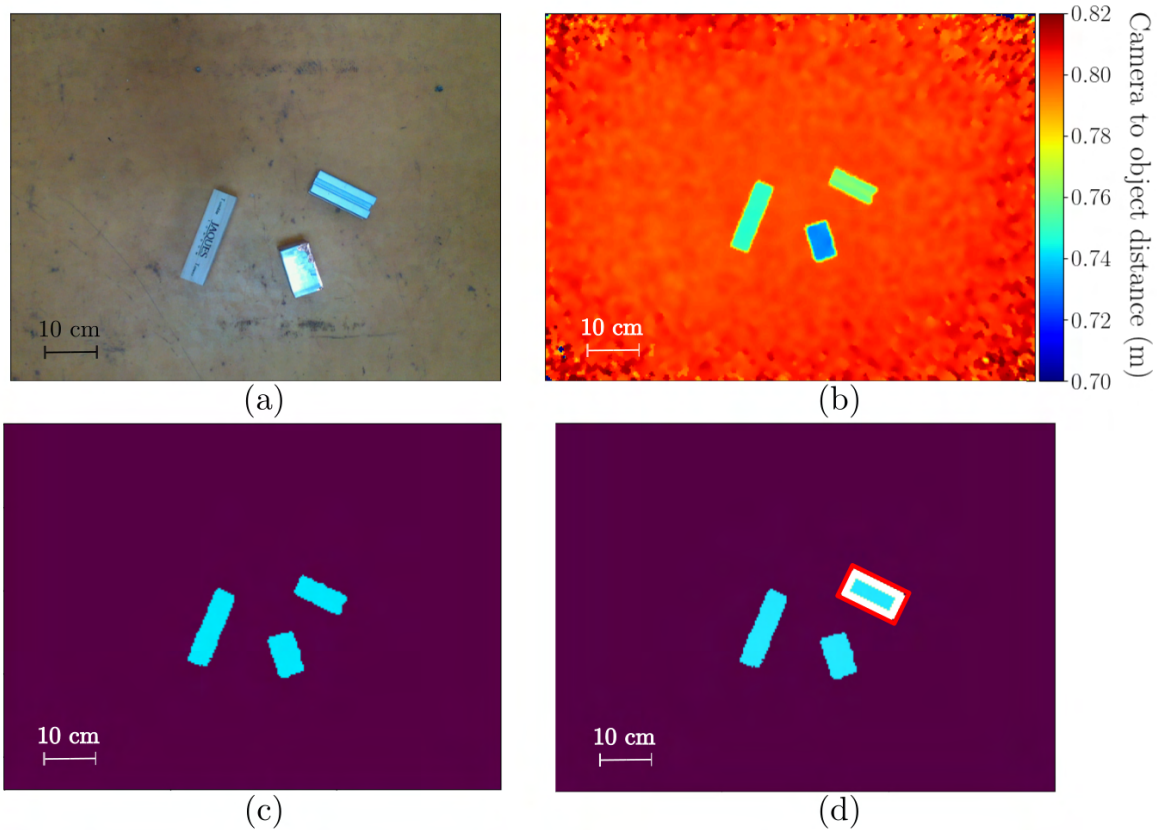


Figure 2.11: (a) shows the RGB colour image of 3 distinct blocks ready to be grasped. (b) shows the depth image of (a). (c) shows the object identification thresholded image. (d) highlights the contour analysis which gives rise to the grasping angle chosen by the robotic system.

The bounding co-ordinate points attained from the minimum area rectangle, as pictured in Figure 2.11 (d), may be used to inform the correct grasping angle for a given object. Simple geometric techniques are used to identify the angle of the rectangle's longest dimension. This ensures that a grasp is made across the shortest dimension, enabling a higher percentage of grasps to be completed. Finally, the centroid of the shape is identified using the simple blob detection algorithm provided by the openCV package [104]. From here the angle of rotation for the gripper may be identified and the corresponding grasp location determined. The affine transformation can be used to direct the robotic system to the correct location in 'robot-space'. Figure 2.12 shows this process being undertaken for a variety of more complex objects, with a successful grasp of a tin can.

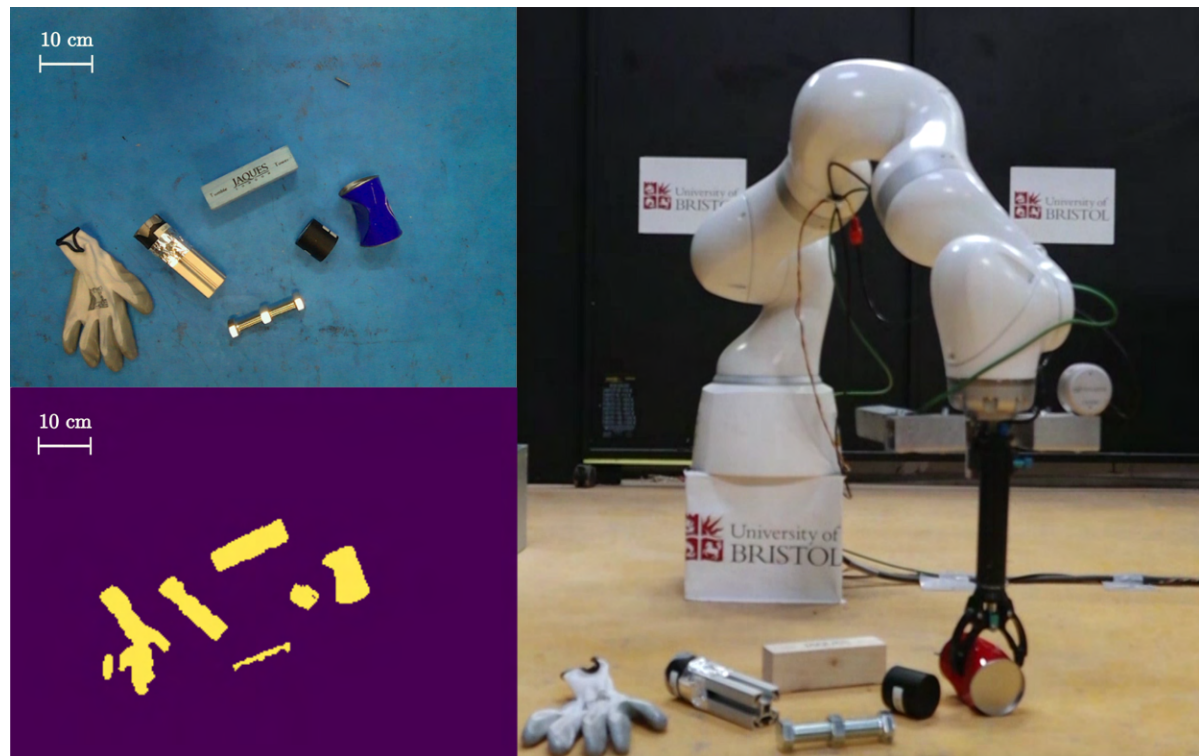


Figure 2.12: Top left shows a colour image of an exemplar waste sorting scenario. Bottom left shows an example ‘grasping image’ of the same scene. Right shows the robotic system grasping a tin can.

This grasping methodology enabled the developed system to grasp and examine a variety of objects for proof-of-concept nuclear waste sorting and segregation. It is noted that there are examples of objects which would not be able to be grasped using such a mechanism. This work was completed to facilitate basic grasping tasks essential for sorting and segregation demonstration. However, the focal point of this thesis is centred on automation and robot-sensor fusion for waste characterisation.

2.5 Radiometric Characterisation

Having resolved robotic manipulation and handling activities for sorting and segregating waste items, the next requirement is their characterisation. As established in the introduction, this is reliant on both material and radiometric techniques. This section will explore relevant radiometric techniques, which are robotically deployable. The purpose of this is to facilitate in-situ radiometric characterisations while waste is in the sorting area. Resultantly, decisions can be made as to the onwards processing routes.

Nuclear waste identified within sorting and segregation activities, is most likely to contain

forms of alpha, beta and gamma radiation². Owing to the wide variety and scope of nuclear waste articles, it is highly likely that radioactive emitters will be obscured by containment materials, such as metallic pipework. This could result in radioactive elements being obstructed by some shielding material. In such scenarios, alpha and beta radiation would not be detectable, unless the obstructing object was structurally altered or relocated. Cutting and size reduction of objects, is currently an undesired outcome of autonomous waste sorting and segregation [11].

Fortunately, the highly penetrating nature of gamma radiation enables gamma emitting objects to be visible through structures. There are a number of pure beta and alpha emitters for which gamma detectors would be blind to, but in waste storage, such emitters are easily contained. Additionally, many can be identified through detection of other gamma-photon emitters. One such example is Pu-241, which decays via beta decay to Am-241. This in turn decays via gamma emission [109]. Hence, the presence of Pu-241 may be inferred by Am-241 detection.

2.5.1 Gamma Radiation Detection

Gamma detection is dependant on an interaction of a gamma-photon with the detection instrument. Weakly interacting and uncharged, gamma-photons do not immediately produce a charged signal within a detector [110]. Therefore, to understand how gamma detectors work, the principles of gamma interactions with materials must first be explained. There are 3 different types of gamma interaction: Photoelectric Absorption, Compton Scattering and Pair Production [111].

2.5.1.1 Photoelectric Absorption

Photoelectric absorption occurs when a gamma-photon is fully absorbed by an atom [111]. This energy is transferred to a bound electron. Subsequently, the bound electron is then ejected with the energy of the incident photon, minus the binding energy of the electron, as defined by equation 2.2 [110].

$$(2.2) \quad E_e = E_\gamma - E_b$$

Where E_e is the energy of the electron, E_γ is the energy of the incident gamma-photon and E_b is the binding energy of the electron. Typically, gamma-photons eject the most tightly bound k-shell electron, with energies in the region of 1 to tens of keV [111]. The subsequent in-fill of

²There may be a small neutron radiation contribution, notably from Beryllium-13 (Be-13), which is a neutron emitter; used in laboratory neutron experiments, nuclear weapons and test reactors [108]. However, Beryllium may be identified by other forms of characterisation, so identification via neutron detection was deemed out of scope for this project.

electrons from higher energy shells releases a characteristic X-ray photon. Generally, this X-ray photon is quickly absorbed, again via photoelectric absorption [111]. Photoelectric absorption is an important for gamma detection, as it is the only effect for which gamma-photons may directly be measured owing to their full photoelectric absorption.

2.5.1.2 Compton Scattering

Compton scattering involves the direct interaction of an atom's electron with a gamma-photon. Part of the gamma-photon's energy is transferred to the electron, giving it recoil. The remaining energy remains with the gamma-photon which is scattered. This process is explained in Fig 2.13.

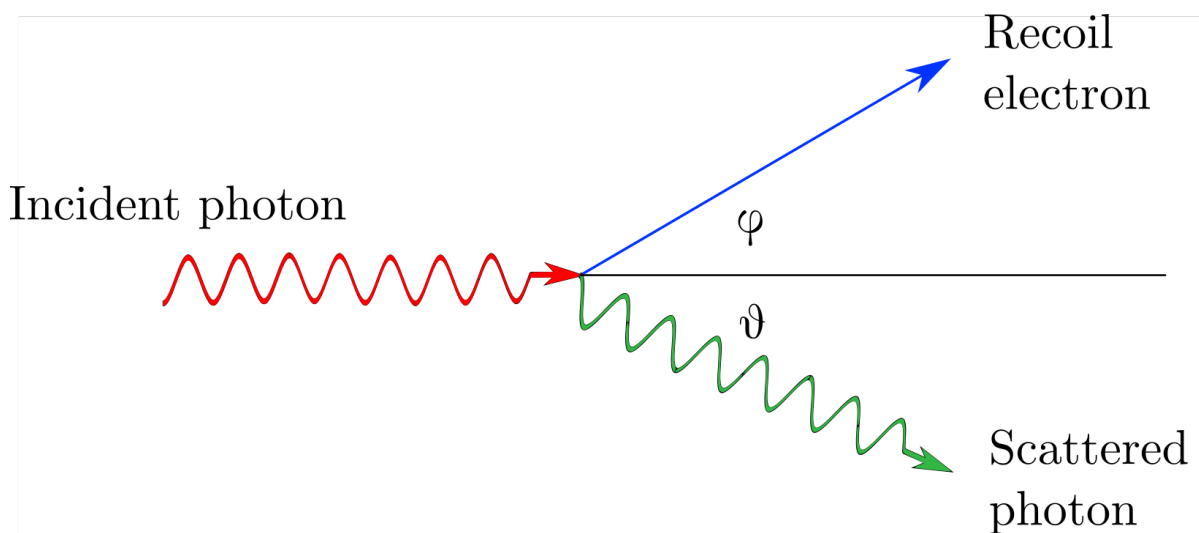


Figure 2.13: Diagrammatic representation of Compton scattering.

The energy of the scattered gamma-photon and electron depends on the interaction angle. This may be described in terms of its initial energy $h\nu$, as e.q. 2.3 [111].

$$(2.3) \quad h\nu' = \frac{h\nu}{1 + \left(\frac{h\nu}{m_0c^2}\right)(1 - \cos\theta)}$$

Where h represents the planck's constant, ν is the velocity of the incident gamma-photon, ν' is the velocity of the scattered gamma-photon, m_0c^2 is the rest mass energy of the electron (0.511 keV) and θ is the scattering angle. Compton scattering probability depends on the number of electrons available within the absorber [111].

2.5.1.3 Pair Production

In pair production, an incident gamma-photon creates a electron and positron, within the coulomb field of an atomic structure [112]. Both an electron and positron require 511 keV to be created, so

the gamma ray involved in pair production must have an energy of 1022 keV in order to stimulate the production. The electron and positron then share between them the excess energy of the gamma photon produced.

2.5.2 Detection

As discussed formerly, radiation detection depends on analysis of gamma-photon interaction with a material. Ostensibly, this has a dependence on the physical density and size of the detection material. A quantity known as the linear attenuation coefficient, μ , is a measure of the probability of an interaction and subsequent removal (attenuation) of a gamma-photon from a material, per unit length [113]. It may be expressed as a linear combination of the probability of **photoelectric absorption**, **Compton scatter** and **pair production** [114]. The mass attenuation coefficient expresses this concept while scaling for density. Mass attenuation coefficient μ_M may therefore be expressed in terms of μ and density, ρ , as equation 2.4 [114].

$$(2.4) \quad \mu_M = \frac{\mu}{\rho}$$

Low energy gamma-photons and highly dense materials represent the greatest interaction probability.

Some consideration must also be given to the interaction effect, as the probability of gamma-photon interaction is also energy dependent. This is demonstrated in Figure 2.14, which shows more generally the energy windows for which interactions are most dominant.

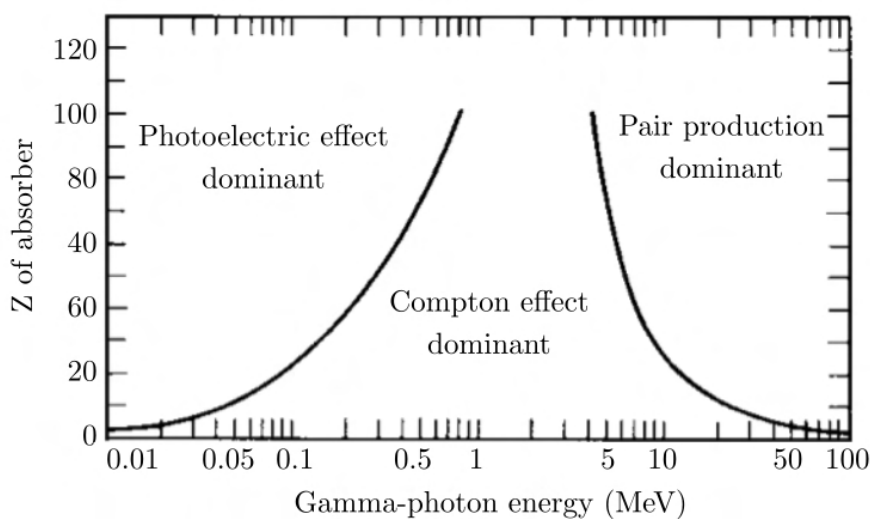


Figure 2.14: Dominant gamma-photon interaction regions with respect to energy. Adapted from [115].

2.5.3 Practical Radiation Detection

Radiation detectors take advantage of these interaction processes, using their responses to indirectly analyse gamma-photons. Here a practical understanding of radiation detection is provided, giving an overview of currently available gamma-photon identification techniques.

2.5.3.1 Gaseous Detectors

Gaseous detectors are simple in their configuration and comprise of electrode plates with opposing charges separated between a gas [116]. When an interaction occurs in which the energy of the gamma-photon is greater than the ionisation potential of the gas, it may be ionised. This results in the displacement of an electron from an atom, creating an ion pair. The ions travel towards the electrodes inducing a current, which can be measured by electronic analysis [116]. There are 3 types of gaseous detector; ionisation chambers, proportional counters and Geiger-Muller (GM) tubes.

Ionisation chambers can theoretically contain any gas, but most frequently air. This gas is situated between two electrodes with a voltage bias applied between them. The gas can become ionised by interaction with a gamma-photon, the resulting ion pair are attracted to the electrodes [111]. The current increase induced at the electrode is representative of the energy deposited by the gamma-photon. Ionisation chambers are advantageous, as they have no dead time³ [117], meaning they can detect all interacting gamma-photons. However, they have a low gamma-photon efficiency [118], but in high-dose applications can provide a viable, if somewhat bulky and sometimes fragile solution.

Proportional counters are similar to Ionisation chambers, however operate with the gas inside a stronger electric field [111]. This results in the electrons formed during an interaction accelerating towards the anode, the process of which induces secondary ionisation which leads to a phenomenon known as Townsends avalanches [119]. Proportional counters using gas at atmospheric pressures have energy ranges limited to around 2-80 keV [120].

GM tubes are the most recognisable form of radiation detector, making a distinctive ‘clicking’ sound in the presence of radiation. They contain gas between 2 electrode plates at a very high voltage difference, of the order of a few hundred volts. Radiation ionises the gas and causes a cascade effect similar to that of a proportional counter. The main difference with a GM tube, is that the high voltages can induce many cascade events, which arise from multiple ionisations. Therefore, the pulse height recorded is independent of the energy the incident gamma photon deposited. Hence, it cannot be used for spectroscopy as there is no ability to measure the photon’s

³Detector dead time is the ‘downtime’ between a gamma detection and the next gamma detection that may take place in a detector.

energy [111]. For some applications simply reporting the gamma counts per second received by a detector is sufficient. This is normally the case when a radiation worker wants to understand how safe a given location is, or the location of radiation is desired without quantification. The low-cost and portability of GM-tubes makes them suitable for these applications, but the limitations of being energy-blind, having low gamma-photon efficiency and low dose saturation levels mean that gaseous detectors are inappropriate for high or even moderate-dose plant characterisation applications. The limitations of energy, gamma-photon efficiency and incapability to produce spectra mean that gaseous detectors inappropriate for sort and segregation. However, for completeness, Figure 2.15 provides an overview of gas detectors operation and functionalities.

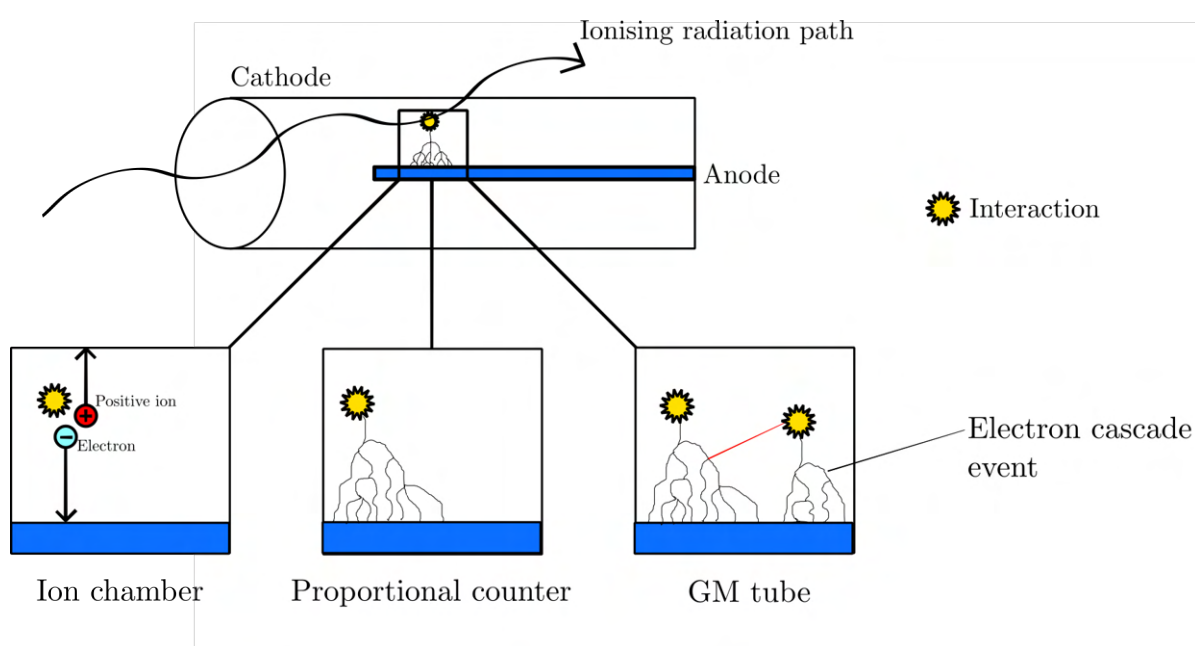


Figure 2.15: Diagrammatic representation of the mechanism used by Ion chambers, Proportional counters and Geiger-Muller tubes.

2.5.3.2 Scintillator Detectors

Scintillating materials produce luminescence following interaction with ionising radiation. This luminescence creates light, which may be measured to infer the presence and energy of the incident radiation [110]. Gamma-photons excite electrons in the scintillator crystal from the valence band into the conduction band, forming an electron-hole pair. This electron-hole pair moves through the lattice structure until it is trapped by a crystal defect, or recombines on a luminescent centre, giving off visible light. Luminescent centres are a key characteristic of scintillating materials and are responsible for the creation of the light [121]. It is at the luminescent centre that the excited electron is de-excited, releasing a photon in the visible spectrum in the process. This process is diagrammatically depicted in Figure 2.16. The wavelength

of the released photon is used to detect and quantify the energy of the initial incident gamma-photon. Doping of crystals with impurity elements is often used to introduce more luminescent centres to the crystal, increasing the photon yield [122]. These photons may be difficult to detect, so they must be amplified to provide meaningful measurement. There are two main options for accomplishing this: photo-multiplier tubes (PMTs) and Silicon (Si) photo-multipliers (SiPMs) [123]. SiPMs are more common than PMTs for many applications, due to their low power consumption, reduced size, high throughput and enhanced sensitivity over the older technology of PMT devices. Common scintillator crystals which are used for radiation detection are: Sodium Iodide (NaI), Caesium Iodide (CsI), Bismuth Germinate (BGO), Cerium Bromide and Lanthanum Bromide [111].

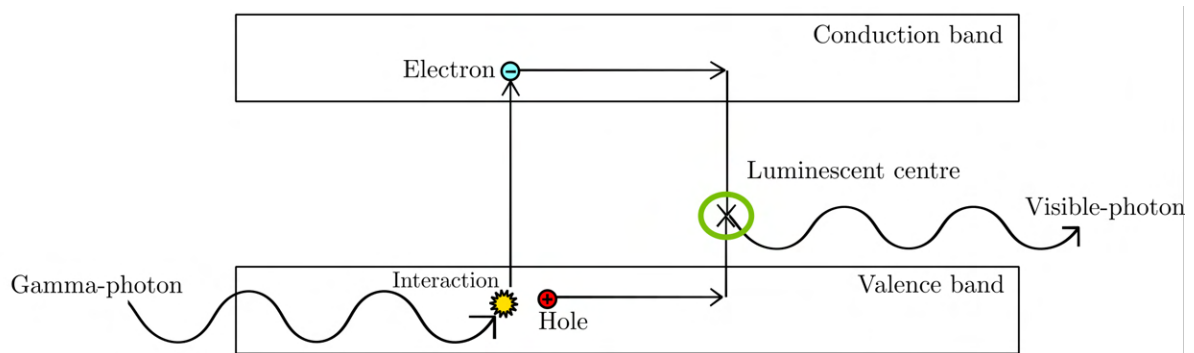


Figure 2.16: Diagrammatic representation of the mechanism behind scintillator detectors.

In moderate and high-dose applications, unless the scintillator volume is extremely small, the device will become saturated. This is partly due to the very high frequency of gamma-photon interactions and the relatively long dead-time for counting, but also because scintillators may become damaged by prolonged exposure to radiation. This manifests itself as a reduction in light output and an increase in ‘afterglow’ which increases noise in spectra, reducing energy resolution [124]. There are several effects of radiation damage, most prominent is the radiation-induced colour centre formation [125]. This causes a reduction in light attenuation length, by absorbing light and hence reducing the light output of the scintillator [125], resulting in a reduction in energy resolution and amplitude of light output.

2.5.3.3 Semiconductor Detectors

Semiconductor detectors also measure the effects of gamma-photon induced ionisation, but do so directly rather than indirectly as per the aforementioned scintillator devices. In a semi-conductor crystal, interacting gamma-photon’s can excite electrons from the valence band to the conduction band, leaving behind a ‘hole’ in the valence band⁴ [111]. This is known as the production of an electron-hole pair. Applying a voltage bias across the crystal by using opposing electrodes

⁴A hole is the absence of an electron, at a location where one would usually be situated.

causes the electron-hole pair to migrate to their respective electrodes. The energy of the incident gamma-photon may then be inferred directly from the electrical signal collected [111]. This process is displayed in Figure 2.17. Semiconductor materials enable this detection process, as they have moderate band gaps at around 1 eV, compared to > 5 eV for insulators, or conductors without band gaps. This increases the probability of pair-production, therefore more interactions may be recorded and statistical fluctuations reduced, resulting in a higher energy resolution [111]. Over time detector material may become damaged by radiation. This usually means a reduction in energy resolution, an increase in leakage current and a photopeak position shift [126]. The precise dose rates inducing these changes are not well documented.

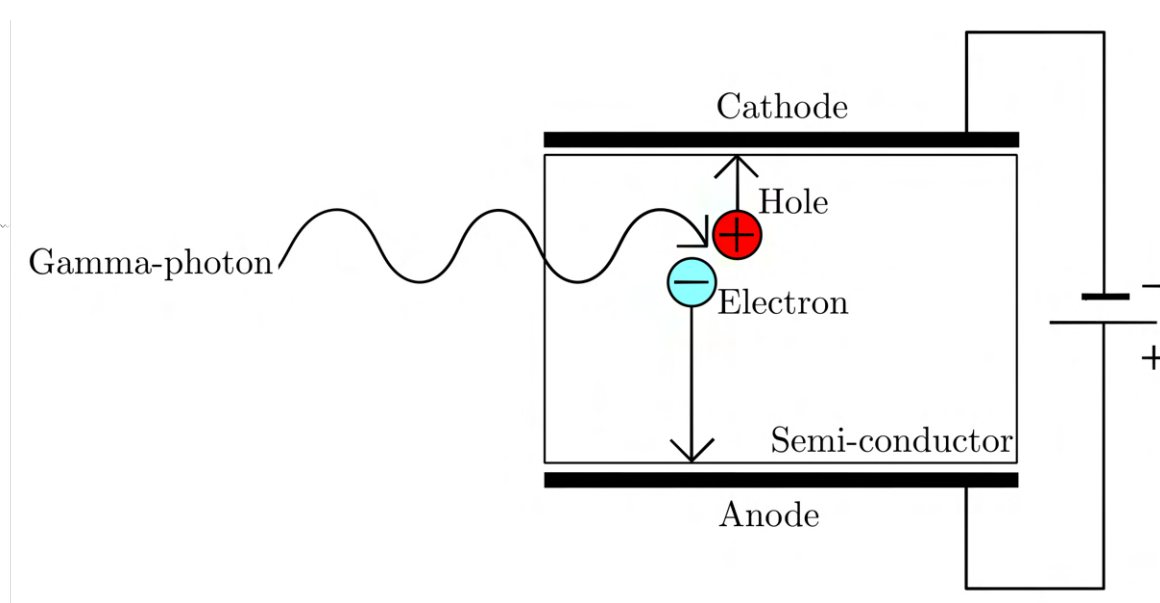


Figure 2.17: Diagrammatic representation of the mechanism behind semiconductor type detectors

2.5.4 Gamma Spectroscopy

Established are a number of different techniques capable of performing gamma radiation detection and spectroscopy, employing the aforementioned technologies. For use and deployment within a hazardous environment, such as within nuclear waste sorting, an appropriate gamma spectroscopy system must conform to certain requirements. It must be able to be deployed as part of a cabled system and should be relatively compact to be mounted on a robotic manipulator. Ideally, it must also be a currently deployable, Commercial Off The Shelf (COTS) system, enabling its verification for use within the nuclear sector.

2.5.5 Currently Deployable Devices

There exists numerous semiconductor and scintillator radiation detection devices that are currently commercially available to the end user. One area of development which is highly applicable

for robotic systems are micro-gamma spectrometers. These are small, handheld radiation detectors, which use namely scintillation and semiconductor type detection. The key advantage of these is the ease of use, many being plug and play components, with no specialist treatment requirements. Additionally, they are typically operable in room temperature conditions and available at a comparatively low cost. Researchers in robotic and sensing fields have rapidly adopted this technology for use in radiological mapping systems. For example, Martin et al. [127], used a ground based mapping procedure to assess the contaminant migration across the fallout zone surrounding the Fukushima Daiichi Nuclear Power Plant (FDNPP) site. A micro-gamma spectrometer for radiation sensing was coupled with a GPS inside a human mounted backpack, to localise the readings to within 0.5 metres. Radiation data has also been collected from numerous different airborne platforms including the more recent use of Unmanned Aerial Vehicles (UAVs). Connor et al. [128] used an airborne system with a micro-gamma spectrometer to map the distribution of radiation at contaminated soil waste storage facilities across the fallout zone. More recently, Bird et al. [129], demonstrated the integration of a micro-gamma spectrometer system on an Unmanned Ground Vehicle (UGV). The tracked UGV system was able to facilitate ground based radiation survey operations, detailing the location of a radioactive source attached to a wall.

Evidently, micro-gamma spectrometers have demonstrable applicability to robotic deployment systems. Table 2.5.5, provides a summary of micro-gamma spectrometer options which are currently commercially available.

Scintillator Crystal	FWHM at 662 keV (%)	Density (gcm ⁻³)	Decay Time (ns)	Relative Price	References
NaI(Tl)	7	3.67	250	£	[130],
CsI(Na)	6 - 7	4.51	630	£	[131],[132]
CsI(Tl)	7-8	4.51	1000	£	[133],[134],[132]
BGO	14 - 23	7.13	300	££	[135],[111]
CeBr ₃	4 - 5	5.1	20	£££	[136],[137]
LaBr ₃ (Ce)	2 - 3	5.1	16	£££	[138],[139]
LYSO	8	7.1	36	£££	[140], [141]

Table 2.1: Summary of the key features in the selection of scintillator detector materials. The £ symbols represent relative crystal costings with £ representing the cheapest systems and £££ the most expensive.

2.5.6 Radiometric characterisation summary

In summary, there are many different detection systems available for deployment on robotic systems. Owing to the low cost, availability, and relatively high resolution, CsI(Tl) scintillator detectors were selected for system development in this thesis. Namely, the KromekTM Sigma-50 [134]. It is noted, that due to the effective ‘plug and play’ nature of detection systems, this could trivially be replaced with a different scintillator. Hence, for proof-of-concept system development, this was deemed acceptable.

2.6 Material Characterisation

It is evident that material characterisation will be essential for nuclear waste sorting and segregation. Accurate, precise and rapid materials characterisation is a highly desirable capability in numerous different industrial settings. Applications such as hazardous waste management [142], forensics [143], environmental science [144] and scrap metal assaying [145] are all key examples from which the nuclear industry can draw from. While many materials and components are readily discernible, by virtue of their colour, lustre and geometrical form, other materials are

more difficult to differentiate. In particular, metals, alloys and corroded/coated objects may appear visually identical, but possess different elemental compositions. Such compositional differences can greatly influence how the material should be subsequently handled or managed. As discussed, within the nuclear sector, a deployable, in-situ and real-time materials analysis capability is highly desired for use as part of waste management operations [45]. In such environments, it is crucial to accurately assay items and consign them to the correct and most appropriate onward processing, recycling and/or disposal route.

In-field assay techniques are essential to accurately and quantitatively determine elemental composition and distribution within objects, surfaces and components. However, readily portable assay techniques have historically been very limited. Many lab-based techniques are unsuitable for application on-site, in-situ and in real-time. Resultantly, this has necessitated material sub-sampling and recovery for laboratory analysis. For direct analysis of solids, scanning electron microscopy (SEM), combined with energy dispersive (X-ray) spectroscopy (EDS) is a widely utilised technique for elemental analysis [146]. Alternatively, inductively coupled plasma mass spectrometry (ICP-MS), which requires acid digestion of samples, is widely used to provide isotopic analysis [147]. Whilst they provide high sensitivity, precision analysis, they are expensive in terms of the high-cost of both instrument operation and upkeep [148, 149]. In addition, they are expensive with respect to the time taken to extract, handle and ship the samples to the laboratory, as well as the analysis reporting time. Therefore, reducing or eliminating the need for sampling can deliver major cost savings for numerous different nuclear waste management and decommissioning scenarios. Accordingly, non-destructive in-situ measurement is highly preferable to facilitate radiological, chemical and material characterisation. Analysis can derive almost instantaneous results, whereas sub-sampling for lab analysis may take several days or weeks to complete, slowing down waste management processes and activities.

An alternative option is X-ray Fluorescence (XRF), combined with Laser Raman Spectroscopy (LRS). These techniques represent highly complementary characterisation methods. While LRS is excellent at characterising plastics and other chemically bonded materials, it is ineffective at metals analysis. XRF can identify metals, circumventing the shortfalls of LRS. Therefore a combination of XRF and LRS were selected for material identification for this thesis. XRF to detect individual elements; in-particular metallic objects and LRS to detect chemically bonded objects, principally plastics. Crucially, both can be used as lightweight and robotically deployable techniques.

2.6.1 X-ray Fluorescence

X-ray fluorescence (XRF) is a well-known and widely adopted characterisation technique used to non-destructively analyse materials. As a methodology, it is able to quantitatively ascertain

elemental compositions with parts per million (ppm) sensitivities for elements between sodium (Na) and uranium (U) [150]. It achieves this through analysis of emitted characteristic X-rays. Every element has an electron configuration consisting of electron orbitals at specific energy levels. Each energy shell is described formally with a letter, with the lowest energy shell denoted by 'L', closest to the nucleus of the atom and containing up to 2 electrons. The second energy shell is named the 'M' shell, with up to 8 electrons situated outside of the 'L'. This continues, following an alphabetical naming structure, with each of the following shells containing up to 8 electrons. When an atom is ionised via the removal of an electron, a vacancy is left. Electrons from a higher energy orbital are removed to fill the electron structure. This process emits X-rays which are known as characteristic X-rays. The most prominent characteristic X-rays are those released when an electron from the L shell fill the vacancy in the K shell. The L to K shell transition X-ray fluorescence is referred to as the k_α and the M to K transition as the k_β .

XRF operates using the principle of X-ray-induced fluorescence; whereby incident X-ray photons are directed onto the sample - resulting in the ionisation of the materials constituent atoms. The ionisation of the atom causes the emission of characteristic X-rays via the aforementioned process. As each element possesses characteristic fluorescence emission energies, it is these that together contribute to the resultant fluorescence spectra [151]. The process of XRF is described in Figure 2.18.

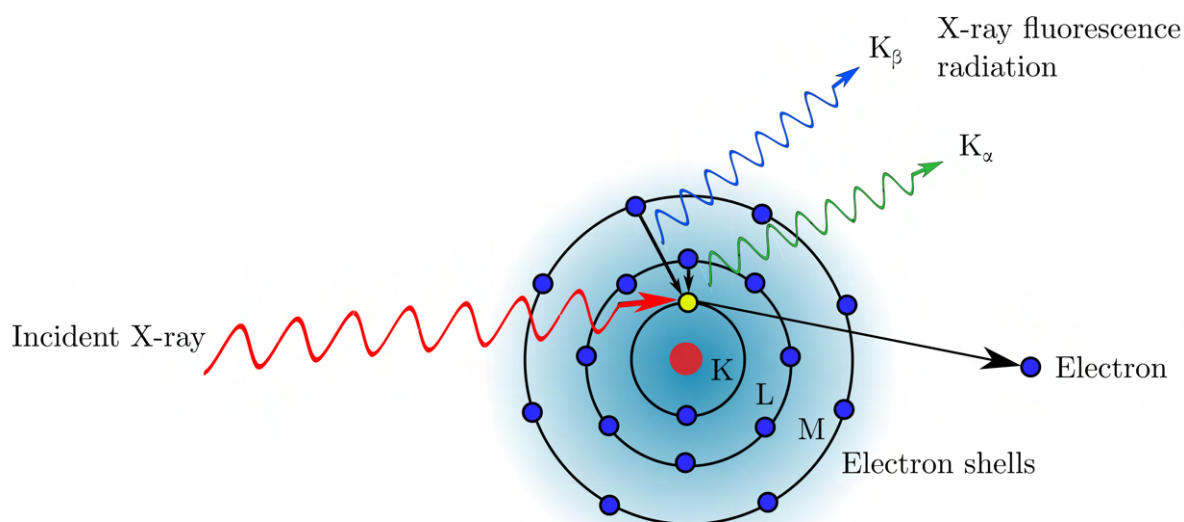


Figure 2.18: XRF of an argon atom, depicting the release of X-ray induced k_α and k_β characteristic X-rays. Image inspired by [152].

The technique requires the simultaneous generation of an incident beam of X-rays; combined with a detection system through which to quantify the fluorescence spectra. Historically, the generation

of sufficient X-ray fluences for rapid quantifiable XRF analysis was the preserve of large-scale synchrotron sources. Subsequently, advanced high-power, yet also large and non-portable, laboratory sources [153]. However, recent advancements in micro-electronics, high-voltage systems, source cooling and X-ray generation have facilitated the development and production of miniaturised 'handheld' portable XRF (pXRF) modules. These pXRF systems can be operated in the field and outside of the laboratory by non-experts, with comparatively low operational costs [154].

Developments in X-ray tube technology have greatly enhanced pXRF, as devices which previously relied upon radioisotope excitation now operate using such tube systems [155]. Complimentary to this is the development of Silicon Drift Detectors (SDDs) which enable X-ray detection on a solid state chip-set using Peltier cooling [156]. This negates the need for cumbersome liquid nitrogen cooled detectors, such as those using silicon and high purity germanium [157]. Resultantly, these pXRF devices are now widely used across research [158–160], with one of the most common use cases for pXRF being within geological field investigations, whereby rocks and minerals are characterised in real time. Their relatively small size, as handheld devices, means they could easily be deployed as part of an integrated robotic system. This could make them a versatile tool within the challenge of nuclear waste sorting and segregation for elemental analysis.

2.6.2 Laser Raman Spectroscopy

XRF has a demonstrable capability on measuring and detecting concentrations of elements, in particular the transition elements. However, it is poor at identifying light materials and chemically bonded substances, such as plastics. An alternative choice for detection of bonded structures, is Laser Raman Spectroscopy (LRS). LRS is used for material identification in a range of industries including agriculture, bio-medicine, forensics, mineralogy, pharmaceuticals, and threat detection [161], [162]. It is an optical technique for analysing and identifying chemical species. By shining a fixed wavelength laser on a sample, a majority of the light either passes through it, or is absorbed [163]. However, a small percentage ($\sim 0.1\%$) is elastically scattered, via a process known as Rayleigh scattering. An even smaller fraction of the light (~ 1 in 10^8) incident photons is inelastically scattered, this process is known as 'Raman scattering' [163]. By definition, the light returned by Raman scattering is at a different energy to its incident beam. This energy difference in energy induced by the Raman scattering event, represents a probing of the vibrational modes of the bonds in the chemical compound. By studying the Raman light, it is possible to identify chemicals present and determine ratios of chemicals. Figure 2.19 shows the possible effects of incident laser light on a Polyvinyl Chloride (PVC) molecule.

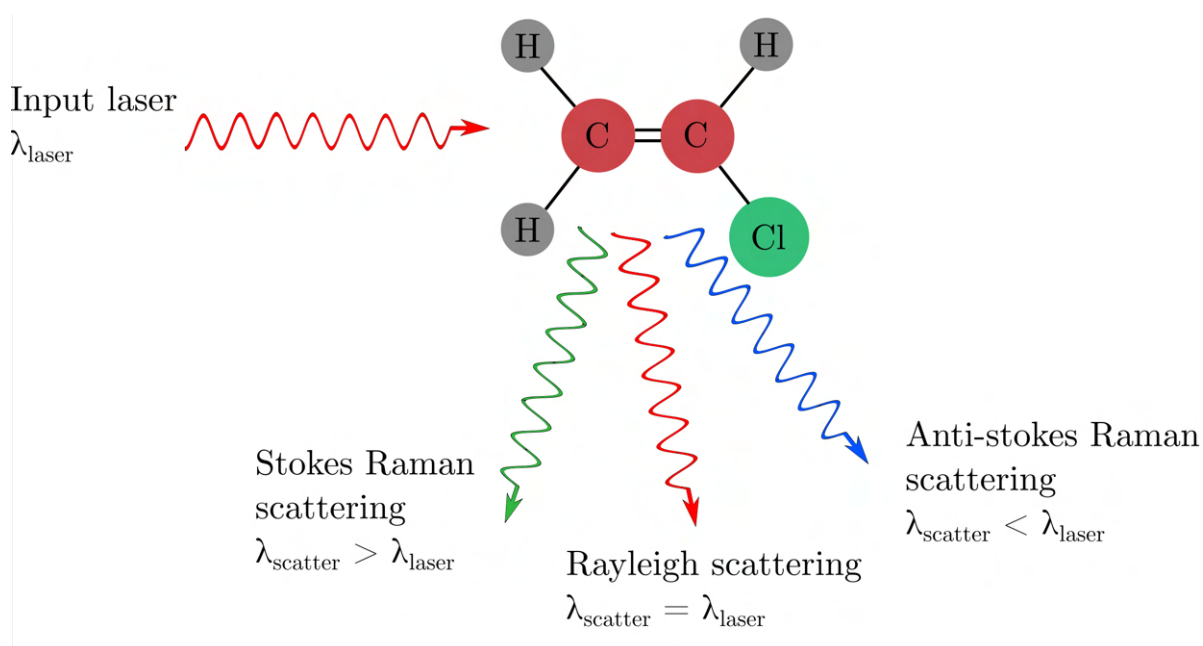


Figure 2.19: Principles of scattering events, showing how LRS can be used to detect PVC. Image inspired by [164].

The precise difference in wavelength is known as its Raman shift [165] [166]. Hence, Raman spectra can provide information on the vibrational modes of molecular bonds [167]. When a photon interacts with a molecule there is a small chance that it will excite the molecule from its ground state to a vibrationally excited state via inelastic scattering. As the photon is inelastically scattered and some of its energy is donated to the molecule, then the photon undergoes a red shift of an energy equal to that of the energy difference between the vibrational states [168]. Measuring and recording the energies of these peaks using spectroscopic techniques, can be used to create a Raman spectrum [169]. This identifies characteristic bonding information and can consequently be used to identify the material being interrogated. The Raman shift equation may be expressed by equation 2.5 [170].

$$(2.5) \quad \Delta\nu = \frac{1}{\lambda_0} - \frac{1}{\lambda_1}$$

Where $\Delta\nu$ represents the Raman shift in terms of wavenumber, λ_0 is the initial laser wavelength and λ_1 is the Raman scattered wavelength. $\Delta\nu$, is most commonly determined in terms of cm^{-1} .

Within a practical implementation, the key to the successful LRS of a sample is the use of a laser of an appropriate wavelength and a Raman spectrometer. The laser is directed at a sample to induce Raman scattering and the spectrometer measures the Raman shift wavelengths to generate spectra.

2.6.2.1 Laser Selection

Appropriate laser selection is crucial for optimising Raman signals. Typically, wavelengths between 300 nm deep Ultraviolet (UV) and 900 near Infra-red (IR) are selected. Scattering efficiency increases with the fourth power with respect to the frequency of the incident light [171]. This means intensity, $I \propto \lambda^{-4}$. Therefore, NIR lasers of order 900 nm and UV of order 300 nm may have a $\sim 80\times$ difference in intensity. This indicates that shorter wavelength, UV lasers would be best for Raman imaging. However, UV light induces significant amounts of fluorescence, which reduce the clarity of the Raman signal, by introducing noise [171]. Therefore, laser selection is ultimately tuned to best support the signal of the samples under investigation.

2.6.2.2 Spectrometry

Ultimately, a spectroscopy technique must collect the Raman scattered light, recording the spectra and thus enabling subsequent analysis. There are 2 types of spectrometer, dispersive and Fourier Transform (FT) [172]. Dispersive spectrometers use diffraction gratings to disperse light, which can then be detected on a multi-channel detection system, typically a Charged Coupled Device (CCD) [172]. FT spectrometers use an interferometer to create an interference pattern. Detection is then typically achieved using an indium gallium arsenide (InGaAs) detector or similar [172]. The results may be reconstructed to provide the Raman spectrum [172].

The spectra derived from spectroscopy techniques shows changes in wavenumber from the incident laser light which relate directly to chemical bonds. It is from analysis of these spectra, that an accurate assay of the material compound under examination can be identified [173]

2.7 Summary

Chapter 1 highlighted the urgent requirement for a fully-autonomous, in-situ nuclear waste sorting and segregation system. This chapter, has sought to investigate some of the technology which may be applicable for resolving such a challenge. Robotic systems were established as key to the solution. Namely, robotic manipulators, which have a proven capability for sensory integration and advanced control, alongside high radiation tolerance. Therefore, the principles of robotic manipulator motion were explained in detail. Further to this, photogrammetry and grasping methodologies were covered, as complementary systems which robotic systems can exploit. Such integrated systems are capable of manipulation tasks within complex, unstructured environments, as would be the case within waste sorting.

It was identified that robotic manipulators could be used as tools for developing advanced robotic-sensor fusion technologies. Hence, in-situ characterisation tools and sensors applicable to waste classification were selected. Key to resolving this problem is an ability for robotic deploy-

ment. Therefore, only robust, lightweight and robotically deployable systems were investigated. Nuclear waste in the UK is broadly classified on the basis of radioactivity per unit mass, hence, radiometric quantification is essential. To resolve this, micro-gamma spectrometer units were investigated as robotically deployable systems meeting these criteria. The waste package specification in the UK, also requires material characterisation to adequately fingerprint containments and prevent negative long-term waste package evolution. The selected systems were XRF and LRS, complementary techniques capable of classification of a broad range of nuclear relevant materials. LRS for lighter, chemically bonded materials and XRF for heavier, metallic and elemental analysis. The basic principles of these techniques were explained in detail.

RADIATION SURVEYING USING ROBOTIC MANIPULATORS

It is evident nuclear waste sorting and segregation relies upon accurate material characterisation techniques to appropriately classify waste objects. As discussed in section 1.2, this involves two major classification objectives: radiometric and non-radiometric. The overarching waste classifier is a measure of the radioactivity per unit mass, making radiometric characterisation fundamental to the sorting and segregation of nuclear waste. However, within each radiometrically defined waste category, knowledge of radioisotopes, material and chemical properties of each waste object are crucial. These characteristics help to determine appropriate storage methodologies, ensuring the structural integrity of each waste package is maintained, whilst mitigating against the effects of long-term waste evolution [9]. Chapter 2 explored a wide variety of sensory techniques which could be applied to fulfil these requirements. Performing these processes manually would be hazardous, due to radioactive and chemically challenging materials being present within nuclear waste. It was therefore proposed that a robotic system could carry out the required sensory and handling tasks in an automated way. Higher waste categories invoke stricter sorting requirements, hence, techniques which can rapidly identify highly radioactive objects within an initial waste assortment of less active objects could be a component of the sorting process. This initial identification should quickly identify higher activity wastes and thus remove the need to meticulously characterise each single waste item. In this way, a survey based approach allows for a data driven waste sorting and processing procedure. The primary objective of this chapter is twofold: to detail the design and implementation of a robotic manipulator based radiation survey system and to comprehensively test the system for use on radiometrically surveying waste ahead of physical sorting.

Results and methods presented in this chapter have previously been published in the peer-reviewed literature:

S.R. White, D.A. Megson-Smith, K. Zhang, D.T. Connor, P.G. Martin, C. Hutson, G. Hermann, J. Dilworth, T.B. Scott, "Radiation Mapping and Laser Profiling Using a Robotic Manipulator", *Front. Robot. AI*, 26 November 2020.

S.R. White, D.A. Megson-Smith, S. Kaluvan, D.Burns, T.B. Scott, "Using Robotic Manipulators for Radioactive Waste Inspection", *Waste Management Symposia*, 2020.

The proof of principle for this research was developed in my MSc project [174], with the work presented within this chapter representing its progression. Prior to the work presented within the MSc project and research article, the use of a robotic manipulator for radiation scanning and survey had not been previously demonstrated. Hence, the system presented within this chapter demonstrates a novel integration of modified COTS equipment to fulfil the objective of a radiation survey on a robotic manipulator.

3.1 Introduction

Chapter 1 showed that nuclear waste contains a wide-variety of potentially radioactively contaminated objects and components arising from nuclear reactors, hospitals, research facilities, military activity and decommissioning activities [31]. This ranges from fuel and fuel cladding, to reactor components, medical and research radioisotopes, but also other consumables, such as gloves and tools which may have been contaminated [175], [176]. As discussed in chapter 1, RWM has a WAC, specifying the requirements for stored radioactive wastes. These specifications provide extensive guidance on the appropriate containment and eventual long-term storage of nuclear nuclear waste packages. In particular, it seeks to avoid the deleterious effects of long-term waste evolution induced by reactions between elements and corrosive effects [9]. For any given waste package contained within storage, the physical, chemical and radionuclide content must be recorded to understand its potential evolution in future [177] (see section 1.2).

Radiometrically, GM counters and ex-situ sampling is carried out to obtain an estimate of the radioactivity of the waste requiring sorting, as part of a slow and labour intensive process [11]. Modern advances in robotics could be used to accelerate this process, with manipulator arms replacing humans in the sorting and characterisation processes. One solution would be for a robot to grasp each waste article individually, subsequently sorting them on the basis of material and chemical characteristics. However, this would be extremely time consuming, as there are some 4,560,000 m³ of waste in the UK alone [52]. Additionally, the wide variety of waste means

that when waste arrives for sorting, some components may be highly active (ILW/HLW), while in contrast there may be objects in which there is no activity detectable above a neutral background level. There are comparatively small volumes of HLW and ILW, compared to the much larger inventory of lower activity LLW/VLLW wasteforms [52]. A more sophisticated approach would be for a system able to identify higher activity wastes to prioritise removal of the most dangerous objects first. This would leave behind lower activity wastes for which the sorting process is more straightforward, requiring fewer regulatory dependencies and carrying lower risks [142]. Achieving the efficient identification of high activity objects within mixed radioactive wastes mandates a survey process designed to identify the most active elements of the waste, extracting those and sorting them independently.

A convenient and dynamic approach to achieving a radiometric survey would be the use of a robotic manipulator with attached radiation detection equipment. Through the implementation of a robotic scanning process, known as a radiation survey, an assessment of the distribution of the radioactivity of the waste can be made. For the application of nuclear waste processing, it is highly probable that radioactively contaminated materials or objects may be hidden or contained within other structures. Since gamma-rays are highly penetrating, they are likely to be identifiable through the obstructions, unlike alpha or beta emitters. Therefore, it is proposed that gamma sensing is the most sensible initial characterisation technique for any waste survey. Micro-gamma spectrometers are small, operationally convenient and have previously been integrated with numerous robotic systems (see section 2.5). By combining a micro-gamma spectrometer with a robotic manipulator, the distribution of radioactive material and relative radiation levels could be observed. This would identify the locations of radioactive emitters, detailing the isotopes and relative activities; thus enabling a more dynamic sorting approach that prioritises removal of the most active objects. From this, automated decisions could be made about the forward processing of the waste in a timely manner, negating the need to individually analyse all waste objects.

The process of gamma radiation surveying using a robotic manipulator, has the additional advantage of enabling measurements to be made with other sensory technologies, while gamma measurements are collected. There are a few key sensory techniques which can exploit this, including, but not limited to: Raman spectroscopy (see chapter 7), XRF ¹ (see chapter 6) and Time of Flight (ToF) sensor ranging. This chapter will explore the use of a ToF sensor in combination with the radiation measurements. ToF sensors measure distance using the delay time between transmission of light, reflection on an object and reception. A system which is used to grasp the objects on the waste table would require a visual interpretation of the scene, to calculate a grasp pose to grip the object. Photogrammetry is a possible solution for this, as discussed in section 2.3. However, such systems are reliant on Charged Coupled Device (CCD) cameras. The

¹There is a nuance here, as while the XRF beam is on, the detector will collect radiation readings in the X-ray energy range. However, if timed correctly, XRF measurements can still be recorded improving time efficiency.

main issue here is that within a highly radioactive environment, CCD-based devices can fail, as the gamma radiation causes damage to Metal Oxide Semi-conductor (MOS) capacitors [178]. Hence, it is possible that a scanning procedure based on a miniature ToF sensor, could replace photogrammetry. Research suggests the total ionising dose before failure is approximately 300 Gy [179]. While this may not be a significant enough dose, for sorting very large volumes of ILW, the key advantage here is that ToF sensors are extremely low cost at approximately £5.00-£10 at the time of writing. Therefore, they may be considered easy to replace, consumable components.

3.2 Methods

This section details the processes undertaken to create and test the prototype robotic radiometric survey systems. Central to the design of the prototype systems were appropriately selected radioactive sources. These sources lay a foundation for the design choices of a suitable radiation detector, collimator, ranging unit and robotic manipulator for the given survey application. Following these design choices, the individual component integration is described, including the scanning methodology and data processing.

3.2.1 Radioactive Sources

Radioactive sources were used for testing the developed robotic radiation survey system. The sources used for testing were sealed within a cavity inside small cylindrical perspex containers, which will be referred to herein as ‘pucks’. A diagrammatic representation of the pucks and internal cavities is shown in Figure 3.1. Two types of radioactive material were used for testing within this chapter, Cs-137 and Naturally Occurring Radioactive Material (NORM) in the form of Uraninite. Source activities were between 1 kBq and 36 kBq were selected to be sufficiently active that they generated a significant detector response.

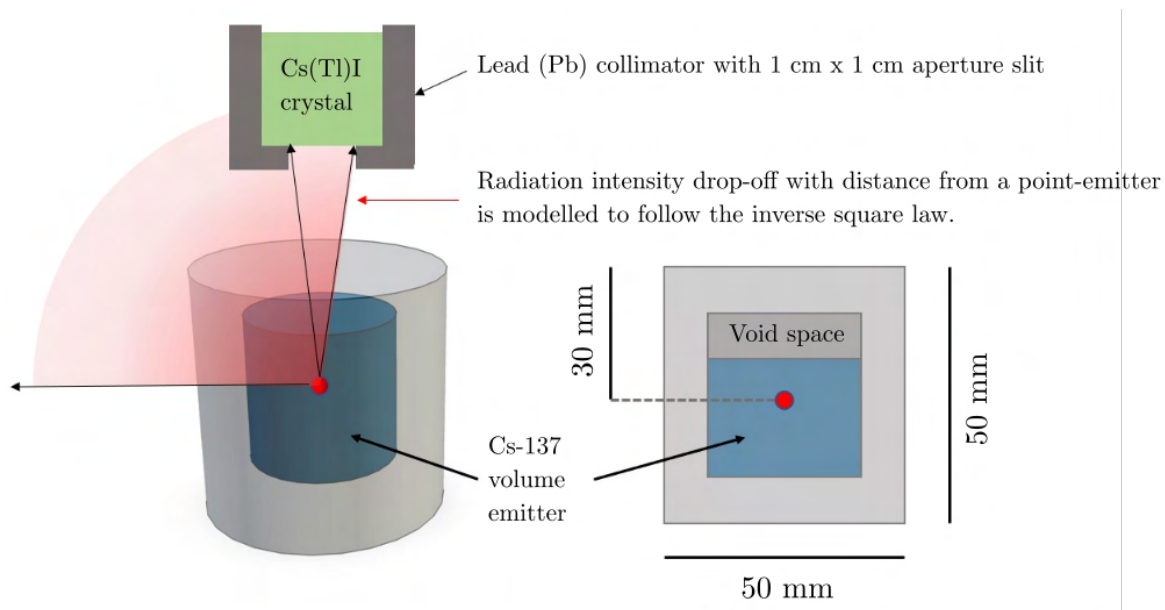


Figure 3.1: Diagram showing the internal construction of the radioactive source pucks. The relative gamma-ray solid angle which reaching the collimated detector is pictorially represented [180].

3.2.2 Sensor selection

3.2.2.1 Radiation Detector

Integral to the design of a robotic arm based radiation mapping procedure is an appropriate radiation detector choice. A KromekTM Sigma 50 CsI(Tl) scintillator detector was selected. This selection was made for a few reasons, firstly, it had demonstrated an ability to detect all the test sources, only approaching a saturation level when directly adjacent to the strongest (36 kBq) source. Secondly, owing to its dimensional size, being longer in one axis, increasing the stopping power in that direction to enhance the radiation survey resolution. The sources used for testing were below the expected activity of LLW (12 Mbqkg^{-1}). For an application involving ILW, an alternative choice of detector may need to be made to avoid detector saturation. However, this is not critical for the proof of concept system described in this chapter, as sources were selected purposefully for testing within a laboratory environment.

3.2.2.2 Ranging Unit

As discussed in the introduction, the ideal ToF sensor must have a small radiation cross section. The VL53L0X ToF sensor was selected for its small size and low cost (<£10 in 2021). Additionally it had shown to be superior to the similarly priced Sharp GP2Y0A41SK0F, in work presented by Gutierrez-Villalobos et al. [181]. A 3 mm ball lens was added to the VL53L0X to further collimate the sensor, increasing the spatial resolution of the scanning.

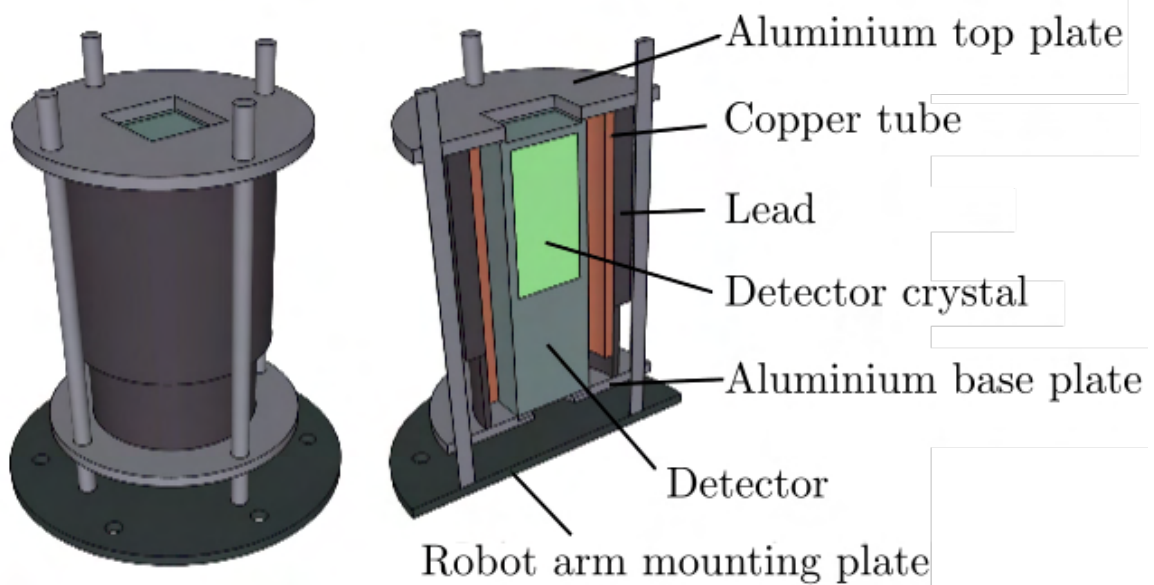


Figure 3.2: Left: Computer image of the designed collimator for robotic radiation mapping. Right: Cross section of the collimator.

3.2.3 Collimator

A lead (Pb) collimator was designed to surround the detector, to reduce as far as possible the higher angle extraneous gamma counts incident on the detector. A square opening on the front face of the collimator enabled the counts to be received from a limited solid angle, perpendicular to the scan surface. A computer model of the detector collimator is shown in Figure 3.2.

3.2.4 Robot Sensor Integration

Essential to the design of the robotic radiation survey system, was the integration of sensory hardware with a robotic manipulator. The selected robotic manipulator for this initial radiation survey testing was the KUKA KR150. Attached to the end-flange of the manipulator were the selected Kromek Sigma 50 radiation detector and VL53L0X ToF sensor. This Kromek 50 Sigma and ToF sensor fusion was provided by ImiTec Ltd as part of their Remote Isotopic Analysis System (RIAS). Control software was used to move the manipulator and assign radiation measurements to spatial positions, according to their (X, Y, Z, A, B, C) spatial positioning (see section 2.2.1), formerly developed within the masters research [174]. Collection of the robot's positional co-ordinates was achieved using the RSI functionality. These were time stamped and attributed to detector outputs from the RIAS system in LabVIEW. During scanning, the radiation detector was set to record measurements at a rate of 10 Hz and the VL53L0X ToF sensor recordings

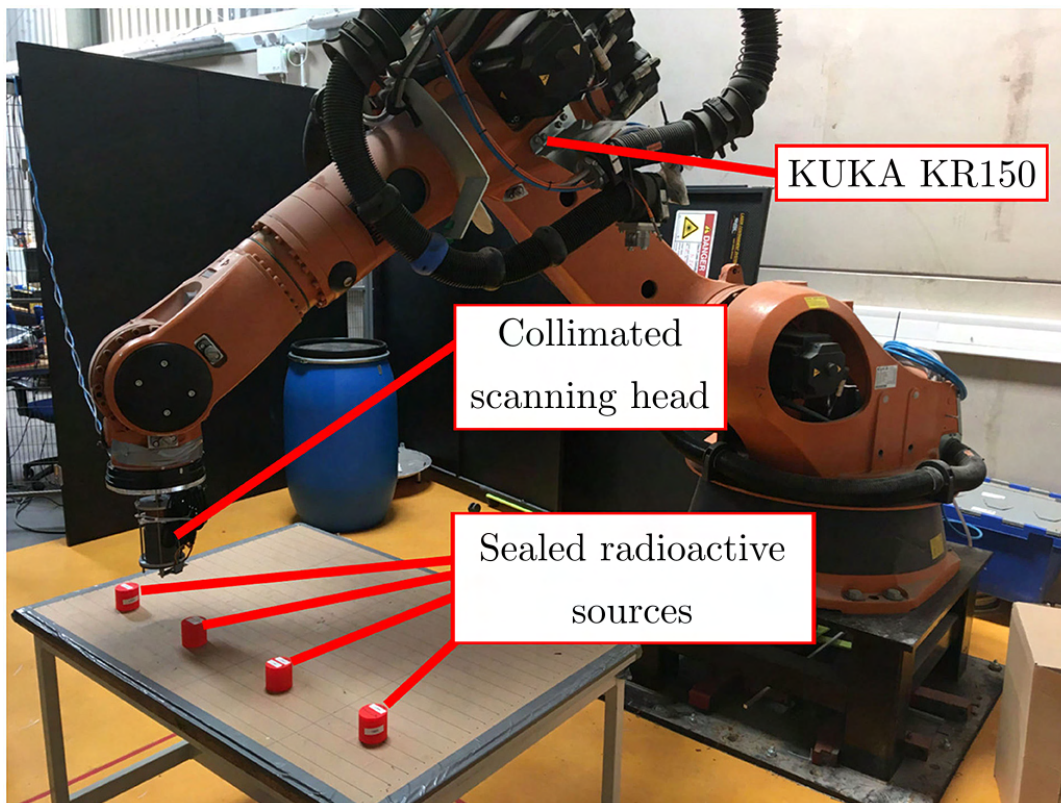


Figure 3.3: Photograph of the developed radiation mapping system on an industrial robot arm.

averaged at the same rate². The combined use of these components formed a combined laser profiling and radiation scanning system. A Photograph of which is shown in Figure 3.3. Recorded measurements could be assimilated with positional data from the robot arm to generate a point cloud, which in turn could create a 3D model using surface interpolation techniques. A flow diagram explaining the communication flow and general setup is given in Figure 3.4. The setup comprises of modified COTS hardware, hence requiring little control performance verification, allowing for easy replacements to be made in case of radiation or operational damages.

The simplest procedure to implement to survey a full table of radioactive objects, is to comprehensively scan each part of the surface. A raster scan style pattern achieves this by using the robot arm to sweep the surface, as directed in Figure 3.5.

²The VL53L0X has a scan rate of up to 400kHz

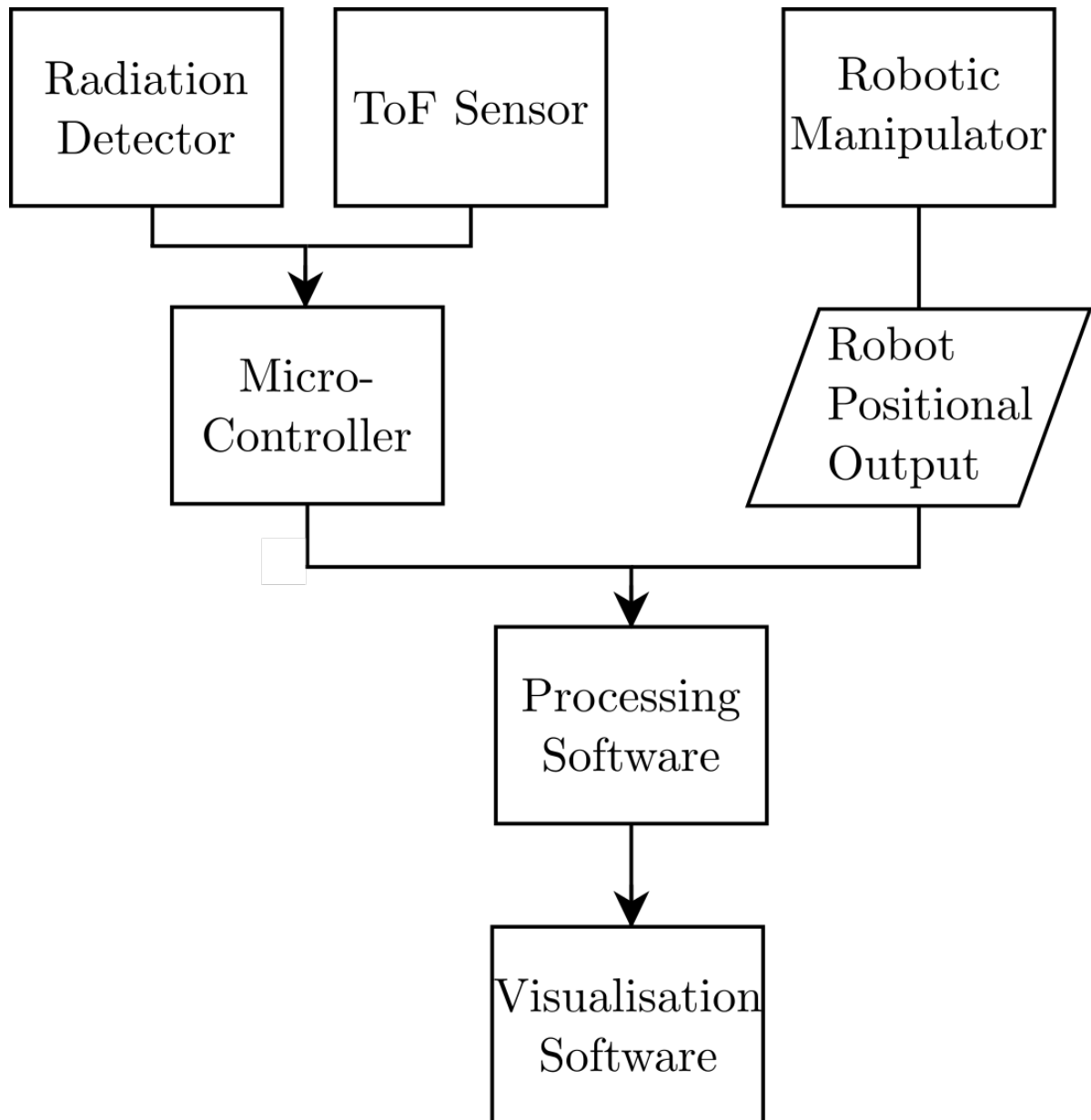


Figure 3.4: Flowchart detailing the information and control flow algorithm controlling the robotic radiation mapping system.

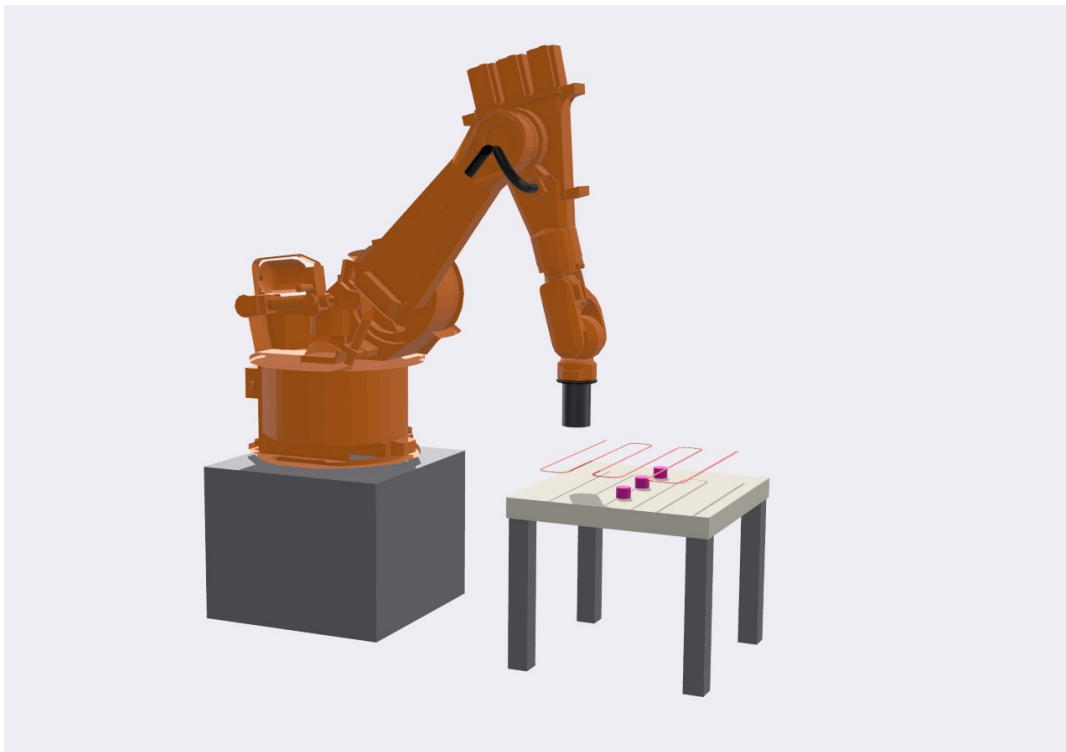


Figure 3.5: Diagrammatic representation of a raster scan path.

3.2.5 Visualisation

The visualisation of results collected from robotic scanning was designed to be application dependant, enabling data to be displayed effectively for each use case. This was achieved using Python scripts which sought to interpolate and combine radiation and positional data to generate 2D and 3D surface maps, representing the distribution of radiation across a surface. In the case of visualising a fixed stand-off distance flat surface, such as a table-based radiation scan, a simple interpolation method was used. A 3D surface implementation was made to include the ToF sensor measurements, generating a point cloud which could be transformed into a 3D surface using PythonTM's 'plot_surface' function.

3.2.6 Spectral Windowing and Dose Rate Conversion

The Kromek Sigma-50 micro-gamma spectrometer collects data into 4096 energy bins ranging from 50 keV to 2 MeV. These energy bins can be calibrated to form a full spectrum. For applications requiring knowledge of the isotopes present within the radiation survey, spectral windowing of the recorded gamma spectrometry data may be applied. Spectral windowing is the process of analysing the required gamma spectrum and only counting in specific gamma-ray energy intervals. This allows for specific isotopes to be identified within the radiation survey. For example, to analyse the system response for Cs-137, only the counts recorded in the energy range of the

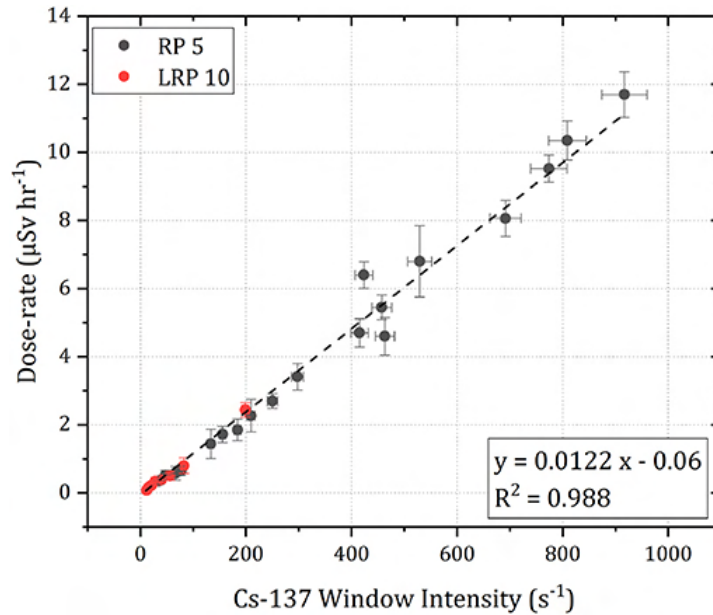


Figure 3.6: Graph showing the calibration method used by Connor et al. to determine the dose rate conversion factor [182]. RP 5 and LRP 10 are labels for the two different sources used within Connor et al.'s research.

662 peak would summed and attributed to the Cs-137 gamma photons for the radiation survey. Connor et al. [182], calibrated a Sigma-50 to allow for a multiplication factor to transform the Cs-137 peak window counts into a dose rate. This conversion factor is shown graphically in Figure 3.6. Using this principle, the data could be processed to give surface dose rate estimates for each collected radiation survey. For each spectrum, the dead-time corrected photopeak counts were summed and multiplied by the conversion factor identified by Connor et al., to yield the dose rate. Given prior knowledge and the geometry of the sealed-source puck, the inverse square law can then be invoked to calculate the dose rate of the surface of the puck. The distance to the centre of the volume emitter can be estimated at 30 mm, corresponding to the thickness of the perspex and a small air gap, as shown in Figure 3.1. Hence, the expected count rate at the surface of the puck may be calculated using the inverse square law and the correction factor can be applied to provide a dose rate estimation for the puck surface.

3.3 Experimental Scenario Setup

A number of test scenarios involving radioactive sources placed in different geometrical combinations on a flat scan surface were created to examine the system response. The purpose of this was to test that the system worked as anticipated for a number of different survey scenarios.

3.3.1 Radiation Survey and Laser Profiling

To investigate the combined laser profiling and radiation scanning system, a scan area of approximately 600 mm x 260 mm was defined on a table. A KUKA KR150 was then programmed to perform a simple raster scan pattern maintaining a constant stand-off distance of 60 mm from the end of the detector to the table surface. It was programmed to move at 10 mms⁻¹ with a detector-source stand-off distance of 10 mm. Individual scenarios involving different combinations and placements of radioactive sources could then be scanned to test the system. Activities of each source and their relative placements on the scan surface can be found in table 3.1.

3.3.1.1 Scenario 1 - 2 Cs-137 Sources 30cm Apart

As identified in section 1.2, Cs-137 is likely to be a prominent constituent present in nuclear waste and therefore likely to be commonly identified in any nuclear sort and segregation activity. Hence, it makes an ideal test source for exploring radiation mapping with a sort and segregation focus within a laboratory setting. Scenario 1 sought to prove the concept of radiation mapping using a robot arm, through exploring a simple source placement. Two sealed source Cs-137 pucks of strengths 30 kBq and 36 kBq were placed 30 cm apart in the centre of the table.

3.3.1.2 Scenario 2 - 2 Adjacent Cs-137 Sources

In a waste sorting scenario, the distribution of radioactive sources across a sorting table will be entirely random, so it is possible that two similarly shaped contaminated objects with similar activities could be placed directly adjacent to each other. The isotropic and stochastic nature of radiation emissions, combined with the inability to directly report the direction of each photon emission, means that the radiation survey will not be able to distinguish these are two emitting objects. This could be instead inferred by visualisation techniques. In this way, different objects which may be contaminated with different materials could be identified. Hence, to explore the limitations of the laser profiling system, the 30 kBq and 36 kBq Cs-137 source pucks were placed directly adjacent to each other.

3.3.1.3 Scenario 3 - 2 Cs-137 Sources 1 cm Apart

An additional laser profiling test was completed placing the sources 1 cm apart. This was designed to further test the capability of laser profiling systems in distinguishing objects at close proximity to each other.

3.3.1.4 Scenario 4 - Mixed Source Scan

Nuclear waste destined for long-term storage will not solely contain Cs-137, and there may be a variety of radioactive sources present within the waste. Scenario 4 sought to explore the use of spectral windowing, via dose rate conversion, to identify the different isotopes used. For this,

2 Cs-137 sources 2 cm apart and 2 Pitchblende (NORM) sources 30 cm apart, were utilised to provide a ‘mixed’ source test.

	Type	Activity (kBq)	X Pos. (cm)	Y Pos. (cm)
Scenario 1	Cs-137	31.0	15.0	14.0
	Cs-137	36.0	45.0	14.0
Scenario 2	Cs-137	31	27.5	14.0
	Cs-137	36	32.5	14.0
Scenario 3	Cs-137	36.0	27	14.0
	Cs-137	31.0	33	14.0
Scenario 2	NORM	2.9	15.0	14.0
	Cs-137	31	27.5	14.0
	Cs-137	36	32.5	14.0
	NORM	3.0	45.0	14.0

Table 3.1: Puck types and placements relative to the robot base coordinates for each scenario.

3.4 Results and Discussion

3.4.1 Scenario 1

The results of the scan and subsequent visualisations in both 3D and 2D are presented in Figure 3.7.

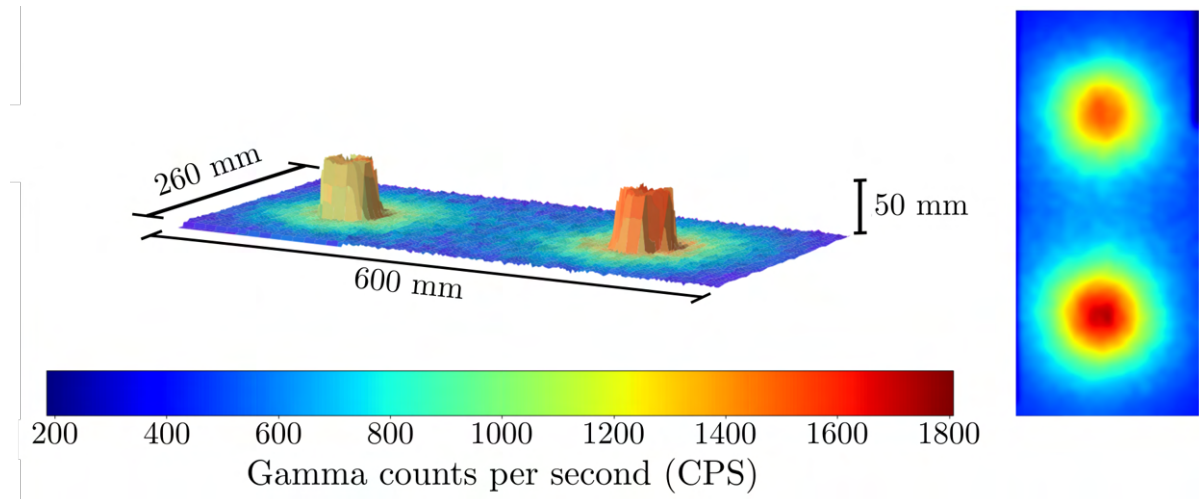


Figure 3.7: 3D model and overlaid radiation map generated from a robot scan above two Cs-137 sources 30 cm apart. Left to right the source activity is 30 kBq and 36 kBq, respectively. The colour represents the gamma radiation counts in counts per second for a given 2×2 mm pixel.

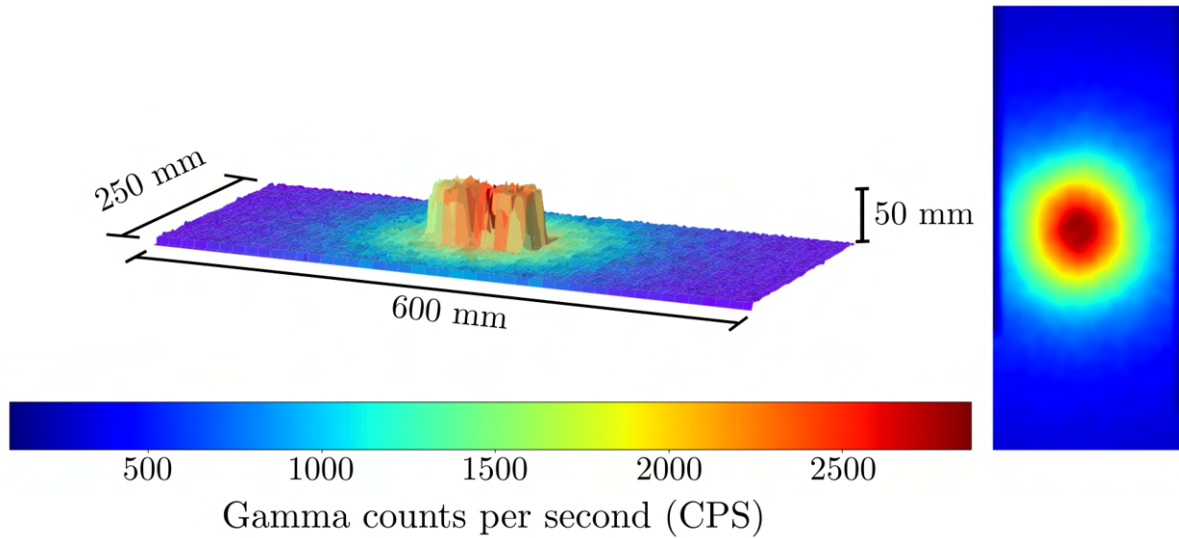


Figure 3.8: 3D model and overlaid radiation map generated from a robot scan above 2 Cs-137 sources directly adjacent to each other. Left to right the source activity is 30 kBq and 36 kBq, respectively. The colour represents the gamma radiation counts in counts per second for a given 2×2 mm pixel.

Relative source strengths are correctly identified by the radiation survey, with the source on the right visibly stronger than that on the left. Figure 3.7 also demonstrates the capability of the laser profiling and the combination of data types to derive a subsequent visualisation, providing an identifiable geometric representation of the radioactive source pucks.

3.4.2 Scenario 2

Adjacent source placement introduced a technical challenge, as the close proximity would make the sources radioactively indistinguishable as two separate objects. Therefore, the laser profiling could potentially be utilised to identify the distinct objects via the 3D representation of the scene. Figure 3.8, shows the result of the adjacent source experiment.

From the 2D radiation map, a single radioactive hotspot is clearly visible, but it is not distinguishable as two separate sources, as expected. The physical separation of the sources could be inferred from the 3D modelling of the scene. It is easier to distinguish on software which enables the rotation and scaled inspection of the generated model. To aid the visual clarity in distinguishing the pucks, Figure 3.9 presents the same data, but from an alternative observation angle, which shows that the laser profiling can adequately separate the two sources.

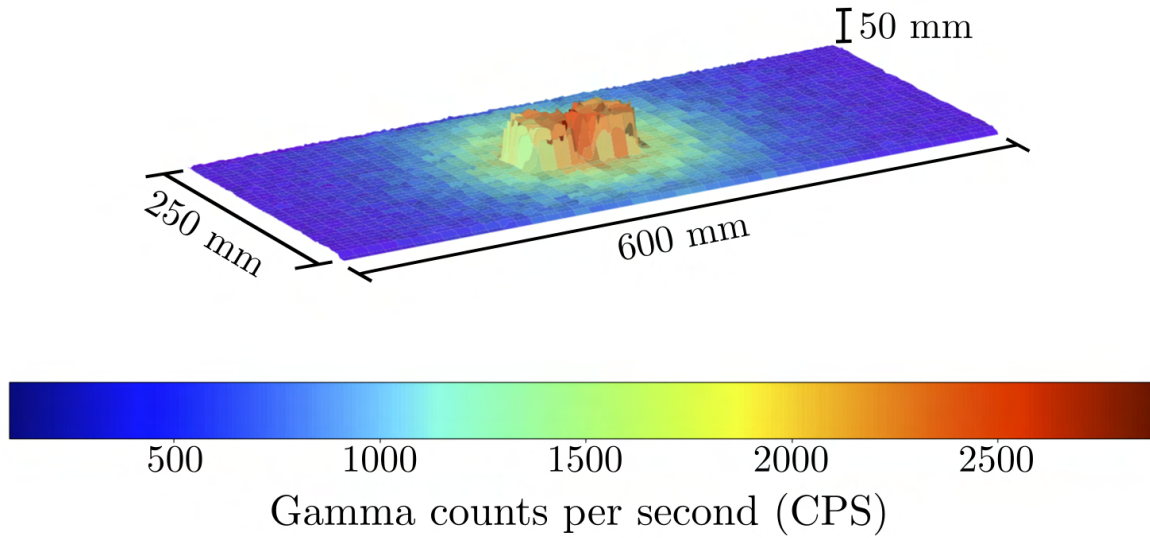


Figure 3.9: 3D model and overlaid radiation map generated from a robot scan above 2 Cs-137 sources directly adjacent, from a second angle to aid visual clarity of the distinguished pucks. Left to right the source activity is 30 kBq and 36 kBq, respectively. The colour represents the gamma radiation counts in counts per second for a given 2×2 mm pixel.

3.4.3 Scenario 3

Scenario 3 was designed to more conclusively demonstrate the 3D modelling, the result for the source placement with a 1 cm separation is shown in Figure 3.10.

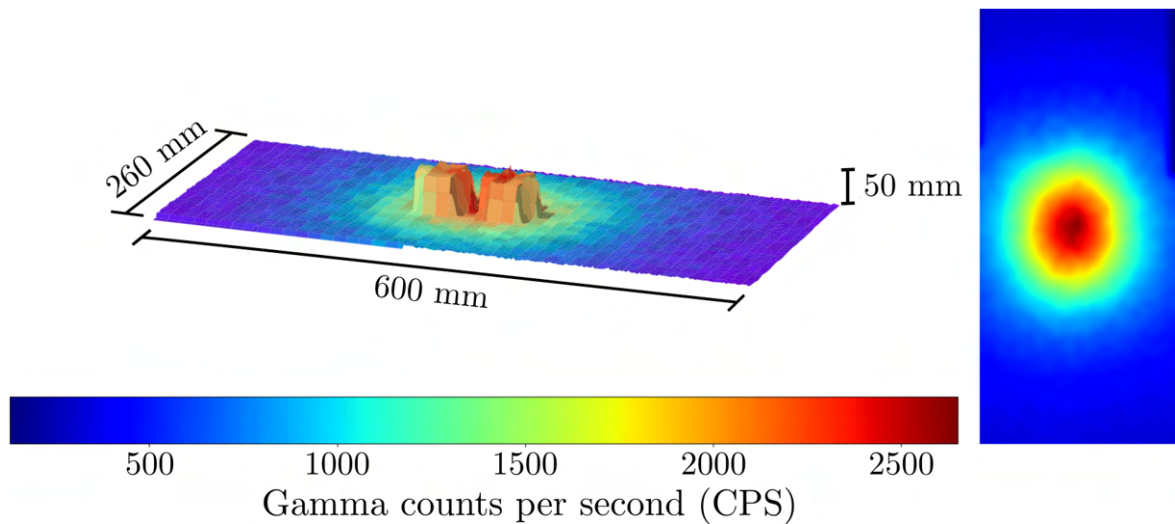


Figure 3.10: 3D model and overlaid radiation map generated from a robot scan above 2 Cs-137 sources 1 cm apart. Left to right the source activity is 30 kBq and 36 kBq, respectively. The colour represents the gamma radiation counts in counts per second for a given 2×2 mm pixel.

Again, the radioactivity is concentrated to a single, slightly elongated zone containing the radioactive sources. The 1 cm gap created by the source placement can be seen very clearly by the laser profiling.

3.4.4 Scenario 4

The use of a spectroscopic gamma measurement technique, means the spectral data may be used to distinguish particular radioisotopes, providing information on the emitters that are present within the solid angle of the detector and collimator. This could be useful for the sorting and segregation of nuclear waste, for identification of different waste isotopes present. A spectral windowing technique could be used to fulfil this, by highlighting only the counts in a particular energy range. The results from scenario 4 use this technique to distinguish the available NORM and Cs-137 sources, simultaneously reproducing the attained Cs-137 dose rate. Figure 3.11, shows the mapped scene without spectral windowing applied.

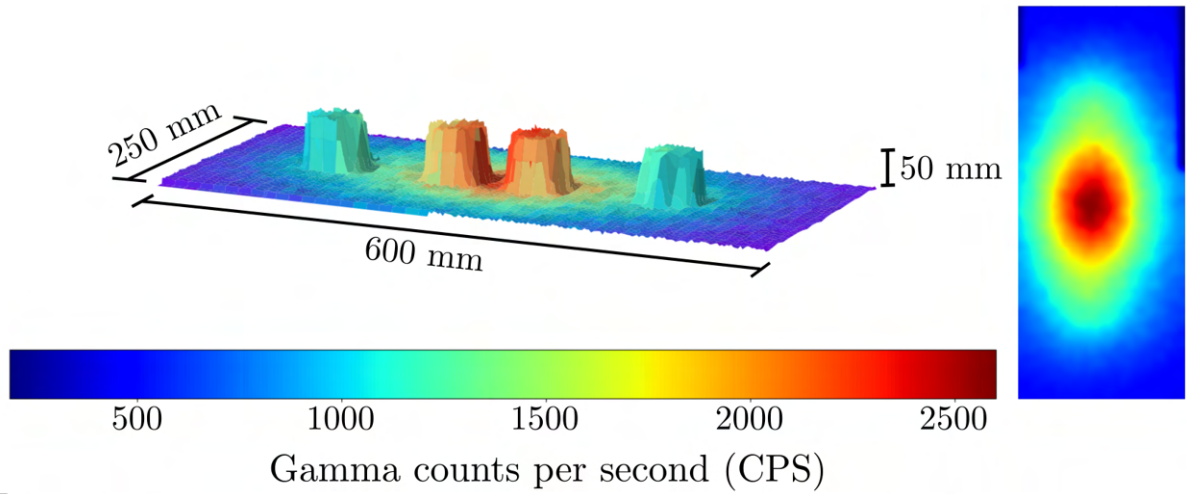


Figure 3.11: 3D model and overlaid radiation map generated from a robot scan completed at a 1 cm standoff above 2 Cs-137 sources 1 cm apart. Left to right the measured source surface dose rates are $4.5 \mu\text{Svh}^{-1}$ Pitchblende, $7.5 \mu\text{Svh}^{-1}$ Cs-137, $10 \mu\text{Svh}^{-1}$ Cs-137 and $4.3 \mu\text{Svh}^{-1}$, respectively. The colour represents the gamma radiation counts in counts per second for a given 2×2 mm pixel.

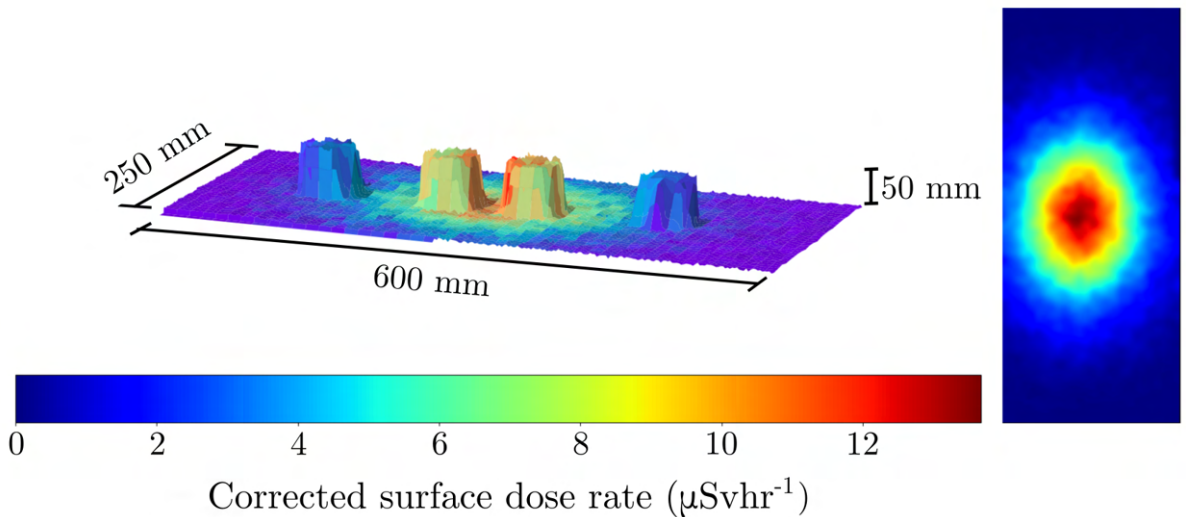


Figure 3.12: 3D model and overlaid radiation map generated from a robot scan completed at a 1 cm standoff above 2 Cs-137 sources 1 cm apart. Left to right the measured source surface dose rates are $4.5 \mu\text{Svh}^{-1}$ Pitchblende, $7.5 \mu\text{Svh}^{-1}$ Cs-137, $10 \mu\text{Svh}^{-1}$ Cs-137 and $4.3 \mu\text{Svh}^{-1}$ Pitchblende, respectively. The colour represents the Cs-137 gamma radiation dose rate for a given 2×2 mm pixel.

The NORM sources are evident as weaker sources than the Cs-137, but are radiometrically

indistinguishable on the basis of only photon count intensity. With spectral gating and dose rate conversions applied, the sources are easily separable, as shown in Figure 3.12. This approach makes the NORM sources blend into the background, but highlights the Cs-137 sources clearly. Displaying the results in terms of dose rate could facilitate accurate radioactive waste assay, as dose rate can be used to identify waste class [183]. Dose rates of 2 mSv h^{-1} are typically used to distinguish between LLW and ILW, for example. A limitation of the dose rate methodology is also evident here, as the area between the Cs-137 pucks has a dose rate higher than either individual puck, owing to the detector receiving counts from both sources simultaneously. It must also be highlighted that there are numerous known prioris required for such a dose rate conversion. In reality, the location of a contained emitter would not be known, therefore only a gross estimate of dose could be recoverable. However, the spectral windowing required to arrive at this dose conversion could have tremendous uses within waste sorting, as individual isotopes may be separable.

3.5 Conclusions

This chapter presented the initial development of a robotic radiation survey system. The system integrated a radiation detector and ToF ranging unit, combined with a robotic manipulator, to fulfil the proof of concept use of autonomous radioactive waste surveying for a variety of test scenarios.

Experiments demonstrated that the developed system methodology was able to make accurate, high sensitivity, high spatial resolution radiation maps for resolving potential nuclear waste objects on the basis of emitted gamma radiation intensity. After applying the system on a KUKA KR150 industrial arm, a 3D visualisation of each test scenario was generated with an overlaid radiation map. This demonstrated that the technique was not only able to locate the radioactive sources, but also distinguish individual shapes from each other despite their close, even adjacent, proximity. Objects were clearly identifiable 1 cm apart, and partially distinguishable when directly adjacent. In reality a 3D depth camera or photogrammetry based technique would normally be optimal for physical object identification. For example, recently Monk et al. [184] demonstrated the use of a Microsoft Kinect to perform the semi-autonomous radiometric scanning of objects. This enables the robot to dynamically survey the environment, enabling the detector-source stand-off distance to be minimised, thus improving the spatial accuracy of the collected data. However, the laser profiling system could be used in environments where radiation is sufficiently extreme that problems arise with using these types of more advanced methodology systems.

While the robotic radiation survey achieves its target of making a spatial identification of radioactive emitters, there are efficiency gains which could be made. In scenarios with sparsely

populated radioactive sources, significant time is used scanning areas without emitters. It is possible, that an AI based approach could be implemented to target and scan only the specific regions of interest, increasing the volume of complementary data. In addition, the spherically symmetric radiative gamma-ray flux which is emitted from the radioactive sources results in limitations on the identification of which physical shape corresponds to which emission on the radiation map. This issue of source localisation could be reduced through further optimisations of collimator design, increasing the volume of Pb in the wraparound. In doing so, the gamma-ray solid angle from the source to the detector would be reduced. However, this comes at the cost of potentially altering the gamma-ray energy measurements, as higher energy particles may be attenuated and scattered by the Pb shroud [185]. A potential solution to this problem could be the implementation of a post processing technique, able to recover the real location of the emitter based on a known detector response function.

RADIATION SURVEY OPTIMISATION

Chapter 3 demonstrated that robotic manipulators are capable of successfully performing radiation surveys, highlighting the locations of radioactive emitters across a scan surface. However, it was noted that the simple raster scanning methodology utilised was sub-optimal for application within nuclear waste sorting - something more dynamic is needed. Raster scanning across an entire surface is not time efficient, in particular when there may be a sparse distribution of radioactive emitters. If more time could be spent surveying only the radioactive sources in a scene, more effective data collection would be realised. A more effective data collection approach would consist of an optimised AI based scanning procedure. One such possibility is the application of computational optimisation algorithms. In effect, a radiation survey is a 2D function defined by spatial co-ordinates and radiation intensity. Computational optimisation algorithms are commonly used to identify optimal solutions to functions, delivering time and memory efficient results. Hence, it may be possible to use such algorithms to identify hotspots within radiation surveys, by applying an ‘optimisation’ to the measured scan surface. This chapter seeks to detail the implementation and testing of current AI based optimisation algorithms for identifying high intensity radioactive sources on a nuclear waste sorting table with a robotic manipulator. While AI optimisation is commonly applied to solve numerous complex problems, such a methodology has not been previously reported for use in identification of radioactive sources. Hence, its use is examined and represents an innovative assimilation of AI and robotics.

4.1 Introduction

Demonstrated in chapter 3, was the capability of a robotically integrated radiation sensor to accurately survey radioactive sources positioned across a 2D surface. This represents a powerful tool for the autonomous identification of radioactive sources within a waste sorting procedure. It was

highlighted, that following radioactive identification, waste removal based on prioritised hazards, may assist in optimising the sorting operation. However, a key benefit of an autonomous process is the acceleration of the sorting time taken over traditional manual approaches. Within many waste processing scenarios, radioactive sources may not be present, or be sparsely populated across the scan surface. In such instances, robotic radiation mapping using a simple raster scan approach may be inefficient, as a significant number of measurements are taken outside of the regions of interest. The raster scan approach is time consuming, as every location must be visited and scanned. Accelerating this process would result in a global resolution loss, requiring either fewer measurement locations, or a reduced detector dwell time.

The identification of the strongest emitter in a given scene, can be broken down into an optimisation problem which may be solved mathematically. Fundamentally, a radiation field is a surface containing radioactive emitters. This may be thought of as a real-valued 2D function, in which position is an input parameter and radiation measurement is an output. Mathematical optimisation attempts to maximise/minimise such real valued functions from an allowed set of input values. For example, if we have some function $f(x)$, which represents a surface containing radioactive sources for which:

$f : A \rightarrow \mathbb{R}$ from some set A to the real numbers

Optimisation seeks to determine the element $x_0 \in A$, such that $f(x_0) \geq f(x) \forall x \in A$ to ‘maximise’ the solution, alternatively, $x_0 \in A$, such that $f(x_0) \leq f(x) \forall x \in A$ to ‘minimise’ the solution. For some functions an analytical solution may be identified using calculus and more specifically differential approaches. However, if a function is non-differentiable, then no analytical solution may be identified. Such functions require numerical or computational solutions. These numerical methods may not yield a precise result, but will iteratively improve towards a final solution. In the case of determining the maximal position on a surface containing radiation, errors introduced by the stochastic variation of gamma emissions combined with any measurement system errors make the optimisation approach a non-differentiable problem. Hence, a suitable computational technique must be utilised to identify a solution. The aforementioned brute-force approach is actually the simplest form of computational optimisation. In brute-force optimisation, regular sampling of the function is completed to identify the optimal value.

Computational optimisation uses AI to take radiation measurements at distinct spatial locations and subsequently make intelligent decisions on where to record future measurements. To explore this, a number of computational algorithms were applied to the radiation survey technique, including brute-force, particle swarms, dual annealing, Simplicial Homology Global Optimisation (SHGO), differential evolution and basin hopping. These are all real-time, sensor

based feed-back optimisation procedures which could have applications across the field of robotic radiation surveying. Implementation would be feasible everywhere from large scale drone surveys to ground vehicle based radiation mapping.

4.2 Method

This section discusses the modifications made to the robotic system used within chapter 3, to enhance its capability, specifically its efficiency. Following this, the fundamentals of each of the selected computational optimisation algorithms applied for the rapid identification of radioactive emitters is covered. Suitable test scenarios were created and justified to assess various hot-spot identification modalities. A simulated environment was built and each methodology tested over 1000 repeats. These simulated results were then complemented by live experimentation over 10 repeats for each.

4.2.1 Radiation Mapping System

To demonstrate the versatility of the technique covered in chapter 3, a similar system was constructed on a different robotic manipulator platform. Experiments in this chapter used a KUKA LBR MED. A photograph of the system setup is shown in Figure 4.1.

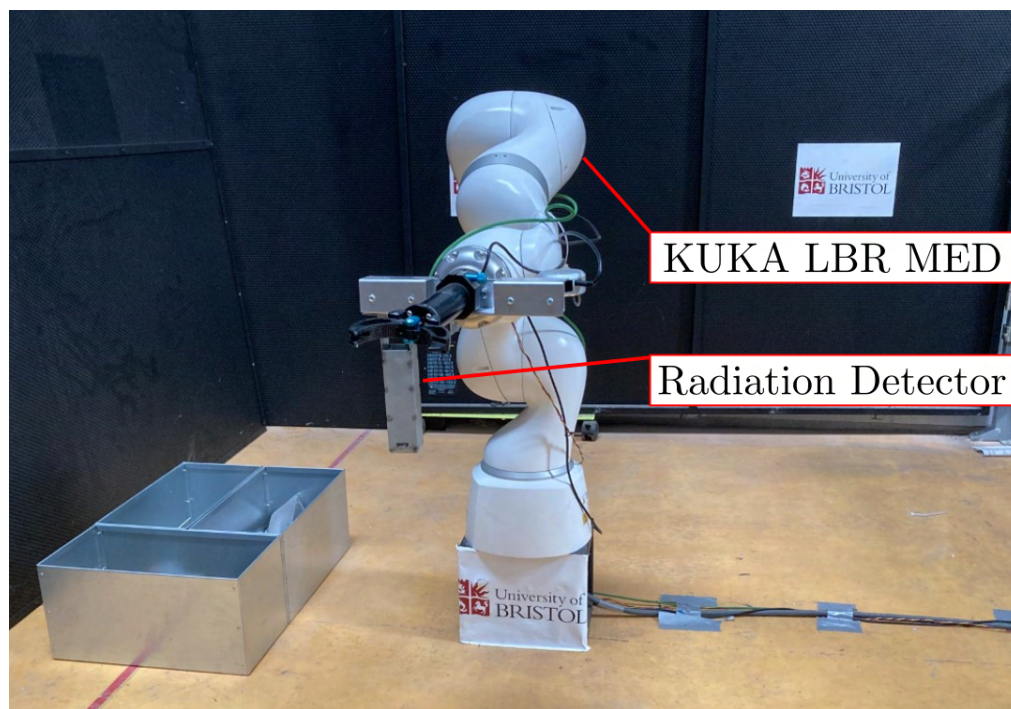


Figure 4.1: Photograph of the developed radiation mapping system on a KUKA LBR MED.

Programming was completed in PythonTM. Control code effectively took positional inputs, the robot arm would move to the specified location, then the radiation detector was triggered to count for a specified time. Hence, the system would collect radiation data at select locations rather than moving and collecting simultaneously. A dwell (counting) time of 1 second was selected at each measurement location.

4.2.2 Radiation Mapping Algorithms

4.2.2.1 Brute Force

The raster scanning process demonstrated in chapter 3 is hereafter referred to as the ‘brute-force’ approach. It is able to comprehensively scan a full surface, identifying radioactive objects. In essence it creates an equi-distant spaced grid of points across a surface to try all values. Figure 4.2, shows the measurement locations used for a brute force method across a simulated radiation map containing 2 sources.

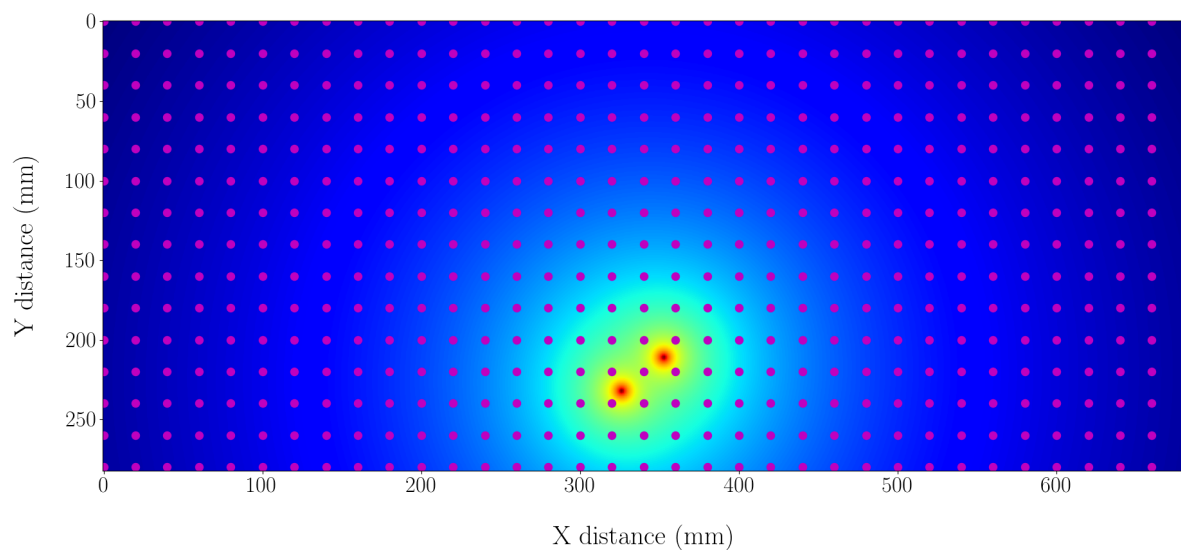


Figure 4.2: An example of the evaluation positioning for a brute force optimisation technique when applied across a radiation field containing 2 sources.

4.2.2.2 Particle Swarms Optimisation

Particle Swarms Optimisation (PSO), is a computational method used for solving optimisation problems, developed by Kennedy et al. [186]. It uses many measurement points, known as ‘particles’ which are interconnected, to iteratively approach an optimised solution. The process may be described informally as follows, within a specified ‘search-space’, particles are free to move,

evaluating the numerical value of the function at each location [187]. Each particle operates by moving iteratively across the search-space, holding the following information:

- Position
- Value at position
- Velocity to compute the next position
- Memory of the previous best position
- Value of the best position

[187]

This information is used to compute each subsequent position the particles visit to take a measurement or function evaluation. There is a topology to determine which particles inform each other, with the set of particles which inform a given particle referred to as its neighbourhood [187]. The complete set of particles is known as the ‘swarm’. When a swarm is initialised, random or specified locations are initially selected for the particles in the survey space. Each one takes a measurement. A velocity is then computed for each particle, based on current position, current velocity, previous best and previous best in the neighbourhood. Using this information, the particle can generate a new velocity to find the new position. Localisation constraints placed on particles restrict them to the search space and pre-defined stopping criteria eventually end the scan and a maximal position can be determined [188].

In the context of radiation mapping and strongest source identification, it may not be immediately obvious how PSO could be implemented, given the restriction of one sensor on one robot arm. However, ultimately each particle is simply a single measurement in space with tracked information. Each particle may instead be tracked in software, with the robot arm moving the detector to each particles ‘position’ in space to collect the full set of data. This was programmed in PythonTM, using the Pyswarms package [189] to handle the PSO.

Each iteration will require the robot arm and sensor to move to the location of a particle within a given iteration. Hence, to fully optimise the problem, the optimal route through each position (particle) in a given iteration must be identified.

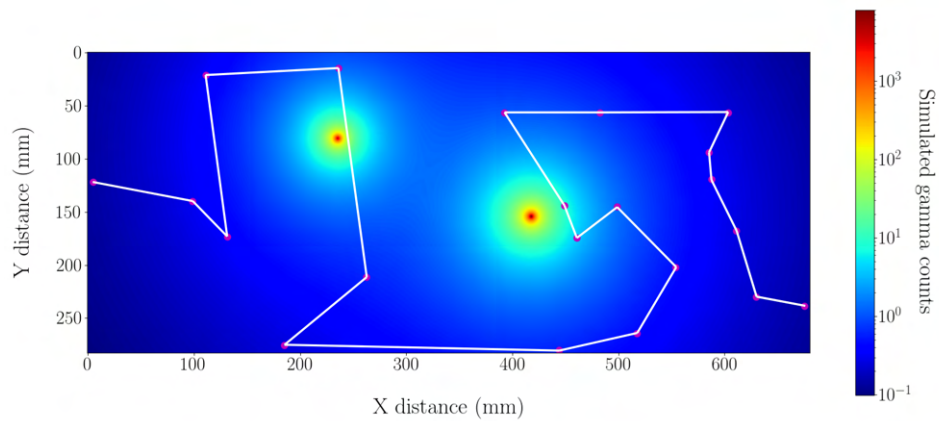
Travelling Salesperson Problem

Each iteration of the PSO requires the robot to travel to multiple locations to collect a radiation measurement. The particulate trail nature of the PSO algorithm means that the measurement locations can be very diversely spread across the search-space. Hence, to fully optimise the problem, a technique to intelligently travel to each location following the shortest possible path

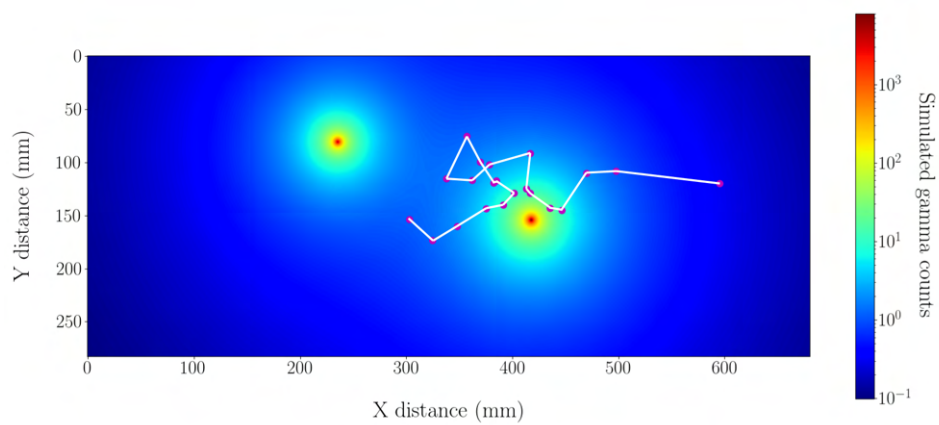
is required. This is a standard combinatorial optimisation problem, known as the Travelling Salesperson Problem (TSP). Imagine a salesperson wishes to visit n cities across the world, if they visit them all, what is the shortest route they can take? There is an obvious brute-force approach to this, solved by simply testing all possible routes and selecting the route with the lowest travel distance. However, the number of solutions which must be calculated is $n!$, which quickly becomes computationally intensive to find a solution, as the value of n increases.

Exact approaches are computationally heavy, but ultimately find the correct solution. Alternatively, heuristic approaches can drastically reduce the search time for solving the TSP, often with only marginal losses in accuracy [190]. To create the optimal approach for use in this work, the python TSP packages were used to solve the problem.

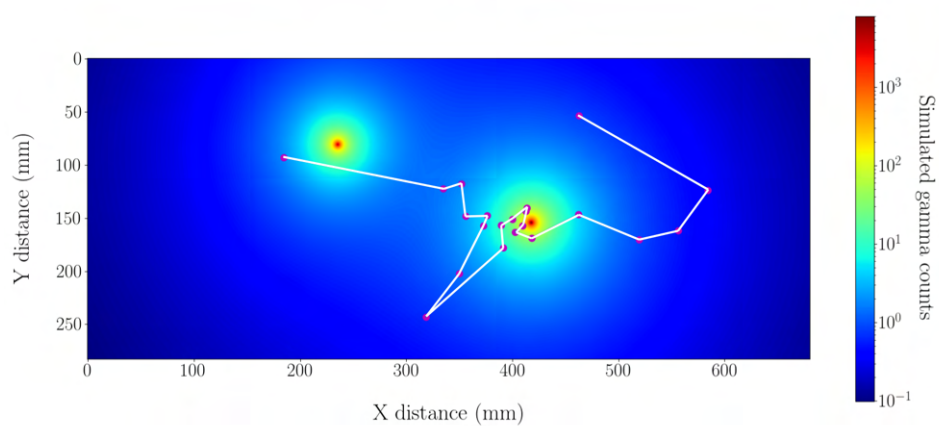
Figure 4.3, shows the progression of a PSO across a simulated radiation survey containing two radioactive sources.



(a)



(b)



(c)

Figure 4.3: An example of the evaluation positioning for a particle swarm optimisation technique when applied across a radiation field containing 2 sources. The progression of evaluation positions tried is shown across iteration one (a), five (b) and ten (c) for a ten iteration procedure containing 20 particles.

4.2.2.3 Simplicial Homology Global Optimisation

Simplicial Homology Global Optimisation (SHGO), is an optimisation technique used for global optimisations of functions. Algorithmically, SHGO creates simplicial complexes which are derived from the sampled evaluations of the function [191]. A simplicial complex for the purposes of understanding required for this thesis, may be defined as a set of co-ordinates which form a shape. In combinatorial mathematics, this is known as a ‘graph’ and is comprised of numerous ‘subgraphs’. These subgraphs can be minimised via Spemers lemma [192], to isolate minimal locations across the search space [191]. The SHGO method iteratively solves these minimisations until a finishing criteria is met. SHGO has been highlighted as particularly useful for optimising Lipschitz smooth functions, which requires for any,

$f : A \rightarrow \mathbb{R}$ from some set A to the real numbers

$$|f(x_1) - f(x_2)| \leq c|x_1 - x_2| \forall x \in R$$

where c is some real constant. These criteria are satisfied by radiation maps, as each spatial location satisfies the real number requirement on x and there is a known real maxima and minima to the function. Figure 4.4, shows the progression of measurement locations for a SHGO algorithm across a simulated radiation survey containing two radioactive sources.

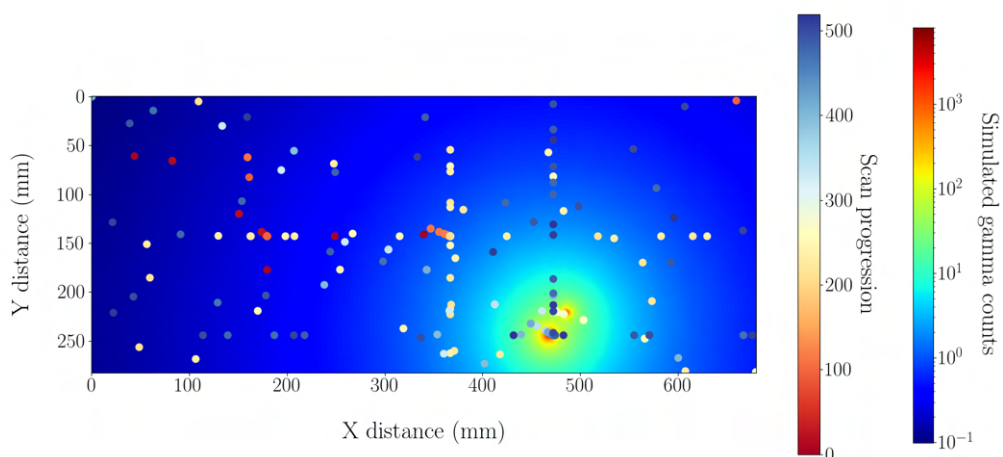


Figure 4.4: An example of the evaluation positioning for a SHGO optimisation technique when applied across a radiation field containing 2 sources.

4.2.2.4 Basin Hopping

Basin hopping (BH), is an iterative process, with a set of search ‘agents’ used to collect measurements at different locations. Each agent is then perturbed, before a local optimisation is performed [193]. Agents are accepted or rejected based on the value returned by the minimised function. This process is repeated until a global optimal location is identified [194]. It is most commonly applied for multi-variable and high dimensional problems [193], such as the characterisation of biological macro-molecules [194] owing to its ability to move between local optima in the variable space. The high sampling and benefits for optimisation within multidimensional spaces make it unlikely that basin hopping will be the fastest algorithm for identifying the strongest source in a 2 dimensional space. However, it may be useful for determining local optima in a scenario where there are numerous sources. Figure 4.5, shows the progression of measurement locations for basin hopping algorithm across a simulated radiation survey containing two radioactive sources.

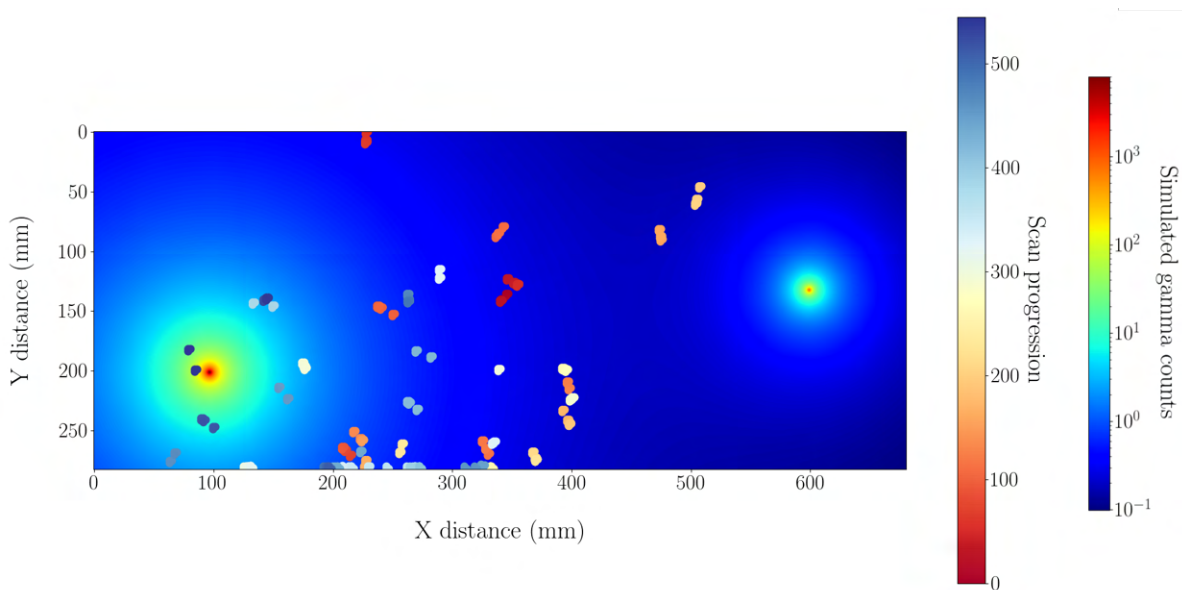


Figure 4.5: An example of the evaluation positioning for a basin hopping optimisation technique when applied across a radiation field containing 2 sources.

4.2.2.5 Differential Evolution

Differential evolution (DE), is a population-based metaheuristic search algorithm developed by Storn et al. for solving optimisation problems [195]. The algorithm works by using multiple ‘candidate solutions’, or evaluation points spread across the scan surface [195]. This forms a ‘population vector’. New population vectors are created by summing the weighted difference

between two population vectors to create a third. This summing process is known as a ‘mutation’. The parameters of this mutated vector are then mixed with those of a predetermined vector, the ‘target vector’, resulting in a ‘trial vector’. If the cost of the trial vector is less than that of the target vector, the trial vector replaces the target vector in future iterations. This process continues until a stopping criterion is met [195].

The differential evolution algorithm is strongly suited for multi-modal problems [196]. These are problems with numerous global solutions, or alternatively, a single global solution containing multiple local peaks. In a radiation field, stochastic variation or errors in measurement could lead to a solution containing multiple local peaks. Hence, it is possible that a differential evolution approach could be advantageous. Additionally, differential evolution was designed for experimental optimisation, in which case there is a significant time cost associated with each evaluation. This is certainly the case for a robotic arm based radiation survey operation, as each evaluation will take at least a second to generate a data point [195]. However, differential evolution is more poorly suited to identifying a singular global maxima. If there was only one radiation source within the survey, it may not be as successful as an alternate approach, but such a scenario is highly unlikely for nuclear waste sorting and segregation, as there will likely be numerous sources. Figure 4.6, shows the progression of measurement locations for a differential evolution algorithm across a simulated radiation survey containing two radioactive sources.

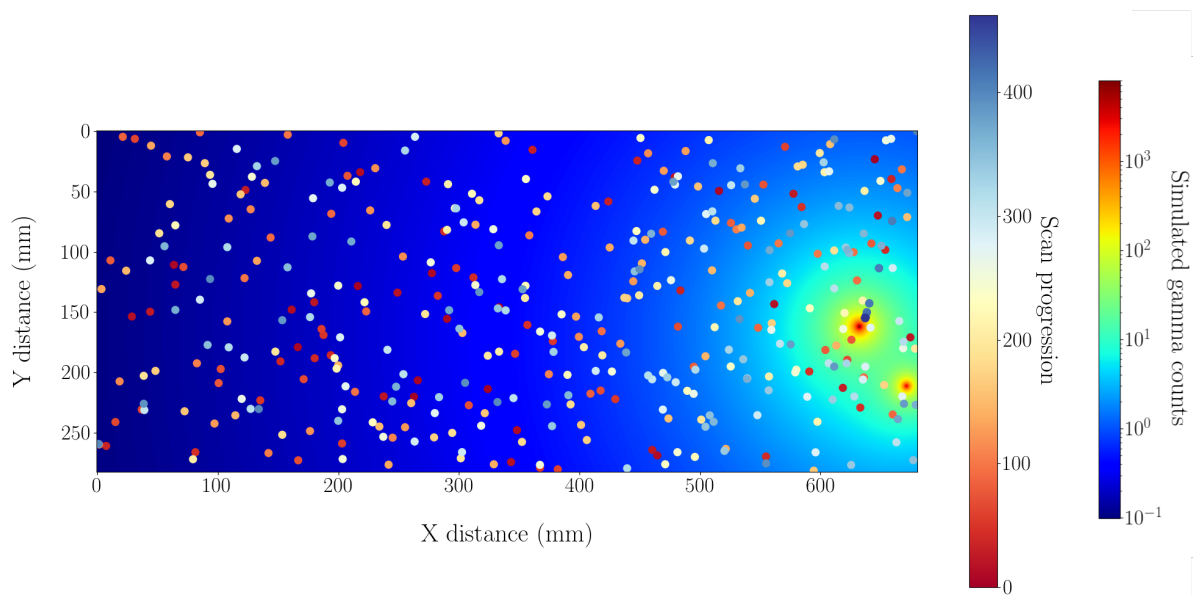


Figure 4.6: An example of the evaluation positioning for a differential evolution optimisation technique when applied across a radiation field containing 2 sources.

4.2.2.6 Dual Annealing

Dual annealing (DA), is a combined classical simulated annealing and fast simulated annealing optimisation algorithm [189], utilising a Cauchy-Lorentz visiting distribution. It has proven ability to solve the Rastrigin function quickly and effectively [197]. The rastrigin function is a very complex function with numerous local optima and a large search space. Similarly to basin hopping and differential evolution, it is likely most applicable for scenarios containing multiple sources, due to its ability to handle numerous local optima.

Algorithmically, the dual annealing technique seeks to use the principles of ‘annealing’ for optimisation. Annealing is the process of heating a metal to reduce hardness and increasing ductility [198]. Kirkpatrick et al. [199] realised there are numerous parallels which can be made between the physical annealing process and function optimisation, developing an algorithm to exploit these links. It applies a distorted Cauchy-Lorentz visiting distribution to each evaluation point to determine the subsequent position. Many of the terms have analogous links to the physical annealing process. With a shape defined by a parameter, q_v , the Cauchy-Lorentz visiting distribution is defined by equation 4.1 [189].

$$(4.1) \quad g_{q_v}(\Delta x(t)) \propto \frac{[T_{q_v}(t)]^{-\frac{D}{3-q_v}}}{\left[1 + (q_v - 1) \frac{(\Delta x(t))^2}{[T_{q_v}(t)]^{\frac{2}{3-q_v}}}\right]^{\frac{1}{q_v} + \frac{D-1}{2}}}$$

Where t represents the artificial time, x is the optimising parameter, Δx represents trial jump distance. T_{q_v} is an ‘artificial temperature’, which is used as a form of relaxation parameter. Figure 4.7, shows the progression of measurement locations for a dual annealing algorithm across a simulated radiation survey containing two radioactive sources

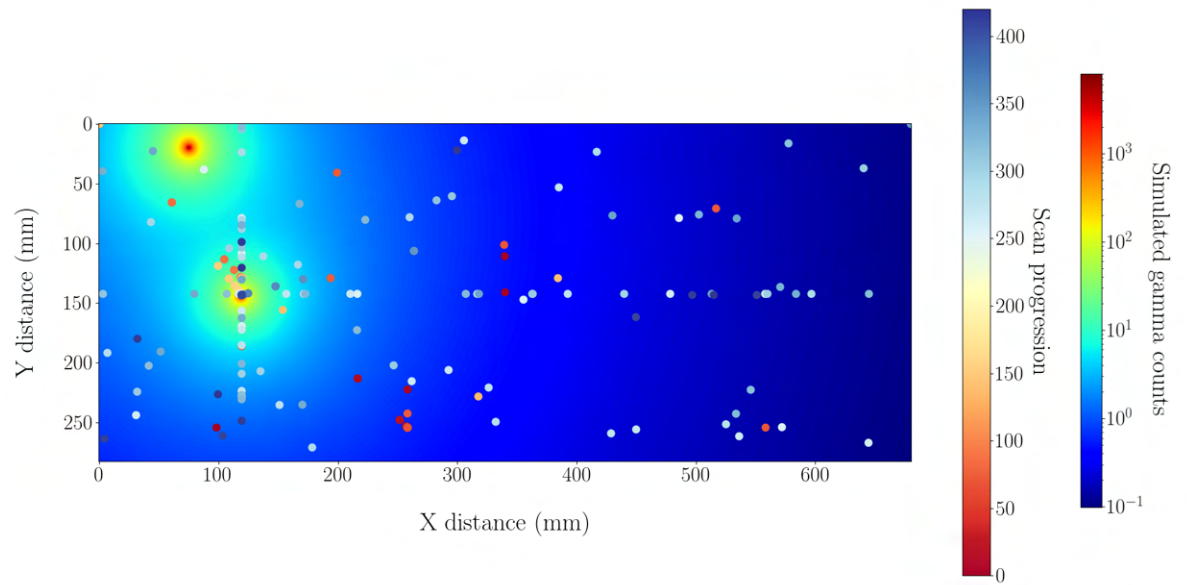


Figure 4.7: An example of the evaluation positioning for a dual annealing optimisation technique when applied across a radiation field containing 2 sources.

4.2.3 Algorithm Testing

To investigate the different postulated intelligent hotspot identification algorithms, simulations of the system response for each scenario were tested. These simulated results were then certified by confirmatory live tests and their arising results.

A simulated environment was created in PythonTM, whereby a surface was created in the form of an array, with grid spacings representing millimetres. Sources could then be placed at random locations across the surface. Each had an associated strength which could either be pre-programmed or randomly assigned within a defined interval. Within the simulation, positions in space could be selected according to the algorithm being tested. Each measurement location would then derive a distance to the source(s) within the simulated surface using Pythagoras theorem. The activity at the measurement location was then determined as the sum of the activities divided by the square of the distances. It was recognised that there is a significant measurement uncertainty on radiation detectors, so a random noise was applied to each measurement. This error was defined as a Gaussian distribution, with an average value of 40 cps and a standard deviation of 10. These values were selected to be consistent with the KromekTM Sigma detector, with a background reading, in the live experimentation space. Simulated radiation surface maps demonstrated good visual agreement with live experimentation maps collected in chapter 3.

The survey area was defined as a 680 x 280 mm flat surface. For most grasping applications it is desirable to localise position to within 10 mm [200]. As such, the optimal approach sought

to identify the sources to within 1 mm, an order of magnitude below the desired centimetre localisation. Sources were placed at various positions across a 680 x 280 mm survey space. For live testing, the sources had an activity of between 1 kBq to 36 kBq. Each algorithm could then be tested within the simulation for 1000 iterations, with the RMS error on positional localisation recorded for each iteration. The same process was applied to the complementary live experiments, with an average taken from a minimum of 10 repeats.

Each optimisation algorithm had different optional parameters allowing them to be tuned. Within each iteration, each algorithm would need to make measurements at numerous positions to understand the surface topology. Ostensibly, the fewest evaluations is desirable, hence reducing scan times. It was recognised that to accurately identify the source to within 10-20 mm a brute-force grid spacing of 20 mm would need to be defined. Each algorithm was tested for 1000 iterations. Theoretically, the brute-force method would require 476 evaluations to be within the region of the desired 10 mm accuracy¹. Therefore, the desired number of evaluations would be 476 or fewer. Basin hopping, PSO and brute-force featured mechanisms to restrict the total evaluation points. For basin hopping, this involved setting the tolerance to one, the maximum projected gradient norm to one, the absolute minimum step size to two, the maximum number of function evaluations to 25, the maximum number of iterations also to 25 and the basin hopping iterations to 160. Particle swarms optimisation used 20 particles for 20 iterations. For dual annealing, the maximum number of global search iterations was set to 30, as this tuned the evaluations to be within the range of the brute force approach. Differential evolution had the population size set to 100, maximum iterations to 25 and the absolute tolerance of the standard deviation across the population to 50. For the SHGO method, the number of sampling points in the simplicial complex was set to 2000 and the iterations used in its construction as four. The latter value had the greatest impact on the evaluation count, with four identified as providing the an evaluation count in the desired range.

Test scenarios were setup, as follows. The source placements can be seen in table 4.1.

4.2.3.1 Scenario 1 - 1 Source

To confirm each algorithm was working as expected, a simple test was designed, where a single 36 kBq Cs-137 puck was placed within the scanning surface. In the simulated environment, this was set to a random position within the constraints of the scan surface. For the live version, this was placed at (-570, -30) mm, relative to the robot base.

¹If it measures every 20 mm, on a grid of 680 x 280 mm, then there are $\frac{680}{2} \times \frac{280}{2} = 476$ positions which must be measured

4.2.3.2 Scenario 2 - 2 Sources

One common pitfall of optimisation is the potential of finding a local maxima rather than the desired global maxima [201]. In sort and segregation, this is unlikely to be a problem, as it is likely a search would seek sources above a threshold strength. However, for completeness, this tested the robustness of each algorithm. The scenario was designed using two sources. For the simulation, the two sources were positioned randomly across the scan surface, with one at 1000 cps and the other at 5000 cps. In the live version, the two sources were placed at (-610, -190) mm and (-510, 0) mm, strong (36 kBq) to weak (6.11 kBq) respectively.

4.2.3.3 Scenario 3 - 7 Sources

Within a nuclear waste sorting application, there will likely be numerous sources present within a survey. Hence, this test sought to examine the response of the algorithms in such a scenario. For the simulated version, seven sources were randomly placed across the survey area, with one source at 5000 cps and the others randomly assigned between 1000 and 3000 cps. For the live version the seven sources were placed, as defined by table 4.1.

	Type	Activity (kBq)	X Pos. (cm)	Y Pos. (cm)
Scenario 1	Cs-137	36.0	-57	-3
Scenario 2	Cs-137	36	-61	-19
	NORM	6.11	-51	0
Scenario 3	Cs-137	36	-70	-26.5
	Cs-137	31	-57	9.2
	NORM	9.32	-54.5	-2.1
	NORM	6.11	60.5	-9
	NORM	2.19	-70.4	0
	NORM	1.21	-72.3	-13
	NORM	0.74	-65.2	9.2

Table 4.1: Puck types and placements relative to the robot base coordinates for each scenario.

4.3 Results and Discussion

4.3.1 Simulated Results

4.3.1.1 Scenario 1

Initial simulations sought to assess the capability of each algorithm when applied to identify the location of a single radioactive source across the defined search space. Following 1000 repeats

of each algorithm, the mean number of evaluations and RMS error from the real location were tabulated. The results are shown in table 4.2.

Algorithm	Mean Evaluations	Mean RMS Error (mm)
Basin Hopping	483 ± 0	192 ± 87
Dual Annealing	510 ± 145	10 ± 7
PSO	400 ± 0	1 ± 5
Differential Evolution	469 ± 20	9 ± 5
SHGO	348 ± 136	30 ± 11
Brute Force	477 ± 0	8 ± 3

Table 4.2: Comparison of simulated optimisation algorithms for identifying the location of a single radioactive source across a millimetre search space.

After this initial test, it is clear that the PSO algorithm is demonstrably superior, with a mean RMS error of nearly an order of magnitude less than the others. This is unsurprising, as PSO has a well documented efficiency in optimisation [188]. The brute force, dual annealing and differential evolution algorithms responded as anticipated, showing a capability to locate the source to within approximately 10 mm and determine the position of the source within the targeted number of evaluations. The basin hopping and SHGO methods show relatively poor RMS errors in localisation. To some extent this is expected, due to the relatively low number of iterations defined for the surveys. The aforementioned methods show strength in their memory efficiency across large survey areas with multiple optima, hence requiring large numbers of evaluations to be applied most effectively.

4.3.1.2 Scenario 2

When a second source was introduced to the simulated environment, there was a noticeable drop in the performance of all methods. The results are shown in table 4.3.

Algorithm	Mean Evaluations	Mean RMS Error (mm)
Basin Hopping	483 ± 0	194 ± 87
Dual Annealing	499 ± 148	47 ± 103
PSO	400 ± 0	55 ± 125
Differential Evolution	469 ± 19	49 ± 107
SHGO	350 ± 135	50 ± 80
Brute Force	477 ± 0	129 ± 159

Table 4.3: Comparison of simulated optimisation algorithms for identifying the location of the strongest radioactive source of two, across a millimetre search space.

The drop in performance for the PSO method is significant. This is likely a result of the known pitfall of the method to identify local optima. However, the result of the brute-force algorithm is surprising, with a very large localisation error, greater than the hypothesised 10 mm. This is potentially a result of the combined effect of stochastic variation of radioactive emission and error in detector measurement. These effects make it difficult to pinpoint the precise location of the source, due to potential error fluctuations increasing counts in locations away from the emitter. This is likely the case for dual annealing, differential evolution and SHGO too. These hypotheses are supported by the noticeable jump in mean RMS error. By comparison, basin hopping does not show much change in localisation error. This is expected for basin hopping it is designed for n-dimensional problems with large search spaces and numerous local optima. Hence, it does not show any significant drop in error within this more complex example.

4.3.1.3 Scenario 3

For scenario 3, seven sources were distributed across the scan area, to mimic a more realistic survey of a waste sorting table. This test repeated the trends observed between the single source and dual source experiment. The results are shown in table 4.4.

Algorithm	Mean Evaluations	Mean RMS Error (mm)
Basin Hopping	483 ± 0	188 ± 89
Dual Annealing	468 ± 138	178 ± 166
PSO	400 ± 0	171 ± 165
Differential Evolution	466 ± 21	176 ± 167
SHGO	414 ± 148	174 ± 166
Brute Force	477 ± 0	230 ± 150

Table 4.4: Comparison of simulated optimisation algorithms for identifying the location of the strongest radioactive source of seven, across a millimetre search space.

With the exception of basin hopping, all show significant increases in RMS error. The limited change in RMS error for basin hopping may be ascribed to the scanning scenario not being sufficiently complex for them to fail, however, there are insufficient evaluations for it to succeed. The observed increases in the other methods RMS errors are likely due to the methodologies identifying local optima rather than the global optima. In a waste sorting implementation of a source identification algorithm, this would not matter, as a threshold activity should be determined and each object exceeding this threshold should then be collected and analysed. Hence, a test was designed to assess how close each algorithm got to each source, with the smallest taken as the result. The results of this test can be seen in table 4.5.

Algorithm	Mean Evaluations	Mean RMS Error (mm)
Basin Hopping	483 ± 0	80 ± 40
Dual Annealing	466 ± 127	6 ± 4
PSO	400 ± 0	0.1 ± 0.3
Differential Evolution	466 ± 21	4 ± 2
SHGO	418 ± 137	15 ± 8
Brute Force	477 ± 0	4 ± 2

Table 4.5: Comparison of simulated optimisation algorithms for identifying the location of any of the radioactive sources of seven, across a millimetre search space.

As anticipated, the RMS error is drastically reduced for all algorithms. For the PSO, brute-force methods, differential evolution and dual annealing approaches, it is clear the algorithms were identifying local optimas previously, rather than the desired global optima. This can be evidenced by the dramatic drop in mean RMS error. It should be noted that basin hopping also shows a similar reduction. This is likely attributable to the fact that any location identified is likely to be closer to a source in this scenario. The PSO is clearly the best methodology in this test, finding a source to within 0.2 mm. Brute-force and differential evolution are close second, with a 4 mm error, well within the desired 10 mm margin. It should be noted that all algorithms show a significant improvement to scenario 1. This is likely a result of more favourable source positioning. If a source happens to align with an evaluation point for any method, it will likely be very accurate. For all algorithms, more sources within a given scene are likely to align with the initial search space, reducing the need to evaluate low value regions. When more sources are introduced to the experiment, there is more chance of a favourable source positioning. Owing to the reduced evaluation requirement, speed and acceptable margin of error, PSO is proposed as the best approach, of those evaluated, for radioactive source localisation within a robotic sorting and segregation environment based on simulated testing.

4.3.2 Live Experimentation

Following the simulations, the scenarios were next run on the real robot system. Then each algorithm was tested using identical settings to those established within the simulations.

4.3.2.1 Scenario 1

The results for the single source experiment are shown in table 4.6.

Algorithm	Mean Evaluations	Mean RMS Error
Basin Hopping	483 ± 0	69 ± 2
Dual Annealing	416 ± 170	8 ± 2
PSO	400 ± 0	8 ± 4
Differential Evolution	483 ± 19	16 ± 5
SHGO	354 ± 58	12 ± 0.1
Brute Force	476 ± 0	16 ± 6

Table 4.6: Comparison of live optimisation algorithms for identifying the location of a single radioactive source, across a millimetre search space.

Broadly, the live data appears to agree with the simulation for the single source experiment. PSO and dual annealing are the lowest RMS error results, capable of determining the source position to within 8 mm. For PSO, this remains true even with fewer evaluations at just 400. A major difference is in the brute-force approach, which reveals a significant decrease in accuracy compared to the simulation, accurate only to within 20 mm. However, this is consistent with theory. Surprisingly, dual annealing appears to be accurate to within the desired 10 mm range unlike the simulated examples. This is very interesting and potentially explained by a favourable source positioning. Dual annealing makes gradual step changes towards the optimised location, so it is possible the source happened to be situated close to an initial trial position. Basin hopping, differential evolution, remain out of range of the required localisation accuracy. Hence, they will be disregarded from future testing.

4.3.2.2 Scenario 2

The results of the live two source case can be seen in table 4.7.

Algorithm	Mean Evaluations	Mean RMS Error
Dual Annealing	580 ± 170	52 ± 120
PSO	400 ± 0	6 ± 4
Brute	476 ± 0	19 ± 8

Table 4.7: Comparison of live optimisation algorithms for identifying the location of any of the radioactive sources of two, across a millimetre search space.

Dual annealing was shown to be significantly less effective in this test scenario, reporting a reduced mean RMS error in combination with an increase in mean evaluations. This is more consistent with the simulated case, making it likely that the live version of scenario 1 had a

much more favourable source positioning, leading to the dual annealing approach demonstrating success. The brute force approach is less accurate. However, the strongest source was placed as far as possible from a evaluation point for this experiment, demonstrating its weakness. PSO performs as well as the initial experiment. This was expected, as the source was relatively weak, making the method unlikely to identify it as a local maxima.

4.3.2.3 Scenario 3

Finally, the results to the live implementation of the seven source scenario are given in table 4.8.

Algorithm	Mean Evaluations	Mean RMS Error
Dual Annealing	544 ± 127	44 ± 60
PSO	400 ± 0	10 ± 5
Brute	476 ± 0	8 ± 6

Table 4.8: Comparison of live optimisation algorithms for identifying the location of any of the radioactive sources of 7, across a millimetre search space.

These results are in good agreement with the simulation in which any source identification was accepted. PSO identifies the strongest source on the radiation survey to within the desired cm accuracy. This is similar to the ability of the brute-force method. However, the brute-force method requires more evaluations to meet the same accuracy and also can have its accuracy reduced by non-perfect source positioning. Such positioning would be unavoidable in a real-world implementation. Hence, PSO also represents the best choice optimisation approach on the basis of these experimental findings.

4.3.3 Applicability to waste sorting

Radiation survey procedures are essential for the automated sort and segregation of nuclear waste. Ultimately, a phased removal process based on removing radioactive waste items starting with the most active items first and working down to lower activity objects until the process leaves behind inactive waste, for which management policies are much less restrictive. Owing to the large volume of radioactive waste awaiting a long-term disposal solution, time is of the essence. Hence, an optimised approach to waste identification could be a solution for the rapid identification of radioactive sources for prioritised removal. Following the analyses presented in this chapter, it has been demonstrated that the brute-force method and PSO techniques are the most applicable to the application of waste sorting. The PSO method offers a significant increase in time efficiency, while delivering a similar source localisation performance to the brute-force method. Whilst an optimised sorting solution could help to swiftly identify radioactive waste components, there are a few scenarios in which this form of optimisation would fail. One such

situation is the case where several radioactive emitters are placed in close proximity to each other. This presents a challenge, as the summation of the emissions may lead to a large area in which the position of the maximal radiation measurement is ambiguous. Laser profiling in combination with radiation data could be used to support optimisation data. In this way, object recognition may help to assist the process, by extrapolating 3D shapes to corroborate with radiometric data, as discussed in chapter 3. A more advanced version of these optimisation procedures may use 3D surface data from a depth camera to define a 3D plane, from which the optimisation may be performed in a 3D space rather than the 2D spaces defined in this work.

4.4 Conclusion

Optimisation algorithms were tested to determine more efficient approaches for identifying the strongest radiation point sources within a given tabletop scene using a robotic manipulator based radiation survey approach. Differential evolution, SHGO, basin hopping, dual annealing, brute-force and PSO were all investigated. All methodologies were demonstrated to be functionally proficient at identifying radioactive sources, proving the possibility of the conceptual use case, integrated on a robotic system. Their relative performance in the timely identification of radioactive hotspots was assessed in both simulated and live settings. Simulated results were shown to broadly agree with the live results. Differential evolution, SHGO and basin hopping were quickly discounted in live testing, as they were unable to find a single source more quickly than simple raster scanning. The aforementioned techniques main advantages are in complex n dimensional problems with numerous local optima. In such scenarios, they have proven memory efficiency and capability to find a global optima. However, the radiation field examples were not sufficiently complex to benefit from these advantages. PSO demonstrated a capability to identify sources effectively in all cases, faster than raster scanning. However, it was found to identify local optima rather than the global optima in scenarios containing multiple radioactive sources. In a nuclear waste sorting setting, this would not be a problem, as there would be a threshold level to determine which sources should be identified. Therefore, it was determined that the most efficient algorithm for this purpose was the PSO approach, owing to its speed and accuracy in achieving sub-centimetre accuracy in the lowest evaluation count recorded in testing. Such an optimisation technique for radiation surveys is not limited to robotic manipulators with a sort and segregation process. It is feasible to imagine optimisation techniques used across the field of nuclear robotics, with potential applications on radiation mapping drones, ground vehicles and submersival ROVs.

ALGORITHMS FOR ACCURATE RADIOACTIVE SOURCE LOCALISATION

Radiation surveys and mapping techniques are a commonly used to understand the distribution of radioactive sources across a variety of topographies at differing spatial scales. These techniques have been demonstrated to be effective on aerial vehicles at the kilometre scale [202], to robotic manipulators at the cm scale [203]. Chapter 3 comprehensively explored the use of radiation surveys using a robotic manipulator, placing an emphasis on their application for nuclear waste sorting and segregation. It was identified as a key tool used for isotopic identification, informing robotic grasping regimes of the locations of radioactive sources across the sorting surface. One major limitation identified in the development of the robotic manipulator radiation mapping technique, was the ability to accurately spatially localise the radioactive sources present. The isotropic nature of the radiative flux, emitted from active sources, resulted in an apparent blurring effect on radiation maps. This occurs due to the collection of radiation measurements, albeit at reduced intensity, when the detector does not directly face a radioactive emitter. Consequently, the precise location of radioactive sources cannot be pinpointed, potentially making it difficult to identify radioactive components within waste materials. If a software/hardware based implementation could be applied to better localise radioactive sources, there would be a reduced imperative to independently grasp and interrogate each object. A reduction in unnecessary grasping would further streamline the waste sorting process through enhanced time efficiency. This chapter explores the use of an algebraic reconstruction method for more accurately localising the position of radioactive sources within radiation surveys. Algebraic methods are commonly applied to other reconstruction problems, such as Computed Tomography (CT), but prior to this research it was yet to be reported for use in radioactive source reconstruction. Hence, the concept is explained, explored and tested within this chapter, seeking to enhance radioactive

source localisation, potentially delivering a step change in targeted object removal in radioactive waste sorting operations.

The following chapter is based on the methods, results and discussion presented within the following previously published, peer-reviewed articles:

White, S.R.; Wood, K.T.; Martin, P.G.; Connor, D.T.; Scott, T.B.; Megson-Smith, D.A. Radioactive Source Localisation via Projective Linear Reconstruction. *Sensors* 2021, 21, 807.

5.1 Introduction

In nuclear waste sorting and segregation, radiation surveys using robotic manipulators are crucial for attaining an initial understanding of the extent and distribution of radioactive sources. Data collected, can subsequently inform waste processing strategies, applying a prioritised removal of the most radioactive components of the waste. However, accurate and precise spatial localisation of radioactive sources is difficult to achieve within radiation surveying. This was evidenced in chapter 3, as a noticeable blurring of emission measurements was highlighted across the radiation surface maps produced. Ionising radiation emitted from a point source is stochastic and isotropic, following an inverse square law. The isotropic nature of radiation emission results in a blurring effect visible on radiation maps. This effect results in the imprecise localisation of radioactive sources as a result of the detection of radiation when the sensor is not directly facing the source. The effect is represented graphically in Figure 5.1.

The source localisation problem may be further compounded by the effect of additional sources, which may be present on the scan surface. Chapter 3 showed that 3D visualisation techniques may be a viable method for distinguishing which objects are emitters, through the generation of 3D models. These 3D models help to distinguish different objects, which could provide additional information to help identify a radioactive emitter. However, it was noted that there would be limitations, particularly when radioactive sources are in close proximity. For example, there may be two identifiable objects, one non-radioactive and the other active. The radiation field from the active component may cover the inactive one; making it difficult to determine which one is radioactive.

One prominent example of a waste sorting application in which source localisation is of paramount importance, is the sorting of Fuel Element Debris (FED). FED is the material generated during the Magnox desplitting process [204]. This is where the cladding and mechanical assembly of the spent fuel rods used in Magnox design reactors are stripped-off and broken into much smaller

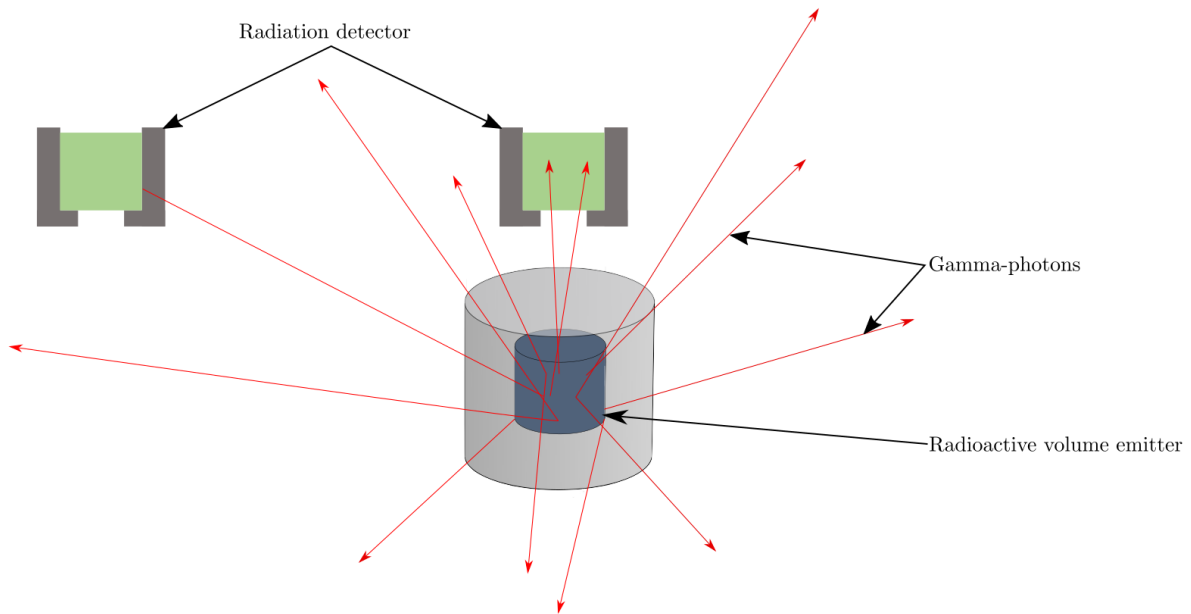


Figure 5.1: Diagrammatic representation of the isotropic emission of radiation and consequent reduction in gamma-photon flux as detector position moves.

pieces. Historically, desplittering was performed in order to reduce packing volumes for waste storage [60]. Desplittering is explained in Figure 5.2, which shows the processing of a fuel rod and its subsequent FED material. FED consists primarily of the fuel rod assembly and cladding, but contains small fragments of fuel [204], a photograph of FED in a Magnox waste vault is shown in Fig 5.3.

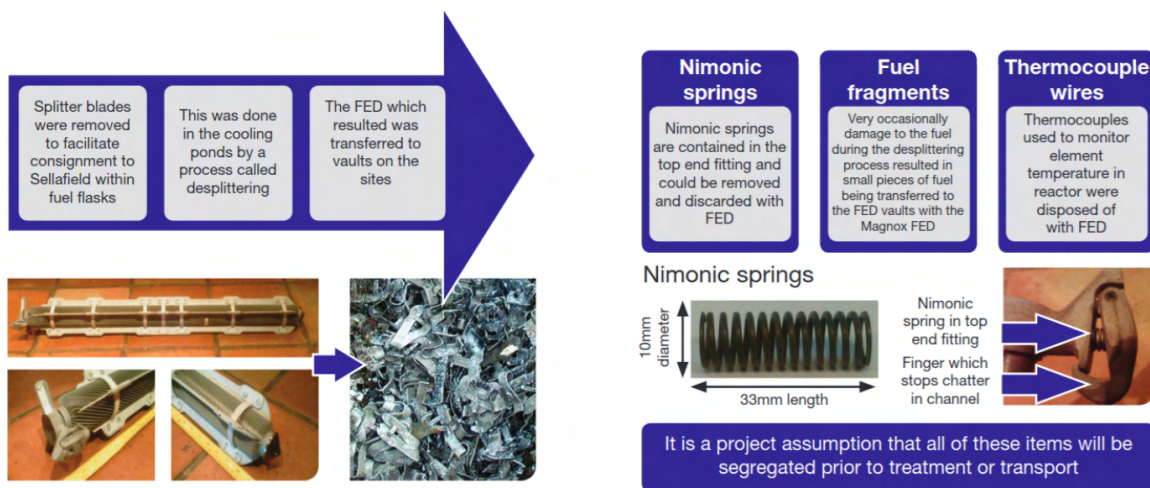


Figure 5.2: Desplittering of a Magnox fuel rod and subsequent FED materials generated. Adapted from [205].

The cladding comprises mostly of Magnox, a magnesium alloy (> 99% Mg) used to shroud fuel rods. However, there are other elements contained within the fuel assembly, including nimonic (Co/Ni alloy) springs, which are associated with the fuel cladding assemblies (see Fig 5.2 left). The Co in the nimonic springs may become neutron activated to form Co-60, a strong gamma-photon emitter. The proportion of this neutron activated Co-60 is comparatively small in relation to other elements, with each spring just 33 mm long and 10 mm in diameter and weighing just 5 g [60]. Despite this, it accounts for a large portion of the radioactivity within FED waste packages, hence the precise identification and subsequent segregation of nimonic springs is essential [51]. Their small size will make them difficult to identify with 3D photogrammetric techniques. Therefore, the springs are currently evenly spread across the waste volume, as far as reasonably practicable, to reduce package dose rates as far as possible [206]. Instead, precise localisation of Co-60 constituents within the swarf mix could be used to identify extraction locations from which a robotic manipulator could grasp the Co-60 elements, leaving the remaining swarf. This could contribute to a volume reduction of ILW, making significant cost-savings associated with waste storage.



Figure 5.3: Photograph of FED in a Magnox waste vault. Taken from [204].

Unfortunately, the precise localisation of radioactive sources represents a technical challenge. In the visible spectrum, light can be focused using refractive and reflective optics. Given the photonic nature of gamma emissions, it may seem possible to use optical focussing techniques. However, refractive index decreases with increasing photon energy, meaning these traditional focusing

methods are not applicable at gamma energies [207]. Hence, conventional optical techniques are unsuitable for radioactive localisation.

An alternative to optical techniques is enhanced collimator design. Sufficient volumes of dense materials, such as lead (Pb), could offer a solution to the problem, by blocking extraneous gamma-photons. Theoretically, this reduces the solid angle for gamma-photons incident on the detector. However, there is a nuance associated with collimator materials, as the thickness of collimator materials must be tuned to account for the relative gamma-photon energy and flux. This is because collimator materials do not block all gamma-ray photons, but rather reduce the amount gamma-photons reaching the detector by means of attenuation [208]. The attenuation coefficient is the exponent which corresponds to the efficacy of a material, based on its atomic number and density, to stop incident gamma-photons by a combination of photoelectric absorption, pair production and internal scattering; both coherent and incoherent [111]. Typically, with increasing photon energy the attenuation coefficient of a material decreases. This means that some gamma-photons might reach the detector. Further to this, when such high-energy photons are attenuated, the associated scattering often produces many lower-energy gamma-photons, which can also be detected [209]. Therefore, collimators offer an improvement to radioactive source localisation, but the spatial localisation offered has potential to be further improved.

There are a number of different devices available COTS that demonstrate a high precision radioactive source localisation. One prominent example of such technology are ‘gamma cameras’ [210]. Gamma cameras can visualise radiation emissions, typically overlaid over a photographic camera image. This is achieved using both/either the Compton effect or ‘coded-masks’. In a Compton based gamma camera, two parallel detector surfaces are used, one is known as the ‘scatterer’ and the other the ‘absorber’. In essence, Compton kinematics are used to relate the scatterer incidence to the subsequent absorber impacts, allowing for the determination of the source to be inferred. The limitation here, is that it is only applicable to gamma-photons’s within the Compton regime. On the other hand, a coded mask functions in a similar way to a pinhole camera, with an entrance plate in an intelligently designed shape created from an element opaque to radiation. This is placed over a photon detector which detects hits at different positions according to its shape, hence, it is able to identify hot-spots. Carrel et al. [211] demonstrated the radioactive localisation of sources using a gamma-camera known as ‘GAMPIX’ within a nuclear environment. The team showed its application on nuclear waste pipes and waste packages, localising radioactive emitters on the surfaces. Lemaire et al. [212] demonstrated the GAMPIX system could be used to perform gamma spectroscopy on sources, something which had previously been a shortfall of gamma camera technology. One problem with coded-mask based gamma cameras are that the coded mask does not completely block gamma radiation in its covered sections, potentially skewing the radiation readings in the reconstruction algorithm [213]. Additionally, it requires a

‘coded mask’ to be selected appropriately prior to operation according to the radiation intensity it will be used to locate.

This chapter seeks to explore an algebraic approach for enhancing radioactive source localisation on radiation survey data. Conceptually, this can be achieved by using a detailed understanding of the spatial response of a detector, enabling a linear inversion method to be performed, to identify the precise location of radioactive sources. Therefore, a key feature that must be qualified is the Detector Response Function (DRF). The DRF describes the spatial response of the detector, detailing how the detector records extraneous radiation measurements depending on its position relative to a radioactive emitter. Once this DRF is determined, it can be used within an algorithm based on the Kaczmarz method in a ‘Projective Linear Reconstruction’ (PLR) technique. In essence, this is a series of iterative projections of what the detector expects to measure, based on its recorded measurement within a radiation survey and the DRF.

5.2 Methods

This section aims to detail the mathematical technicalities which facilitate the application of a PLR algorithm for the linear inversion of radiation maps. Such details are covered from first principles, first establishing the problem and breaking it down into mathematics which may be solved through iterative linear projection. Following this, the process facilitating the collection and processing of a semi-empirical DRF model are explained, reducing stochastic variation in experimentally collected measurements. Lastly, the algorithmic implementation is given, to underpin the algorithmic improvement of radiation survey data.

5.2.1 Radiation Survey Data as a Linear Problem

Radiation detectors used for surveys, such as those in chapters 3 and 4, may be thought of as a non-directional sum accumulators of gamma-photons. Therefore, a ‘counts’ measurement may be represented as the summation of all the gamma-ray interactions within a time-period. If the emitting surface is quantised into a set of points, then any single measurement made by a detector placed above the surface will have contributions from all radioactive sources within its line of sight. The relative proportion of the contributions will depend on the source strength, the distance, and the direction of intersection with the detector assembly. One reading represents a single summation of gamma-photon counts, while multiple readings represent multiple summations. This representation can be formulated as a linear system $\mathbf{Ax} = \mathbf{b}$, where \mathbf{x} is the unknown solution of the surface radiation emissions, \mathbf{A} is a matrix which is represented by a subset of the DRF, and \mathbf{b} is the measured response. Using this system, the ‘best-solution’ of a scene containing one or more radioactive emitters in a radiation map, can be estimated. The problem then becomes one of mathematically obtaining such an estimated solution to the linear system.

5.2.2 General Linear Problem

A general linear problem may be expressed as a system of linear equations. For example if we have m equations of n unknowns, the system can be expressed as equation 5.1.

$$(5.1) \quad \begin{aligned} b_1 &= a_{11}x_1 + a_{12}x_2 \dots a_{1n}x_n \\ b_2 &= a_{21}x_1 + a_{22}x_2 \dots a_{2n}x_n \\ &\vdots \\ b_m &= a_{m1}x_1 + a_{m2}x_2 \dots a_{mn}x_n \end{aligned}$$

The full equation may be expressed in matrix form, as shown below,

$$\begin{bmatrix} a_{11} & a_{12} & \cdots & a_{1n} \\ a_{21} & a_{22} & \cdots & a_{2n} \\ \vdots & \vdots & \ddots & \vdots \\ a_{m1} & a_{m2} & \cdots & a_{mn} \end{bmatrix} \begin{bmatrix} x_1 \\ x_2 \\ \vdots \\ x_n \end{bmatrix} = \begin{bmatrix} b_1 \\ b_2 \\ \vdots \\ b_m \end{bmatrix}$$

which may be more concisely expressed using equation 5.2,

$$(5.2) \quad \mathbf{Ax} = \mathbf{b}$$

where A is a matrix of dimension (n,m) , \mathbf{x} represents the unknown 'x values' and \mathbf{b} the solution 'b values'.

5.2.3 Algebraic Reconstruction Techniques

Algebraic Reconstruction Techniques (ARTs) are iterative methods which can be used to solve systems of linear equations. Mathematically, ART's are based on research by Kaczmarz [214], who discovered a process now known as the Kaczmarz algorithm. One of the primary uses for the Kaczmarz method is computed reconstruction and determining solutions to linear systems of equations. It was first used by Gordon et al. [215], who demonstrated its ability to reconstruct 3D objects from images taken by electron micrographs. Its capability in this field means it is commonly used for medical imaging, such as magnetic resonance imaging (MRI) [216], X-ray computed tomography (CT) [217] and more recently, magnetic particle imaging (MPI) [218]. Theoretically, an implementation of the Kaczmarz method can be used to improve the spatial resolution of radioactive sources derived from a radiation map.

5.2.4 Kaczmarz Method

The general Kaczmarz equation, given in Equation 5.3 [219], describes an iterative process for estimating a solution to the equation $\mathbf{Ax} = \mathbf{b}$.

$$(5.3) \quad \mathbf{x}^{k+1} = \mathbf{x}^k + \lambda(k) \frac{b_i - \langle \mathbf{a}_i, \mathbf{x}^k \rangle}{\|\mathbf{a}_i\|^2} \mathbf{a}_i$$

[214] where \mathbf{x}^k is the calculated solution for the k^{th} iteration, λ is a relaxation parameter affecting the rate of convergence, b_i is the i^{th} row of \mathbf{b} and \mathbf{a}_i is the i^{th} row of \mathbf{A} . Therefore, according to equation 5.3, \mathbf{x}^{k+1} is in essence the projection of \mathbf{x}^k onto its hyperplane¹ H_i [219]. This process iteratively approaches potential estimated solution in the case where noise or other factors have made the solution indeterminate. Kaczmarz method is best applied on an over-determined system of equations [220], satisfied when there are more equations than solutions, i.e $n > m$ in the case of the general system.

5.2.5 Implementation of Kaczmarz for Radioactive Source Localisation

Section 5.2.2 showed that radiation survey data may be broken down into a linear system of equations. Hence, it may be solved using an implementation of Kaczmarz method. For the case of radiometric source localisation Kaczmarz is implemented as follows using equation 5.3. Where \mathbf{x}^k is the calculated solution for the k^{th} iteration, b_i is the measured radiation intensity at the i^{th} position, \mathbf{a}_i is the i^{th} row of the DRF and λ is a relaxation parameter affecting the rate of convergence. Specifically, a randomised implementation of Kaczmarz deconvolution was applied for this study. This was selected over a conventional implementation due to its greater efficiency for this type of problem, reaching convergence more than 3 times faster [220]. The overdetermination requirement may be satisfied by ensuring there are always more measurements taken than accounted for in the solution space. In other words, such that the number of measurements in the \mathbf{b} matrix are greater than the number of unknowns in the solution \mathbf{x} matrix². A key concern in using the Kaczmarz method for source localisation on radiation survey data is experimental noise. Each measurement within the radiation survey data, has an associated error owing to the stochastic emission of radiation. This error will propagate through the Kaczmarz method. Needell [221], mathematically proved that in such a case where, $Ax \approx b \pm r$, where r represents the measurement error the convergence rate remains the same, although there is an additional limiting error in the solution of \sqrt{r} .

5.2.6 Detector Response Function

A crucial component of the Kaczmarz method is a well qualified DRF. This DRF is central to the projections from the measurement space to the solution space within equation 5.3. Initially,

¹A hyperplane H_i , can be defined by $H_i = \{x : \langle \mathbf{a}_i, x \rangle = b_i\}$, in essence a dimension one less than its ambient space.

²i.e. the measurements contained in the radiation survey array must be greater than those contained in the solution array.

the DRF of the detector assembly was determined experimentally by measuring the detector efficiency as a function of 3D position relative to a small radioactive source. The experiment mapped the total intensity in multiple planes above a radioactive source using the KUKA KR 150 robotic manipulator and associated gamma scanning technology, (see chapter 3). A photograph of the system is shown in Figure 5.4.

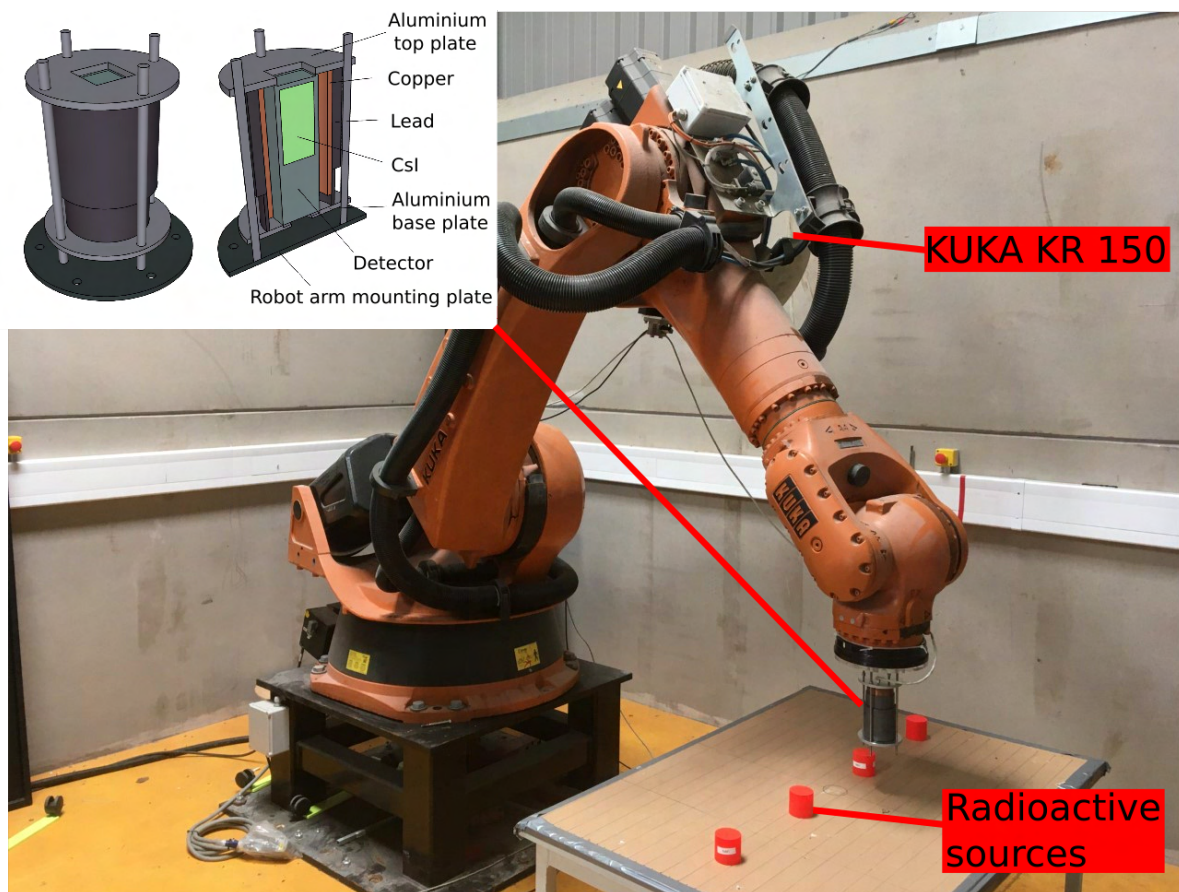


Figure 5.4: Photograph of the KUKA KR 150 system used, with a set of four sealed sources arranged on a table top. Inset - a detailed schematic of the detector and collimator setup.

The active radioisotope scanned in this experiment was a Cs-137 puck (identical to those used in chapters 3 and 4) with 36 kBq of activity. The perspex containment used had a cylindrical shape, 50 mm in diameter and 50 mm in height. It was placed standing upright, in the centre of a 0.6 m x 0.6 m horizontal, scan area. The system was setup to scan across the surface in a raster pattern with a swath width of 1 cm. After each horizontal plane was completed by the scanning head, the robotic arm was raised vertically by 1 cm and the scan was exactly repeated at 10 different heights.

The detector was mounted within a lead (Pb) collimator, as described in Figure 5.4 inset. The gamma-ray counts and spectral data from the detector were recorded at a rate of 10 Hz and the

robot arm was set to move at a predefined speed of 1 mms^{-1} . The radiation measurements were synchronised with the robot arm position (accurate to the nearest 0.1 mm). Given the raster step size was set to 1 cm, the detector response data was averaged in 1 cm^3 voxels.

5.2.7 Fitting the Detector Response Function

After collection of the experimentally based DRF data, the random nature of radioactivity meant that the raw DRF contained a degree of stochastic variation. This is shown in Figure 5.5 (left). Hence, to reduce these variations, the raw DRF measurements were used to fit a mathematical model of the detector. This DRF model was developed empirically to account for the two principal physical phenomena; the inverse square law and detector collimation. The inverse square law describes how the intensity of radiation emitted from a point source is proportional to $\frac{1}{R^2}$, where R is the distance. Detector collimation was modelled using a complementary error function (erfc) [222] shifted to transition from 1.0 (full detection) to 0.0 (no detection) at the collimation angle.

The final structure of the model was based on a product of erfc() and the inverse square law. Combining these two functions resulted in a model with two tuneable parameters: collimation angle (η) and collimation gradient (ϵ). Collimation angle is the solid angle for which gamma-photons can directly reach the detector without scattering effect. On the other hand, the collimation gradient parameter allows for scattering and varying efficiencies at different photon energies around the collimator aperture. This model calculates the expected detector sensitivity for a source located at a position relative to the detector centre, as shown in equation 5.5,

$$(5.4) \quad \text{DRF}(x, y, z) = \frac{\text{erfc}(\epsilon \cdot [\theta(x, y, z) - \eta])}{R(x, y, z)^2}$$

where DRF() is the Detector Response Function, x, y, z , are the spatial coordinates relative to the detector, erfc() is the complementary error function, θ is the angle between each point in space and the principle detection axis (the z axis in this instance) and R is the distance of any point to the detector.

To fit the detector parameters, the model was convolved with a 3D model of the source on the table. This was done to account for the fact that the source was not a ‘point source’, but rather a volumous source. The result was compared with the raw DRF data shown. A least-squares optimisation procedure then adapted the ϵ and η values, such that the modelled DRF accurately represented the raw DRF. The final result was an idealised DRF, as shown in Figure 5.5(right), free from measurement noise which was important for the stability of the iterative Kaczmarz deconvolution.

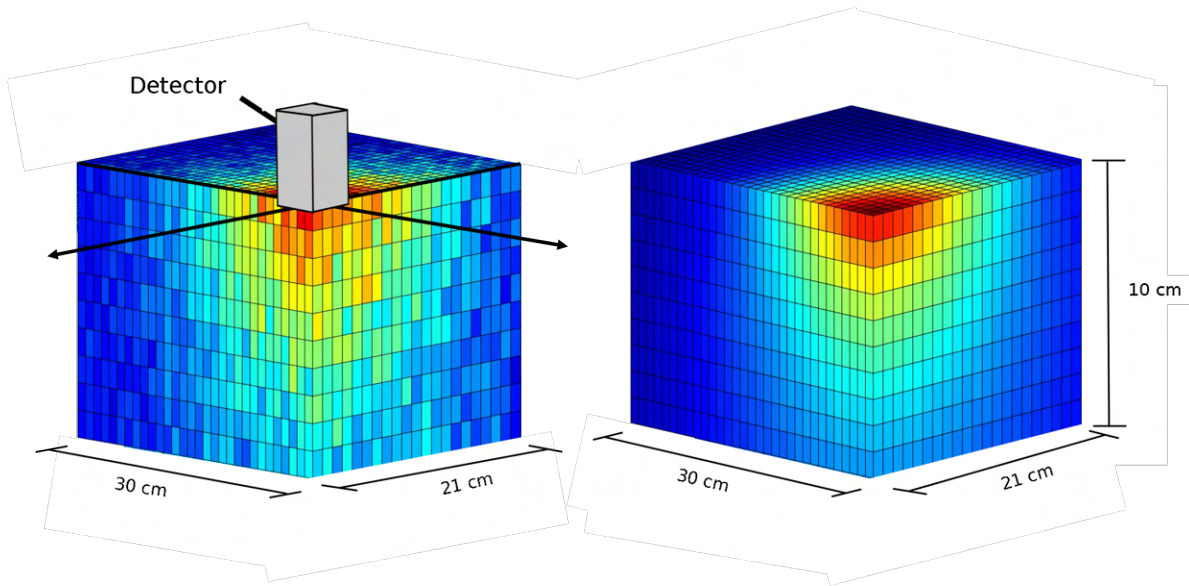


Figure 5.5: Quadrant cross-section of the as measured Detector Response Function (left) and the fitted model Detector Response Function (right). On the left-hand image, a model detector crystal (collimator and aluminium case not shown) is superimposed to highlight the experimental method. The detector crystal is outlined as an oblong shape with finite volume, although the algorithm assumed a perfect point, and all distances and angles are measured relative to the centre of the crystal.

5.2.8 PLR Algorithm

The essence of the PLR algorithm involves the computation of convolutions of the semi-empirical DRF and the collected dataset. The randomised Kaczmarz procedure first selects a random pixel within the dataset. Due to the 2-dimensional size of the response array being smaller than the collected dataset, an appropriate sub-sample is next chosen, such that they match. The convolution of these is computed, as the sum of the two arrays multiplied. The result of this is subtracted from the selected pixel result, representing the ‘remnant’. The remnant is multiplied by the response function, which iteratively updates the solution space. This is multiplied by the aforementioned relaxation parameter.

The relaxation parameter was adapted such that $\lambda = \frac{1}{10^{k/300000}}$, where k is the iteration number. This parameter was tuned to optimise the speed of evaluation of the solution. In this way the algorithm initially prioritised convergence rate over stability, before gradually transitioning to prioritising convergence stability. The solution is updated in accordance with Equation 1 and this process is repeated until a manually predetermined number of iterations has passed.

5.2.9 Experimental Scenarios

In order to evaluate the algorithm four scenarios were set up to assess its capability. All radioactive materials used for testing were identical in form to those used previously in chapters 3 and 4. The source activity and location of the pucks is given in Table 5.1.

	Type	Activity (kBq)	X Pos. (cm)	Y Pos. (cm)
Scenario 1	Cs-137	31.0	15.0	14.0
	Cs-137	36.0	45.0	14.0
Scenario 2	NORM	2.9	13.0	12.5
	NORM	4.7	41.0	14.0
	NORM	2.7	71.0	14.0
	NORM	3.0	97.0	14.5
Scenario 3	Cs-137	36.0	23.5	10.0
	Cs-137	31.0	35.5	10.0
Scenario 4	NORM	6.11	71.5	44.0
	NORM	1.38	58.0	20.5
	Cs-137	31.0	38.9	19.7
	Cs-137	36.0	49.5	34.0
	NORM	1.21	43.5	48.0
	NORM	3.49	25.5	35.3
	NORM	0.97	17.8	19.7

Table 5.1: Puck types and placements relative to the robot base coordinates.

Scenario 1 was designed as simple test of the algorithm to resolve the location of two well spaced Cs-137 sources placed 30 cm apart. The second scenario used four pucks containing a different and much weaker source material (NORM). Scenario 3 attempted to determine the spatial limitations of the PLR algorithm. This was achieved by determining the closest source placement the PLR algorithm could resolve. The two Cs-137 pucks used for scenario 1 were initially placed 15 cm apart and then moved progressively closer, in 1 cm incremental steps, until the limit was identified. It was not possible to resolve two distinct point sources at separations of less than 12 cm. The fourth scenario tested the ability of the PLR algorithm at resolving sources of different strengths; for this, seven pucks were placed randomly across the table. For each scenario the raster was either 1 or 2 cm, to explore the recovery capability at different resolutions.

5.3 Results and Discussion

5.3.1 Scenario 1 - Two sources

The results of the scan and subsequent processing are presented in Figure 5.6. To visually highlight the effectiveness of the PLR algorithm, the data has also been initially processed using a simple 2D linear interpolation. Figure 5.6 a, shows the approximate location of the radioactive

sources used in the scenario, but their precise locations cannot be pinpointed. The data was subsequently input to the PLR algorithm, yielding the high spatial resolution result shown in Figure 5.6 b.

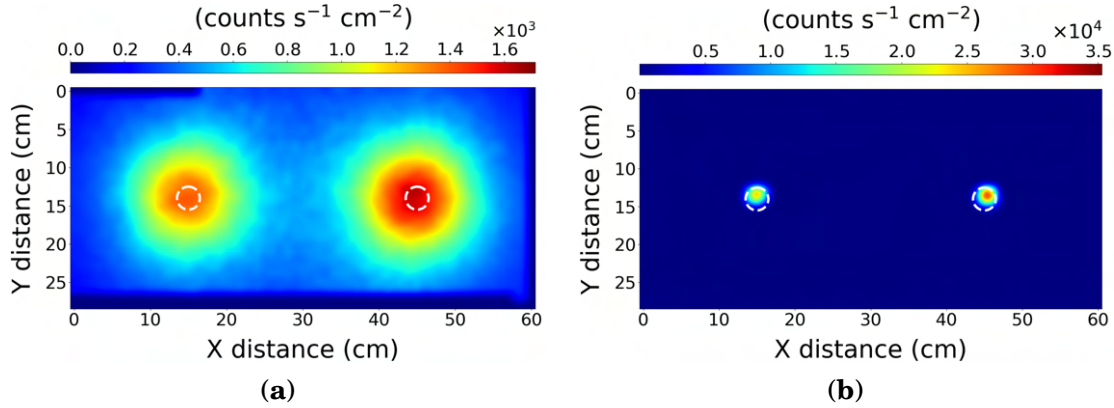


Figure 5.6: The results from scenario 1 - using two similar sources. After processing with (a) simple interpolation, and (b) the PLR algorithm. The scan used a 1 cm resolution. The dashed white circles represent the true location of the source pucks.

This simple test indicated that the PLR method could successfully locate the sources to within 1 cm, reducing the blurring effect measured by the system in the initial map. The PLR algorithm reported the sources positions at $15 \text{ cm} \pm 1 \text{ cm}$ and $45 \pm 1 \text{ cm}$ on the X axis respectively and both $14 \pm 1 \text{ cm}$ on the Y axis, which was in agreement with their actual placement. It is possible that the accuracy is higher than 1 cm as when the physical construction of the radioactive source pucks in use is considered, they are of 5 cm diameter with an active internal cavity of 3 cm. However, the distribution of the active material within the cavity may not have been uniform. If the active material was set to one side of the cavity, the PLR algorithm would only identify that particular side. This might explain the misalignment seen Figure 5.6 b (right-hand puck), but there was no experimental ability to verify the internal distribution of material within the pucks.

5.3.2 Scenario 2 - Four lower activity sources

The results for scenario 2 are shown in Figure 5.7 a and 5.7 b for the simple interpolation PLR processing respectively. The results demonstrated that the algorithm accurately located four similarly active, but relatively weak radiation sources to within 1 cm. The X positioning of the sources, left to right respectively was: $13 \pm 1 \text{ cm}$, $42 \pm 1 \text{ cm}$, $72 \pm 1 \text{ cm}$ and $98 \pm 1 \text{ cm}$. On the Y axis, the positioning of the sources left to right was: $13 \pm 1 \text{ cm}$, $14 \pm 1 \text{ cm}$, $14 \pm 1 \text{ cm}$, $15 \pm 1 \text{ cm}$. It accomplished this while preserving the relative source strength data, however, the PLR algorithm does not recover the absolute source strength. It should be noted that the raw data collected for this map was of lower scan resolution (2 cm) than the first scenario.

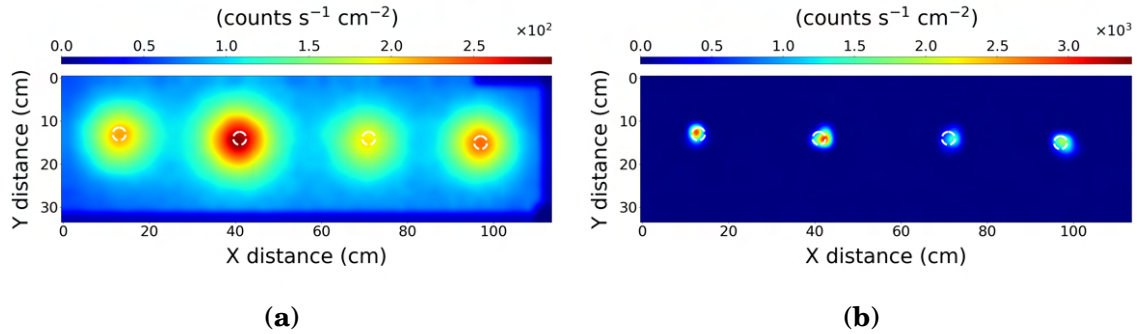


Figure 5.7: The results from scenario 2 - four lower activity sources. After processing with (a) simple interpolation, and (b) the PLR algorithm. The scan used a 2 cm resolution. The dashed white circles represent the true location of the source pucks.

5.3.3 Scenario 3 - Proximity limit

The third scenario attempted to determine the spatial limitations of the PLR algorithm. This was achieved by determining the closest source placement the PLR algorithm could resolve. After progressively reducing the separation of the pucks, a limit was identified where the PLR algorithm did not resolve two distinct point sources at separations of less than 12 cm. The interpolated raw data is shown in Figure 5.8 a, where it is not possible to identify that the radiation pattern is the result of two distinct separated sources. Interpretation of the data in this form could be ambiguous, in that this may be interpreted as a single elongated source. The PLR algorithm resolves the data into two distinct sources as shown in Figure 5.8 b.

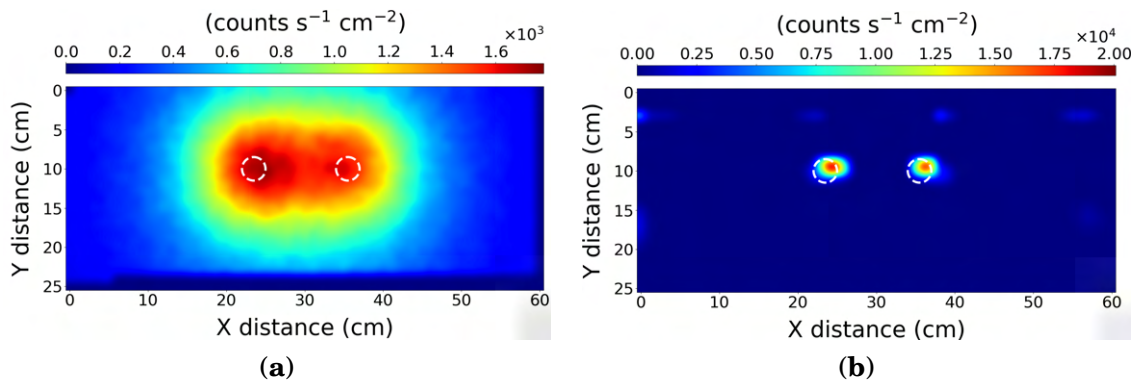


Figure 5.8: The results from scenario 3 - proximity limit. After processing with (a) simple interpolation, and (b) the PLR algorithm. The scan used a 1 cm resolution. The dashed white circles represent the true location of the source pucks.

The white dashed circles indicate the independently measured positions of the radioactive sources. The identified positions of the sources on the X-axis, left to right respectively are 24.5 ± 1 cm and 36.5 ± 1 cm. The sources are less localised than scenarios 1 & 2, as the peak values are not contained entirely within the white rings. This can be explained by weak radiological

contributions from relatively distant sources skewing the local position of closer sources. This is ultimately a limitation of the method, however, it could potentially be improved with some prior knowledge of the source setup, or a higher resolution scan.

5.3.4 Scenario 4 - Mixed source strengths

The fourth scenario tested the ability of the PLR algorithm at resolving sources of different strengths. For this, seven pucks were placed randomly across the table at the locations described in Table 5.1. In the interpolated raw data (Figure 5.9 a), the sources are significantly blurred together.

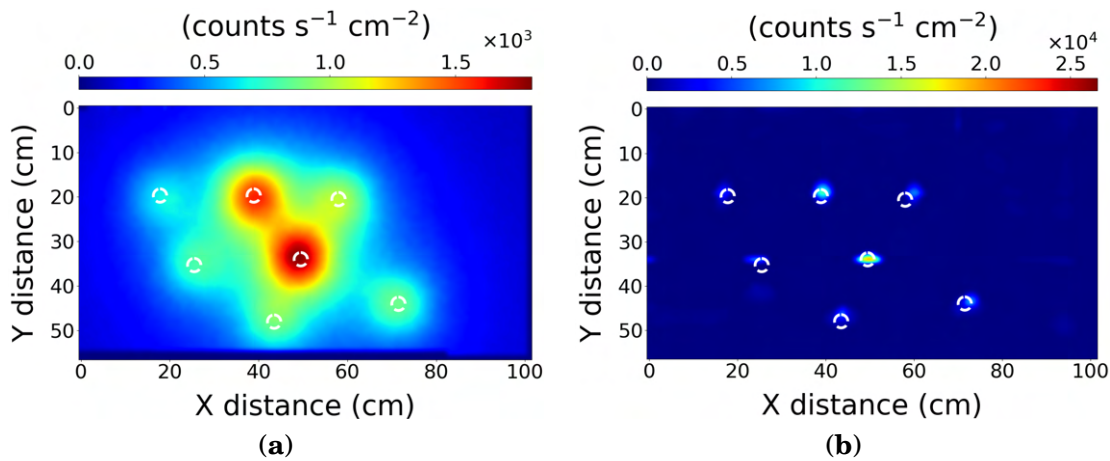


Figure 5.9: The results from scenario 4 - mixed source strengths. After processing with (a) simple interpolation, and (b) the PLR algorithm. The scan used a 1 cm resolution. The dashed white circles represent the true location of the source pucks.

The identified source positions were at co-ordinates (X,Y) cm respectively, as ordered in Table 5.1, Scenario 4: $(73,44) \pm 2$ cm, $(60,19) \pm 2$ cm, $(40,19) \pm 2$ cm, $(50,34) \pm 2$ cm, $(44,46) \pm 2$ cm, $(25,34) \pm 2$ cm and $(17,19) \pm 2$ cm. The sources were only identifiable to within 2 cm in this scenario. This resolution was ascertained by measuring the distance from the centre of the expected source to the reconstructed centre point, for the least accurate source identified in Figure 5.9 b. This reduction in accuracy is likely a result of the disparity in the source activities, ranging from 970 Bq to 36 kBq. It should be noted that there are a few artefacts present in the PLR algorithm result for both scenarios 3 & 4. These take the form of additional weak hot-spots which might be interpreted erroneously. These weak hot-spots can possibly be attributed noise in the measured raw data leading to the algorithm converging on a partially incorrect solution. To resolve this issue, the raw data set might be collected with greater detail, using denser raster widths, or slower movement. Therefore, reducing the effect of random errors, or, with additional algorithmic checks to identify and remove erroneous results. The capability of the algorithm to recover

the source locations in this scenario demonstrates the power of the PLR algorithm to analyse distributed with significant activity differences.

5.3.5 Quantitative Measurement of PLR

In order to quantitatively assess the effectiveness of the PLR algorithm a performance metric was developed. A single line transect of the 2D data through the centre of the pucks for scenarios 1 & 2. The values for both the raw data and the best solution reconstruction are shown in Figure 5.10. A Gaussian distribution was fitted to each peak of both the interpolated and PLR processed data and the standard distribution is used to act as a measure of the quality of the localisation. A smaller value indicates a sharper fit, therefore indicating the effectiveness of the PLR method of reducing the blur inherent to the interpolated results. It is recognised that a Gaussian fit is a suitable approximation for small sources, but less applicable for unusually shaped sources.

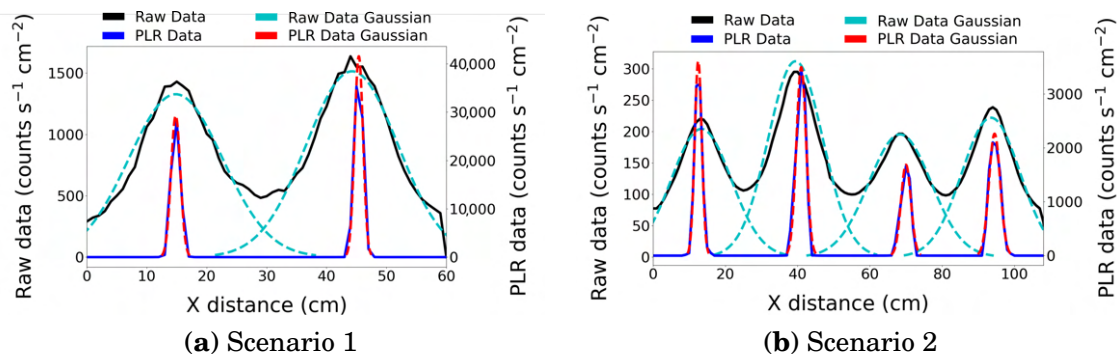


Figure 5.10: Comparison of 1D transects through the interpolated raw measurements (Raw Data) against the best solution estimated by the linear reconstruction technique (PLR data). Best fit Gaussian distributions have been fitted to both to enable a quantitative resolution assessment to be made.

	Source number (left to right)	Standard deviation raw data (cm)	Standard deviation PLR data (cm)	Enhancement
Scenario 1	1	7.8 ± 0.2	0.78 ± 0.01	10
	2	7.6 ± 0.2	0.70 ± 0.01	10.9
Scenario 2	1	8.3 ± 0.3	0.98 ± 0.01	8.5
	2	7.5 ± 0.2	1.35 ± 0.01	5.6
	3	8.6 ± 0.3	1.37 ± 0.05	6.3
	4	8.0 ± 0.3	1.55 ± 0.04	5.2

Table 5.2: The standard deviations of the fitted Gaussians as in Figure 5.10.

The standard distributions for the fitted Gaussian's are presented in Table 5.2. An enhancement factor has been calculated for each puck as the ratio of values. The enhancement ranges from

approximately 5-10× with an average of 7.8× improvement. This quantitative analysis demonstrates that the PLR process improved the localisation and the overall positioning accuracy of radioactive sources scanned by a gamma-ray detector on a robotic arm.

5.4 Conclusion

This chapter demonstrated a unique post-processing technique, to aid the localisation and visualisation of radioactive sources measured by radiation mapping. Experimental testing using a robotic arm validated the benefits of the PLR method for several multi-source scenarios. The algorithm demonstrated a capability of pinpointing radioactive sources to within 2 cm. Improvements between 5× and 10× were observed with a mean enhancement of 7.8×, compared to the simple 2D linear interpolation of the raw data. In addition, a mathematical model was presented that approximated the Detector Response Function of a detector, within a collimation assembly. This was fitted to experimentally measure data. Conceptually, this could be generalised to any collimated detector. The PLR algorithm then utilised an iterative randomised Kaczmarz method to compute best solution estimates.

The capability to accurately locate radiation on objects could be a powerful tool for a wide variety of nuclear decommissioning challenges, including the removal of nimonic springs from FED. Although the focus of this research was on micro-gamma spectrometers on robotic manipulators at the sub-metre scale length, a PLR algorithm like this could be applied on many different radiation mapping platforms, including but not limited to, UAV's and ground robots, covering different spatial scales. It is also conceivable that the method could be applied in real time, as part of an automated mapping platform. This would drastically reduce data collection and processing times whilst delivering fast and accurate radiation maps.

ROBOTIC MATERIAL CHARACTERISATION WITH XRF

Critical to nuclear waste sorting and segregation is chemical and material analysis. As discussed in chapter 2, XRF may be part of a solution to resolving such analysis. Laboratory and synchrotron X-ray fluorescence (XRF) analysis have both served as mainstay rapid and quantitative elemental analysis techniques for decades, attaining parts per million sensitivities for the majority of elements. Formerly, XRF was the reserve of large X-ray generating systems and national facilities. More recently, developments in miniaturised X-ray generators and detectors have allowed for this non-destructive technique to be utilised for portable and in-situ elemental characterisation of materials away from the confines of the laboratory. When combined with a robotic manipulator, these usually handheld systems present a powerful method for autonomous assessments of material composition. This has enormous potential within a wide range of nuclear characterisation and decommissioning scenarios in which autonomous, in-situ material analysis is desired. Hence, this chapter seeks to explore the proof-of-concept use of an XRF system integrated with a robotic manipulator to autonomously identify a suite of nuclear relevant materials. This aims to facilitate the autonomous material characterisation of nuclear waste materials for analysis ahead of long-term disposal. The details of the integration of the XRF system with the robotic manipulator will be covered for a range of nuclear applicable scenarios. Further to this, the augmentation of the system with a depth camera will seek to deliver a further improvement to the functionality of the system, through the development of a novel camera-based object targeted technique. The developed system will be tested on example applications pertinent to the waste sorting problem.

It is envisaged that this robotically-deployed XRF system will comprise part of a wider autonomous characterisation ‘toolkit’; capable of extensive large-area mapping alongside targeted

compositional ‘point analysis’. The system was demonstrated to rapidly and repeatably derive accurate and precise compositional information of different test materials. It was able to achieve this autonomously on both flat and complex, object-rich surfaces.

The following chapter is based on the methods, results and discussion presented within the following previously published, peer-reviewed articles:

S.R. White, P.G. Martin, D.A. Megson-Smith and T.B. Scott, “Application of automated and robotically deployed in-situ X-ray fluorescence analysis for nuclear waste management.”, *Journal of Field Robotics*, accepted.

6.1 Introduction

Established in chapter 2, material characterisation is of key importance to nuclear waste sorting and segregation activities. XRF represents one analysis technique which could deliver a step change in autonomous and in-situ waste characterisation. Through XRF point analysis, surfaces can be mapped by making many measurements in a defined pattern, thereby yielding an elemental concentration map, referred to herein as an ‘XRF map’. Perhaps the most notable example of an XRF point analysis system is the Perseverance Rover’s Planetary Instrument for X-ray Lithochemistry (PIXL) [223]. PIXL was mounted on the Rover’s robot arm and was capable of high accuracy XRF point analysis of collected samples. Campos et al. [224] presented a portable XRF mapping system, whereby a 3-axis stage mount with an attached X-ray source and detector was used and moved across a 35 cm x 35 cm scan area. Using a point sampling method, the X-ray source and detector collected XRF data at multiple locations. This demonstrated a capability to create highly accurate elemental maps - noting discrete chemical changes. The system reported high spatial accuracy, with an elemental map resolution of 1.4 mm. However, the inability to alter the projection angle restricted its ability to scan unusual shapes, such as curved surfaces. Another system offering an XRF mapping capability is the Zetium XRF, produced by Malvern Panalytical [225]. The Zetium system consists of a bench-top machine that offers XRF mapping with a measurement step size of 100 μm . One major limitation of this setup, is that it is not capable of analysing larger, metre scale objects, which may be required for an in-situ analysis technique.

Evidently, the limitations including limited sample sizes and laboratory based sub-sampling render XRF mapping options redundant for an in-situ characterisation tool for sorting and segregation. One methodology to negate such limitations is the application of robotic manipulators paired with portable XRF (pXRF) devices. A critical feature for in-situ analysis for nuclear materials is that pXRF can be deployed as a non-contact analysis technique, thereby avoiding

potential pickup of contamination. However, the technique does require a close proximity to a sample surface (0-30 mm), which presents a technical challenge for remote deployments - to get very close, but not so close that contact is made.

pXRF mapping across a sorting and segregation table could be used to characterise reactive metals and other similarly recyclable materials, ahead of disposal. Waste on a table presents an automation challenge for XRF, as it contains features that may be spread across a large surface on the order of a 1-5 m², which currently cannot be achieved using standard XRF devices due to surface size constraints.

A robotic manipulator system fitted with a pXRF device has enormous potential for addressing many of the current XRF mapping limitations. Owing to the large range of processes that such systems currently undertake, robotic manipulators exist in a wide variety of sizes. Many feature a reach of greater than 2 m, thereby facilitating XRF mapping over centimetre to metre length scales. A unique feature of robotic manipulators, compared to a linear stage setup, is their ability to rotate the end flange, known as the 'end-effector', to different orientations. This functions very much like the human wrist, while maintaining a high level of spatial and angular precision of a robotic system. Rotational action in this way, provides the system with the ability to deploy the XRF unit to derive maps of surfaces with curved or highly varied topology, by keeping the instrument at the appropriate close stand-off distance and perpendicular to the surface. Chapter 2 demonstrated the versatility of robotic manipulators when combined with additional sensory inputs, such as vision-based technologies. Such a vision based system could be implemented to increase the efficiency of a process by negating the need to blindly scan across a whole table, instead targeting only the objects of interest and without coming into physical contact. Modern collaborative robotic manipulators could be used here to act as a secondary fail-safe against an unintended collision, reducing damage and contamination risks.

Ultimately, this waste is destined for storage in waste containers, which themselves must be periodically monitored [226]. For example, the UK's intermediate level waste (ILW) inventory comprises of some 40,000 stainless steel drums containing grouted wastes. The structural integrity of these drums must be maintained and checked to avoid a radiological release. If the container surface is contaminated with an aggressive species such as a chloride salt, then pitting corrosion may ultimately cause failure of the container [227]. In the UK, the Nuclear Decommissioning Authority (NDA) has stringent guidance on monitoring of nuclear waste drums in storage [142]. Currently, the drums are monitored for chlorides using remotely deployed contact techniques such as swabbing, tape lifting or direct flushing of the surface [228]. The arising samples all require transporting to a laboratory for analysis, which creates a delay in discerning the outcome of the monitoring and introduces complexity. Non-contact XRF scanning using a

robotic manipulator represents a valuable in-situ analysis technique for assessing the concentration and distribution of such salts on container surfaces. Hence, the opportunity to provide such analysis in-situ and in real-time is highly desirable for nuclear waste storage sites worldwide.

Ostensibly, any radioisotopes which may be present within scanning objectives in a nuclear setting, may themselves introduce X-rays. These X-rays will be recorded as a fluorescence and consequently, skew the results. It is anticipated that the only problematic isotope is from the americium-241 (Am-241) 60 keV gamma-ray [109]. This may coincide with the characteristic x rays of tungsten, rhenium and potentially lutetium. Although, it is unlikely that there would be a sufficient gamma-ray emission flux from Am-241 to cause such a statistical anomaly. However, it should be advised that a secondary gamma spectroscopy check is undertaken should any of the aforementioned elements arise via XRF analysis.

While the focus of this chapter, is the development of a nuclear-applicable manipulator-integrated XRF system. A pXRF-robot fusion could also be applied more widely; for example, to municipal waste processing or recycling facilities. In electrical waste recycling scenarios, components containing toxic chemicals including lead, cadmium, mercury and beryllium [229], may be distributed across a sorting table, awaiting material characterisation to provide a safe, environmentally conscious disposal route.

6.2 Method

6.2.1 X-ray Characterisation

The combined X-ray generation and fluorescence analysis instrument utilised was the Vanta™ C-Series pXRF from Olympus Corporation (MA, USA) [230]. The device is lightweight (1.70 kg with battery) and compact (8.3 cm × 28.9 cm × 12 cm when the optional integrated device handle is removed). A 4 W, 50 kV, X-ray tube combined with a silver anode target yields an excitation X-ray source energy of range 8–50 keV. Resulting from the characteristic X-ray emissions of the different elements occurring across the full 8-50 keV energy range, a ‘3 beam’ mode is used whereby three specific beam energies are used to enhance the sensitivities for groups of elements best achieved by that ionisation energy. These energies can be tailored to the specific elemental compositions likely to be encountered. The detection of the X-ray induced fluorescence is performed by the Vanta™ using an integrated Silicon Drift Detector (SDD). It is capable of operating under wide temperature ranges of 10 C to 50 °C, enabled by the integrated cooling fan installed next to the SDD module. The mobile unit possesses an Ingress Protection rating of IP55, meaning it is protected against dust and low pressure water jets. Therefore, it is well suited for use within contaminated and hazardous environments where material ‘pick-up’ and subsequent

decontamination are of concern.

For more routine, manual deployments, the Vanta™ is typically used in the ‘gun’ configuration, for performing single spot/point compositional assays by hand. Quantitative results can be displayed in real-time on the instruments integrated touch-screen. However, the device is also an ideal detector for robotic research and deployment owing to its programmable operation. Hence, rather than relying on a user to manually initiate each analysis event, it is possible, through the USB-serial connection using a dedicated Linux (Python™) software package, to enable X-ray analysis to be triggered remotely. In addition, the Vanta™ parses both the spectral and peak fitted elemental data. It can then be sent directly to the tethered computer, where it can be subsequently processed using custom design software developed.

6.2.2 Robotic Integration

A KUKA LBR iiwa R820 [99] was selected for these nuclear-applicable scanning applications. The Vanta™ analyser was attached to the end effector of the robotic manipulator, using an adjustable and configurable sensor rack, photographed in Figure 6.1. This rack could accommodate a range of other sensory options, such as a depth-sensing camera or tactile probe. Prior to each of the subsequently detailed applications, a tool centre point (TCP) calibration was performed, using the KUKA XYZ 4 point method to precisely determine the location of the XRF scanning head relative to the end effector. This method entails orientating the ‘tool piece’ around a defined centre point in four different directions. A transformation can then be generated, locating the instrument relative to the end effector.

A custom control software was developed in Python™ to synchronise the Vanta™ and KUKA LBR iiwa. The robotic XRF system was programmed to sequentially move through a set of situationally dependant, pre-generated scan positions and pause while XRF data was acquired. Acquisition of pXRF data was set for 10 s on beams 1 and 2, with 20 s on beam 3, for all measurements. A set of control parameters were customisable, enabling the user to fine-tune the robotic movements and data collection, including the position, point density and scan surface type. Point density was configured according to the time available for the scan and dependent on the level of detail required. The scan surface type enabled the robotic system to interrogate a choice of flat surfaces or curved surfaces. The location and orientation of the XRF scan head was recorded for each measurement relative to the robotic manipulator, constituting of the collection of an $[x,y,z]$ and $[a,b,c]$ co-ordinate, where $[x,y,z]$ represents the position in free space relative to a predefined base, and $[a,b,c]$ represent Tait-Bryan angles of the XRF module. When the arm was in position, the Vanta™ was triggered from a stand-off distance of 0.5 - 3 cm and the XRF data collected. The collected results, including elemental concentration and associated errors, were recorded

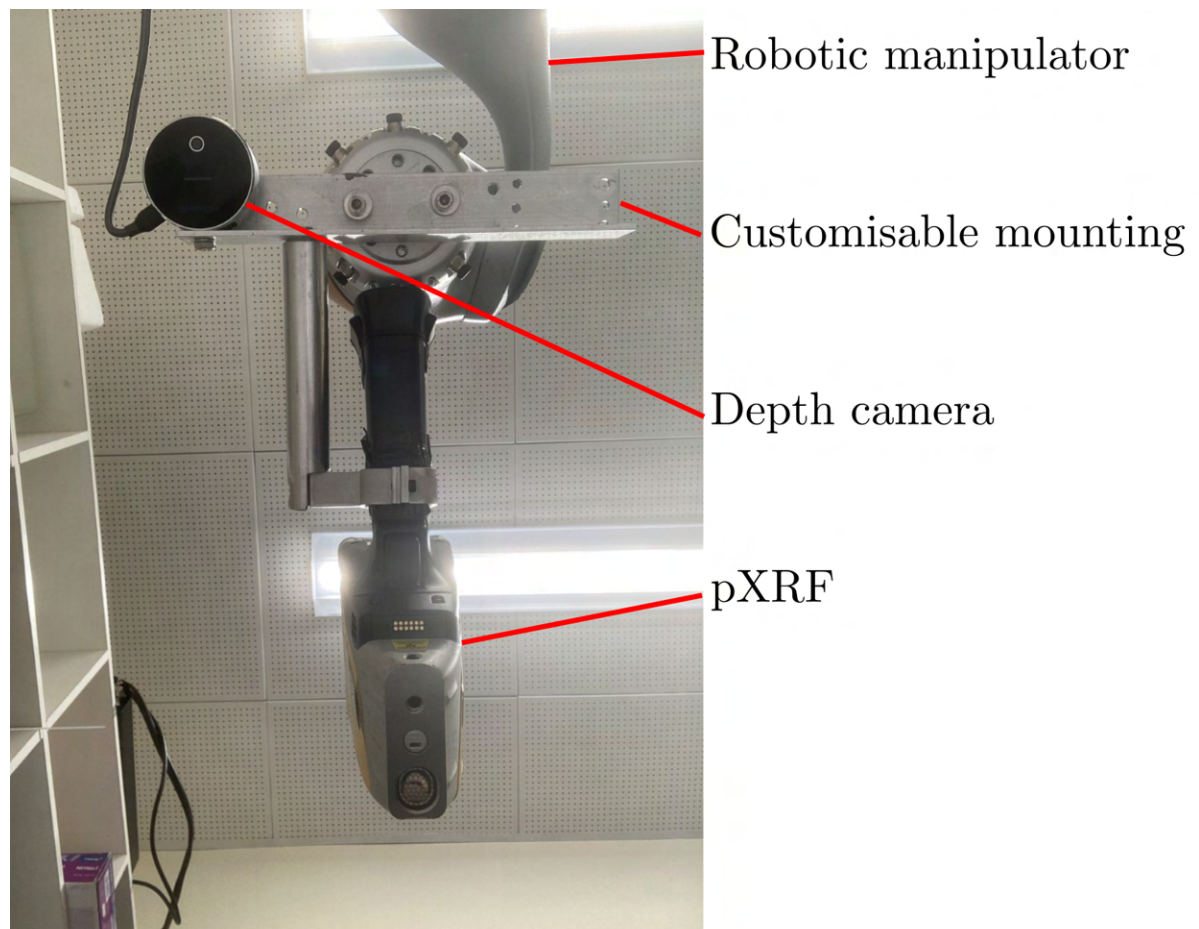


Figure 6.1: Customisable sensor rack used within this chapter. Attached is the Vanta and the RealSense L515.

in a csv file. Data could then be graphed as an XRF ‘map’ of elemental mass fraction, as part of a visualisation software that was developed in PythonTM. Each visualisation was bespoke to the scenario for which it was applied and the results could be plotted as discrete, raw values in space both in 2D and 3D. Maps allowed for visualisation of the distribution of different elements recorded by the XRF. A flowchart detailing the system setup and workflows is shown in Figure 6.2.

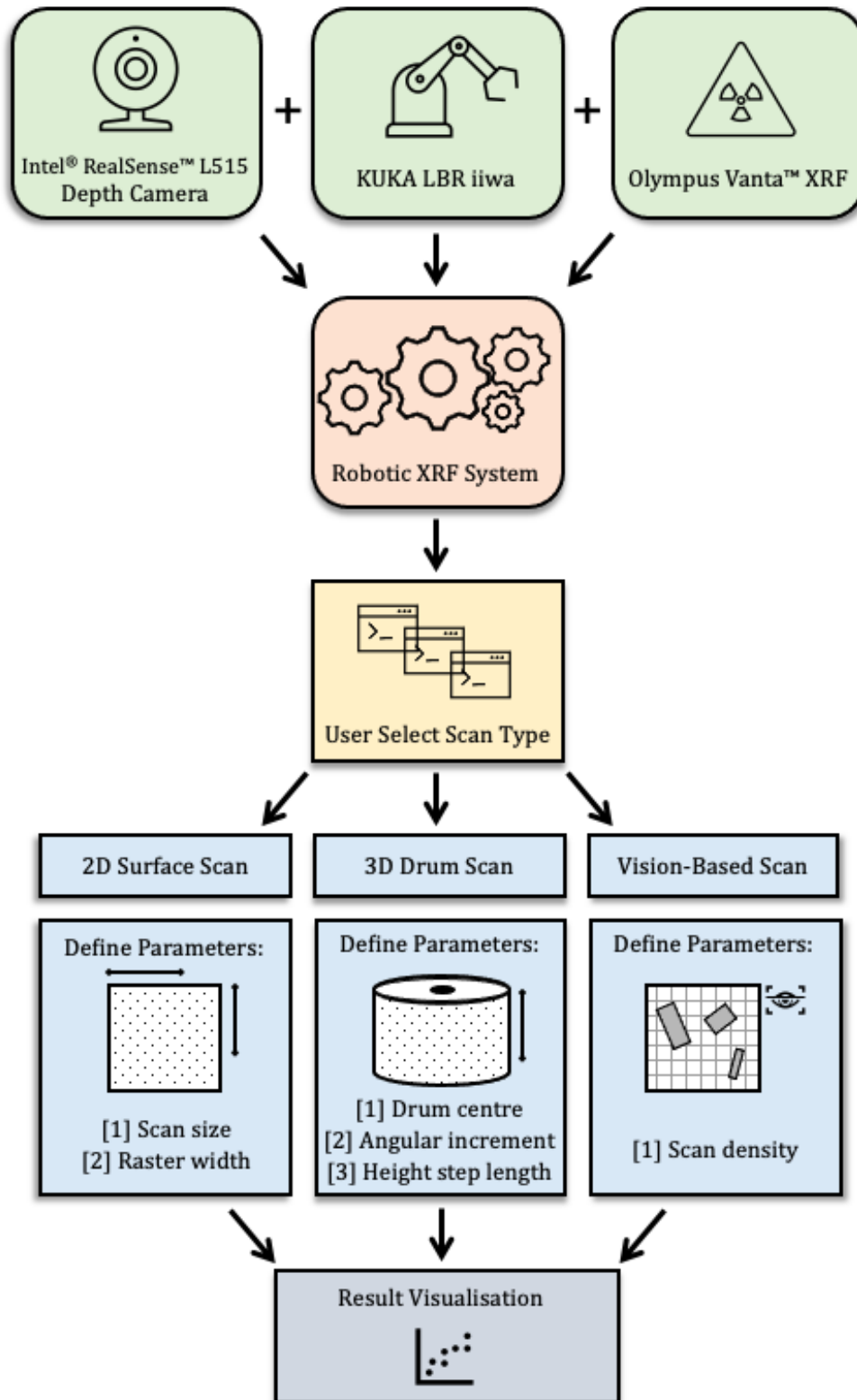


Figure 6.2: Schematic flowchart illustrating the platforms configuration and workflow, including details of the application-specific user parameters necessary to undertake each scanning scenario.

Figure 6.2 shows the versatility of the system, demonstrating how it may be setup for multiple different applications, including flat surface scanning, waste drum monitoring and individual object assay.

6.2.3 Assessing the Quality of Elemental Analysis Results

Operation in a stand-off configuration is not recommended by Olympus. Hence, to validate the precision of the concentration values obtained by the XRF mapping system, a paint solution doped with known quantities of caesium chloride (CsCl) was analysed as part of a calibration activity. Equal portions of paint (2 ml) were doped with CsCl masses ranging from 0.0 g to 3.0 g, in increments of 0.5 g. A strip was produced containing these varying concentrations of CsCl. The robotic XRF system was programmed to perform a line transect scan across the strip, collecting data at 2 mm intervals. A 5 mm stand-off distance was set for the full line transect. The experimental results from the robotic system, were then compared with the results from a laboratory bench-top Octane plus EDS (EDAX, Inc., Mahwah, NJ, USA). This was completed to ensure that the data derived from the pXRF was well calibrated.

6.2.4 Assorted Object Assay

In nuclear waste sorting and segregation activities, mixed objects may be randomly distributed across a sorting table, including contaminated pipe work, tools and rubble [45]. These objects will need to be assayed to assess their elemental compositions ensuring that the waste can be stored with confidence. For this process, scanning across the whole analysis area, would be time consuming and contain many data points where no objects are located on the sorting table. Hence, a robotic vision based procedure was implemented, using a computer-vision ‘region of interest’ methodology. The process was similar to the grasping algorithm detailed in section 2.4. A depth camera was used to identify the objects of interest and consequently inform the robotic XRF system of specific intelligent scan locations to perform XRF. Therefore, reducing scanning time and increasing elemental information about objects of interest through a targeted ‘denser scan’ of the non-background material.

To achieve this object targeted scanning, the Intel[®] RealSense[™] L515 depth camera [102] was used in combination with the robotic XRF mapping system to derive an XRF map. The robotic XRF system autonomously moved to an initial camera pose, where it took a depth photo of the scene. This depth image could then be compared to a reference image of the scan area. The resulting depth comparison image reveals positional information about the objects on the surface. A height and area threshold was applied to the comparison image to locate the objects of interest, in this case programmed as 625 connected pixels (approximately 0.04% of the image) for an area-of-interest and 2 cm for object height. This thresholding process identified the pixels of

interest from the depth image. An affine transformation was then applied to convert pixel space into XRF system co-ordinate space. The robotic XRF system could then scan the autonomously thresholded co-ordinate points.

Measurements were taken at a pre-defined stand-off distance from the sample. The stand-off distance has a large effect on the relative concentration of elements within each scan. Therefore, a positional accuracy test was completed on a flat metallic object, where the system was set to scan 50 points at a 15 mm stand-off. A metallic object was selected, as the reflectivity of such surfaces was noted to introduce the largest errors to the system. The test revealed a standard deviation of 2 mm with a range of 10 mm. To be conservative, an error of ± 8 mm was assumed, owing to this being the maximal divergence from the true value.

The pXRF module itself emits a pencil beam with a small divergence. The geometric specifics of the system are commercially protected, but working at a 30 mm stand-off distance, the calculated beam divergence diameter is 11 mm. At a stand-off of 5 mm, the beam divergence diameter is just 2 mm. The error in positional accuracy in the horizontal plane, from the calibration was found to be 10 mm. Hence, an effective spot size of 21 mm diameter was assumed for the purposes of this work. The primary objective of the system is to quantify the elemental composition of large objects through multi-point analysis. Therefore, such errors were deemed acceptable.

RealSense™ L515 depth cameras have positional accuracy's of approximately 5-14 mm dependant on the vision area, which is up to 9 m² [102]. Combined with a tool accuracy of ± 8 mm from the LBR, there is a targeted positional accuracy of 10-15 mm. Hence, if the device is programmed to target a distance of 15 mm, it is likely to be within an appropriate XRF stand-off distance. In addition, it should be highlighted, that the force-torque sensing capability of the KUKA LBR acts as an additional fail-safe, in the event of a collision between the pXRF and the sample. This camera based algorithm enables the intelligent 'region-of-interest' mapping of objects. To test this procedure, two scenarios were prepared using a mock-up waste sorting table of dimension, 30 cm \times 60 cm. The first attempted the vision based mapping of 3 rectangular metal blocks containing aluminium (Al), copper (Cu) and silumin (an alloy containing Al and silicon). This scan was completed at a fixed height, as all the objects were of the same dimensional height. In the second test, a metal file (Fe), a rock (quartzite), copper tubing (Cu) and a small piece of galvanised steel sheet (Zn) were placed on the mock-up waste sorting table. These objects were selected as they are examples of potential materials which may appear in nuclear waste [45]. Owing to the physical dimension of the pXRF, a stand-off distance of 20 mm was programmed for this test. This stand-off was selected to ensure the pXRF did not make contact with the objects of non-uniform height. Figure 6.3 shows the object placement and the robotic XRF system scanning in progress.

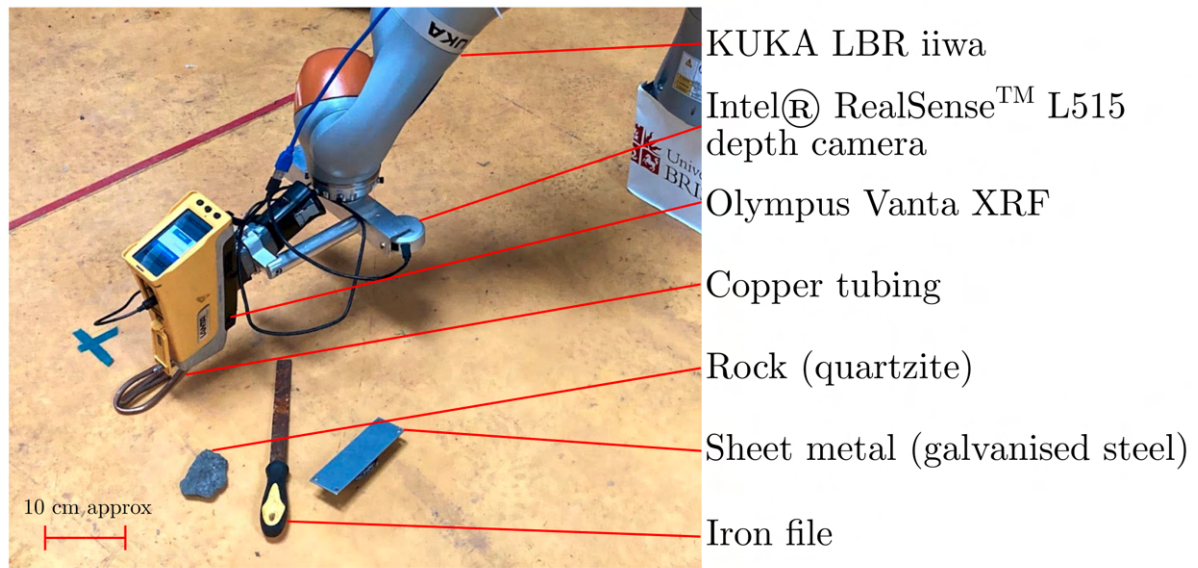


Figure 6.3: Photograph of the vision-based scanning system in progress; showing the assorted objects on the scan surface, the KUKA LBR iiwa, Intel® RealSense™ L515 and Olympus Vanta™.

6.2.4.1 Verification of depth sensor based positioning

Implementation of the depth and colour sensing camera based robotic motions required a positional accuracy verification. There are a number of parameters which introduce error, including the accuracy of the camera, robotic manipulator, the calibration and pXRF instrument.

Error in the robotic manipulator is reported at ± 0.1 mm. However, ultimately, the accuracy of the positioning will depend on the accuracy of the affine transformation calibration. This is something that must be tested experimentally to deliver an understanding of accuracy. The X-ray beam is described as being ‘highly collimated’. Therefore an assumption was made that the pXRF system had a mm error beneath the emission diameter.

The test was designed using a laser pointer and cylindrical alignment object of diameter 50 mm, with a well defined cross etched onto the centre. Object of interest identification tools would then identify the cylinder and direct the robotic system to the centre point. The robot calibrated using two methods. One method attempted to calibrate the laser without it being switched on. This was to mimic the calibration of the XRF system which did not have a laser assistance directing the calibration. The second was calibration with the laser switched on, enabling a higher precision affine shift to be calculated. It was then set to autonomously target the centre of the cylinder. Error was measured as the distance from the target location to the dot using vernier calipers. The cylindrical object was then placed at the extremes of the cameras vision and directly beneath

the camera. This aimed to account for the best and worst case parallax errors introduced by the angles of the camera to the target objects. A photograph of this experiment can be seen in Figure 6.4

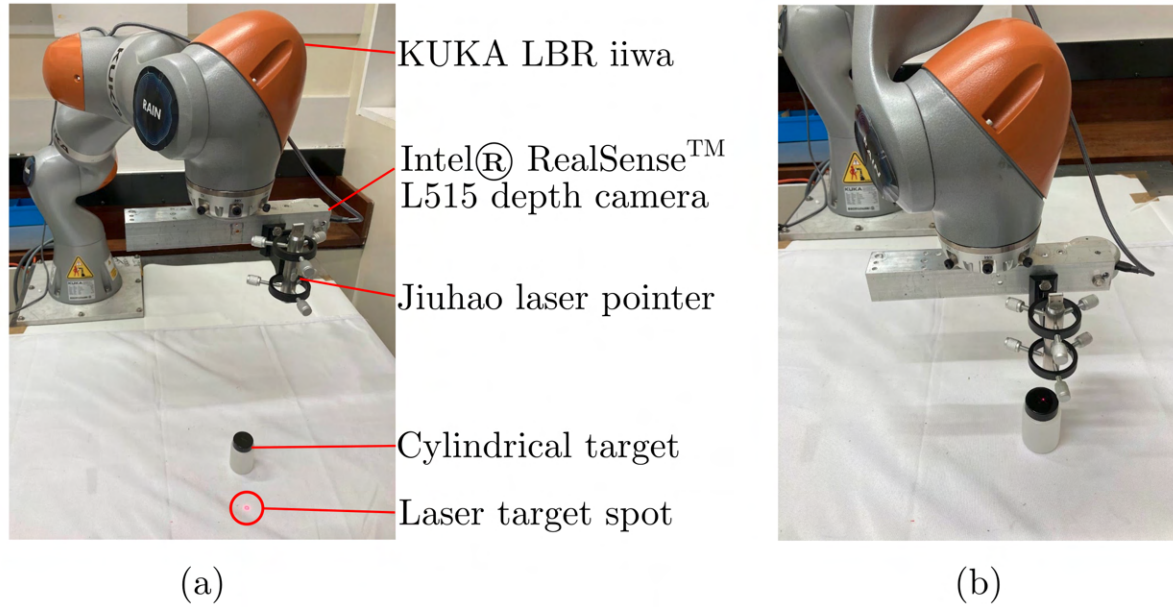


Figure 6.4: Photograph of the depth sensor based positioning experiment. (a) shows the robot in the predefined ‘camera pose’. This identifies the cylindrical object on the table. An affine transformation is then used to guide the robot to the object. (b) when the robot is in position, the laser may be used to measure the accuracy of the transformation.

6.2.5 Exterior Drum Scanning

Orientation control provides the robot-integrated XRF system with a unique capability to compositionally analyse curved surfaces. This ability was tested by performing an area scan on a region of a 200 L plastic drum. When the centre point and radius of the curved object (e.g. a drum) relative to a manipulator are known, then it is possible to numerically plan a series of equi-spaced points which traverse an arc via a number of geometrical calculations. By inputting the centre point and radius of the drum into the custom scanning control code, such point locations were identified. These locations included the manipulators position, XRF scan locations and Tool Centre Point (TCP) orientations. Each position ensured that the XRF device was always directed towards the centre of the drum, normal to its surface. The robotic XRF mapping system was then able to obtain elemental composition measurements at each such point. Precise point locations were based on the additional pre-defined user input parameters. Point density was defined as a function of angular increments on each arc and vertical height step lengths. Using the 3D implementation of the developed plotting software, a surface map of the drum with elemental concentrations was generated. This was tested with different elements applied to the

surface including copper tape (Cu), undoped paint, paint doped with caesium chloride (CsCl), an aluminium sheet (Al) and a stainless steel disc (Fe), as shown in Figure 6.5. The arm was set to scan for approximately 10 hours, at 1 degree increments around a 60 degree portion of the circumference of the drum, with 1 cm vertical height steps. Measurements were taken from a stand-off distance of between 10 - 25 mm, owing to irregularities in the drums circumference.

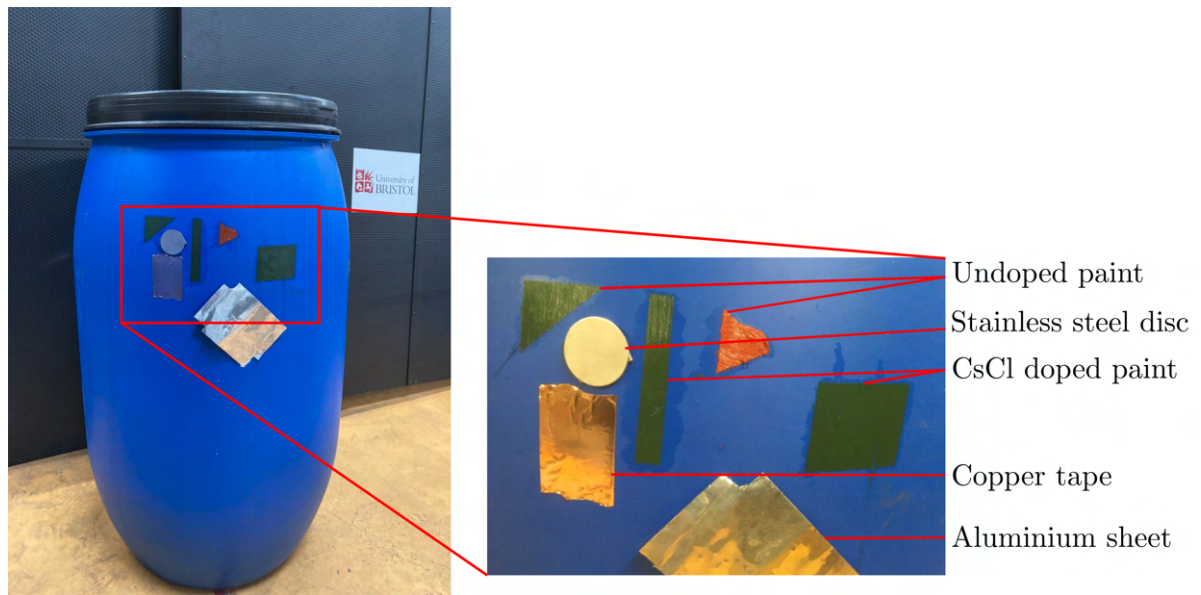


Figure 6.5: Photograph of the drum setup, detailing the positions of the copper tape, CsCl doped paint, undoped paint, aluminium sheet and stainless steel disc.

6.3 Results and Discussion

6.3.1 Concentration Calibration

The results of the concentration line scan test are shown in Figure 6.6. Results collected were interpolated using a linear interpolation technique. This was done to aid the visual clarity of the graph.

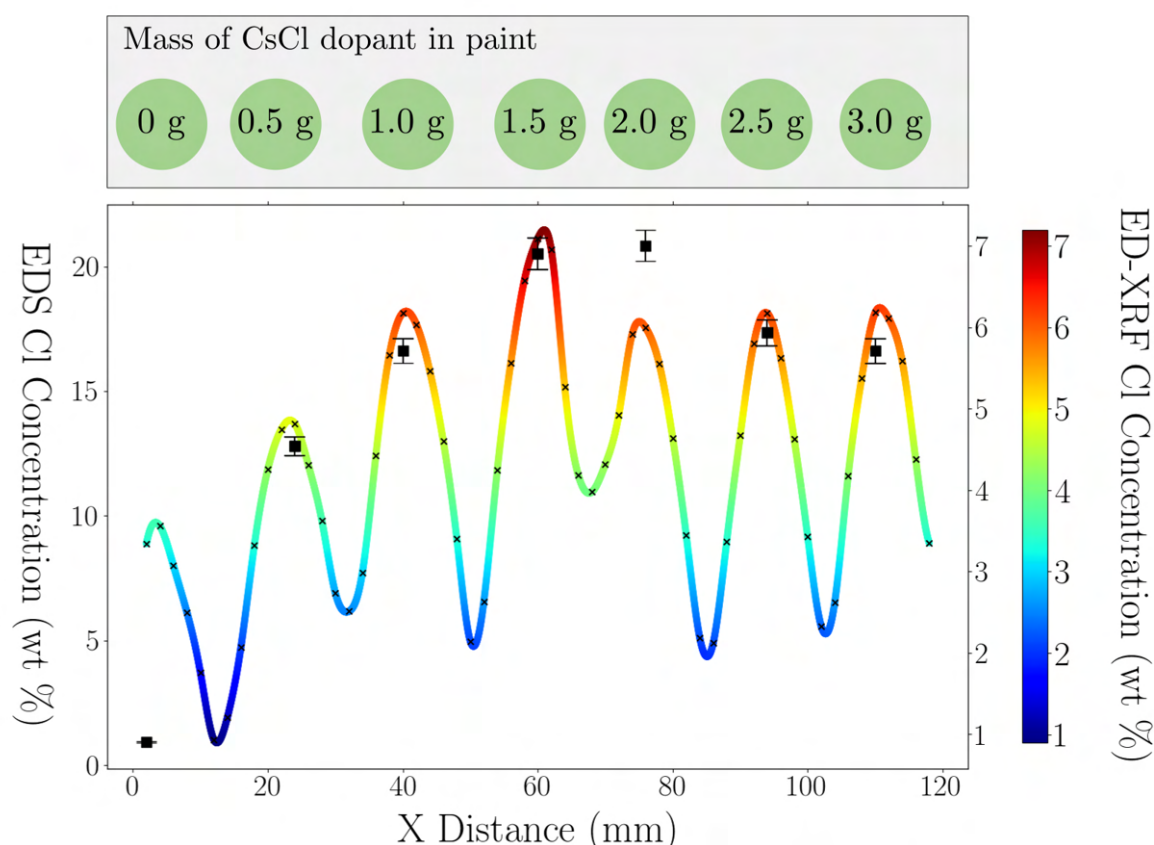


Figure 6.6: Concentration profile of the pXRF line scan over a linear transect of the CsCl doped paint. Left to right, the mass of dopant added to the paint was 0.0 g, 0.5 g, 1.0 g, 1.5 g, 2.0 g, 2.5g, 3.0g. The colourful line is an interpolated concentration wt% for Cl along the transect. The black squares represent the results of the laboratory EDS testing, with associated error.

Figure 6.6 demonstrates it is possible for the robotic pXRF system to not only detect certain elements, in this case Cl, but also derive relative concentrations. The results output from the robotic pXRF system are proportionally in good agreement with the bench-top EDS setup. However, the pXRF results show a large reduction in attained concentration. This is likely a result of a reduced X-ray flux being received by the system, due to the stand-off configuration. A capability to discern approximate weighted concentrations using this system is a powerful proposition. This could be particularly useful for applications where there are threshold limits on

concentration of certain compounds. One prominent example of this is the search for chlorides on the exterior of stainless steel ILW drums, where acceptance levels for such contamination are in place for species such as Cl (see section 6.1).

6.3.2 Positioning Accuracy Verification

The results of the calibration test revealed a difference in results arising from the laser targeting method and the non-laser target method, in terms of measurement positioning.

Across the 5 positions investigated, the non-laser target method attained an average of 7.26 mm positioning accuracy error with a maximal error of 10 mm. Therefore, for robotic XRF experimentation, a positioning error of 10 mm was assumed.

For the laser corrected method, an average of 1.4 mm XY plane spatial positioning accuracy error was attained, with a maximal error of 3 mm. Hence, to be conservative an error of ± 3 mm was assumed. This was a much higher level of accuracy than anticipated. Given the established error of the pXRF unit in a stand-off configuration, it does not make a significant contribution. Future research using an XRF instrument may benefit from laser assisted affine transformation determinations, in particular for situations which require high levels of spatial accuracy. For example, the measurement of objects of less than 2 cm wide.

6.3.3 Assorted Object Scanning for Sorting and Segregation

The result of the vision-based scan of the experiment investigating a set of metallic blocks is shown in Figure 6.7.

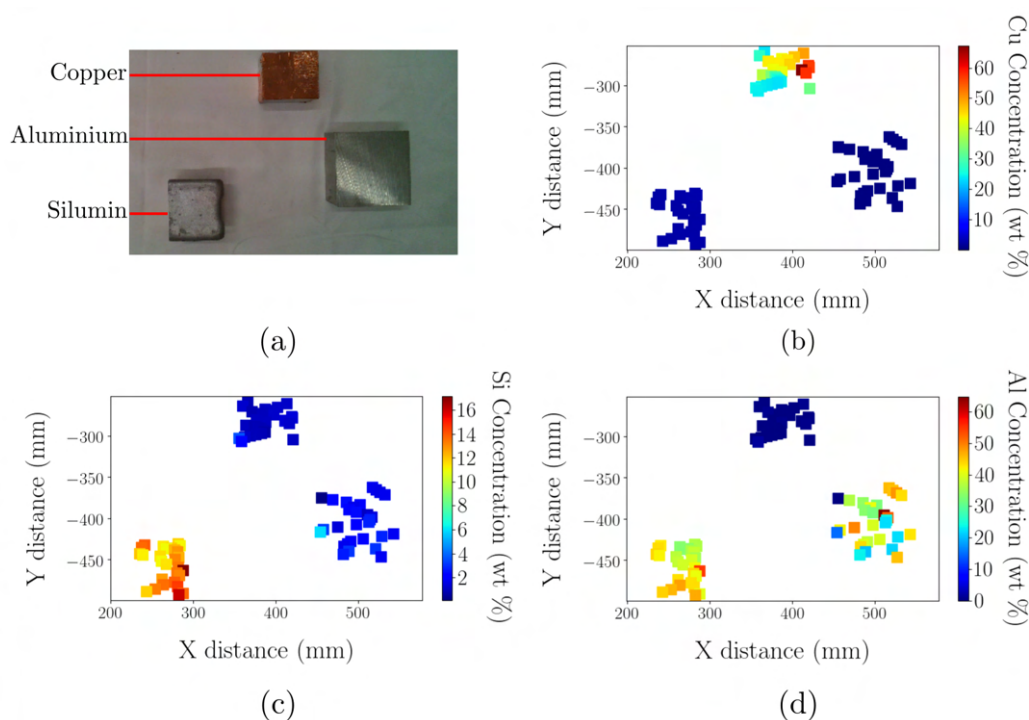


Figure 6.7: Results of the vision-based autonomous robotic XRF mapping of system identified objects of interest for the metallic block experiment. (a) shows the experimental setup. (b-d) show the elemental concentrations of (b) Cu, (c) Si and (d) Al.

The results show a good agreement between the metal and alloy compositions determined by the XRF and the true metallic species. This experiment confirms that the vision-based region-of-interest algorithm functions, as expected and provides good utility for this application. All blocks scanned were of the same height, hence analysis of stand-off distance could be completed. The results showed that an average stand-off of 10 mm was recorded across the dataset, with a standard deviation of 2 mm. These results were greater than anticipated, but within the tolerance of the system. As discussed, the Vanta system is designed to be used in a contact configuration. Therefore, any air gap between the device and the sample being measured will result in a decrease in attained weighted concentration. The variation of stand-off is likely the cause of the fluctuation in measurement across individual samples. This is especially the case in the Al block, where values of between $14.9\% \pm 0.7\%$ and $64\% \pm 0.2\%$ were attained. Because Al is a light element, it has a very low fluorescence peak at 1.486 keV, meaning the X-rays become easily attenuated by air. Ultimately, this technique may be implemented to detect the presence of certain metals, but caution should be taken on using it to determine absolute sample concentration. Arguably, this should be sufficient in sorting and segregation scenarios. A more representative example of a waste sorting scenario was completed in a second experiment, the results of which can be seen in Fig. 6.8.

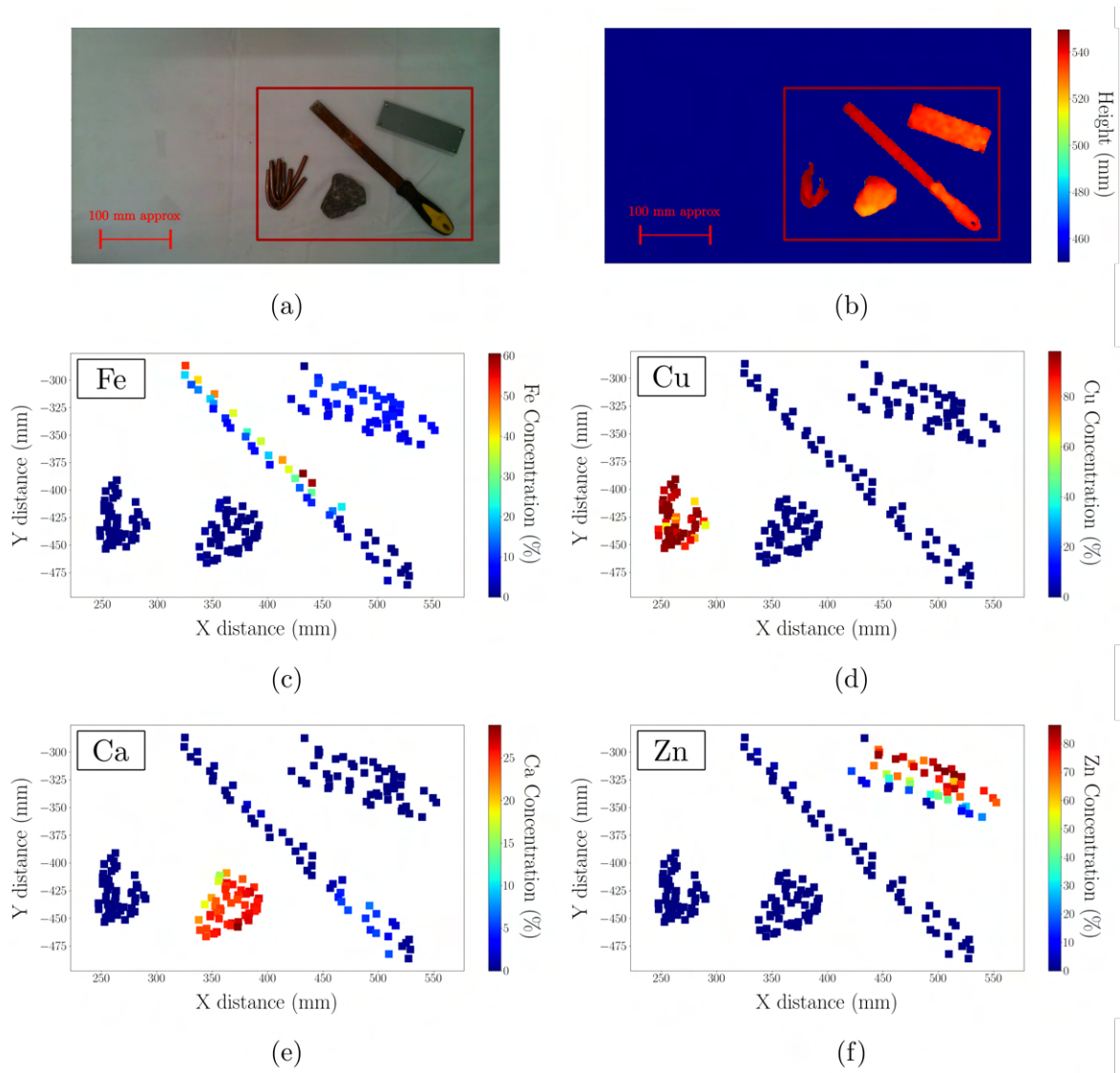


Figure 6.8: Results of the vision-based autonomous robotic XRF mapping of system identified objects of interest, as shown in Figure 6.3. (a) initial colour image from the RealSense™ L515 camera, (b) depth image of (a). The red box in (a) and (b) indicates the region which is displayed in the sub-figures, showing the single element XRF maps of: (c) Fe, (d) Cu, (e) Ca and (f) Zn.

The assimilation of camera-based object identification subsequently delivers targeted XRF elemental analysis with each object sharply identified by the vision based XRF scan to within ± 1 cm. Nonetheless, the results represents a powerful result and validation of this technical approach as a methodology for object assay, facilitating the characterisation of individual objects. Whilst caution should be exercised in attributing quantitative analysis to the elemental concentrations, the system is able to accurately identify the key elements present. All of the objects were scanned in approximately 2 hours, hence the surface was analysed in a time efficient process without sacrificing detail, as there remains a high point density on the objects of interest. To attain this

level of detail using a basic flat surface scan would take in excess of 8 hours, more than 4 times as long. Such an optimised system has an applicability to the sorting and segregation of mixed nuclear wastes, enabling individual objects to be identified in terms of material composition. It is envisaged that this will be used as a complementary tool alongside gamma spectroscopy and LRS, to provide in-situ material characterisation.

By developing a toolkit of complementary in-situ analysis tools, able to discern materials by shape, colour, radioactivity and material composition, the technical capability to more efficiently sort mixed nuclear wastes is improved. At the same time, this toolkit is equally useful for the sorting of other waste types that may arise from municipal sources e.g. mixed domestic plastic and metal wastes or mixed hospital wastes. Hence, this work is expected to have utility well outside of the nuclear industry and thereby have a broader appeal and value, which strengthens the business case for commercial development.

6.3.4 Drum Surface Scanning

The recorded XRF maps of the drum surface are shown in Figure 6.9, with the element of interest and concentration in mass fraction (wt%) presented for Light Elements (LE), calcium (Ca), chlorine (Cl), aluminium (Al), chromium (Cr), and copper (Cu) for Figures 6.9 (a)-(f), respectively.

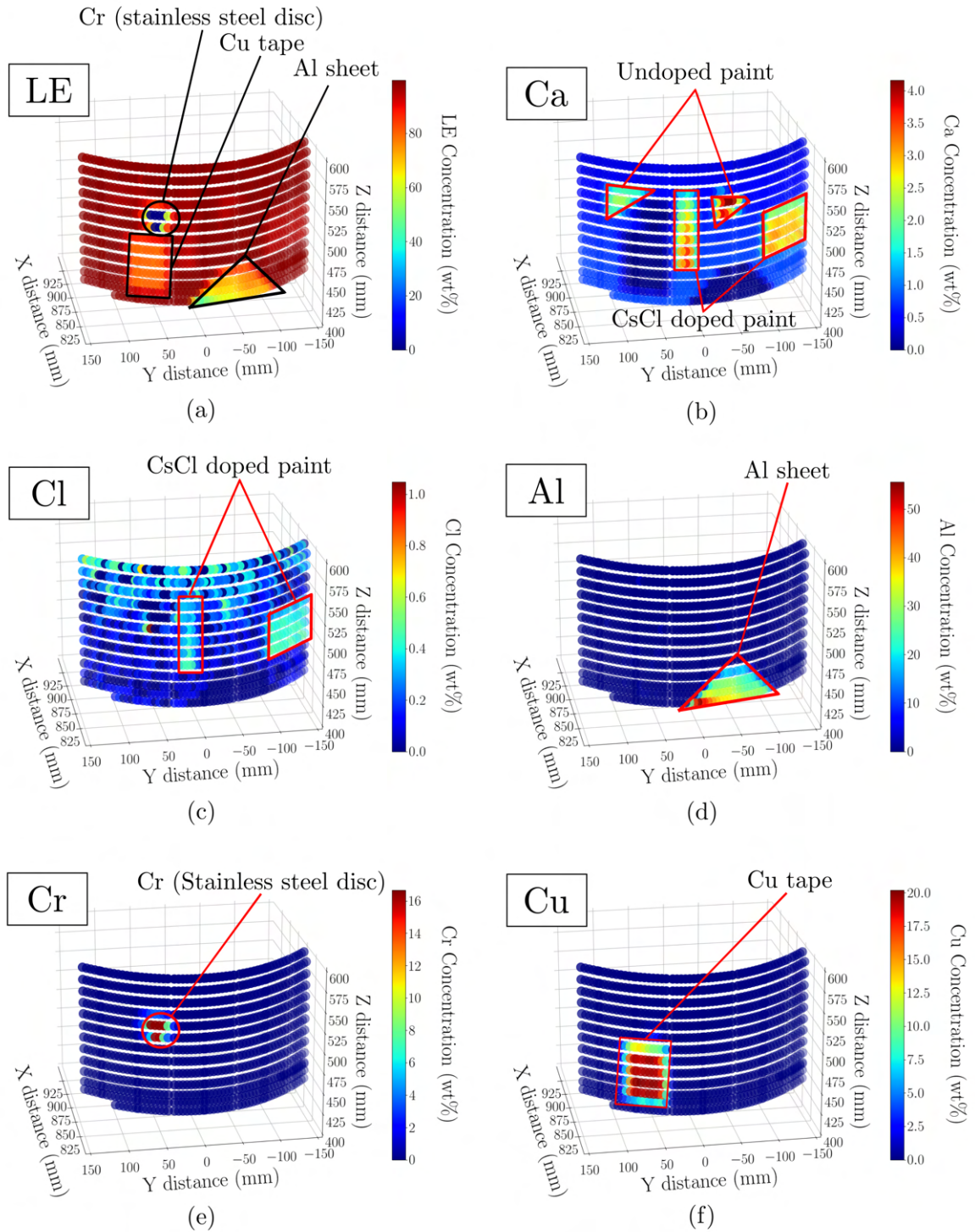


Figure 6.9: 3D surface concentration maps of the 200 L drum. (a) LE, (b) Ca (identifying the paint), (c) Cl (CsCl doped paint), (d) Al (identifying the aluminium sheet), (e) Cr (identifying the stainless steel), (f) Cu (identifying the copper tape).

Figure 6.9 shows the robotic XRF mapping system successfully located and identified the elements adhered to the drums surface. Ca is naturally present in the paint, with the painted shapes clearly identifiable on the Ca map of Figure 6.9 (b). The CsCl, which was dissolved into the paint, can also be observed in the Cl map of Figure 6.9 (c). It should be noted that additional Cl spots can be seen within this figure, likely a result of sweat from fingertips being deposited on the drum surface during experimental setup. Metallic objects are also clearly identifiable in Figures 6.9 (d), (e) and (f), demonstrating the XRF's capability to accurately differentiate metals. The ability to scan a drum surface, shows how XRF mapping can be achieved outside of regular 2D surface scanning. This has many potential applications, including routine in-situ drum scanning in ILW waste stores. In such scenarios it is crucial to identify and remove aggressive species on the drums exterior, thereby preventing localised corrosion.

6.4 Conclusions and Future Work

Following the comparatively recent developments in pXRF systems, such platforms have been almost exclusively used for discrete hand-held single-point compositional analysis, undertaken by human operators. This chapter has shown the successful application and subsequent testing of miniaturised XRF to undertake efficient, robotically automated elemental analysis across a range of nuclear-applicable scenarios. The details of the programming and robotic integration are covered in full with the created XRF system showing a demonstrable capability to perform point mapping at a controlled stand-off distance across flat surfaces, over metre scale lengths. A system calibration was completed to test the accuracy of the XRF device, showing a limited capability to recover the relative concentration of Cl in multiple paint samples collected on a strip. However, crucially, the system demonstrated a capability to detect the presence of elements, which was the primary objective of the system. The dynamic nature of the robotic manipulators orientation control facilitates XRF mapping on more complex 3D surfaces as demonstrated with the scanning of the curved surface of a 200 L drum. The system was able to accurately discern five different elements on the surface, displaying the results in 3D with custom designed visualisation software. Robotic manipulator systems are versatile platforms, which can take advantage of sensory technology. In this case an Intel[®] RealSense[™] L515 depth camera was used, to enable 3D object data capture prior to object targeted short stand-off analysis. Thereby the system exhibits a degree of intelligence in targeted mapping for enhanced assay, through identifying objects on a surface and subsequently characterising them. The system demonstrated here was able to autonomously identify and characterise different objects in a time efficient manner. It is possible a system could be developed to more intelligently scan different areas and components within object. This could be done in a similar way to that of the human eye, perhaps noting discrete changes in colour, lustre or form within objects.

The robotic XRF system is highly applicable to a number of different applications, owing to the versatility of the scanning methodologies. Surface scanning could be applied on historical artefacts for XRF analysis, or used in a nuclear or other industrial setting for routine monitoring of objects and surfaces searching for contamination. Such a scanning methodology for the identification of contaminants, could be combined with a decontamination procedure, such as pressure washing or swabbing, to provide a time and resource efficient solution without placing humans at radiological risk. The vision-based scanning of target objects is highly applicable to the sorting and segregating of mixed nuclear wastes to ensure the correct characterisation and consignment for storage and disposal. In such a setting, this would be particularly powerful as a complementary characterisation tool in combination with gamma spectroscopy and LRS. Together these in-situ analysis techniques would be capable of identifying a full spectrum of chemicals, materials and compounds. Similar systems are desired for waste electronics recycling, sorting mixed medical wastes and municipal recycling, so it is easy to see how the vision-based scanning methodology could be re-applied for use in other applications.

To further improve the accuracy of the elemental composition results, the stand-off distance must be substantially reduced. Therefore, improvements to the XRF system positioning would be crucial. Such positioning improvements could be resolved through the implementation of a multi-camera setup, in which cameras are placed at different known locations around the scan area. Analysis of all images would reduce parallax error and theoretically increase the fidelity of the resultant point cloud. The XRF system could then be more accurately positioned relative to each sample, reducing the stand-off distance and enhancing the data collection.

ROBOTIC MATERIAL CHARACTERISATION WITH RAMAN SPECTROSCOPY

The preceding chapters have addressed initial assay approaches which can adequately identify the radiometric and elemental characteristics of objects for waste sorting operations. However, both XRF and radiation detection, are unable to identify key material and chemical characteristics. XRF showed a demonstrable capability to recognise elemental compositions of materials and is well proven industrially for discerning different metals. Radiation detection was able to identify gamma emitting radioisotopes. Although, both are unable to detect chemically bonded or lighter material components, such as plastics and fibrous materials. As discussed in chapter 2, Laser Raman Spectroscopy (LRS), is a technique that uses lasers to identify key bonding structures within a variety of chemicals and materials based on measuring characteristic bond vibrations. Using a focused Raman probe with an attached LRS system, stand-off LRS can now be achieved. This means LRS can be completed away from radioactive materials; both reducing potential radiation damage to expensive optical and electronic components and reducing the need for robotic deployment of bulky spectroscopic camera gear. Explored within this chapter is the combination of stand-off LRS with robotic manipulators for waste inspection purposes. Initially, this was accomplished using a naive pre-programmed approach to test the principle. This was subsequently enhanced through the integration of a depth camera combined with an AI colour recognition software, based on a K-means clustering approach. Ultimately, this meant the LRS probe could be autonomously directed to distinct colours identified on object surfaces, which are likely to be indicative of different materials. Hence, object scan times can be reduced while optimising useful data collection.

7.1 Introduction

Chapters 3 and 4 demonstrated radioactive objects may be distinguished and characterised by robotically deployed radiometric scanning techniques. Chapter 6 explored robotic XRF analysis, which may be used to perform elemental characterisation of elements between Na and U, identifying transition metals and also distinct alloys. However, other chemically bonded materials such as PVC, material fibres, other plastics and asbestos cannot be identified using either of the aforementioned techniques. These are crucial for sorting and segregation of nuclear waste both for fulfilling documentation and safety protocols. Equally, for actinide compounds, whilst XRF can identify the presence of U, it cannot determine if it is metal, oxide, hydride, carbide, hydroxide or nitride. Hence, a technique that can determine metal-containing but not metallic compounds is valuable for materials sorting.

A large amount of plastics are generated in nuclear wastes. PPE such as air-fed suits and gloves contain plastics and rubbers [11]. In addition, tooling and containers which may be used within nuclear processes may also contain plastics [11]. Plastics comprise 5,680 tonnes of the UK's nuclear waste inventory [231], equating to approximately 6000 m³ of plastic waste, equivalent to more than 2 Olympic swimming pools full of material. One prominent example of an undesirable plastic that may be found in a significant portion of nuclear waste is polyvinyl chloride (PVC). PVC is used widely in the nuclear industry for a variety of applications including glove box posting bags and protective suits [232]. Mixtures of PVC with hydrogen containing species such as water can result in the production of hydrogen chloride (HCl) and molecular hydrogen (H₂) [233]. Such products may induce volume expansions within waste containers or cause corrosive effects. Evidently, H₂ is also highly combustible, which is undesirable for long-term waste disposal. Therefore, it is critical that PVC is identified and separated within waste sorting activities to avoid any detrimental occurrences that might compromise the long-term performance of waste packages for storage and disposal.

Asbestos is another material found in nuclear waste sorting activities [11], which requires urgent identification. It is well known that asbestos is hazardous to human health, causing numerous lung related illnesses [234]. A technique which could identify it within waste piles, in-situ and without any laboratory analysis requirement, would therefore introduce a drastic health and safety improvement. LRS has been shown to identify all six types of asbestos [235], and accordingly has good pedigree for integration into a nuclear material sorting capability.

Radioactive contaminants on materials may be found with radiometric techniques. It is clear that plastics and other fibrous materials cannot. Therefore a different material and chemical characterisation must be implemented. LRS is an alternative approach, capable of analysing such materials. As discussed in chapter 2, LRS uses laser light to identify vibrational modes in

chemical bonds within a materials structure. It is a well established material/chemical analysis technique, with a known functionality at stand-off distances of metre scale distances [236]. This is ideal for a robotic process, as it reduces the potentially harmful effects of a contaminated probe system, whilst additionally making the robotic positioning process more forgiving. Although, the key advantage here, is the ability to keep the radiation susceptible and expensive spectroscopic equipment away from radiation. While it is noted that optical hardware is also radiation susceptible, it can be replaced at a significantly reduced cost. Robotic stand-off Raman spectroscopy was previously reported by Coffey et al. [237], using a PAR M3000 to take both contact and stand-off Raman measurements. The contact Raman results showed an excellent capability to separate materials from Raman spectra. However, the peaks were shown to be less distinct in a stand-off configuration. It is suggested that a highly collimated and tightly focused beam may improve results. Therefore, the laser used within this work will be collimated in an attempt to rectify these issues.

This chapter seeks to prove the principle of robotic stand-off Raman spectroscopy, by demonstrating a simple scanning process is possible. Following this, it will further develop the region of interest scanning methodology discussed in chapter 6. AI and computer vision tools will be applied to enhance autonomous data collection and spectral recognition.

7.2 Method

To resolve the limitations of radiometric and XRF analysis techniques, a stand-off LRS system was combined with robotic manipulator platforms. Initial testing was completed using the KUKA KR150 industrial robot, with the Clifton Photonics stand-off Raman probe [238] attached. The purpose of this was to assess the quality of the stand-off Raman data attached to the robotic system. In the first instance, this was done naively, with the system directed to pre-programmed positions, at a 3 cm stand-off to collect Raman data for a data capture time of 1 s. Subsequently, a more advanced system was developed, as part of the developed robotic Raman inspection system. This system used the KUKA LBR iiwa robotic manipulator, with an attached RealSense L515 depth camera and stand-off Raman probe. A photograph of the system is shown in Fig. 7.1.

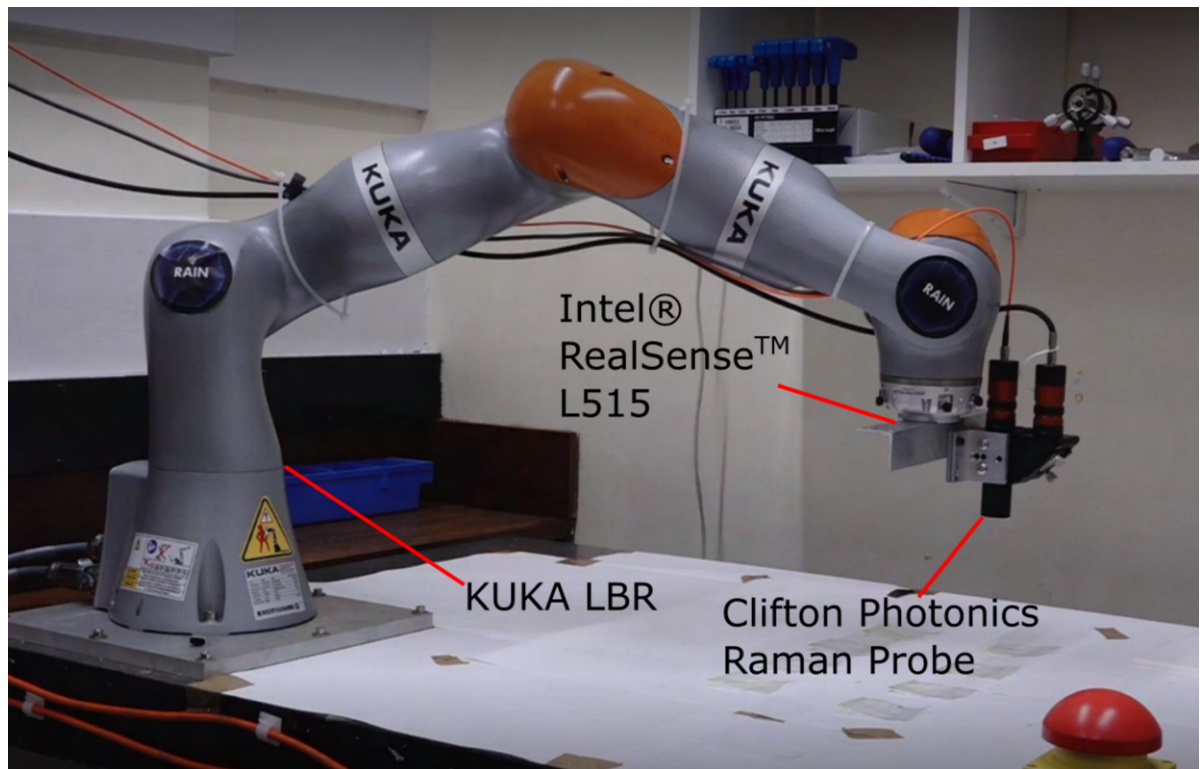


Figure 7.1: Robotic Raman inspection system setup.

7.2.1 Raman Spectroscopy System

The Clifton Photonics Portable Raman Spectrometer was used in combination with the fibre optic Raman probe [238], to complete the LRS system. The full setup consists of a near infra-red laser wavelength of 830 nm, Raman probe and the portable spectrometer. Each component was connected via optical fibres. An optical focal point was adjusted to enable Raman spectra to be collected from 3 cm stand-off distance.

An incident laser wavelength of 830 nm was chosen, as working in the near infrared region (NIR), reduces fluorescence, thus improving acquisition of relevant data [171]. A stand-off of 3 cm was selected, as it is noted that the closer the stand-off the higher accuracy the data [237]. This meant a stand-off height of 2 cm could be targeted before an optimisation technique (see section 7.2.3.4) could be used to reach the desired 3 cm focal point.

7.2.2 Robotic Raman Data Collection

The Raman probe was mounted on the arm, with the associated optical fibre cabling attached safely to the exterior. Experimental robotic Raman data collection was achieved by positioning the

robot, then triggering the data acquisition. The laser source remained on for the entire duration of the experimentation.

7.2.3 AI Based Vision Scanning

An intelligent, sorting and segregation focused, scanning mechanism was designed. This sought to further develop the methodology utilised within the previous chapter's XRF integrated robotic vision system. Raman spectra did not reproduce elemental composition like the pXRF system which was used. Instead, it produces distinct wavelength shift spectra from which analysis must be undertaken manually. Therefore, it was decided that a sub-sample of 'interesting' locations should be taken from each object, as representative Raman spectra. Theoretically, different colours are likely to represent different materials within an object, so a colour analysis tool was used to autonomously identify different colours across an object surface. The LRS system could then be directed to different coloured regions to record Raman spectra.

Initially, the robot moved into an initial camera pose from a known stand-off distance, in which a depth camera image was taken. Subsequently, the LRS probe was autonomously navigated in a series of short stand-off measurement positions to address the different objects within the scene.

7.2.3.1 Image Masking

An aligned depth and colour image was collected from the camera pose. This was possible using the Pyrealsense2 PythonTM library [102]. It matched the depth and colour image pixels, such that determining a pixel from the colour image, aligned with those of the depth image. From this depth image alignment, objects above a certain distance threshold were removed revealing only the objects of interest. The objects of interest were identified using a depth threshold of 5 mm. Such an image may be 'masked' such that only the objects of interest are visible.

Owing to the depth and colour image alignment, the pixels identified by the thresholding technique may be extracted. This process reveals the colour images of the objects of interest. Each individual object may then be analysed by applying a 'connected components' filter, extracting pixels which are directly connected to each other. Each object could then be examined independently of the others. Colour identification could be achieved using a K-means cluster analysis, that was implemented in the software.

7.2.3.2 K-means Cluster Analysis

K-means is a form of non-deterministic, unsupervised Machine Learning (ML) [239]. Unsupervised learning is ML, with only data inputs. This means a numerical trend is automatically sought depending on the system itself, rather than a learned system which may involve a teacher.

K-means clustering is an analysis technique which connects data points into clusters on the basis of the data's characteristics. In a data-set, it seeks to partition n observations into k clusters. It assigns k cluster centres, known as centroids, then minimises the sum of the distance of the data points to its cluster centroid [240]. This is described by Fig. 7.2. It iteratively updates the distribution centroids in so doing. This is described by Fig. 7.2. The PythonTM scikit-learn package [240] was used to implement the K-means clustering within this chapter.

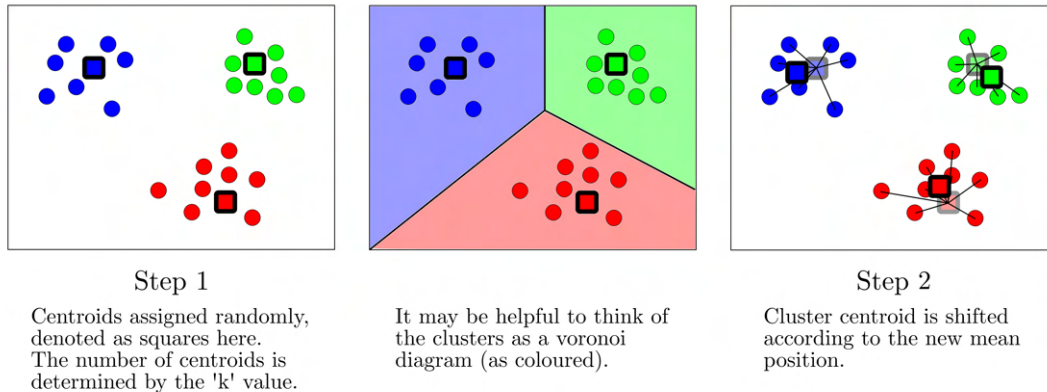


Figure 7.2: Example of the K-means clustering process.

Each colour can be defined by a Red Green Blue (RGB) additive colour model. Hence, every colour can be defined by an amount of red, green or blue. Within this research, colour images delivered by the camera are defined by pixels, with each pixel represented by an 8-bit RGB value. This means that each pixel has an associated intensity of red, green and blue in quantities of 0-255. These pixels can be reformatted and graphed as individual data points in 3D. From this, k-means cluster analysis can be used to determine clusters for each colour within the image.

Observations, n is inherent to the problem, as the data. However, choice of k must be determined carefully. Any human analysing the object image could rapidly determine the number of different colours present. However, computerised technologies cannot immediately reach this conclusion. Hence, an autonomous determination of k must be reached. This can be achieved by graphing the sum of squared distances from the centroid to the data points located in each cluster for a number of determinations of k . The point at which diminishing returns are identified can provide an accurate indication of k . A solution to identifying this is the Kneedle method, which is a heuristic approach used to identify the point at which diminishing returns are found on graphs, known as a knee [241]. The Kneedle algorithm in essence seeks to identify the minima/maxima of a curve if it was rotated about the line drawn between minimum value on the y axis and its maximum. Simply put, it is the point at which the curve begins to flatten. The 'kneed' toolkit available on PythonTM was used to estimate the knee, identifying the number of colours. An example of this method is given in Fig 7.3.

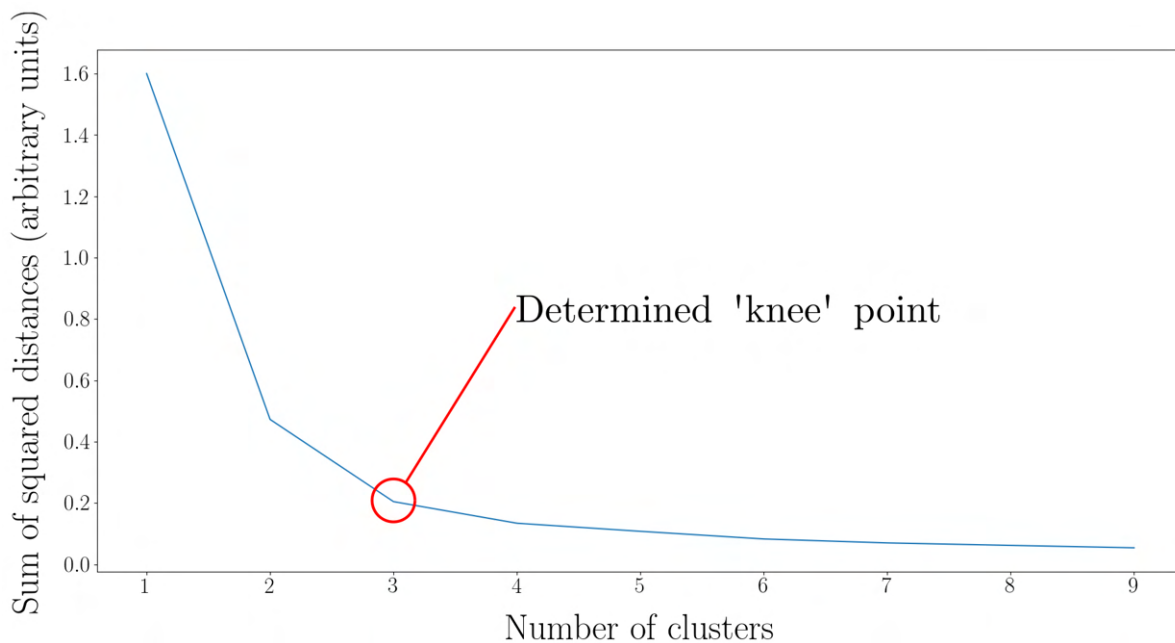


Figure 7.3: Demonstration of k-means clustering technique. Circled is the ‘knee’ identified by the knee method.

In nuclear waste scenarios, differentiation of objects on the basis of their colour is potentially very useful. Radioactive sources or containers are often coloured bright yellow, or have trefoil demarcations which are distinctly coloured, typically black and yellow. Equally, items of PPE are also distinctive in colour for example orange or white disposable over-suits and pale blue nitrile gloves. Automated object or item recognition could therefore usefully utilise colour differentiation as part of an integrated capability.

For use in this case, the method was set to identify a ‘knee’ point on convex and decreasing data curves. When the Kneedle method is applied to the k-means cluster analysis of the pixel RGB clusters, it can determine the number of different colours on the object. The pixel locations which correspond with the clusters representing distinct different colours can then be highlighted and automatically identified, as important scan locations. An example of this is shown in Fig. 7.4.

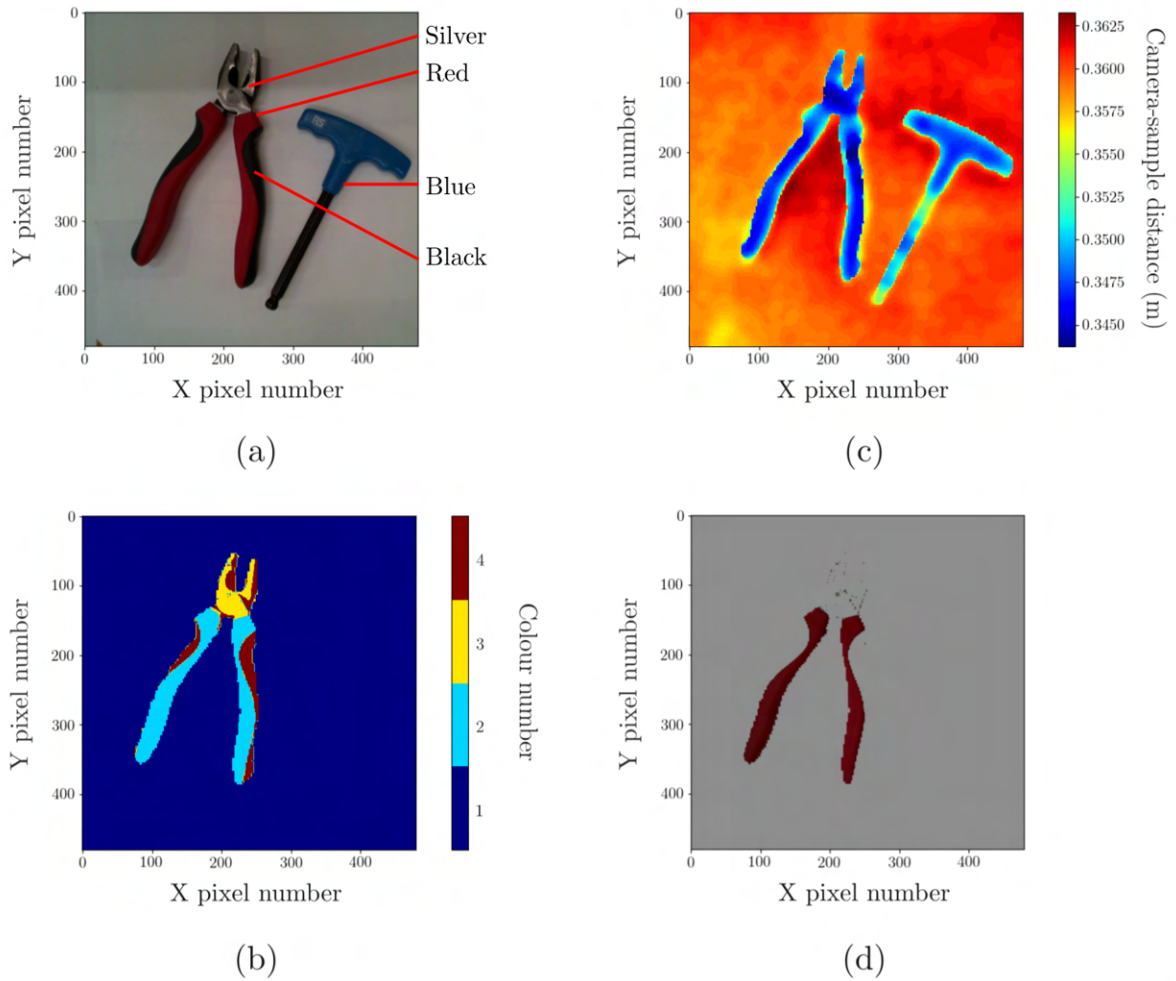


Figure 7.4: Colour identification of Raman scan locations. (a) shows the initial colour figure, (b) shows the identified colours using the methods outlined and their locations, (c) shows the depth camera image and (d) shows one cutdown colour representation.

7.2.3.3 Analysis Point Identification

Once the different colour locations have been identified within each object, analysis points must be identified for each. A second connected components algorithm was then applied, identifying each connected colour set. These were then area tested, with areas of less than 1500 pixels selected as scan regions.

A single analysis point was identified by each colour region using an erosion algorithm. The purpose of this was to reduce the regions to determine a position away from the edges of each colour identified as possible. This means that the laser targeting required to enable a Raman point measurement is less likely to inadvertently measure the wrong colour and hence, produce a

representative measurement. An example of a progressive erosion performed on a simple square plate is shown in Fig. 7.5.

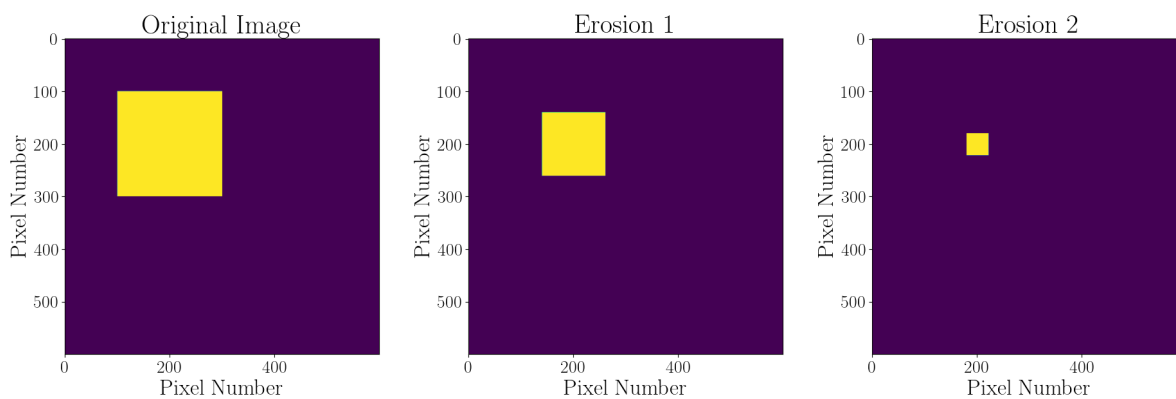


Figure 7.5: An example of progressive erosion of a square, illustrating how the algorithm reduces the surface area of shapes.

Each masked area was eroded iteratively using a 2x2 erosion matrix. Erosions were completed until the mask was removed. The previous masked image prior to removal was then recovered and a central pixel identified. This had the effect of progressively narrowing down a central measurement point

The programming for robotic positioning was completed using a very similar procedure to the XRF scanning demonstrated in chapter 6. However, since this component of research was completed later, minor improvements to the methodology were made to the system, improving the robustness of the programming. This included the implementation of the laser targeted affine transform methodology discussed in chapter 6. The affine transformation calibration used here can therefore take advantage of the inherent laser produced by the LRS system. Experimental findings from Chapter 6, section 6.3.2, indicate that performing a laser based affine calibration should provide an error of ± 2 mm positional accuracy. A sample of each colour can then be Raman analysed to provide an indication of the objects material properties.

7.2.3.4 Raman Focusing

The variance in the positional accuracy of the robotic arm system meant that the focal point of the Raman system at 3 cm may not be immediately attained by the robotic system. Therefore, the

system was programmed to approach the inspection location at a stand-off of 2 cm. This ensured the robotic arm would not crash, but also ensured the error would not exceed the 3 cm optimal stand-off. The arm was then programmed to move up in steps of 1 mm testing the spectra for a 0.1 second exposure. Signal intensity was then measured by comparing the maximal difference between low and high value signal. The position of maximum intensity was then returned to as the height for a Raman measurement. An optimal signal exposure time could then be calculated by calculating the time required to get the maximal signal to reach 10,000 counts. Figure 7.6, explains this process.

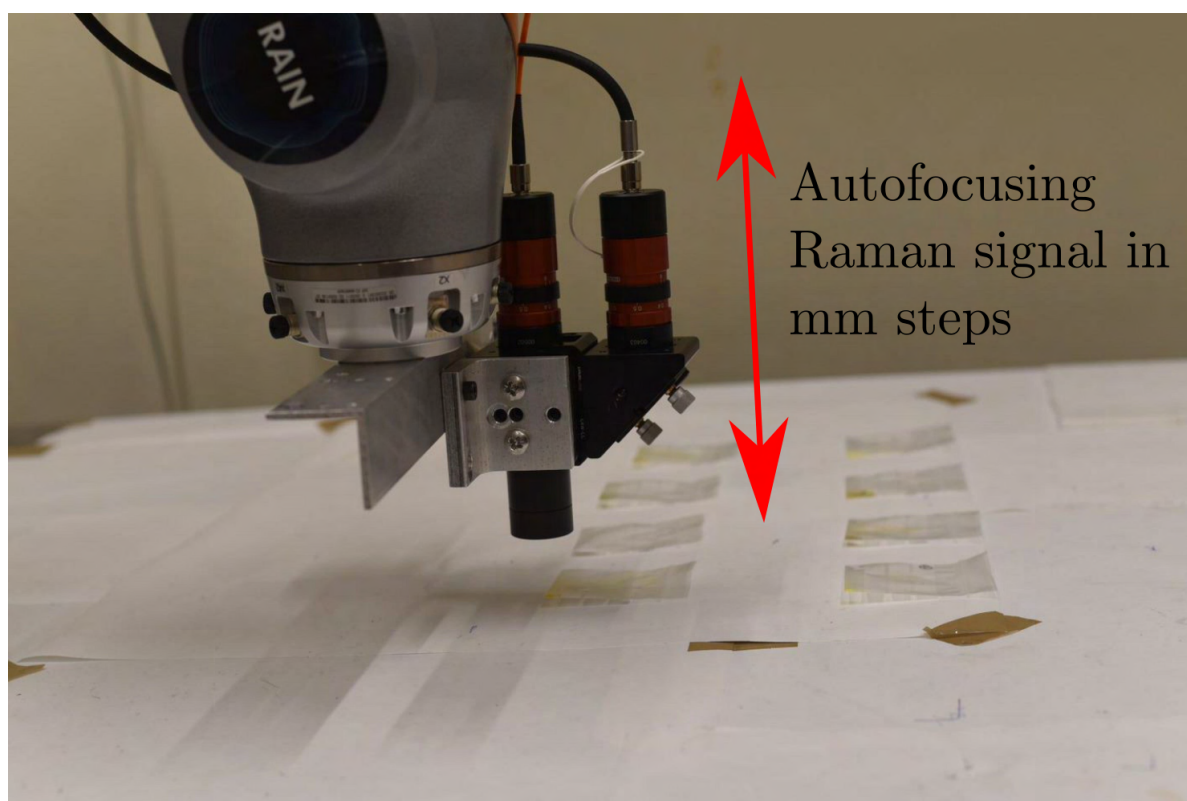


Figure 7.6: Raman auto-focusing system methodology in progress.

7.2.3.5 Autonomous filing system

Cataloguing the data produced from the developed system was complex. This was owing to the need to collect not just Raman spectra, but also to link each spectra to the appropriate position. Therefore, an autonomous filing system was used to collate the data appropriately. This system created folders for each object. It then created a folder for each shape. Inside each object folder, a masked photograph of the object was saved, showing the regional colours. Each colour had a folder, where the Raman spectra was contained. This is explained succinctly in Fig. 7.7

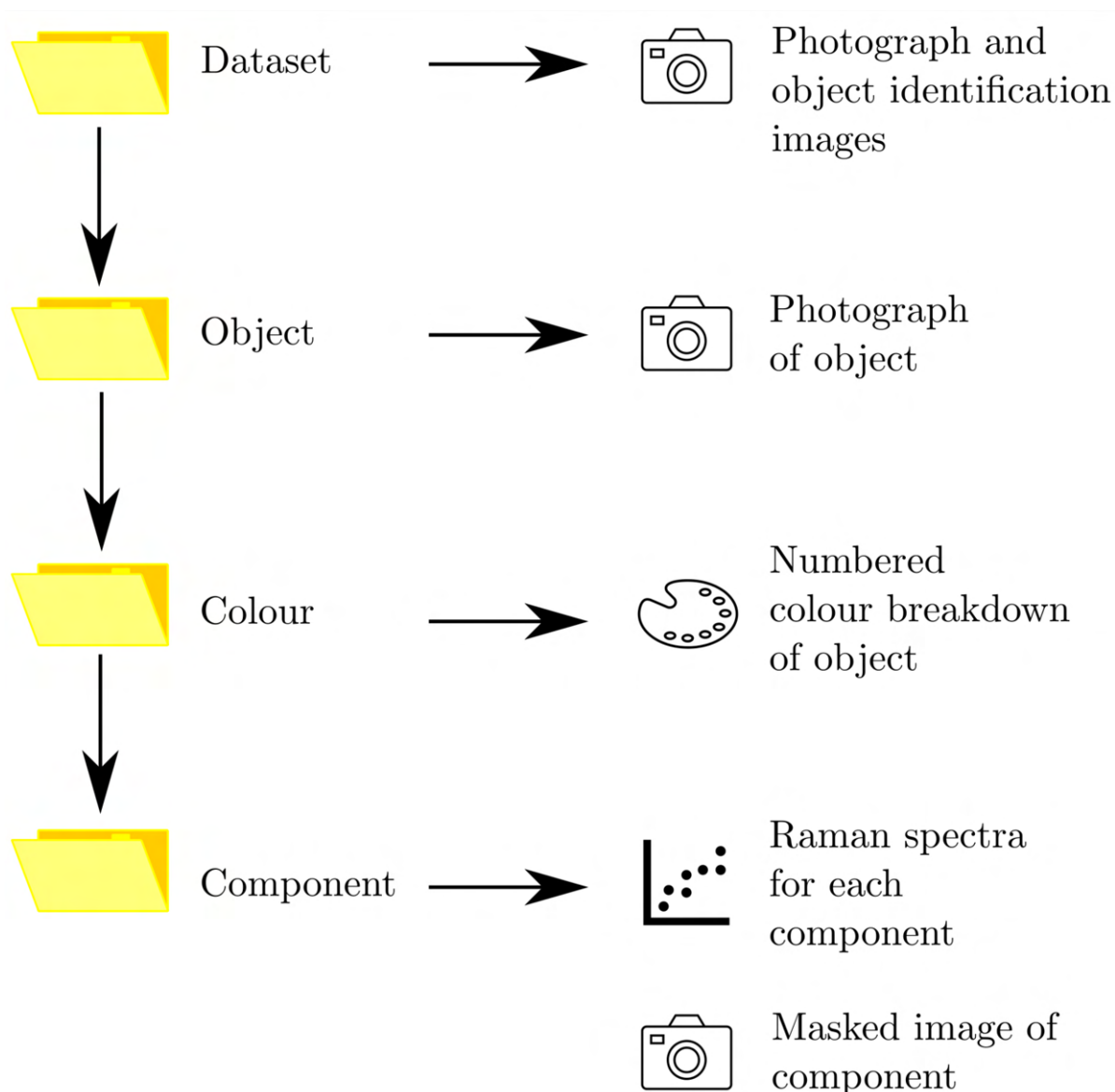


Figure 7.7: Autonomous filing system used to catalogue Raman data.

Such a filing system was used to catalogue the data appropriately, so it could be accessed as seamlessly as possible for future analysis.

7.2.3.6 Raman Database

To successfully identify Raman spectral data, a reference database of known Raman active materials must first be created. For this work, a database of the expected Raman signals was compiled, from each colour and object. In the example of the pliers, this entailed taking spectra for 'pliers red', for the red rubber, 'pliers black' for the black rubber and 'pliers metal', for the

tooling. It is noted that for a full sort and segregation system, a much larger database would be required.

This library could be used as a ‘lookup table’ for all analysed objects. A program was created to search through each database spectrum, fitting the experimentally collected data against the database spectra. The resultant output was a list of the ‘best fitted’ spectra, with a confidence interval applied. Fitting was achieved using Pearson’s product-moment correlation coefficients. This is a method for testing the goodness of fit of a straight line. Hence, the calibration spectra were plotted against the experimental spectra and tested with Pearson’s product-moment correlation coefficient. This is a technique commonly used for matching Raman spectra to experimentally collected data [242]. If the two spectra are identical, it will give rise to a perfectly straight line, giving a coefficient value of 1. Alternatively, if there is no match whatsoever, a value of 0 will be derived. Each experimental spectra was iteratively tested in this way with each calibration until a maximal product-moment correlation was identified. The result was returned as the best fit for each collected spectra.

7.2.3.7 Graphical User Interface

A Graphical User Interface (GUI) was designed for this project using the PySimpleGUI™ package [243] in Python™, to provide an immediate visual feedback during data collection. An example of this is shown in Figure 7.8. It included the original depth camera image, a masked image detailing the object under inspection, a mask of the region under inspection, and a collected Raman spectra. The Raman spectra could be set to display the live spectral data, or alternatively the most recently collected dataset.

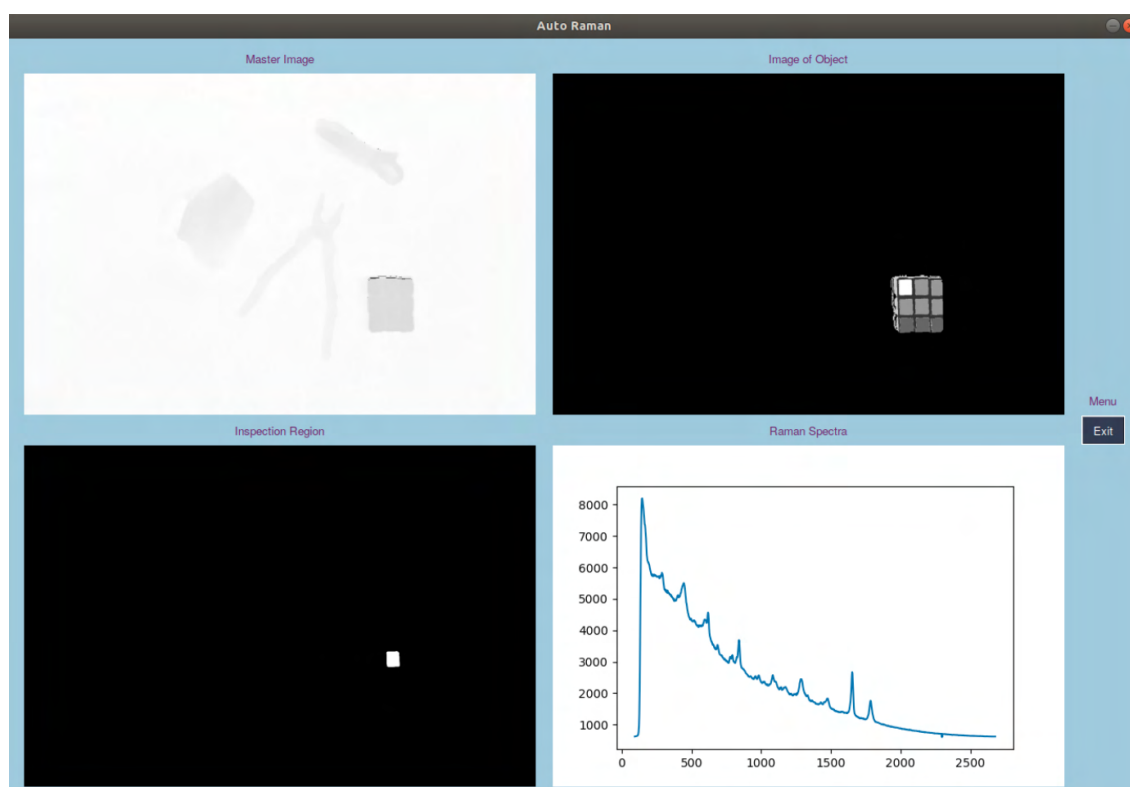


Figure 7.8: GUI developed for the robotic Raman system.

7.2.4 Experimental Setup

First, testing was completed using the naive, pre-programmed robotic system. The purpose of this testing was to demonstrate robotic stand-off Raman was possible. Second, the AI based vision scanning system was tested within a sorting and segregation relevant scenario. Following such a step-wise implementation allowed debugging and optimisation of the different progressive elements of the control, data capture and processing.

7.2.4.1 Proof of Concept Test Scenarios

To test the KR150 based system, shown in Figure 7.9, a collection of ‘mystery’ white powders were analysed. Each powder was placed carefully on a scan table, as shown in Figure 7.10. The nature of the work environment meant that background fluorescence from natural daylight was impossible to avoid, because of this a background correction was made to the Raman spectra.

The samples used were potassium fluoride KF, potassium chloride KCl, concrete, barium sulphate BaSO₄, iron oxide Fe₃O₄, caesium chloride CsCl, calcium carbonate CaCO₃, strontium hydroxide Sr(OH)₂, strontium fluoride SrF₂, magnesium hydroxide Mg(OH)₂ and ‘corroded magnesium

sludge'. These were provided to the University of Bristol from Sellafield Ltd, as nuclear relevant materials.



Figure 7.9: Stand-off Raman probe attached to KUKA KR150.

To test the system scientifically, the 11 samples were placed blindly at 11 locations pre-programmed into the KUKA, each with an attached letter between A and H, this is shown in Fig. 7.11. The robot then moved to each pre-defined position and saved a file including the spectrum of each given letter in each scanning methodology used. Each recorded spectrum was passed through the aforementioned data matching system which identified the source with a confidence rating applied, to provide a measure of how certain the system was that it had correctly identified the subject material.

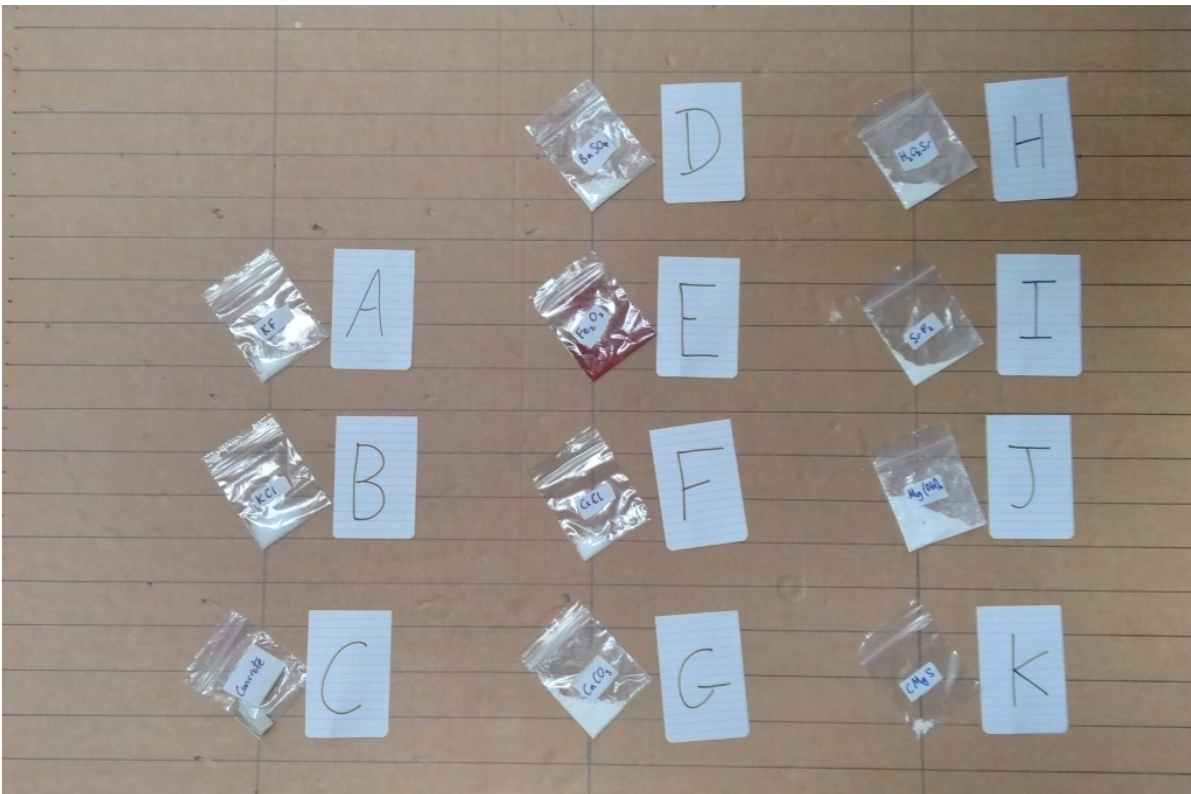


Figure 7.10: Experimental positioning of the 11 'mystery' powders.

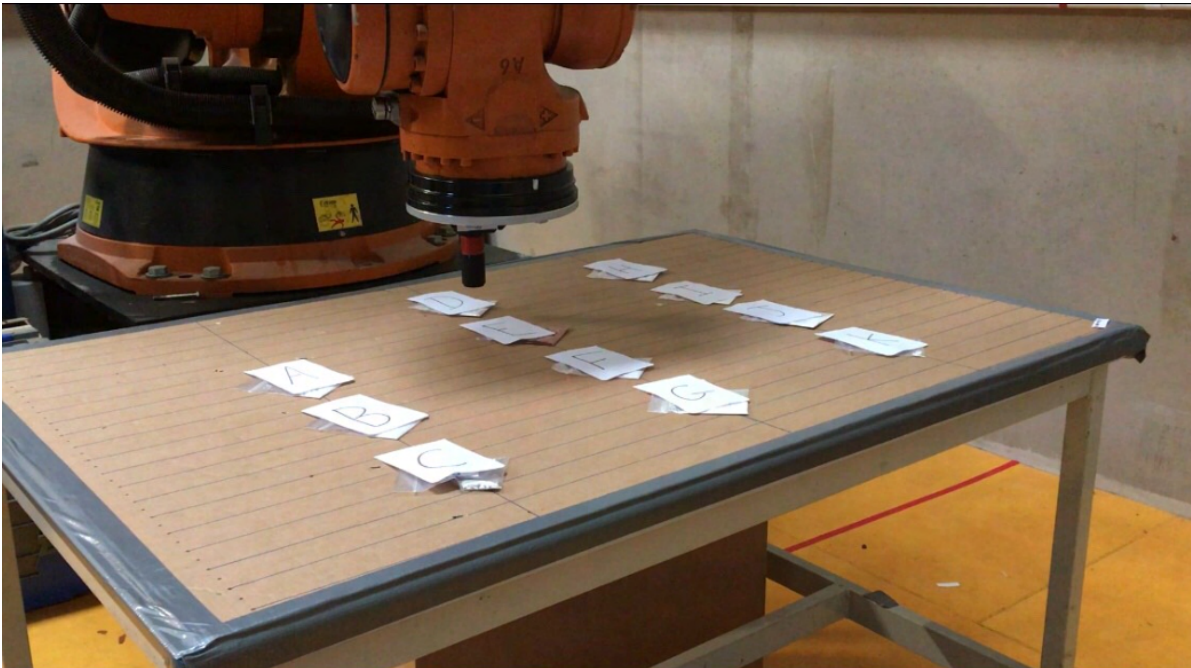


Figure 7.11: KUKA KR150 powder scanning in progress.

7.2.4.2 AI Based Scanning Scenarios

To test the AI based scanning system, a mix of Raman active and inactive materials was analysed. These included a nitrile glove, sheathed electrical wiring, pair of pliers and a Rubik's cube. The nitrile glove represented commonly identified safety equipment [11]. The sheathed electrical wiring was added to serve as a potentially contaminated decommissioning sample [11]. Pliers represented tooling which may contain mixed rubbers and metals [11]. Finally, a Rubik's cube was added primarily as a test for the colour identification system. In addition, it represented a plastic which may appear in sorting and segregation.

It is recognised that despite being noted as 'problem' waste articles, neither PVC, nor asbestos were tested. However, it is highlighted that PVC is a well known Raman active compound [244] and so is asbestos [235]. This means that if the technique is shown to work, it will undoubtedly identify PVC and asbestos within waste sorting activities.

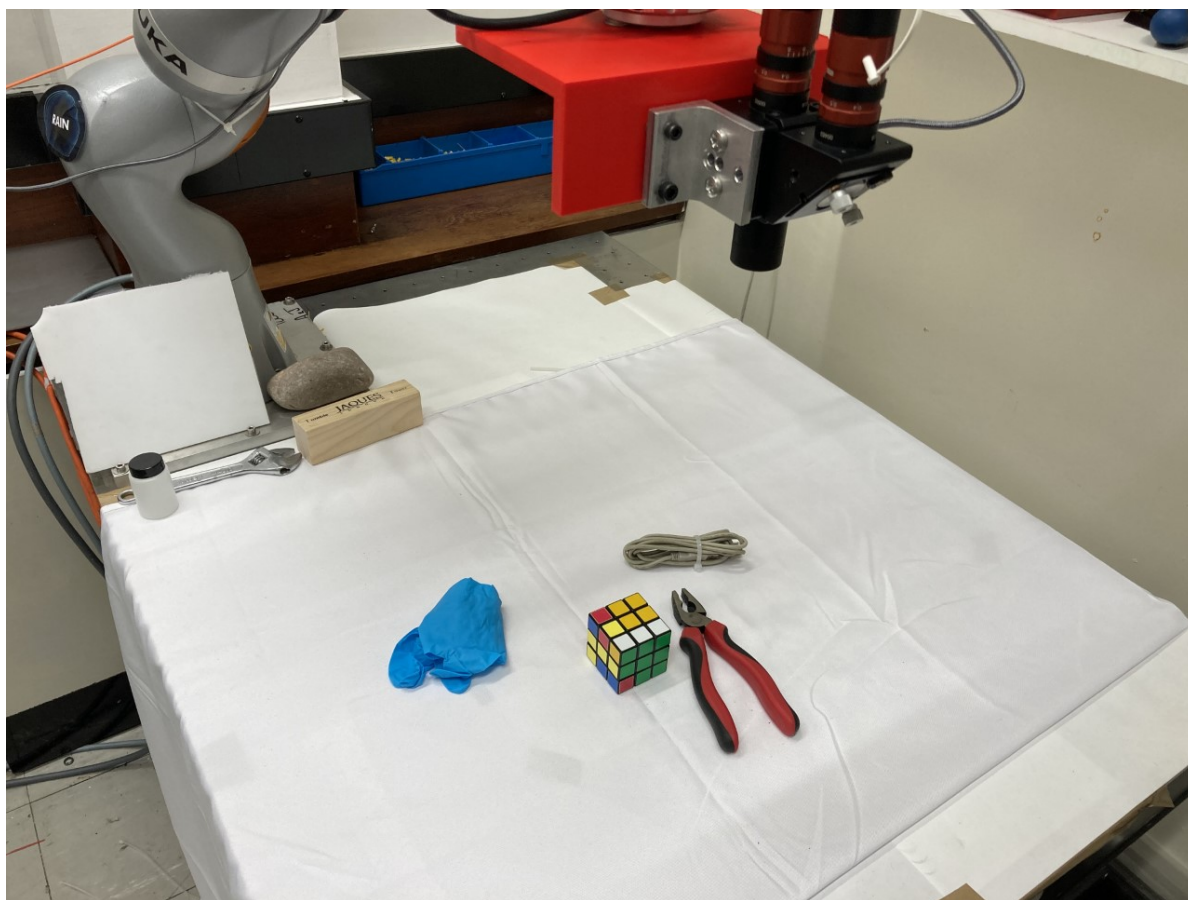


Figure 7.12: Setup of the sorting and segregation applicable test scenario. Shown are the nitrile glove, pliers, Rubik's cube and electrical wiring.

7.3 Results and Discussion

7.3.1 Proof of Concept Test Scenarios

Of the 11 powders tested, seven were recognised clearly, identified with very high confidence metrics, >99% confidence, one was accepted ‘tentatively’, due to low signal quality and three were rejected. Of the three that were rejected, all yielded a very weak Raman signal with a low signal to noise ratio. It is possible that with better alignment and focusing these could be improved. Figure 7.13, shows an example spectra from a concrete sample.

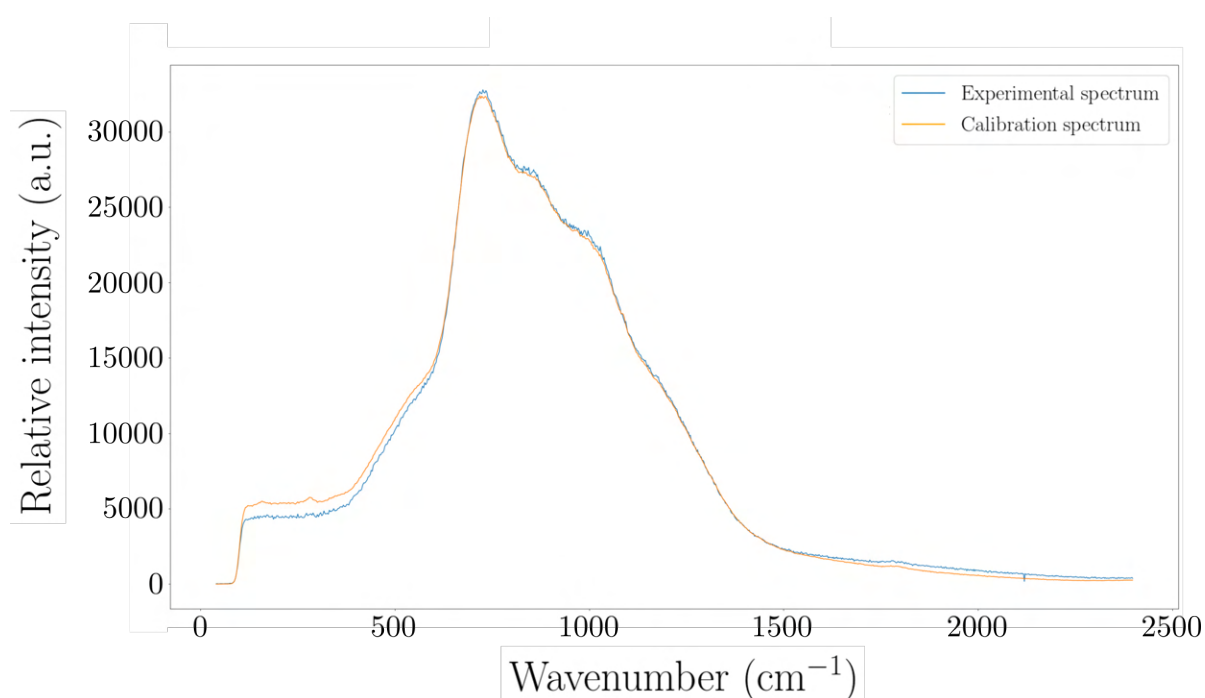


Figure 7.13: Experimental Raman spectra collected for the concrete sample, alongside the matched calibration spectra. 99.8% match determined.

This shows a very strong correlation to the reference concrete spectra, demonstrating concrete can be detected on a robotic Raman system. The spectra does not have distinct wavenumber peaks, as concrete is comprised of many phases, for example, quartz and calcite. Hence, the sample and reference is actually a composite of several spectra. Detection of concrete is important for sorting and segregation [11]. Concrete, like materials may become activated by leaching of contaminants such as Co-60, Cs-137 and Eu-152 [245]. Such compounds would be visible using radiation detector based techniques. However, active materials typically are in their highest concentration near the surface, naturally reducing in concentration with depth. This means in the decontamination processes, active materials can be removed. Thus identifying concrete as part of a mixed waste may help determine appropriate decontamination and subsequent volume

reduction methods [246].

Figure 7.14, shows the tentative acceptance of a Raman spectra of iron oxide.

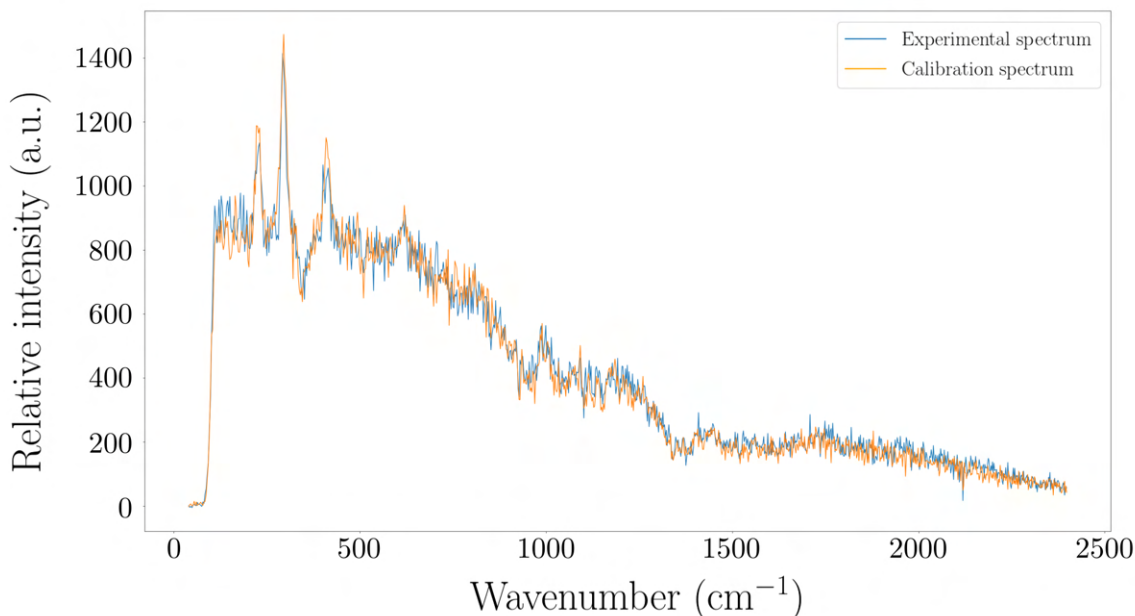


Figure 7.14: Experimental Raman spectra collected for the iron oxide sample, alongside the matched calibration spectra. 97.6% match determined.

Evidently, a close match is identified between the Raman signals. However, there is significant noise on the signal resulting in a tentative acceptance. This spectra has been included to demonstrate the limitations of the LRS scanning system. Iron Oxide is an example of a compound which could be confirmed via XRF scanning, as Iron is very XRF active. However, in waste sorting scenarios, it is necessary to be able to determine with any iron what type of steel or alloy it is present within. For example, to determine if it is present as stainless or mild steel. This could be determined by using Raman to search for the presence of iron oxides. Iron oxides phases are usually only moderate to weakly Raman active, but as demonstrated the signal is typically statistically strong enough to determine whether certain types of oxides are present or not. For mild steel, which is corrosion susceptible, the surface would likely have a coating of iron oxide phases such as magnetite and haematite, which are common iron oxide phases [247]. By comparison, stainless steel forms a very thin protective oxide consisting of chromium oxide and magnetite, but is almost always too thin to be Raman active, unless using a very high powered instrument [248]. Raman spectroscopy is blind to the presence of metal and hence it could potentially be useful in confirming whether a metal is heavily corroded or not - the measurable presence of oxide being a key indicator of notable corrosion. This supports the concept of XRF and LRS as being used

coincidentally as complementary methodologies for sorting and segregating nuclear wastes.

Figure 7.15, shows the spectra recorded for the CsCl powder which was used.

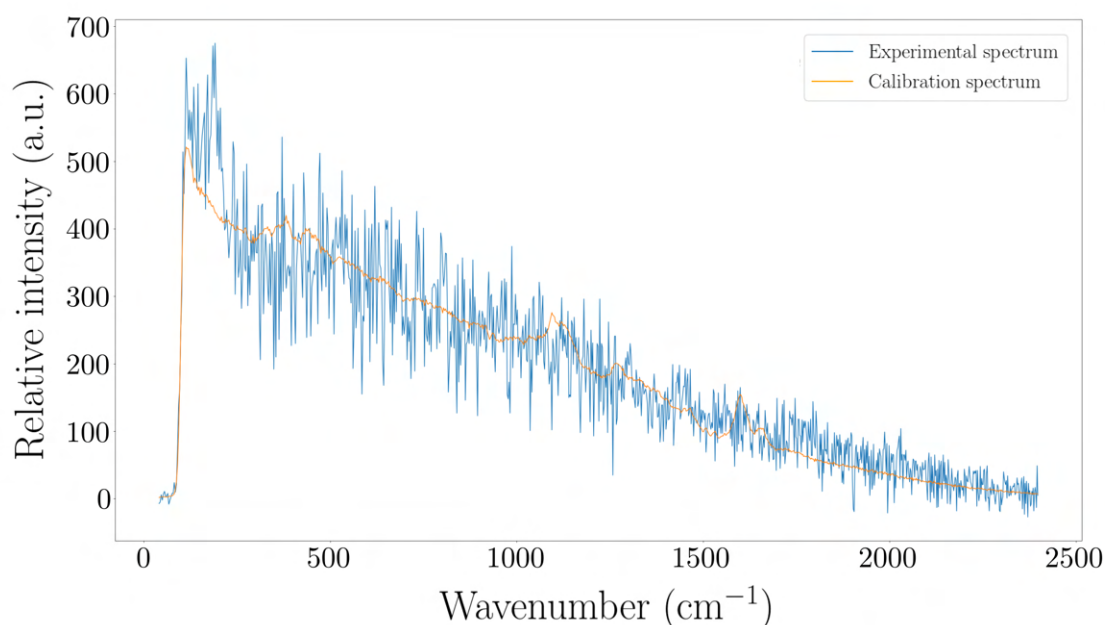


Figure 7.15: Experimental Raman spectra collected for the CsCl sample, alongside the matched calibration spectra. 86.9% match determined.

No clear spectral fit can be made here, however, literature suggests CsCl should be Raman active [249]. CsCl was very accurately assayed by the XRF system in Chapter 6. Hence, a complete system could identify a failed Raman measurement and attempt an XRF scan instead. This further illustrates how the two systems could be designed as complementary material characterisation systems.

7.3.2 Sorting and Segregation Scenarios

This initial research demonstrated the capability of a stand-off LRS system operating on a robotic system. Next the methodology could be deployed with confidence as part of the fully-automated sorting and segregation applicable system.

The initial camera pose photograph taken can be seen, as photographed in Figure 7.16.

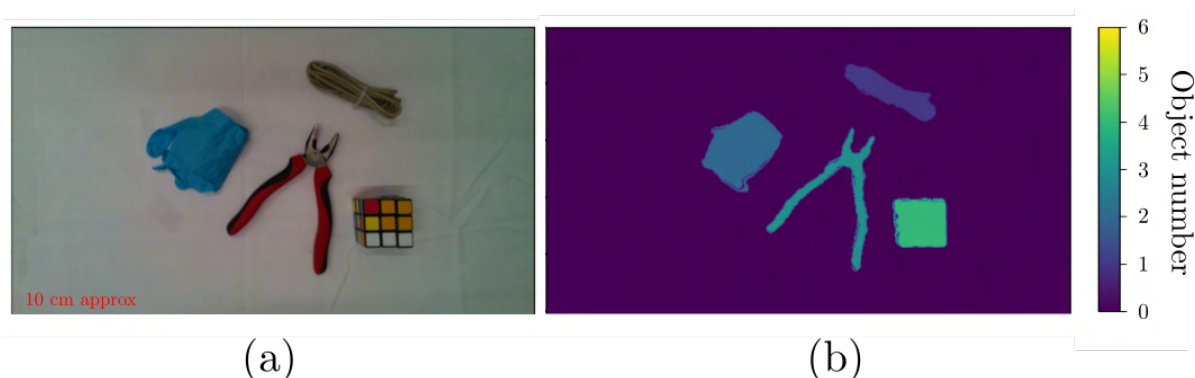


Figure 7.16: (a) shows a colour photograph taken by the robotic system. (b) shows the objects identified by the system.

Curiously, the system identified two additional objects to the four placed objects that were present. In the files containing the masked images, no image was present. It is suspected that some very small (<10 pixel) objects were identified as connected components and thus not visible to the human eye.

Having collected this initial image, the system was then able to autonomously step through each object, colour and region of interest component. It successfully collected Raman spectra and masked images and saved them to the relevant folders as per the filing system discussed in section 7.2.3.5. The whole test was completed in approximately 20 minutes.

7.3.2.1 Wires

The first object the system visited was the bundle of wires. In terms of colour, it identified two colours. Evidently, there should only have been one. However, the two identified colour regions most likely corresponded to the black grey shaded sections and the lighter grey sections of the wire sheathing that were directly illuminated by the lights in the laboratory. Visiting both inspection locations, it recognised the plastic of the wires with 99.7-99.9% certainty. One such spectra can be seen in Figure 7.17.

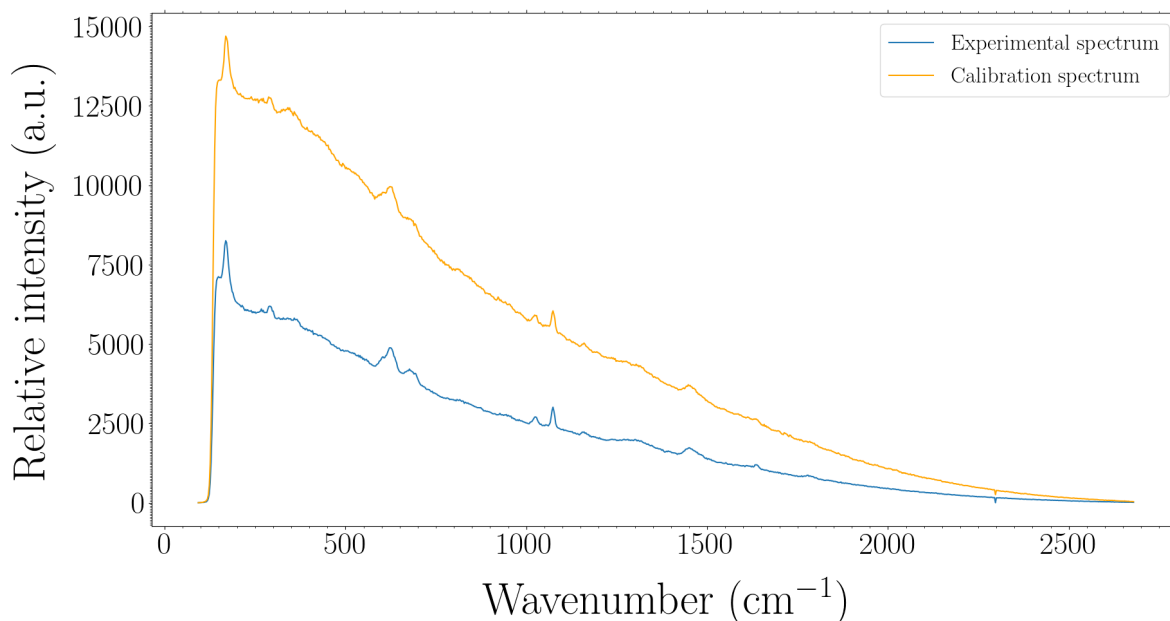


Figure 7.17: Experimental Raman spectra collected for the electrical cabling, alongside the matched calibration spectra. 99.67% match determined.

It is evident from Figure 7.17 that the two spectra record similar peaks. Different intensities and spectral backgrounds were recorded. However, the fitting still identified the peaks correctly. This is a powerful result, as it suggests a capability to fit spectra when peak intensities and background shapes are varied. It should be noted on the left hand side of each recorded spectra there is no light received. A filter is added to a stand-off Raman system which means that light at 830 nm is blocked on the return to the spectrometer. This is due to the fact that most light is not Raman shifted. The lens is not perfect, so a range of approximately 825-835 nm [238] is removed. This results in no light being recorded in this region, which is a small technical limitation. However, it is not of major importance, as vibrational peaks within this range are not crucial for analysis.

7.3.2.2 Nitrile Glove

On the nitrile gloves, the system identified 4 different colours, when it is evident that there should only be one. Looking at the photograph of the glove, it is possible that given the K-means clustering tests for 6 different colour clusters, the algorithm mistakenly identified different shading patterns across the glove. In any event, for a sorting and segregation scenario, more data is preferable, to ensure an accurate characterisation. Each spectra was confirmed to be the glove material with certainties of above 99.9%. An example spectra is shown in Figure 7.18.

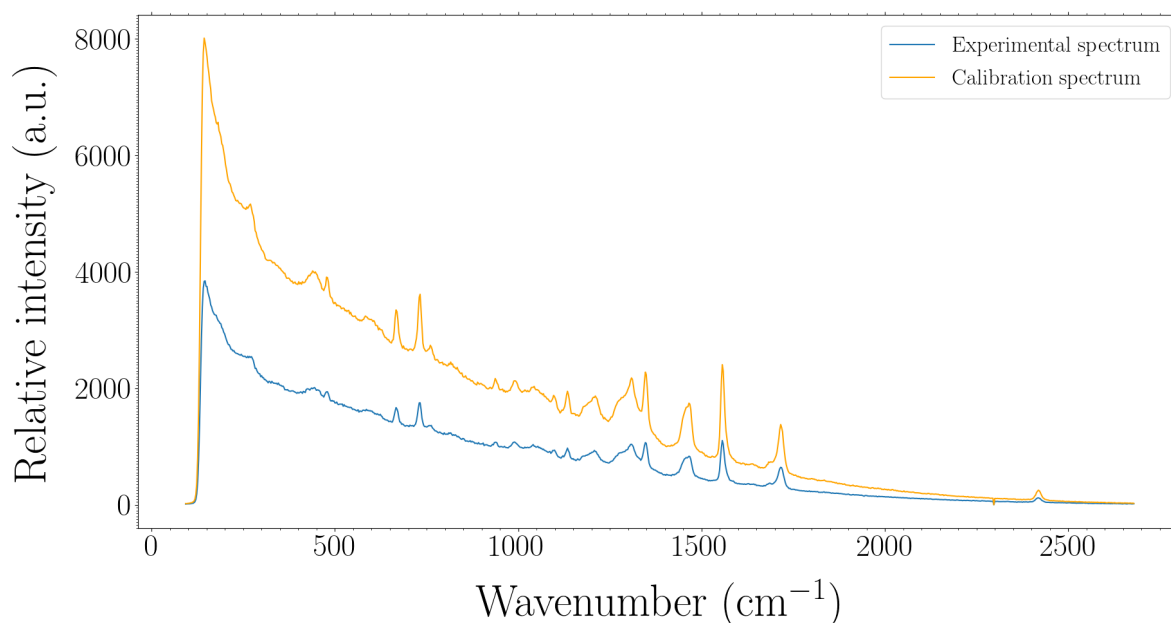


Figure 7.18: Experimental Raman spectra collected for the nitrile gloves, alongside the matched calibration spectra. 99.97% match determined.

It is visually clear from Figure 7.18 that the calibration spectrum is a close match to the experimentally collected spectrum.

7.3.2.3 Rubik's Cube

The Rubik's cube yielded some interesting results. It successfully identified all the squares and the central black dividing plastic. Unfortunately, it could not distinguish the yellow square from the four orange squares. However, it is probable a human may struggle with this identification, due to sun bleaching and discoloration of the orange. The Raman spectra showed good results generally, with the majority of scan locations identifying at least the Rubik's cube plastic. The two exceptions to this were the red square which did not collect a recognisable spectra, thus identifying the 'pliers metal'. The other was a Rubik's cube side which was detected through parallax on the camera, which identified the 'wires'. Additionally, there was a measurement taken within the black cube spacing which identified the 'yellow square', likely due to positioning inaccuracy at targeting the black cube spacing. While there was not much difference in spectral peaks for the individual colouration's, most were identifiable. Of the five orange squares that were identified, four were correct. The system matched the yellow as orange too. In addition, the three white squares were correctly identified. An example of one of the orange squares is given in Figure 7.19.

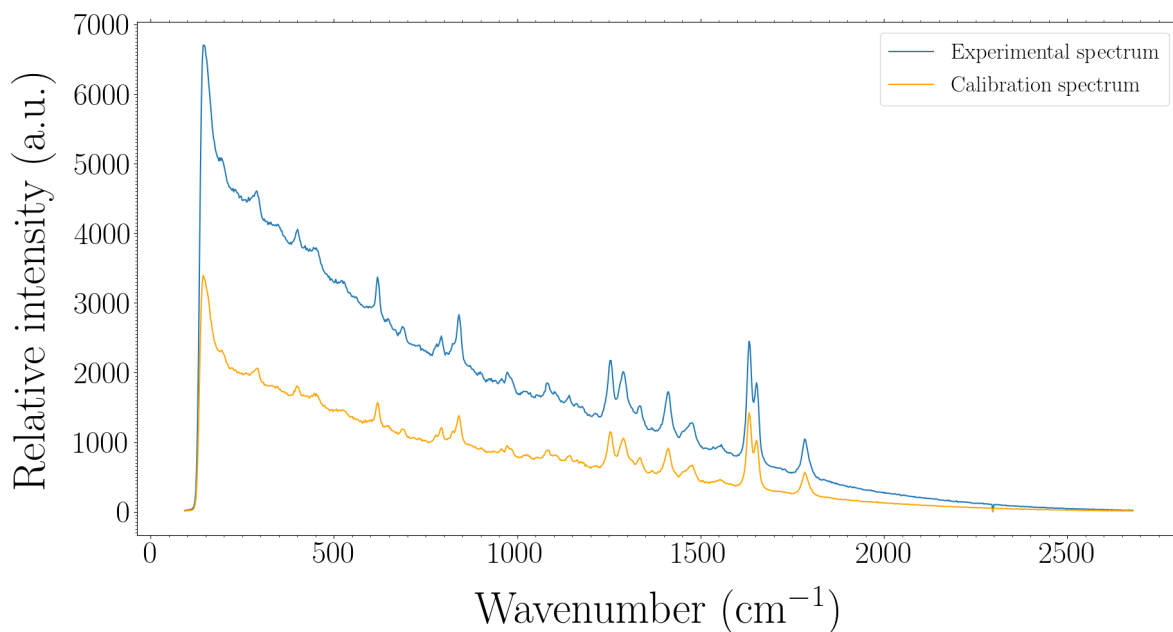


Figure 7.19: Experimental Raman spectra collected for an orange rubics cube piece alongside the matched calibration spectra. 99.05% match determined.

7.3.2.4 Pliers

The pliers represented an interesting dataset. All measurements located were in good agreement with reference data. However, this should be analysed with some caution, as only the red on the rubber was Raman active. Figure 7.20 shows the result from the red rubber, the calibration data clearly matches the experimental data.

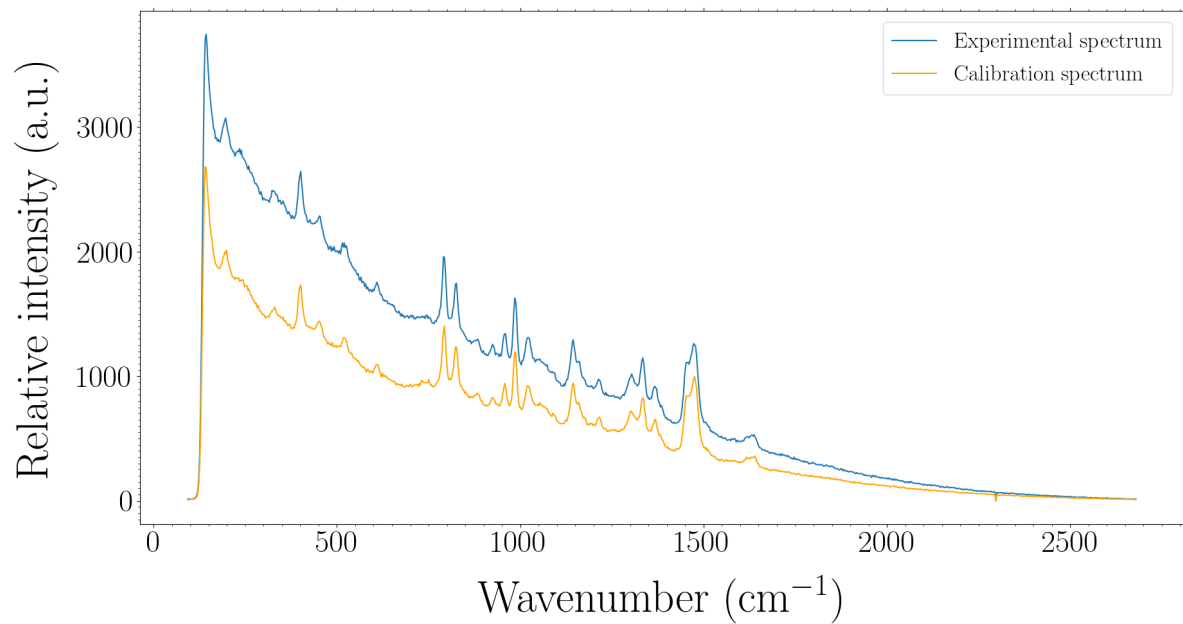


Figure 7.20: Experimental Raman spectra collected for the red rubber on the pliers, alongside the matched calibration spectra. 99.71% match determined.

While the components of the black rubber and the metal on the pliers are also identified to a similar level of accuracy, both are Raman inactive. This means that while the inactive signal has correctly detected the similarities on spectral shape, it has not done so through accurate peak recognition. Figure 7.21 shows the calibration and experimental data for the black rubber on the pliers. Figure 7.22 shows the calibration and experimental data for the metal on the pliers.

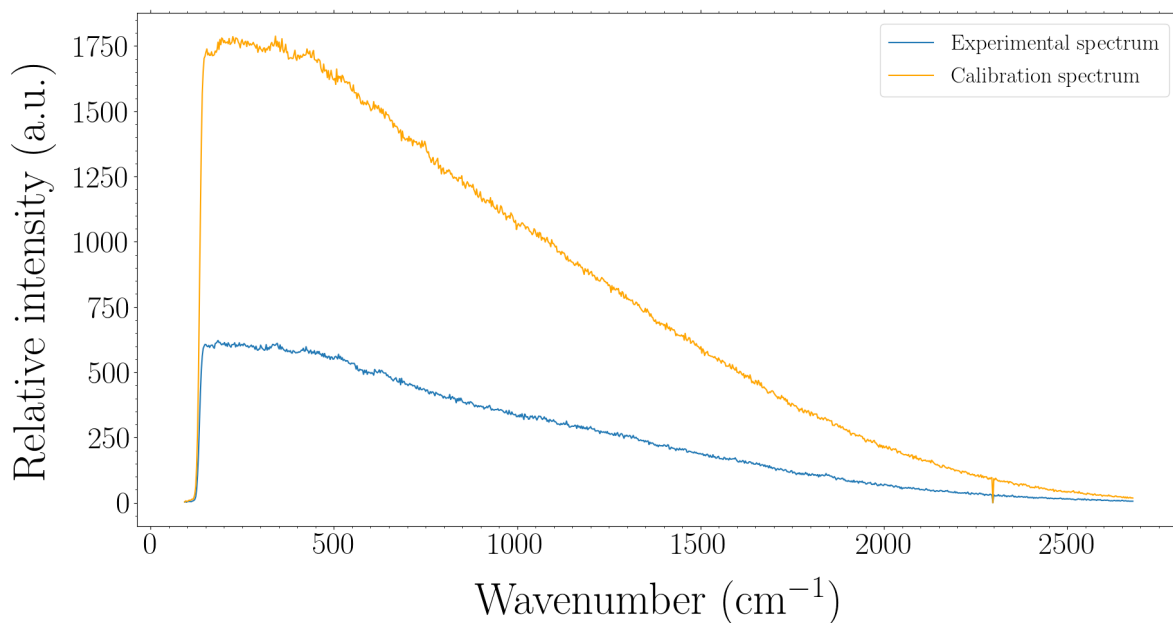


Figure 7.21: Experimental Raman spectra collected for the black rubber on the pliers, alongside the matched calibration spectra. 99.84% match determined.

The metal on the pliers was identified, as shown in Figure 7.22. However, evidently the metal in the pliers is not Raman active, so therefore should be treated as a null result.

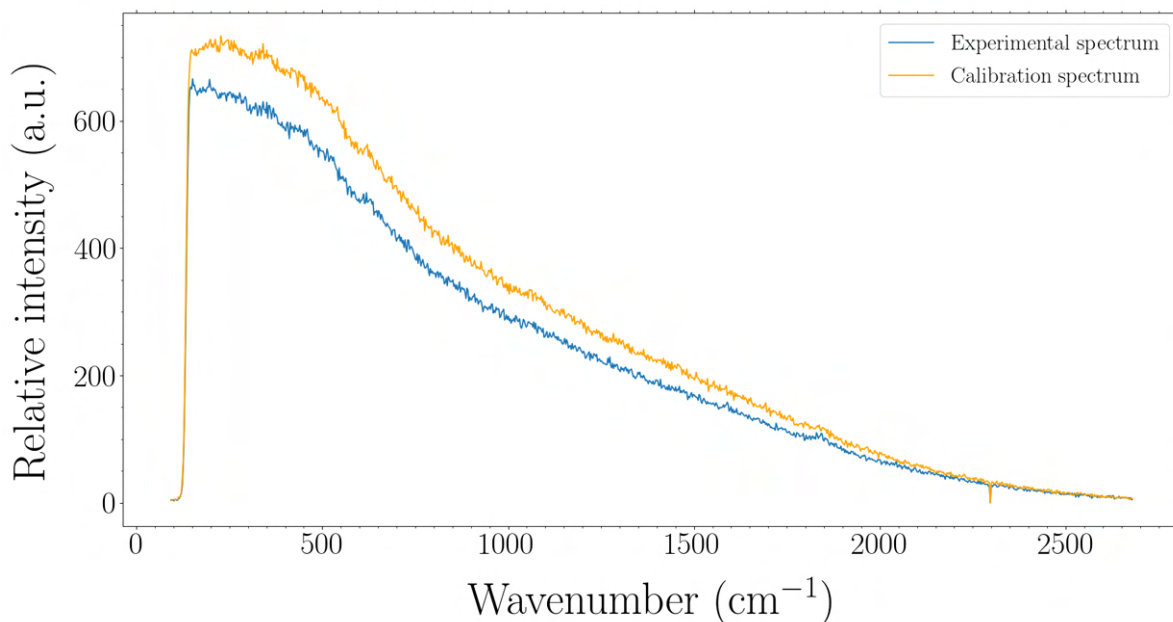


Figure 7.22: Experimental Raman spectra collected for the nitrile gloves, alongside the matched calibration spectra. 99.91% match determined.

Caution should be exercised with this, as the metal on the pliers is a Raman inactive material. Such materials should not be added to the catalogue of Raman spectra for an active waste sorting implementation of this work, as they cannot be used to accurately identify components. In this example, it works, simply owing to the fact it is the only non-active material in the database. A background removal technique could be used to remove this issue. The result of this would be no fluorescence in the background of each spectrum. Hence, all non-Raman active samples would simply produce a flat line, to which they could be matched to a confirmed null result.

Future work may seek to integrate embedded ML into the spectral identification. This may begin with an operator making manual assessments, while the system may be trained to provide autonomous detection. Eventually, the training model may be applied and used to identify materials fully-autonomously. Such assessments may be trained alongside object recognition algorithms, that may seek to identify components arising in nuclear waste, such as nitrile gloves or electrical cabling purely on the basis of visual inspection using a neural network approach [250]. This could further improve the accuracy of the systems judgement. For example if there was a glove covered in $\text{Sr}(\text{OH})_2$, the visual inspection would recognise the glove and the Raman the $\text{Sr}(\text{OH})_2$. In this way, the object may be recorded as containing both nitrile and $\text{Sr}(\text{OH})_2$, which may be missed if the camera recognition or the Raman approach was used independently.

7.4 Conclusion

In conclusion, robotically deployed stand-off Raman spectroscopy has been demonstrated to offer a powerful in-situ solution to material characterisation within nuclear waste sorting and segregation applications. An initial proof-of-concept test scenario demonstrated a capability to autonomously identify a collection of Raman active samples in a blind test. Seven out of 11 were successfully identified, with one tentatively accepted owing to a low signal to noise ratio and three further materials assigned as unidentifiable, because they did not yield a Raman signal.

Next, a more advanced system was created, integrating machine vision, Artificial Intelligence (AI) and Machine Learning (ML) techniques. The system was shown to be capable of identifying objects within a scan, autonomously identifying colours and intelligently navigating to and recording Raman spectra at regions of interest. Processing was achieved instantaneously and the identified Raman scan locations enabled high quality Raman characterisations to be accomplished in a timely manner without sacrificing accuracy. A sort and segregation relevant test scenario was setup and results showed good agreement with calibration data, with all Raman active materials successfully identified. Raman inactive samples were also identified, however, this should be taken with caution, as the matching was achieved through receiving a similar null result.

The developed system and methodologies represent a powerful additional piece of the nuclear inspection toolkit. While the individual components of this work are not in themselves novel, their integration and use as part of a sensory inspection system has not been previously reported. As alluded to in Chapter 6, XRF and Raman will prove to be powerful complementary techniques for in-situ materials characterisation. Enhanced delivery mechanisms and AI toolkits such as the one developed within this chapter offer a step change in robotic sensor capabilities, reducing scan times and increasing useful data collection.

CONFIRMATORY CLASSIFICATION TECHNIQUES

The previous chapters identified techniques which may be used to classify waste objects in-situ, while they remain on a sorting table or scan surface. Such techniques provide comprehensive overviews of the radiometric and material qualities of waste. However, when objects are analysed on sorting tables, components may be obscured or covered, leading to measurement errors. This poses a particular problem when performing radiometric analysis, as the gamma-photon radiation count may be altered, due to attenuation and scatter resulting in an inaccurate activity calculation. In addition, adjacent radiation emitters were noted to skew the radiation measurement, inadvertently increasing the detected gamma-photons. Hence, it is prudent to perform a confirmatory classification after grasping. Currently, radiometric evaluations are made by measuring large volumes of waste. This leads to significant error in waste classification, as inactive objects may be placed in containment with highly active ones. This chapter offers an improvement to this problem by isolating objects by picking them up individually and moving them in front of a detector, away from other sources of radiation. In combination with this radiometric measurement, objects will be analysed with a 3D stereo vision camera to make a rough assessment of the 3D shape of the object. This can then be combined with a monte-carlo simulation technique to make an accurate estimation of the activity - exceeding that of any currently available system. Therefore, objects may be more accurately classified, with a reduction in error introduced by adjacent sources or gamma-photon scattering effects. To fulfil the waste sorting requirements, the mass of the object must also be ascertained; as per the radioactive waste classification guidelines. Alluded to in chapter 2, this can be achieved in-situ using in-built force torque sensing capabilities of the KUKA LBR robotic manipulators. In this way, the measured torque on the robotic manipulator may be used to make accurate mass

measurements, in-situ and without the need for ‘double handling’¹ of objects which may result in the contamination of weigh scales. This chapter seeks to describe and investigate both the in-situ activity calculation and in-situ weighing algorithms.

The following chapter is based on the methods, results and discussion presented within the following previously published, peer-reviewed articles:

S.R. White, D.A. Megson-Smith, S. Kaluvan and T.B. Scott, “Demonstration of a Prototype Autonomous Sort and Segregation System”, Waste Management Symposia, 2021.

S.R. White, D.T. Connor, D.A. Megson-Smith, S Kaluvan and T.B. Scott, “A Radiometric Classification Technique for Nuclear Waste Objects”, Waste Management Symposia, 2022.

8.1 Introduction

The key to defining the correct classification of a waste object relies upon establishing (by measurement) an activity in terms of becquerels (Bq) being calculated. Chapter 3 demonstrated the use of robotic manipulators, combined with attached sensing systems, for identifying the location of radioactive sources. It was found that coincident radiation from adjacent sources contributed to the radioactivity recorded at any given measurement location, causing a skewing of results. Chapter 5, offered an improvement to this, by improving the positional localisation of radioactive sources with the application of the PLR algorithm. However, whilst the recovered ‘solution’ radiation signal accurately identified the source location, it was unable to accurately recover the activity or CPS of the emitter within the solution space. This was a result of the current inability to ray-trace individual gamma-photons from sources and consequently quantify the energy of each incident gamma-photon. Therefore, radiometric analysis could not be completed, as full spectral information for individual sources cannot be recovered. Ultimately, this means that an estimation of an objects activity in Bq, would be inaccurate.

One solution to this problem is the application of post-grasp radiometric scanning. Post-grasp scanning may be defined as the process of presenting the grasped objects to a fixed sensor suite, located away from the waste table in a shielded location. This enables the object to be oriented directly in front of a sensor to collect confirmatory data as comprehensively as possible. Radiometrically, this step is crucial, as the distance from the sensor suite to the waste table should be sufficiently large that any coincident radiation from the sorting surface should not influence the measurement. Hence, the grasped object will be able to be scanned in isolation, away from other

¹Double handling refers to approaches which require grasping, followed by the release placement and subsequent re-grasping.

radioactive emitters. This means that the object may be more accurately characterised in terms of radioisotope and activity.

Calculation of activity in Bq is a non-trivial process. Detector systems typically return radioactivity measurements in counts per second (CPS) readouts. This is the number of gamma-photons recorded as measured by the detector. However, this CPS readout does not directly correlate to the activity in Bq. Converting from CPS to activity in Bq, is an involved process which demands detailed understanding of several scenario and detector specific quantities. Included is the dead-time correction, the energy dependent intrinsic efficiency and the sample-detector geometrical efficiency. Using a well calibrated radiation detector and correcting for all these factors, the activity of the sample may be calculated. A detector's intrinsic efficiency and dead-time may be qualified by well documented laboratory analysis approaches. Geometric efficiencies are more challenging to determine; owing to the random shapes and dimensions of objects that may appear in sorting and segregation. This chapter attempts to resolve the issue of geometric efficiency by applying a depth camera feedback technique to resolve the geometric efficiency more accurately. Using these detector quantities, the activity of the waste object in Bq may be determined.

In addition to determining activity in Bq, waste sorting guidance mandates the measurement of the mass of each object. A few techniques are possible for waste article mass determination. The most obvious approach is to use weighing scales to make a mass assessment; classically this would be achieved with a weigh scale. Weigh scales could be implemented in a few different ways. The first is underneath the waste table, with measurements made from the mass difference once each article is removed. This technique would be sensible to implement, but additional verification may be required in-case components become stuck or part of the collected object is unintentionally dropped. The second is a weigh scales in which the robot places the object onto, takes a measurement, then collects the object. However, introducing the second technique would require a 'double handling' approach. This would introduce additional challenges, as the robot would be required to place the object on the scales and then re-grasp the object, which introduces unnecessary complexity. Thirdly, a scales underneath the destination waste containment could be implemented. This should be implemented to determine the total weight of the waste container. However, if the object is weighed at this end stage, it could be difficult to extract if waste class determination made is incorrect. Therefore, weighing at this stage will be important for waste documentation purposes, but not useful for determining waste classification. A potential solution to these problems is the use of the force-torque sensors integrated into the KUKA LBR; an algorithmic development could make a mass measurement in-situ. Such a technique would negate any double handling requirements, reduce inadvertent cross contamination and involve technology inherent to the waste sorting process.

This chapter is divided into 2 halves, the first covers autonomous activity determination, and the second, the in-situ robotic mass article determination algorithm.

8.2 Activity determination

8.2.1 Activity determination methods

8.2.1.1 System Setup

An autonomous process was designed, to facilitate the robotic grasping and object manipulation required for waste article inspection. This centered around a KUKA LBR MED robotic manipulator [99]. A Kromek™ Sigma-50 [134], CsI(Tl) based scintillator detector was selected to generate the radiometric data, upon which the activity of the sample could be calculated. An Intel® RealSense™ D435 [101], depth sensing camera was used to generate a volumetric reconstruction of each object, required for determining the geometric efficiency. Using the collected spectra, in combination with the depth sensor feedback, the activity of the object could then be estimated. A photograph of the complete setup is shown in Fig 8.1.

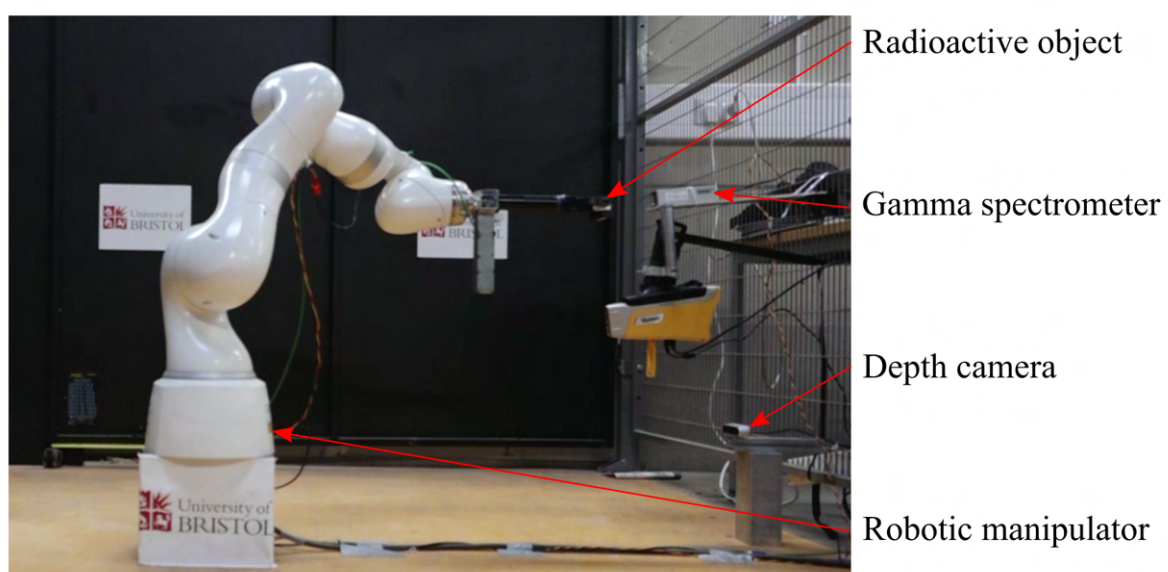


Figure 8.1: Diagrammatic representation of the geometric response of a radiation detector.

8.2.1.2 Dead time correction

When a radiation spectrometer processes a gamma-photon, there is a period of time, known as the dead time, for which the detector cannot process a new measurement. Equation 8.1, defines dead time mathematically. .

$$(8.1) \quad N = \frac{n}{1-t}$$

where N is the corrected counts in 1 second, n is the recorded counts and t is the dead time. This dead time may be determined in software for most detection systems available off the shelf. However, it is possible to determine it experimentally. The Kromek™ Sigma-50 reports a dead time of 58 μs [134], hence this will be the value used for this experimental work. Typically, dead time is in the range 5-100 μs for a single pulse.

8.2.1.3 Geometric Efficiency

The isotropic emission of radiation from active emitters means that only some of the gamma-photons released will reach the detector. Therefore, the geometric efficiency of a detector may be defined as the ratio of gamma-photon emissions which are emitted in an appropriate direction, such that they reach the detector. Mathematically, this means the percentage of gamma-photons which are emitted within the solid angle subtended by the source and the detector. The mechanics of geometric efficiency may be explained by Figure 8.2, showing a simple case of a point source emitter. The equation for determining geometric efficiency is given by Eq. 8.2.

$$(8.2) \quad \epsilon_g = \frac{\Omega}{4\pi}$$

Where ϵ_g is the geometric efficiency and Ω is the solid angle subtended between the emitter and the detector. For emitter shapes of complex volume, the solid angle may become difficult to ascertain. Hence, Monte Carlo (MC) simulation approaches can be used to estimate geometric efficiencies using volumes of point emitters and random simulated gamma-photon emissions [251]. The percentage which reach a detection volume in the simulated setup may define the geometric efficiency of the setup.

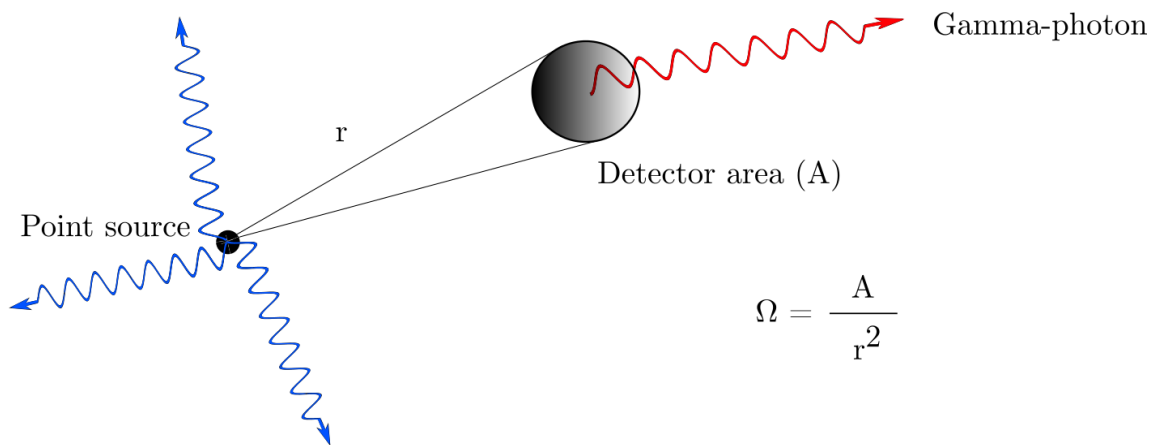


Figure 8.2: Diagrammatic representation of the geometric response of a radiation detector.

8.2.1.4 Monte-Carlo simulation

An in-house, Python™ software based, Monte-Carlo simulation approach, developed by Connor [252] was used to determine geometric efficiency. The approach defined a volume from which gamma-photon emissions may emanate and a detector volume geometrically in space. Within the software, gamma-photon emissions are randomly sampled, with isotropic directionality. Each gamma-photon is tracked, and geometry is used to determine which emissions pass through the detector volume. The gamma-photon emissions which do pass through, are used to determine the percentage fraction, which is equal to the geometric efficiency. Simulation of 1 million gamma-photon emissions was used to calculate the geometric efficiencies used of all examples.

8.2.1.5 Energy conversion

Radiation spectrometers collect measurements into discrete ‘energy-bins’. These energy bins are arranged by a pre-defined hexadecimal number. Each bin corresponds to an energy range window, defined by the detection ability of the detector. They are linearly related to the discrete energy range. The relationship between energy and energy bin may be determined by recording spectral data from known radioactive sources. Known energy peaks can then be related to bin numbers, converting bin number to energy [252].

8.2.1.6 Emission intensity

Emission intensity, I_e is fraction of gamma-photons which are released of a specific energy. This is in accordance with the decay chain of the isotope being analysed. For example, Cobalt-60 (Co-60) has two distinct gamma-photon peaks at 1.173 and 1.332 MeV, with I_e 's of 99.85% and 99.9826% respectively [253], as shown in Figure 8.3.

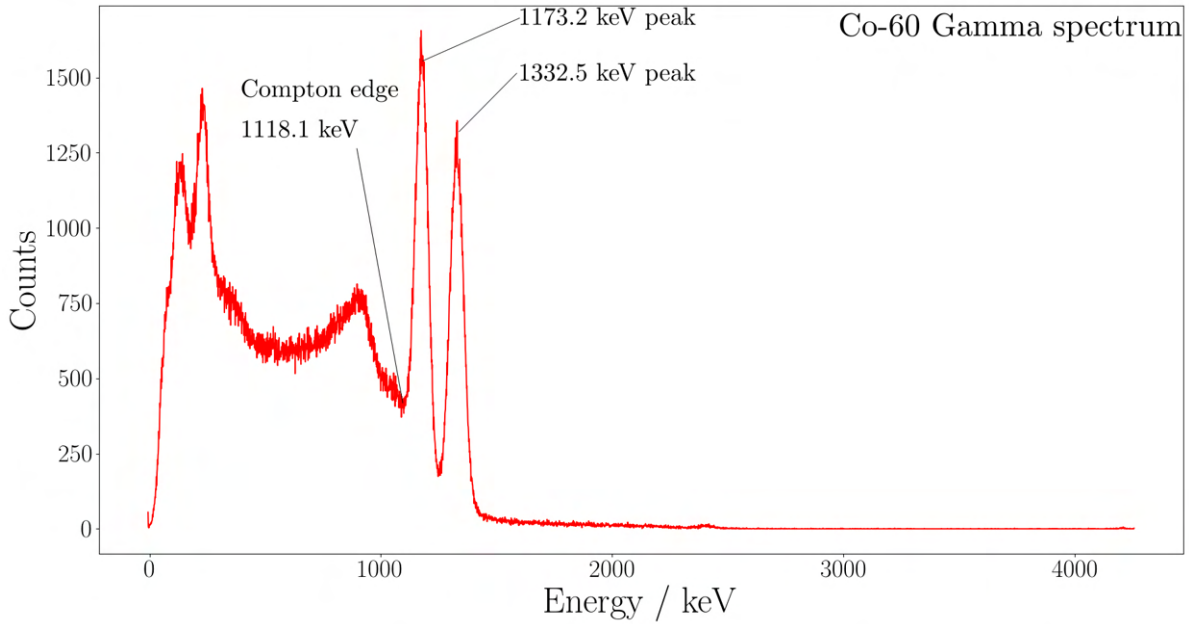


Figure 8.3: Example Co-60 spectrum.

8.2.1.7 Intrinsic Efficiency

The intrinsic efficiency of the detector is the ratio of the number of gamma-photons which enter the detector and the number which register as counts. This should not be confused with the total efficiency, which is the ratio of gamma-photons registered by the detector and the total gamma-photons emitted by the source [254]. Intrinsic detector efficiency may be given by Eq. 8.3.

$$(8.3) \quad \epsilon_i = \frac{N_i}{A \cdot \epsilon_g \cdot I_i}$$

Where N_i represents the number of counts recorded, A is the total activity expected, ϵ_g is the geometric efficiency of the scenario and I_i is the emission intensity expressed as a fraction. The intrinsic efficiency of a detector varies with gamma-photon energy, typically reducing with energy [255]. By measuring the counts recorded, by specific energy peaks and comparing it to the expected number, a function may be fitted to relate intrinsic efficiency to energy. McFarland [256] showed this fitting may be completed using a logarithmic polynomial, as given by Eq. 8.4.

$$(8.4) \quad \epsilon_i = \frac{p_1 + p_2 \ln(E) + p_3 \ln^2(E) + p_4 \ln^3(E)}{E}$$

Where p_1 to p_5 are fitting parameters calculated by the least squares regression algorithm and E represents the energy.

Measurements of Eu-152, Co-60 and Cs-137 effective ‘point sources’², were taken to identify the intrinsic efficiency. Each sample was exposed for a minimum of 500 s with the precise time of the exposure recorded. Additionally, the distance of the source to detector distance was recorded, to calculate the geometric efficiency. By integrating under the peak, with a baseline correction made to account for the background activity, the total peak counts could be calculated. An example of the baseline correction is shown graphically in Figure 8.4.

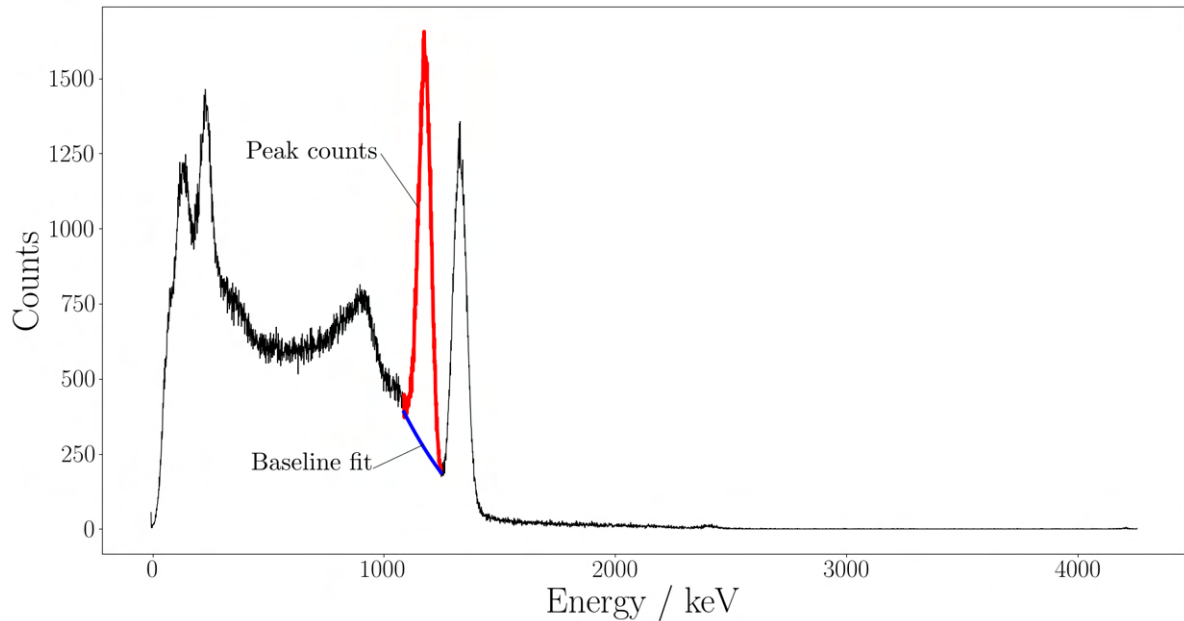


Figure 8.4: Co-60 spectrum showing the baseline fitting procedure diagrammatically.

For each sample, the geometric efficiency was calculated using the MC code implementation. The intrinsic efficiency, for the energy measured, could then be calculated using a reformulation of Eq. 8.3. Results for each peak could then be recorded graphically, and the peaks fitted using the logarithmic polynomial of Eq. 8.4.

8.2.1.8 Activity calculation

Once all parameters are adequately quantified and calibrated, the activity can be ascertained. This is achieved using Eq. 8.5.

$$(8.5) \quad A = \frac{N_i(E)}{\epsilon_i(E) \cdot \epsilon_g \cdot I_i}$$

Where N_i represents the number of dead-time corrected counts received at a given energy, ϵ_i is the intrinsic efficiency, ϵ_g is geometric efficiency and E is energy. The activity is calculated for

²The sources were approx. 1 mm in diameter.

each energy peak, then averaged to estimate the activity of the source in Bq. For this work, the radioactive emitter used was an input of the developed program, enabling the peak regions to be measured. However, it is noted that automated photopeak identification, such as the work by Fearn et al. [257] could be applied to resolve this autonomously in future work.

8.2.1.9 Depth Camera Tracking

In order to autonomously determine the activity of an object, the geometric efficiency must be calculated in-situ. This can be achieved using depth sensing technology to quantify the objects' volumetric qualities, generating a 2.5D model. To generate the 2.5D model, the robot orients the object in front of the depth camera at a known position and a depth image is taken. Robot position and orientation are then stored with the depth image, aiding the reconstruction to be computed in software. The image is then processed to ensure the optimal 2.5D model estimation is made. Processing steps include removing pixels above a maximum distance³, filtering the image with a Gaussian filter and 'blob analysis'. These are completed to ensure only the largest connected pixels are analyzed, removing any noise introduced from the depth image. From this image an average distance measurement is taken. This average distance approximates the camera-object stand-off distance. Subsequently, this is used in combination with the camera's field of view, $87^\circ \times 58^\circ$, which can be geometrically processed to inform pixel width and height. These pixel widths and heights are used to generate an accurate 2D shape. Using geometry, the 2D shape of the object and the measured stand-off distance between the depth camera and the object, the depth of the object can be estimated. This is achieved by subtracting the known camera to back of gripper distance, from the minimum distance from the camera to the object. When combined with the calculated maximum depth of the object, an estimation of the 3D model can be made in 2.5D. A full workflow example of this working on a glove is shown in Figure 8.5.

³This distance is set as the distance from the back edge of the gripper to the camera system.

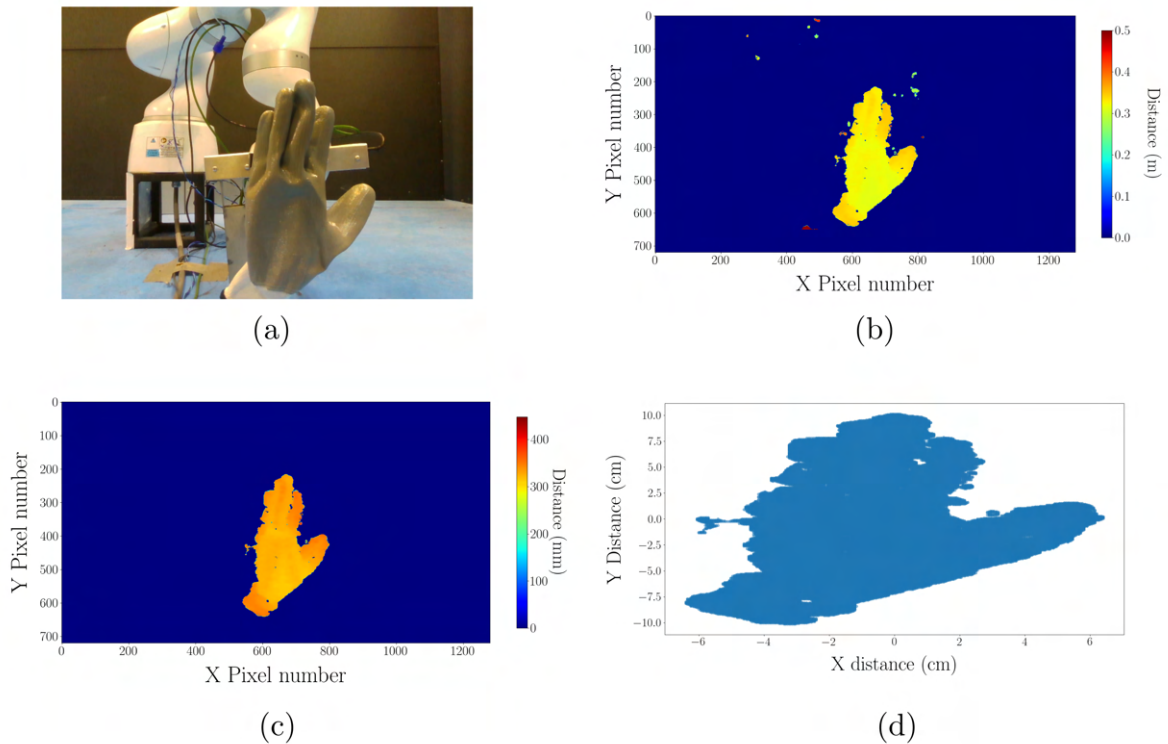


Figure 8.5: Processing workflow for the autonomous geometric efficiency calculation. (a) Shows the photograph of the object in front of the depth camera. (b) Shows the unprocessed depth image. (c) Shows the processed depth image. (d) Shows the point samples to be input into the MC geometric efficiency code.

From the generated 3D model of the object, the geometric efficiency of the detector system may be ascertained. This is accomplished autonomously, by inputting the volumetric information into the MC code, as possible gamma-photon emission locations. An example is covered in the results section.

8.2.1.10 Camera error

There is an associated error on depth camera measurements which is defined by the manufacturer as a ‘distance error <math>< 2\%</math>’. This means that for a depth image taken at 300 mm, the associated error would be $< \pm 6\text{ mm}</math>. The error in pixel distance on the x-y plane is likely to vary more significantly, as it requires stereoscopic interpretation. Additionally, the object surface will have an impact, with metallic or shiny surfaces introducing a larger error, due to causing both specular and diffuse reflections [258]. To identify these errors, a wooden block of dimension 150 mm by 50 mm and an aluminium block of dimension 105 mm by 40 mm, were photographed and analysed.$

8.2.1.11 Overview of robotic process

A process was implemented on a KUKA LBR MED robotic arm system, enabling the autonomous determination of the activity of a given sample object. The robot arm autonomously grasped each object, subsequently presenting it to the depth sensing camera. A volumetric determination of the object was then made from the depth sensing procedure as outlined above. This enabled the estimation of a geometric efficiency. The object was then presented at a known distance from a radiation detector for spectral acquisition. This corresponded to the parameters passed to the Monte Carlo simulation used to calculate the geometric efficiency. Combining the calculated geometric efficiency with the experimentally derived intrinsic efficiency, the activity of the collected gamma spectrum was calculated using Eq. 8.5.

However, there was a recognised nuance associated with this process. The active emission area will always equal to, or less than, the volume of the object⁴. Therefore, the calculated geometric efficiency will always be greater than or equal to the ‘real value’. The result of this is an under-reporting in the actual activity for certain radioactive objects.

8.2.1.12 Trial experiments

The robotic process was trialed on sources of known activity. First a test was completed on two calibrated ‘point sources’, of Eu-152 and Co-60 with activities of 37 kBq each. The purpose of this was to assess the quality of the detector calibrations, as the geometric setup of the system was known. Secondly, test scenarios were setup using sources of known sizes and activities, contained within larger objects. The containment’s used were identical to those described in chapters 3, 4 and 5. For one experiment, a Cs-137 containing puck was used with an activity of 36 kBq, for the other, a 31 kBq Cs-137 puck was used. This is shown in Figure 8.6, left. The activity of these pucks was measured using the software developed in this work. As a control measure, each example was also assessed using the known geometric efficiency of the setup’s internal emitter volumes. Finally, the 31 kBq Cs-137 puck was attached to an aluminium block, as shown in Figure 8.6, right. This sought to be a representative example of an object that may be identified within radioactive waste sorting operations.

⁴Excluding the additional error in measured volume.

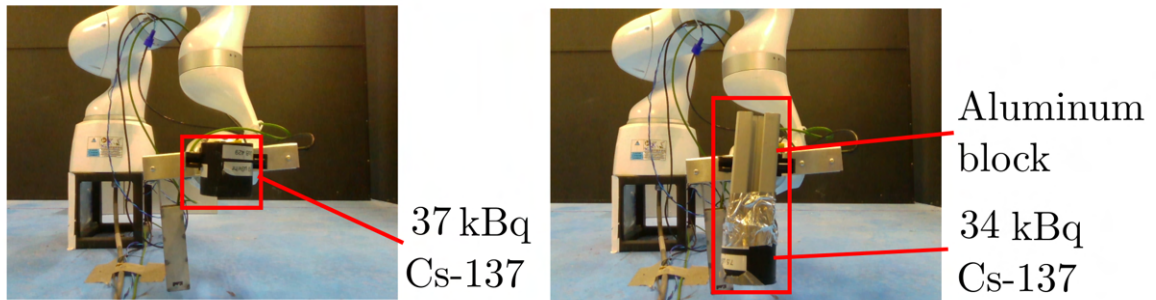


Figure 8.6: Photograph showing the radioactive source pucks used. Left shows the individual puck. Right shows the puck attached to the aluminium block.

8.2.2 Activity determination results and discussion

8.2.2.1 Detector energy calibration

The detector energy calibration was graphed, connecting the channel numbers and the associated energies. Cs-137, Eu-152 and Co-60 sources were used to identify the specific peak energies. The resultant graph can be seen in Figure 8.7.

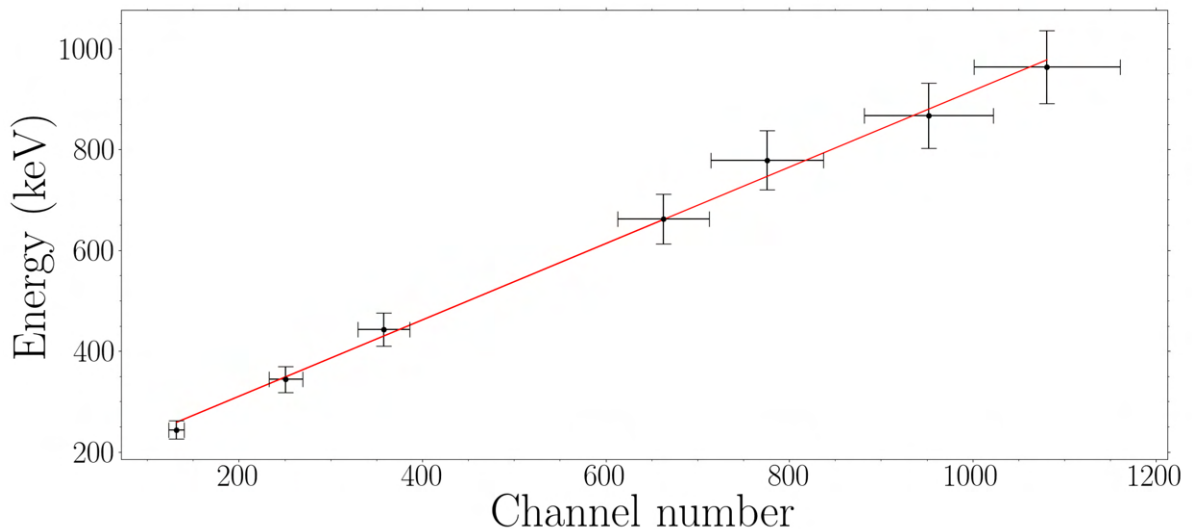


Figure 8.7: Energy calibration graph.

It should be noted that this calibration graph is specific to the detector which was used. Every detector, even of the same manufacturer and crystal type, will display a different result.

8.2.2.2 Detector intrinsic efficiency calibration

Figure 8.8 shows the graph of intrinsic efficiency.

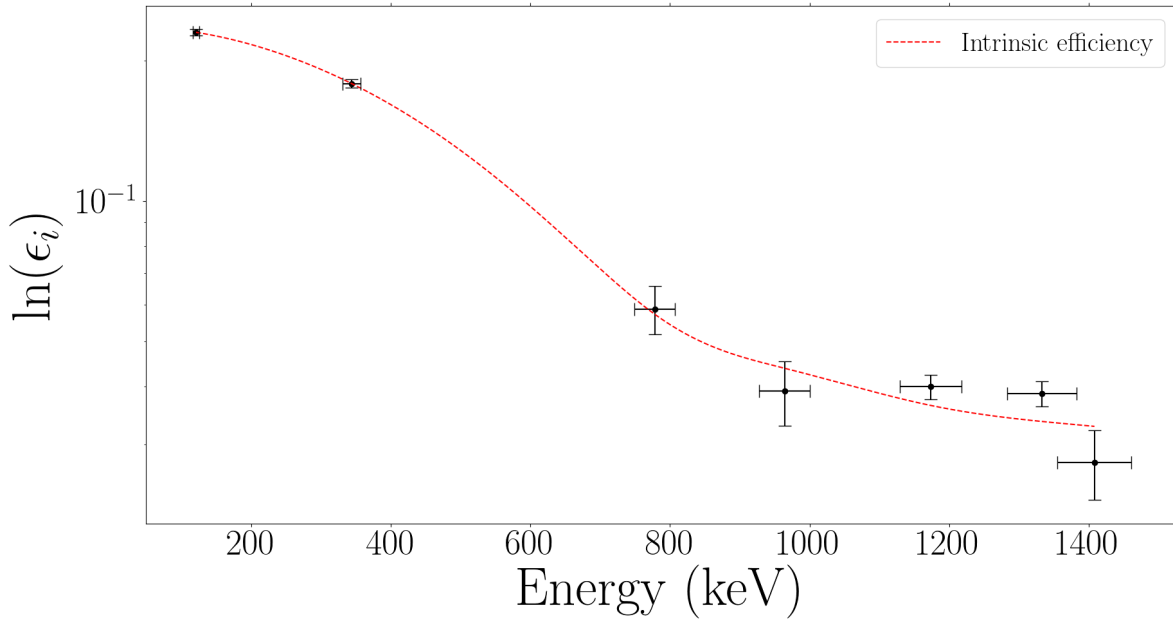


Figure 8.8: Graph of gamma-photon energy vs intrinsic efficiency.

8.2.2.3 Camera error

Assigning an error to the physical surface reconstruction of the depth imaging process was difficult. As shown in Figure 8.9, partial holes appear in the computerised surfaces. These are far more pronounced on the shiny metallic surface, than the matt finish wooden surface. Additionally, there was an associated error with the co-ordinate positioning's, as seemingly 'straight-line' sections contained noticeable fluctuations along the line. The error could be measured by identifying the size of the largest fluctuation on a straight-line section. Interestingly, for the matt finish surface, this was more pronounced on one side of the block, whereas on the shiny surface, this was pronounced on both.

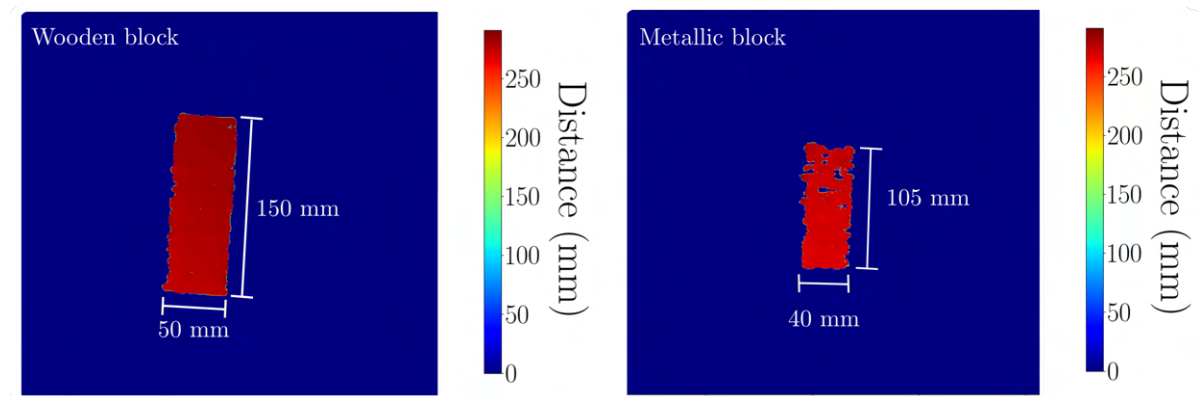


Figure 8.9: Depth images taken on the Intel RealSense D435 camera. Left, shows an example of a matt finish 'wooden block'. Right, shows the reflective 'metallic block' surface.

Upon analysis of 10 images of the same wooden block, the error on the x-axis was determined to be ± 3 mm and the error on the y-axis was determined to be ± 5 mm. As expected, the aluminium block introduced more error; parts of the surface were determined as missing on the surface and there was a noticeable error on the edge detection. It was found to be ± 10 mm in both the x and y axis.

This error introduces an error in geometric efficiency, as there will be a discrepancy in the volume calculation undertaken. An increase/decrease of 10 mm in both x and y, will lead to a scalable error in geometric efficiency. To account for this, the minimum volume and maximum volume geometric efficiency should be calculated, and their discrepancy will provide the error in measurement.

8.2.2.4 Geometric efficiency

The geometric efficiency was calculated from the collected depth camera image of the object. A simple example will be covered here. The robot positions the object in front of a depth camera at the same orientation it presents the object to the radiation detector. The result of this depth image analysis is shown in Figure 8.10.

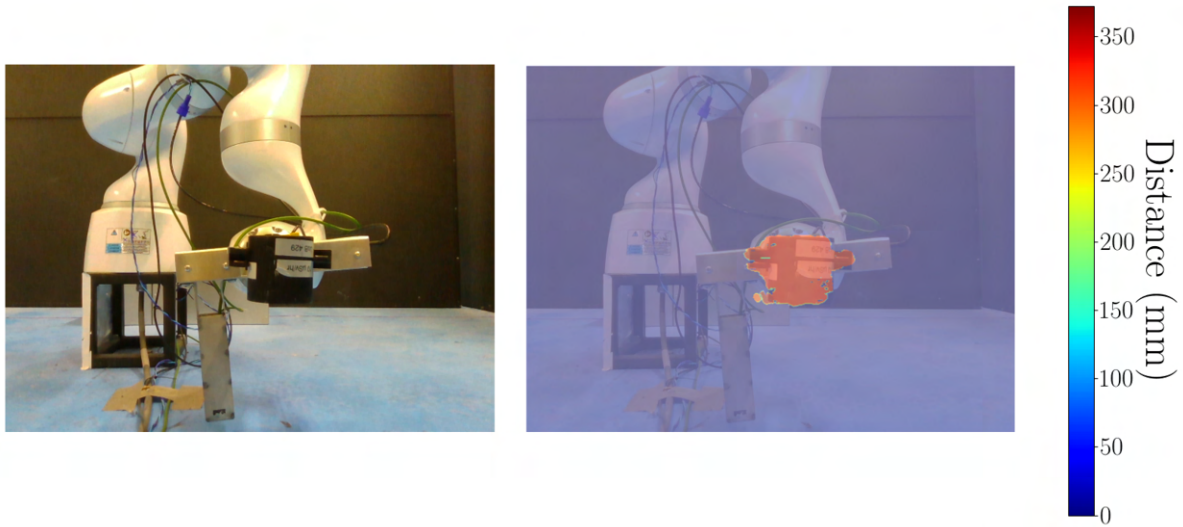


Figure 8.10: Left, shows a colour image of the scanned object. Right, shows an overlaid depth image of the detected object.

In Figure 8.10, the grasped object is clearly highlighted as a superposition on top of the photographic image. Knowledge of this image and the 3D geometry of the object can be used to inform the geometric efficiency, through implementation within the MC code.

8.2.2.5 Error in geometric efficiency

The error in the geometric efficiency for each scenario was dependent on the camera error. There is an error associated with object depth and an error associated with the object shape as photographed (see Figure 8.9). This error can be measured by determining the geometric efficiency of a shape which is maximal and minimal within its calculated error bound. An estimation of error was made by determining the change in geometric efficiency corresponding to an area change at many different stand-off distances. The resulting graph can be seen in Figure 8.11.

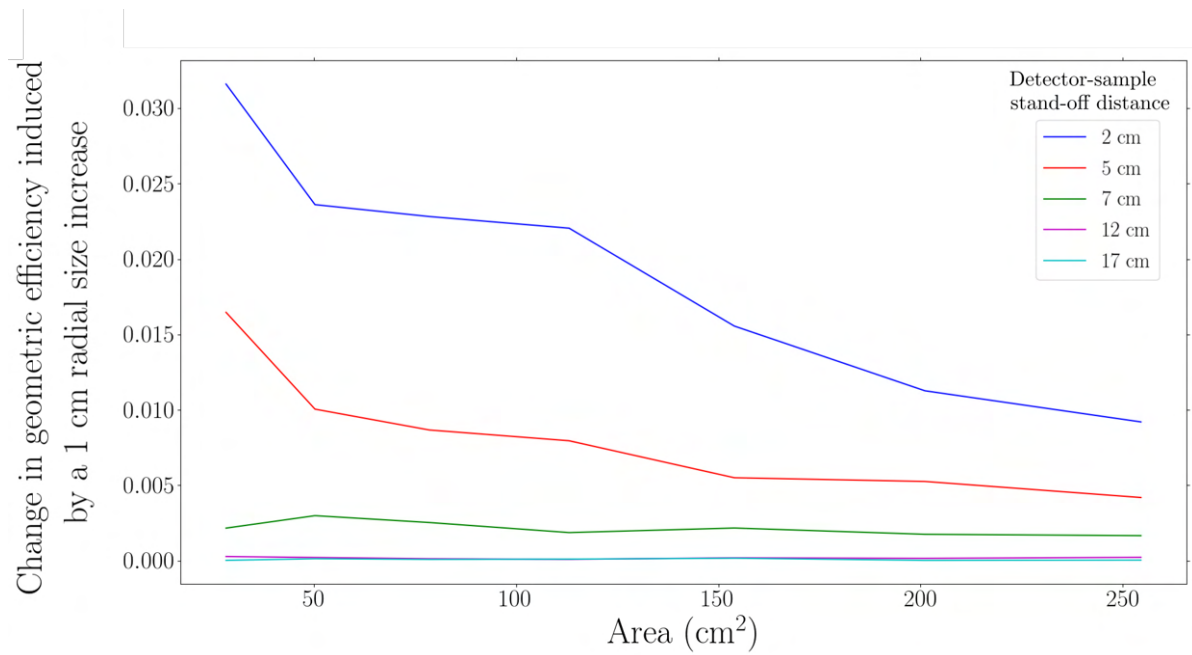


Figure 8.11: Graph showing the effect of shape area and stand-off distance on geometric efficiency error.

The change in geometric efficiency reduces with increasing area change, as anticipated. For the distances used in this work, the change in geometric efficiency remained the same for detector-sample stand-off distances greater than 12 cm.

8.2.2.6 Trial experiments

The results of the trial experiments can be found in table 8.1.

Object	Geometric efficiency	δ Geometric efficiency	Measured activity (kBq)	Real activity (kBq)
Eu-152 'point source'	0.109233	0.0003	53 ± 3	37 ± 1
Co-60 'point source'	0.109233 3	0.0003	59 ± 13	37 ± 1
Cs-137 puck whole	0.0262565	0.0005	151 ± 12	36 ± 1
Cs-137 puck internal cavity	0.024246	0.0003	164 ± 13	36 ± 1
Cs-137 puck whole	0.2061545	0.01	91 ± 9	31 ± 1
Cs-137 puck internal cavity	0.1553505	0.0003	121 ± 9	31 ± 1
Cs-137 puck connected to Al extrusion	0.0313915	0.0006	78 ± 2	31 ± 1

Table 8.1: Results of the trial activity calculation experiments.

All errors were calculated using a partial derivatives-based error propagation method. The 'point source' measurements show a reasonable agreement with the real values, being identifiable to within 20 kBq. This confirmed the detector calibrations were of suitable quality for further experimentation. Ideally, a closer agreement would be identified, with reduced error in the intrinsic efficiency and energy calibration datasets. However, the purpose of this work was to present an autonomous workflow, so no improvement was made. Results for the Cs-137 source pucks showed a comparatively reduced agreement to the true values. It is possible that there is a problem with the determination of the true value here. The validation using the measured geometric efficiency of the setup using the internal cavity also displays a significant discrepancy between the true and measured value. The only way to measure an activity accurately is using the methodology provided within this work but excluding the autonomous geometric efficiency calculation.

Therefore, the Cs-137 puck internal cavity value will be the reference point for discussion. The geometric efficiency of the whole pucks is slightly greater than the geometric efficiency of the internal cavities. This results in a discrepancy in calculated results, with a loss reported for the larger whole puck scenario, as anticipated. The Cs-137 puck connected to the Al extrusion shows a larger difference in true and measured result. This is because of the system identifying the whole shape as a volume emitter. In reality, only a small component of the object was an emitter, therefore inducing a loss in measured activity. It should also be noted that the error on this measurement is very small. This is likely a result of the fact that the error was largely dependent on geometric efficiency error which does not account for the discrepancy in emitter volume. In the Al extrusion case, geometric efficiency error was comparatively small, due to the larger size.

The autonomous activity calculation methodology developed within this work showed reasonable results when object volume and emission volumes were close. However, poorer results were collected when there was a large discrepancy in object and emitter volume. While a depth camera-based method can approximate the activity of the object as a full volume emitter, it cannot determine the volumetric details of the emitting particles. Therefore, it always over-reports the geometric efficiency of the system and consequently under-reports the activity. For some scenarios, the active material will be spread across the whole object, in which case, the methodology developed would suffice as an appropriate activity calculation method. Other scenarios may have a small area containing a high activity emitter, as indeed was the case within this experimentation. In such scenarios, a radiation surface map of the object could be used to identify the most active position on the surface. Subsequently, this location should be placed directly in front of the detector to collect the spectra, thus harnessing the maximum activity for the volume. Further to this, a radioactive source localisation technique, such as the one demonstrated in chapter 5, could be used to better estimate the volume of the emitter. This would result in a more accurate emitter volume calculation capability, improving the accuracy of the calculated geometric efficiency.

Literature suggests that currently nuclear waste is already classified using gamma spectroscopy [9]. However, it is unclear exactly how the spectrometer is positioned with respect to the samples. Historically, it has been completed by scanning large volumes of waste (0.03 m³) across whole tables of waste [9]. For a system designed to generate a reduction in higher activity waste volumes, such a process is undesirable. Inactive objects will receive blanket categorisation as active ones, potentially increasing the effective volume of radioactive waste, incurring higher costs due to apparent larger volumes of higher activity wastes. Hence, it is possible that the results of this test would represent an improvement compared to current techniques.

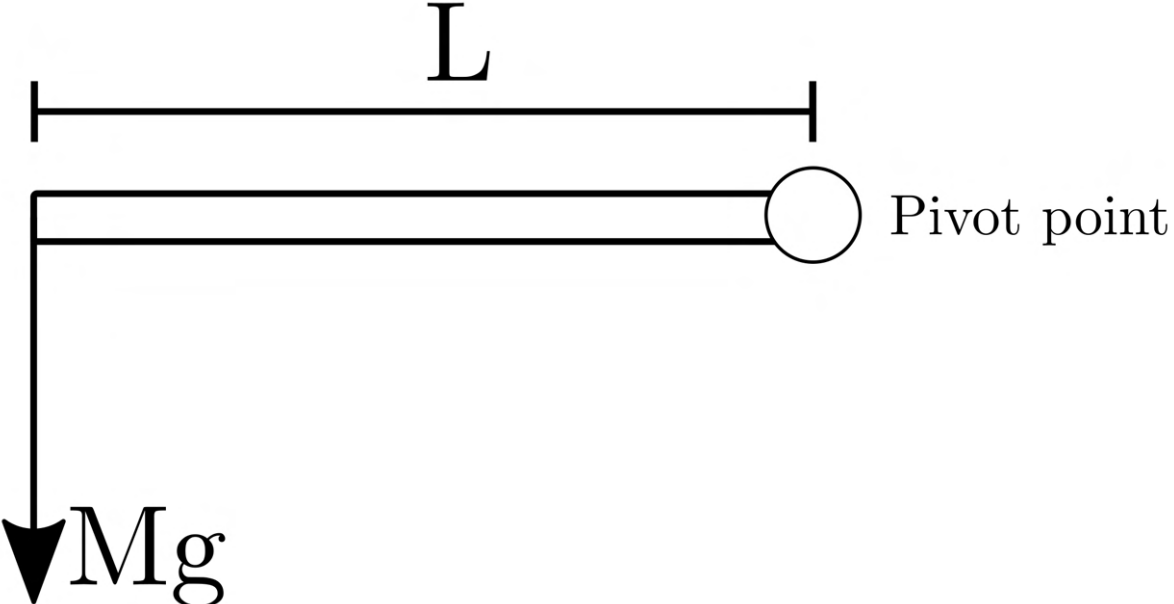
It is also recognised that within a real sorting and segregation setting, beta radiation lev-

els are also monitored, ideally also alpha and neutron measurements. Clearly, the methodology reported negates such measurement and therefore alternative processes should be explored to determine the radioactivity of each object in full.

8.3 Robotic article mass determination

The development of an in-situ robotic article mass determination algorithm using in-built force torque sensing, was dependent on the physical principles of torque. In effect a torque is a turning force which acts about a pivot point. The basic equation of torque can be expressed by equation 8.6 and a diagram explaining the terms can be found in Figure 8.12.

(8.6)
$$M = \frac{T}{gL}$$



The diagram shows a horizontal line representing an arm. Above the line, a dimension line with vertical end-caps is labeled 'L'. At the right end of the arm, there is a circle labeled 'Pivot point'. From the left end of the arm, a vertical arrow points downwards, labeled 'Mg'.

Figure 8.12: Force diagram explaining how torque can be applied about a pivot point.

Where m is the mass, T is the torque, g is acceleration due to gravity and L is the length from the force inducing the torque, to the pivot point. As discussed in chapter 2, torque can be measured by the KUKA LBR robotic manipulator. Measurements of T may be made about axes 2, 4 and 6. To maximally reduce the error recorded in the 'L' value, the robot makes a T measurement about axis 2. Hence, the arm is positioned in a 'weighing pose', which is configured as such. In this pose, the arm is set straight with each axis at 0 degrees, except from axis 2 and 6. Axis 2 and 6 should be set at opposing 90 degree angles, such that the end-flange is directed upwards and the arm is

parallel with the floor. A labelled photograph of the arm in the weighing pose is shown in Figure 8.13.

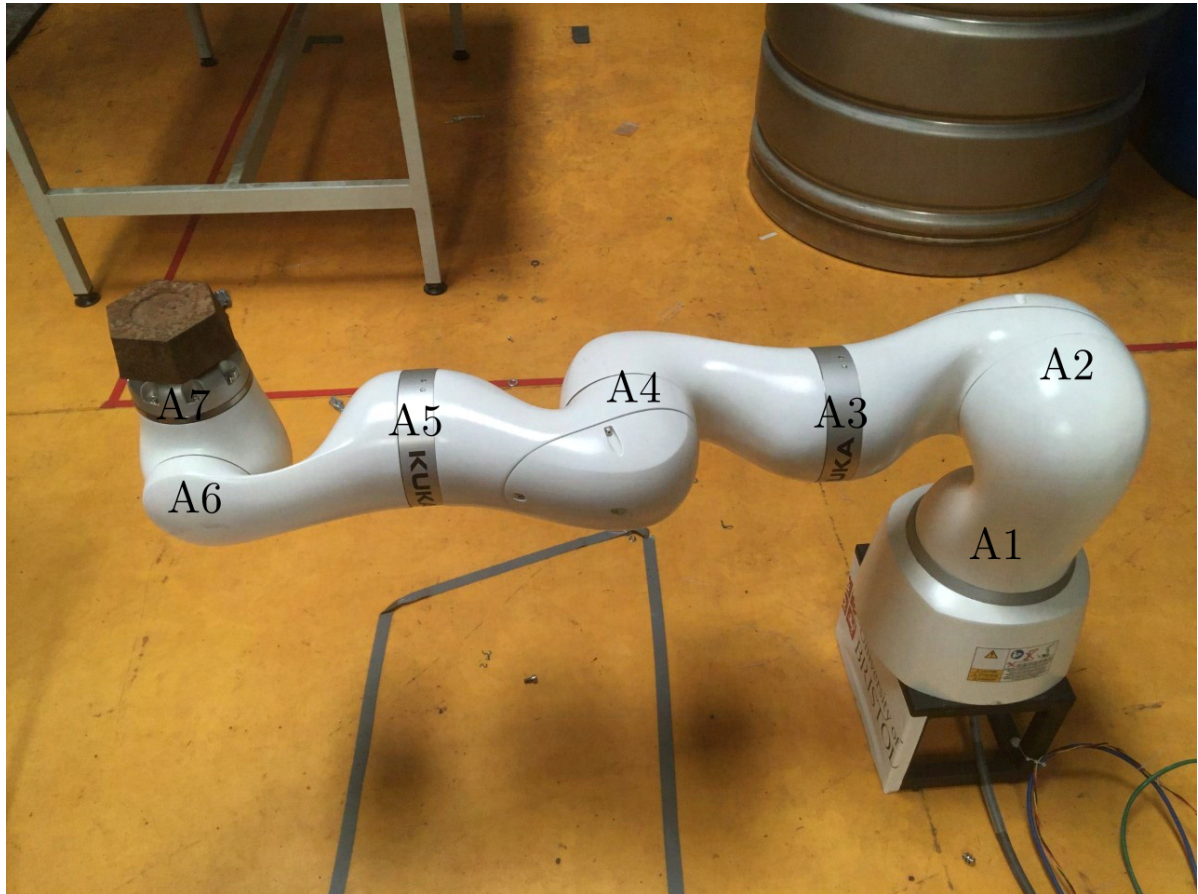


Figure 8.13: Photograph of the robot in the weighing pose. Labelled are the robot axes.

In the weighing pose, the weight at the end flange acts vertically, towards the floor. This induces a torque about axis 2, with a force Mg , acting on axis 2 at a distance of L from the axis. While positioned in the weighing pose, joint 2 has an active load of the robot arm itself, and so without any weight applied, there is a torque. This may be described as a reference torque, T_{ref} . Hence, for calculating the mass of an object using the robotic manipulator, the torque used to determine the mass, must account for T_{ref} . This yields the following modifications to equation 8.6, giving equation 8.7.

$$(8.7) \quad M = \frac{T - T_{\text{ref}}}{gL}$$

Where the additional T_{ref} , is the reference torque without any mass applied at the end-effector.

During testing, it was noticed that statistical variation could result in anomalous mass readings,

due to the tendency for the torque to retain its previous value. This was a probable result of the robotic braking mechanism holding the arm and causing the value of torque reported to remain the same. To resolve this issue, a re-positioning ‘jolt’ was performed in between each weight measurement. This removed the risk of a fixed torque value being recorded. The jolt consisted of each joint moving a random angle of ± 4 degrees, before re-positioning to the weighing pose.

An initial test was completed to accurately measure the reference torque. This would be subject to change dependent on grippers, sensors and other additional tooling which may be added to the end-flange of the robotic manipulator. To calibrate the reference torque, the algorithm was run 100 times, recording the torque on the second joint axis for each, with a ‘jostle’ between each measurement. The result of 100 iterations is shown in Figure 8.14.

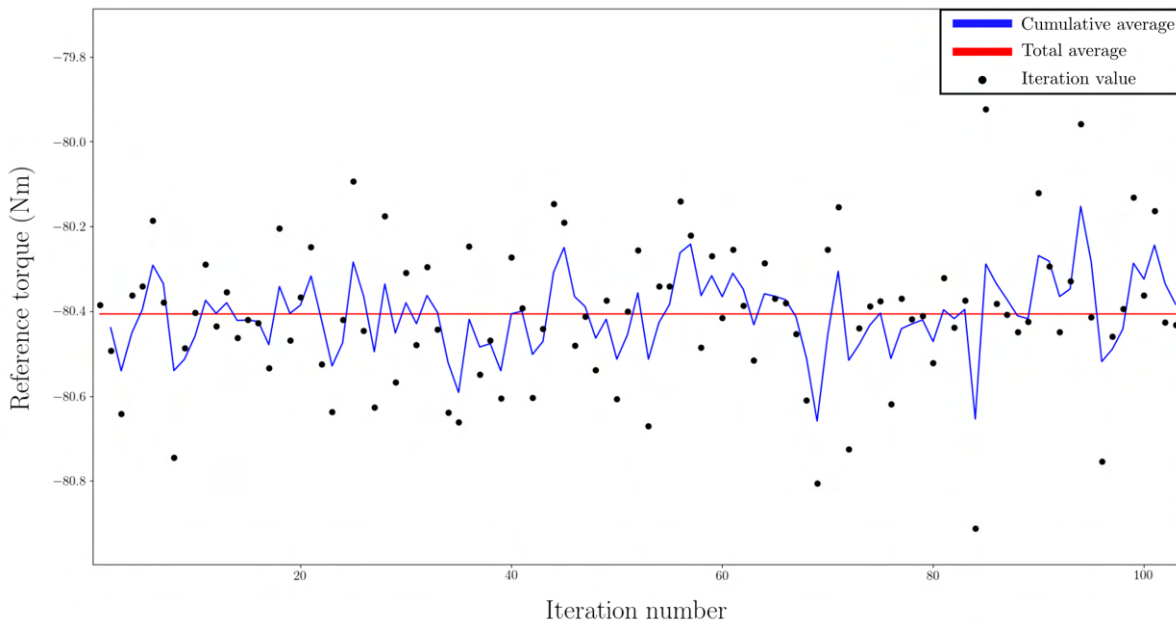


Figure 8.14: Reference torque measurement recorded at axis 2 for 100 iterations. Error bars are omitted for clarity of visualisation.

The reference torque varied by approximately ± 0.4 Nm on each iteration. This was in agreement with the quoted $<2\%$ accuracy in torque measurements. It translates into a mass of approximately ± 90 g, if the centre of mass for the robot arm is assumed to be in the centre, at 0.4125 m. Owing to the random distribution of the reference torque data, it was decided a mean averaging technique would be appropriate to enhance the accuracy of the mass data collected. Hence, an average of 100 readings were taken to assess the reference torque of each measured waste article, theoretically reducing the error in measurement to ± 0.04 Nm.

8.3.1 Testing Weighing Algorithm

To test the in-situ robotic article mass determination algorithm, a number of different experiments were conducted. Firstly, preliminary testing was completed with different objects without an attached gripper. Secondly, testing was carried out with the Blue Robotics Newton gripper attached to the end-effector. All errors were calculated using a propagation technique. This assumed a errors of 2% on the measured torque, a 0.04 Nm on the reference torque, a ± 1 cm on non-gripper length measurement and ± 3 cm on the gripper based measurments.

8.3.1.1 Without gripper

For an initial test, no gripper was added and a $2.003 \text{ kg} \pm 0.001 \text{ kg}$ mass was added directly to the end-flange of the robot arm. First, this added mass was repeat weighed over 50 iterations, collecting individual mass readings. Second, the same test was repeated, taking an average of 10 iterations of the weighing algorithm for each singular iteration. The purpose of this was to explore how the accuracy was improved, by taking a mean of many recordings. In this instance, 30 iterations were recorded. This approach was found to be the most accurate, but also took the most time. Hence, offering a trade-off for consideration.

8.3.1.2 With gripper

The introduction of a gripper to the weighing system had potential to introduce uncertainty into the measurement. This is a direct result of the potential for a non-perfect grasp, in which the gripper does not grasp the object about its centre of mass. The consequence of this would be an additional inaccuracy in the value of length given in equation 8.7. It was expected to have a minor impact, but its effects should be explored regardless. In addition to the impact of a non-perfect grasp, any effects induced by the gripper swaying, or moving as a result of an object being grasped could have an effect on accuracy. These effects are difficult to quantify, so must be experimentally recorded and confirmed.

To test these effects, measurements of objects were taken including the grasping system. In the first instance, small cylindrical non-active radioactive waste pucks were used. They each had a mass of 110 g. These were selected initially, as they had a very strong symmetry, meaning the effects of non-perfect grasping may be ignored and any gripper sway effect should be minimal, owing to their light mass. Following this, testing was completed using a 128 g, cuboidal, wooden block of dimension 150 x 40 x 50 mm. For the aforementioned objects, the robotic grasping routing described in chapter 2.4 was used. Due to the uncertainty in grasp location, it is anticipated that offsets may result in a larger error in the mass determination. Next a test was completed analysing a larger 2.011 kg mass in the gripper, the purpose of this was to explore the response of heavier objects. Supplementary to the 2.011 kg test, was a test of a copper plate of weight 2.66

kg. To test the limits of the weighing capability a test was completed with a 6.498 kg and 10.489 kg blocks. For these heavier tests, the objects were strapped into the gripper to ensure they were safely restrained.

8.3.2 Robotic article mass determination results and discussion

8.3.2.1 No gripper

The results of the 2.003 ± 0.001 kg mass measurements are shown in Figure 8.15.

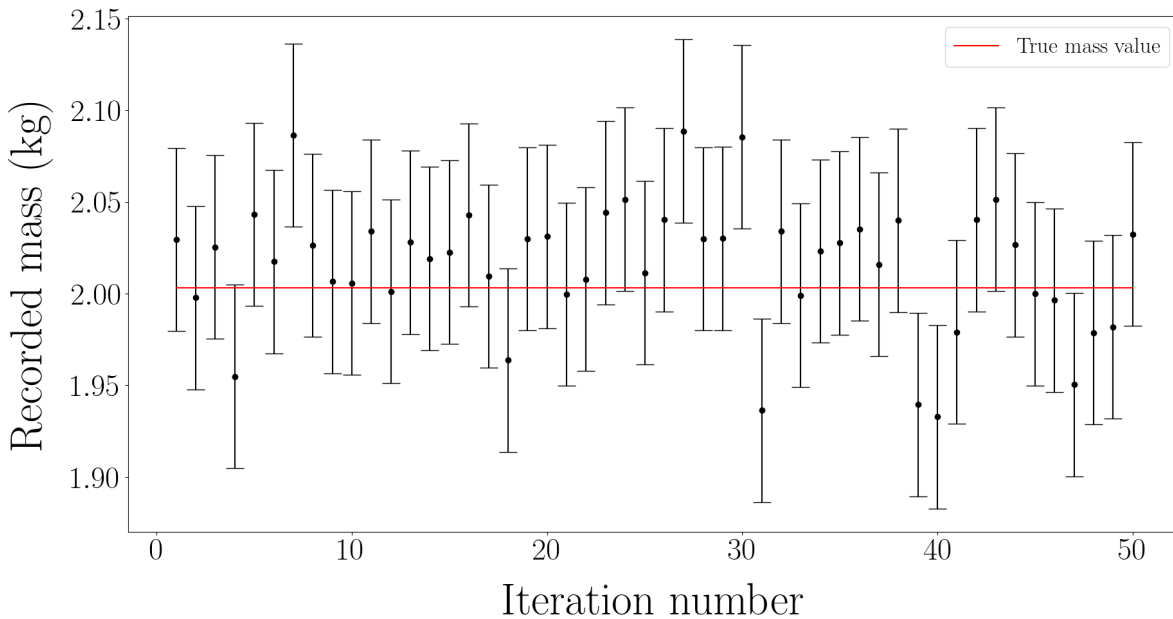


Figure 8.15: Results of 50 iterations of the weighing algorithm with a 2.003 ± 0.001 kg mass and no gripper. Error bars calculated as ± 50 g.

The majority of the measurements fit within the calculated ± 50 g error margin. There are a few outliers which are visible, however there was no obvious cause of the larger errors on these readings. The calculated standard deviation was ± 40 g. Calculation of mean average of all results yields 2.01 kg, which is exceptionally close to the determined value of 2.003 kg.

Ostensibly, the mass derivation was further improved using the proposed mean averaging technique. Figure 8.16, shows the results of 30 mass measurements made, each with an average of 10 torque readings.

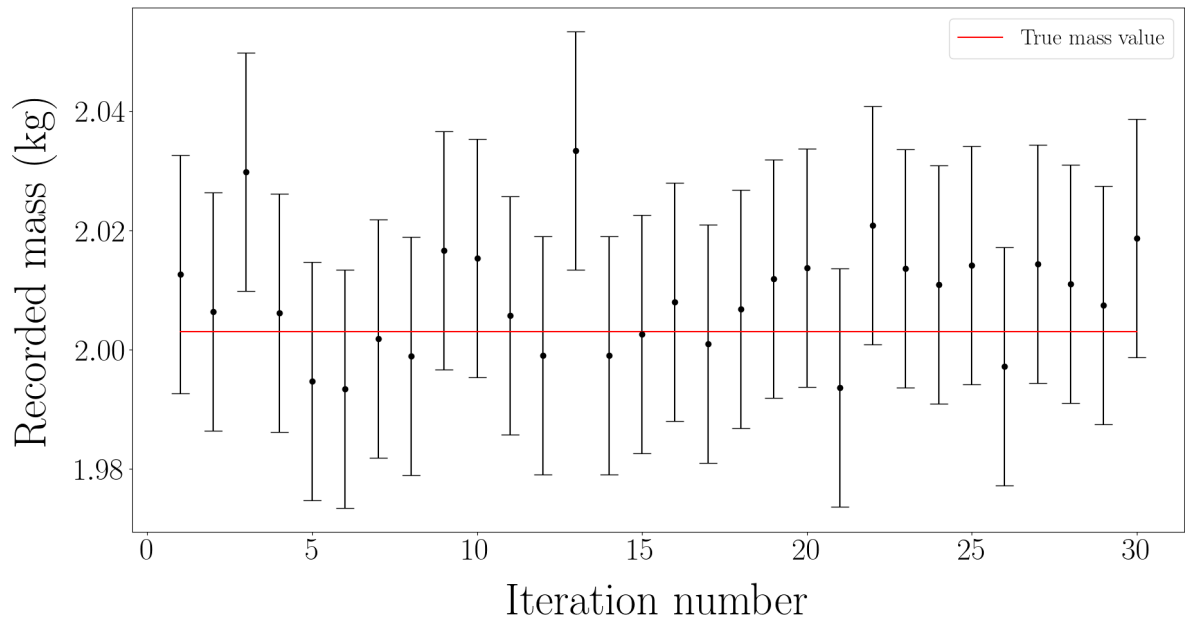


Figure 8.16: Results of 30 iterations of the mean averaged weighing algorithm with a 2.003 ± 0.001 kg mass and no gripper. Error bars calculated as ± 20 g.

With the exception of 4 outliers, it can be seen that the mass may accurately be recorded to within the calculated error of ± 20 g, or approximately 1% in this scenario. Indeed all measurements can be recorded to within ± 30 g. An average of 2.009 kg was recorded across the whole dataset. Both non-gripper experiments prove the principle that in-situ mass measurements using in-built torque sensors is possible. Conceptually, it appears like the more averages taken, the closer to the true value the algorithm can achieve. However, there is an obvious trade-off to be met here in terms of speed of determination and accuracy. It is likely that for waste sorting, time will not be a limiting factor, so more averages would be recommended to enhance accuracy.

8.3.2.2 With gripper

The result of the 110 g cylindrical object test including the gripper can be seen in Figure 8.17.

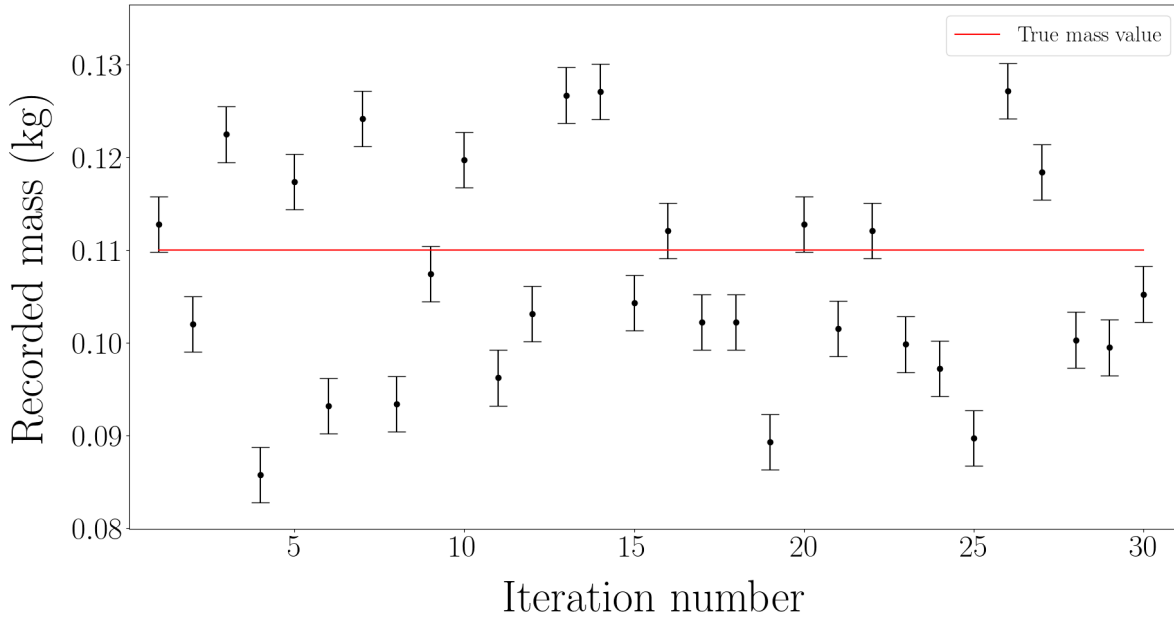


Figure 8.17: Results of 30 iterations of the mean averaged weighing algorithm with a 0.110 ± 0.001 kg mass and attached gripper. Error bars calculated as ± 2 g.

The error identified based on the error propagation method determines an error of ± 2 g on each measurement. Evidently, this is not an accurate reflection of the true result. This is very interesting, as it suggests there is a larger error which is unaccounted for. However, all values are contained within a ± 25 g error margin. The standard deviation on measurement was recorded as 20 g, therefore it was proposed that for low mass measurements, a minimum error of 20 g was used. An average of 0.107 kg was identified across all 300 readings, representing a 3 g error. A high level of accuracy was anticipated, as the grasping occurred with the object being very close to the centre of mass and any sway effects were negligible with a relatively small mass of 110 g.

Next a wooden block was grasped and weighed by the robotic system across 30 iterations, yielding Figure 8.18.

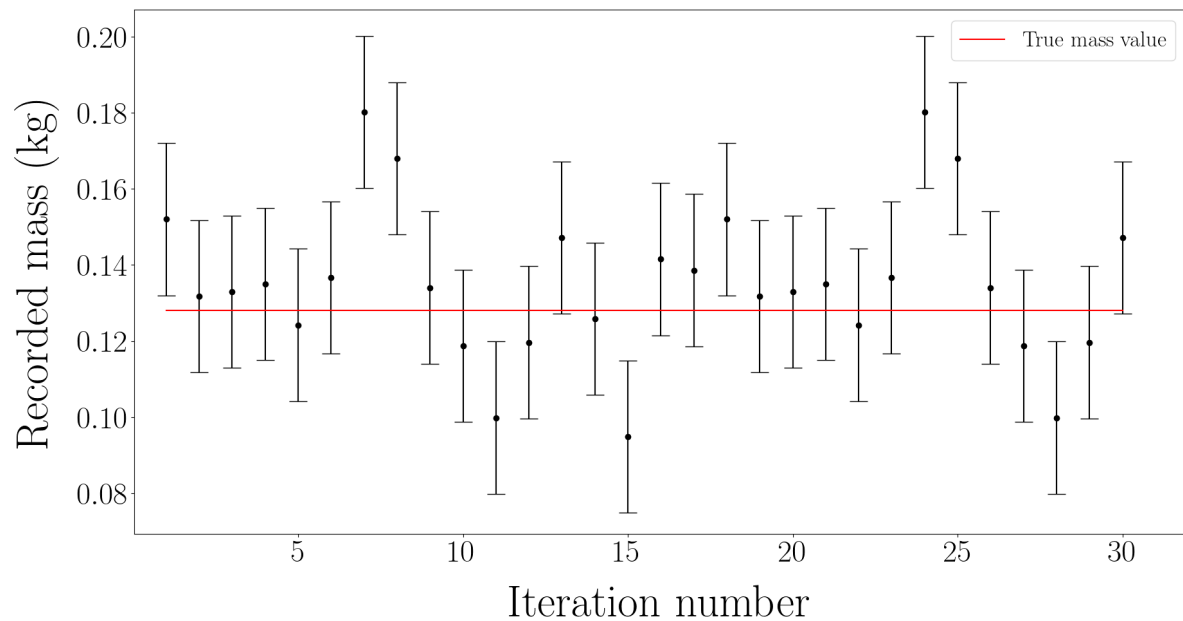


Figure 8.18: Results of 30 iterations of the mean averaged weighing algorithm with a 0.128 ± 0.001 kg wooden block and attached gripper. Error bars calculated as ± 20 g.

Results showed a good agreement with the weigh scale determined value, with all readings contained within a ± 30 g error margin. In addition, the standard deviation was measured to be 20 g, which was plotted as the error following the 110 g test. The 30 g error margin is likely a result of the discrepancy recorded in the grasp positioning of the block; due to there being a greater potential offset in centre of mass, thus inducing a change in L . The uniform density of the block and the cm accuracy of the grasping, meant that any shift would be likely to have a small impact. This was determined to be approximately 1% owing to a shift in L . Otherwise, the system records the mass to a similar level of accuracy, as the plastic puck experiment.

Interestingly, this is not the case for the 2 kg, gripper test. The results of the test are shown in Figure 8.19.

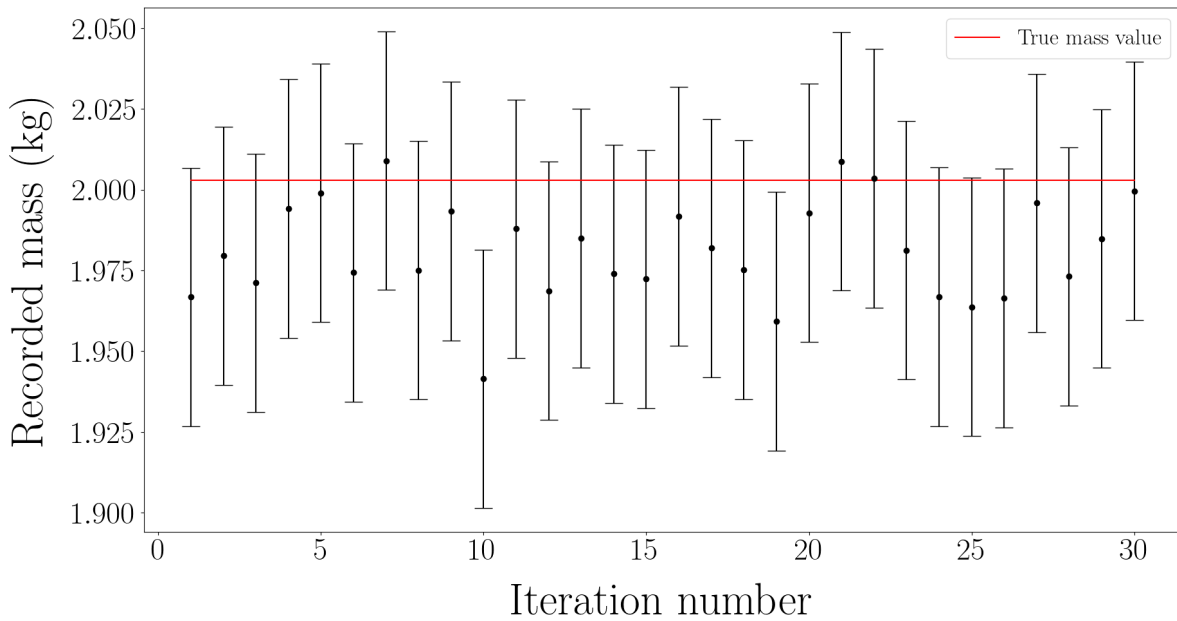


Figure 8.19: Results of 30 iterations of the mean averaged weighing algorithm with a 2.011 ± 0.001 kg mass and attached gripper.

Error here was again calculated with the error propagation method. It was found to be ± 30 g. There is a noticeable trend with the mass reporting less than the actual value. For this test, the standard deviation was recorded as 20 g, indicating there is a systematic error. It is most likely that this error emerges from a non-perfect centre of mass while the object is between the gripper jaws. Due to it being a higher mass than the previous experiment, such a shift would incur a greater impact. An accuracy of ± 30 g still represents a percentage error of 1.5 %.

This test was repeated with a similarly sized 2.66 kg block. The results can be seen in Figure 8.20.

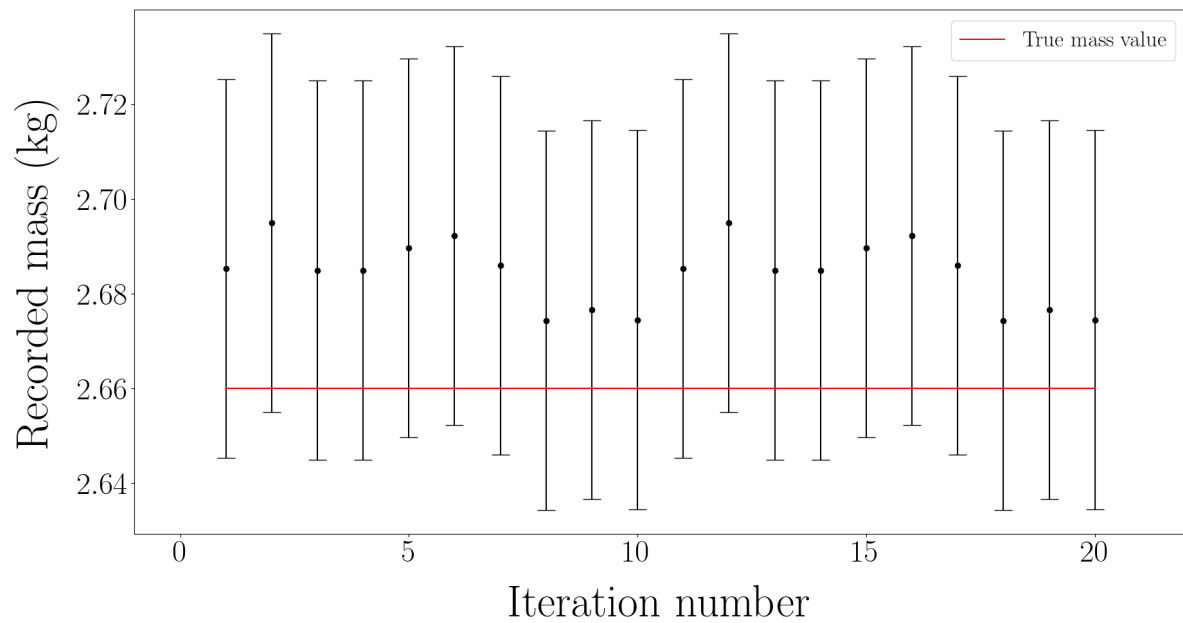


Figure 8.20: Results of 10 iterations of the mean averaged weighing algorithm with a 2.660 ± 0.001 kg mass and attached gripper.

All measurements are accurate to within ± 40 g. However, in this experiment, all recorded measurements were above the real mass value. The test reported a standard deviation of just 10 g. This further supports the claim that a systematic error introduced by the non-perfect mass centring within the gripper is possible.

Next a 6.498 kg block was loaded into the gripper. The weighing algorithm was tested with the loaded mass, reporting the results shown in Figure 8.21.

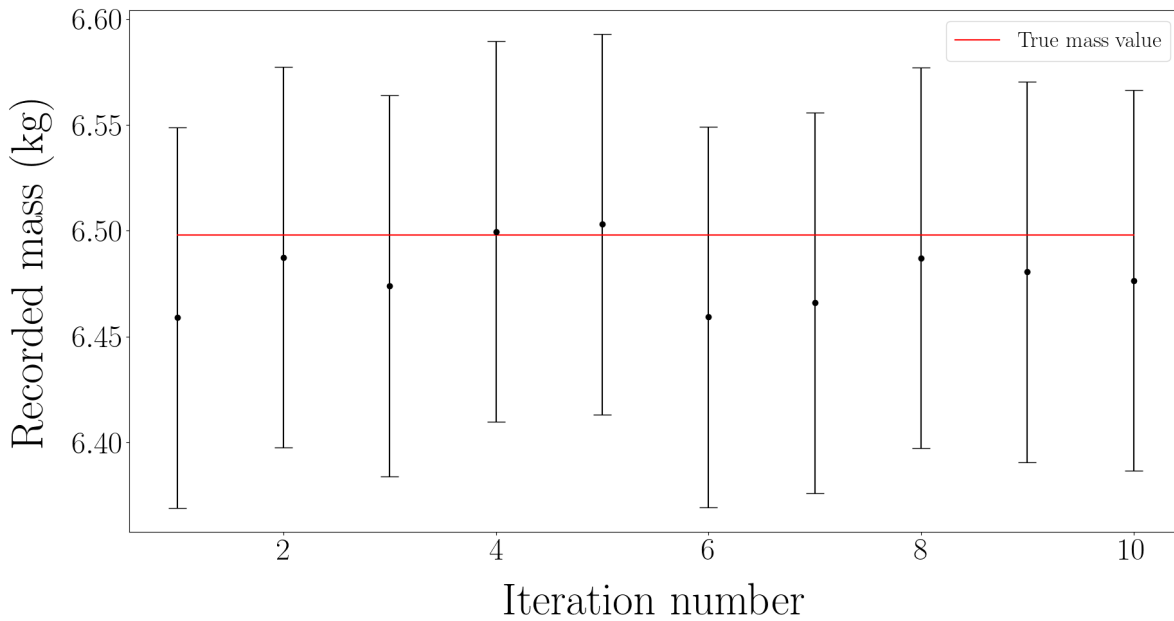


Figure 8.21: Results of 9 iterations of the mean averaged weighing algorithm with a 6.498 ± 0.001 kg mass and attached gripper.

The results indicate the mass can be identified to within 90 g, representing an approximate 1.5% error recorded in measurement. There is a reported standard deviation of 15 g and the measurements can all be clearly made to within an error margin of much less than the calculated 90 g. They can all be found to within ± 50 g, which represents an error of less than 0.8%. This indicates that as loading increases, mass determination becomes more accurate.

A further test was completed with an object weighing 10.489 kg. Unfortunately, on the gripper, this mass induced a resonance effect leading to an instability in the attached object. This was likely induced by the control software attempting to keep the axis 6 positioning centred.

8.3.3 Discussion of in-situ weighing

The findings of the in-situ robotic mass determination algorithm were very interesting. Between 0.110 - 6.5 kg, measurements can confidently be made to within ± 50 g. There appears to be a relatively high percentage error on the lower end of this range, with results indicating an error of ± 20 g, leading to an approximate 20% error. However, at the higher end, results indicate a much lower error of $<1\%$. It is anticipated that such an inaccuracy would be acceptable for a waste sorting procedure. Within waste sorting, such a determination may be clearly defined within a waste class, including the associated errors. If the activity and mass level was close to a classification boundary, a further more accurate ex-situ sampling method could be used to determine waste class more accurately. Redundancy in techniques must be expected in real

sorting and segregation operations to ensure waste is correctly categorised. Therefore, it is highly likely mass measurements would need to be verified by several different means. This may include weighing plates at multiple stages of the process, as described in the introduction. Alternatively, conservative measures could place the waste into a higher category.

8.4 Conclusions

This chapter has demonstrated processes that can be used to classify nuclear waste objects based on radioactivity and mass. Both measurements can be made in-situ negating the need for any ex-situ laboratory analysis, hence streamlining and accelerating the waste sorting process.

The work presented herein describes a new technique for the autonomous radiometric classification of nuclear waste articles. The technique is dependent on a well calibrated detector, and the quantification of the geometric efficiency of the system being measured. Geometric efficiency calculation is demonstrated through an autonomous process which uses depth camera images to reproduce a volumetric reconstruction of the object under interrogation. From this reconstruction, a MC based model is used to determine the geometric efficiency of the detector-sample setup. This geometric efficiency is combined with the other detector calibrations to yield an estimate for the activity of the radioactive object being analysed. Results were of higher precision for examples in which the emitter geometric efficiency was close to the measured volume. However, it was noted that this was not the case for examples without these traits. Ultimately, the geometric efficiency was the limiting quantity, so it is possible that radioactive source localisation could be used to further improve measurement results by identifying the true emitter volume.

Measurements of mass were successfully shown to be able to be made in-situ on the force-torque robotic manipulator system. This is important, as it negates the need for a double-handling based solution; thereby limiting the potential spread of contamination and consequently accelerating the sorting process. Measurements were demonstrated to be possible to within 50 g. However, it was recognised that with further work, the process may quantify the activity and masses of individual components to a higher degree than is currently demonstrated.

Evidenced by the UK nuclear waste classification guidelines, appreciating the activity per unit mass of each robotically sorted object is key to the agenda. This chapter has shown it is possible to autonomously identify both quantities autonomously and in-situ. Ostensibly, the error margins determined were relatively high. However, it is anticipated that a vast amount of the waste will be clearly LLW, with a smaller volume of ILW. This means that a high percentage of the waste will be correctly classified, even within the error margin. Any result which produces an error which straddles the boundary must therefore undergo further testing, or re-measurement, to

ensure the waste package is categorised correctly.

CONCLUSIONS AND FUTURE WORK

The preceding chapters have shown that various different technological aspects thought to be essential for nuclear waste sorting and segregation can be achieved using a combination of integrated robotic, sensory and algorithmic techniques. This final chapter seeks to conclude on the developments presented in the thesis and explore how such technology could be more comprehensively integrated into a more extensive autonomous sorting and segregation prototype. Presented and discussed is a summary of a potential high level process workflow, the design requirements and implementation of a prototype sorting and segregation system.

9.1 Chapter Conclusions

This thesis has successfully integrated a wide variety of advanced emerging technologies, together with robotic manipulators, to develop a variety of nuclear-relevant inspection and characterisation tools. The focal point of research has centred on the challenge of sorting and segregating nuclear waste. It has been shown that this is possible, via a step-by-step breakdown of relevant systems, which were demonstrated to adequately meet the requirements. This section seeks to recap the key developments which were made within each chapter.

Chapter 1

In this chapter, the background theory to the challenge of nuclear waste sorting and segregation was discussed. This involved discussion of the effects of ionising radiation, nuclear fission and the radioactive waste lifecycle. These ideas were assimilated towards a discussion of a fully autonomous robotic system, which could alleviate a major challenge for the nuclear decommissioning and waste disposal community. Suggested, was a system which would integrate

robotic manipulators with advanced emerging technologies. These would be developed into a fully autonomous and in-situ waste sorting and segregation solution.

Chapter 2

Chapter 2 explored the key concepts and techniques deemed essential for understanding the thesis. This began with a discussion of current waste sorting systems. Following this, an in-depth exploration of robotic manipulators, their functionality, programming and capability. Machine vision techniques were then discussed, including time of flight sensors, LiDAR and stereo vision cameras. It is such technology that serves as a primary sensory technique facilitating advanced robotic motions in unstructured environments. This will be required for waste sorting operations, where unknown wastes will be delivered to a processing area in order to be separated on the basis of object type, radioactivity, mass and material composition. Essential to the problem of waste sorting is characterisation, both material and radiometric. Such characterisation tools would need to be remotely deployable on a robotic system and for higher activity wastes would need to be suitably radiation tolerant or shielded to enable work over long periods. Radiometric sensing options were explored, ultimately focusing on micro-gamma spectrometry units. For material characterisation, Laser Raman Spectroscopy (LRS) and X-ray Fluorescence (XRF) were chosen. The techniques have been shown as being complementary to each other and are the most viable methodologies currently available for remotely operated stand-off materials analysis.

Chapter 3

In-situ gamma-photon radiation surveys on robotic manipulators were explored within this chapter. It was demonstrated that a robotically integrated micro-gamma spectrometer combined with a micro-sized time of flight sensor, could be used to make accurate 2.5D radiation and surface maps of test ‘scenes’ containing multiple simple radioactive source objects. The resulting 2.5D representations had overlaid radiation data which could be delivered in both counts per second and corrected surface dose rate. It was proposed that such a technique could be deployed to identify the presence and define the locations of radioactive emitters on a waste sorting table.

Chapter 4

Chapter 4 sought to further develop the radiation survey research. AI based optimisations including basin hopping, dual annealing, particle swarms optimisation (PSO), differential evolution, simplicial homology global optimisation (SHGO) and brute force were explored. The purpose of this testing was to optimise the speed and accuracy of the identification of the strongest radioactive emitter on a waste sorting and segregation table. Theoretically, this would allow for the rapid identification of the most dangerous (active) radioactive object within a radiation survey, which could then receive prioritised removal. Simulated testing was supplemented with live experimentation. Ultimately, using data collected from both the simulated environment and the live experimentation, it was determined that PSO was the optimal technique for sorting and

segregation activities. This was because the PSO method delivered the fastest source identification alongside the lowest positional errors, for the same computational power, across a range of tests.

Chapter 5

Radiation surveys produced on robotic arms, but also other robotic platforms, such as drones, are unable to reproduce the precise active source localisation. This is a result of the isotropic nature of gamma-photon emissions and the inability to restrict the solid angle of the detector without implementing heavy and cumbersome shielding to provide sufficient collimation. An image reconstruction algorithm based on the Kaczmarz method was designed and implemented to improve radiation survey data. All the steps behind this process are detailed within this chapter and include a variety of test examples. The algorithm was shown to enhance radioactive source localisation by a factor of 5-10 \times .

Chapter 6

Developments in XRF characterisation have led to the availability of portable XRF (pXRF) devices. Such devices offer similar functionality of a bench-top XRF system, but within a handheld unit. Such a unit was integrated with a robotic system, in combination with a depth camera. A customisable system was designed which could perform XRF scanning based on user-input parameters, characterising in terms of elemental composition. Targeted object of interest scanning was completed, showing that using depth camera feedback, objects could be autonomously scanned without the need to measure an entire surface. This increased the point density of each object. In addition, it was shown the system could autonomously scan the exterior of a waste drum. This could offer waste package certification, by checking for aggressive corrosive species, such as chlorides, ahead of disposal.

Chapter 7

This chapter explored LRS as a technique for robotically deployed and in-situ waste characterisation. A stand-off Raman probe was integrated onto the robotic manipulator alongside a depth camera system. The object of interest scanning methodology developed in chapter 6 was further explored. AI and Machine Learning (ML) tools were implemented to determine intelligent scan locations based on colour. The system was shown to be able to identify objects, check for continuously connected colourations within each one and subsequently scan a sample location within each. Materials could then be autonomously identified by automated comparison of database spectra, with results showing a very strong agreement.

Chapter 8

Ultimately, waste must be classified in terms of radioactivity per unit mass. Therefore, an accurate activity in Bq and a mass in kg must be derived for each constituent waste component.

Chapter 8 accomplished both. Activity measurements were made using a combination of detector calibrations, spectral analysis and autonomously derived geometric efficiency. Following this, an in-situ weighing algorithm was demonstrated, using the in-built force torque sensors on the robotic manipulator. Accurate waste class classification could then be made.

9.2 Future Work: Towards a Prototype System

The technology developed within this thesis could conceptually be integrated within a prototype sorting and segregation system. With this technical goal in mind, a prototype system workflow was designed. The process begins by assuming waste has been delivered to a sorting table where it is tipped out for processing. Once the waste arrives at the table, a sequence of procedures must be carried out to assess, characterise and sort the waste. Owing to the differences in hazard between VLLW, LLW and ILW, it was decided that the overarching goal should be to prioritise removing objects of LLW and ILW. Any remaining VLLW, which constitutes the largest volume of waste, can then be swept into appropriate containment, or sorted by material type (e.g. for recycling metals) using more conventional processing. Objects suspected of being LLW and ILW must be interrogated more closely to ensure correct assignation. The designed process overview is provided below.

1. Start with a pile of assorted wastes in the survey area.
2. Perform 3D scanning to measure dimension, volume and surface height of waste objects.
3. A robotic manipulator mounted with radiation spectrometers and suspended from a movable frame surveys the radioactivity levels across the table.
 - a) If it is clear there is no ILW or LLW, the waste is inferred to be VLLW, in this instance the waste may be sent down the VLLW chute and disposed of through normal recycling and waste processing routes.
 - b) If there are ILW/LLW objects, they must be picked up individually and characterised robotically in a shielded area away from the activity of the other objects in the sorting area.
4. Attempt robotic separation of waste objects to separate objects as much as possible.
5. In case 3(b), perform XRF survey to understand what elements are present.
6. Perform a Raman survey to understand what plastics and other bonded material structures are present.
7. Gross estimate of object masses made to ensure they do not exceed the robot arm weight limit. This can be achieved with the material characterisation, in combination with the 3D scan.

8. Robot grasps objects, starting with the most radioactive.
9. Weigh object in-situ on the robot arm.
10. Perform confirmatory classification techniques, including XRF, radiation and Raman scanning.
 - Assess activity in Bq.
 - Check material of object with Raman and XRF by rotating object.
11. Place in 'laydown' area for packaging after a volume optimised container has been identified.
12. Conclude appropriate long-term waste storage route.
13. Repeat until conditions of 3a) are met.

9.2.0.1 Robotic System Design

To accommodate the requirements of the system, it is important to consider what the physical motions will need to be made. Ostensibly, there should be a waste sorting area. The robotic system will then be required to move freely across this space. Eventually, objects will be required to be extracted from the sorting area. These will need to be radiometrically qualified in absence of any other radiation. Hence, a suite of sensor systems should be situated away from the sorting area, preferably behind a shielded wall. Ultimately, waste must be transferred to a suitable container. Therefore, a 'laydown' area must be established to perform an optimised packaging routine ahead of storage. Such a routine would enact volume reduction through photogrammetric analysis advising 'Tetris style' packing solution. There should be a system capable of moving storage containers in and out of working area. Finally, damage to systems should be anticipated as a result of accumulated radiation dose. To prevent this limiting the systems life, all robotic and sensory components should be accessible and manually movable to a maintenance bay, where staff would be able to repair systems.

After careful consideration of the requirements, a prototype system was designed. This can be seen as a CAD model in Figure 9.1. The model is numbered to denote the regions of the workflow. It centres around a 3-axis linear stage setup with an attached robotic manipulator (3 & 4). The centre of this stage will contain a waste table (2) upon which the waste will be delivered by (1). There will be 5 cells around the perimeter of this area, separated by thick concrete walls to limit, as much as practical, gamma radiation emitted from the waste table entering the other areas. In cell (2) there will be a waste chute (11) leading to VLLW containment boxes on a rail system (12). Cell (7) and (8) will contain separated waste 'laydown areas', one for LLW and the other for ILW. Objects will arrive in these before they are eventually packaged into their respective waste drums (9 & 10). The waste drums will be on a rail system to support their

delivery and extraction from the sorting and segregation system. In the third area there will be a sensor bay (6), including radiation sensors, Raman spectroscopy and XRF units, to facilitate accurate waste classification. Area (5) will contain a tool change area, facilitating the replacement of grippers and sensors for in-situ inspection. Finally, area (14) will contain a robotic maintenance area, where the systems can be retracted in the event of a system failure.

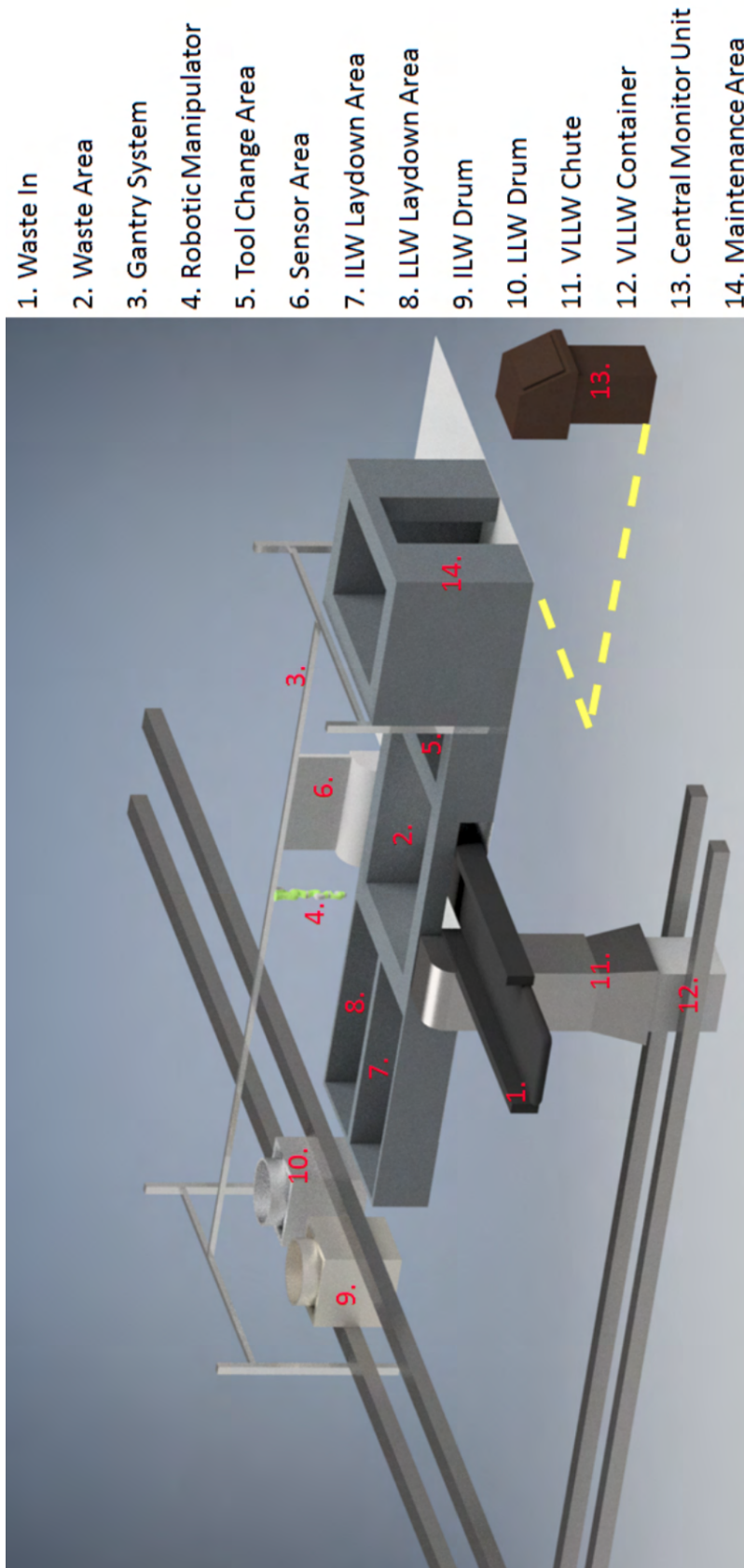


Figure 9.1: System design of complete working system.

9.2.1 3D Photogrammetry Survey

Initial depth camera images should be taken to visualise the waste present on the sorting table in 3D. The purpose of this, would be to make a rapid assessment on the appropriate scan height for the robotic characterisation surveys. In this way an appropriate height for the robotic tool piece or sensor can be selected.

Such developments have been made within chapters 6 and 7 for in-situ waste material characterisation. However, these concepts should be explored further in future work. For example, several depth cameras positioned around the scan surface could reduce the parallax error introduced, to supplement the data provided using a single arm mounted camera.

9.2.2 Robotic Radiation Survey

A robotic radiation survey procedure and subsequent source localisation should be carried out, similarly to routines discussed in chapters 3, 4 and 5. The purpose of this would be twofold. Firstly, to identify if there are any radioactive sources within the waste. If there is no radiation identifiable or it is clearly below the VLLW classification, then the waste may be discarded through a municipal waste disposal route. Secondly, the radiation map could identify the locations of the radioisotopes present within the waste, which could subsequently inform the robotic arm of emitters which are more active, dangerous and should therefore be handled separately from the rest of the waste. Hence, the radiometric survey, will determine the forward processing of the waste. The solutions developed within chapters 3, 4 and 5 are close to deliverable. However, further testing should be carried out with sources within the range of ILW. The purpose of this would be to monitor the effects of detectors in high radiation fields.

9.2.3 Robotic Separation of Waste

Ideally, the waste should be separated as much as possible. This simplifies processing steps, as individual objects can more easily be tracked using photogrammetric techniques. This will aid in both autonomous inspection techniques as well as the robotic grasping of waste items. A mechanism for achieving object separation does not appear to exist. However, it should be investigated in future work.

9.2.4 Robotic XRF Survey

In the case where waste articles are sufficiently active, an XRF survey procedure should be performed, as outlined in chapter 6. The purpose of this step is to identify the elemental composition of different waste articles, with a particular focus on transition metals.

In future work, it may be possible to develop more intelligent characterisation path-planning by

exploring the aforementioned further depth camera analysis. A higher fidelity point cloud image taken from such depth camera analysis may facilitate more advanced robotic inspection. In this way rotational movements can be explored, increasing the level of detail attained for each object's characterisation.

9.2.5 Robotic Raman Survey

Many of the developments described for the robotic XRF survey would be equally applicable to the improvement of the robotic Raman survey. However, a more fundamental component of future work for the robotic Raman system, would be to further develop the calibration database. This would be essential for autonomous material recognition in a waste sorting environment. In addition, background removal for spectra should be explored. This would catch the non-Raman active spectra, ensuring they are not mistakenly matched. To take developments to the next level, a machine learning database could be implemented seeking to supplement autonomous matching with object recognition. This would mean the system would corroborate the Raman spectral output with a physical interpretation of an object. For example, the object recognition would identify a nitrile glove, indicating a presence of nitrile, but the Raman spectral output may identify surface contaminants.

9.2.6 Robotic Grasping of waste articles

Objects with sufficiently high detectable radiation counts must be grasped and characterised using confirmatory techniques. The grasping mechanism used within this thesis could be applied to a future prototype system. However, it is noted that the current grasping routine would be a limiting factor for more unusual shapes and objects. Hence, improving grasping should be a critical focus of future work. Exploration of different gripper systems may help to reduce the complexity of vision based grasping options.

9.2.7 Confirmatory Classification Techniques

Finally the grasped waste object will be subject to confirmatory waste classification techniques, as discussed in chapter 8. This includes, isolated radiometric analysis, in-situ weighing. It has been shown that these techniques can adequately characterise waste class.

Further developments should seek to perform an additional XRF and Raman characterisation while the object is grasped. This would allow for the underside of each object to be checked for conformity and increase the level of detail of the material understanding of the waste article. It should be possible to reverse the methodology of the current inspection mechanisms such that the robot articulates the object in front of the sensor instead.

9.2.8 Determine Waste Stream

By harvesting both radiometric and material data on each object, wastestream can be confirmed, meeting the guidelines of the WAC. Objects can then be assigned to long-term waste storage and disposal routes with confidence. It is conceivable to imagine this being accomplished with a butterfly chart. However, a prototype system could take advantage of modern data processing techniques. In this way, Machine Learning (ML) and AI algorithms could be applied to make better guesses at each waste object using data driven approaches. In this first instance, this could be particularly useful for recognising unusual or potentially dangerous objects.

9.2.9 Optimised Packaging

To reduce the volumes of each wastestream as far as reasonably practicable, an optimised packaging solution should be established. Conceptually, this could entail the placement of waste objects in a ‘laydown’ area. Each object can then be spatially and volumetrically analysed. This can then inform an optimised packaging solution, in which waste objects may be emplaced ‘Tetris’ style.

9.2.10 Radiation Damage Resolution

Radiation dose rates are likely to be high, so radiation tolerance is an important consideration. The deleterious effects of radiation on detectors and robotic systems are likely to be experienced. Knowledge of the ‘mean dose to failure’ on radiation susceptible components would be important to quantify. Monitoring of cumulative dose may then help to mitigate these problems, as they can be extracted and replaced ahead of failure.

9.3 Alternative Implementations

Beyond nuclear waste sorting and segregation, the developed systems have tremendous application within nuclear environments more generally. Radiation survey and source localisation methodologies could be applied for contamination spread assessments across nuclear facilities. Potentially, an integrated robotic radiation scanning system could even be deployed within a glovebox environment. This would enable operators to ensure radioactive material has been removed before further processing commences. Alternatively, if deployed as part of a mobile robot system, it could carry out material and radiation inspection within larger environments such as rooms or storage facilities. This could form part of a radioactive dispersal event cleanup tool, which could detect and remove hazardous radioactive materials.

Away from the nuclear industry, robotically integrated XRF and Raman spectroscopy technologies could be applicable in alternative arenas. Municipal waste sorting and recycling demands similar

material classification techniques. Hence, it is easy to see how the technology developed within this thesis may be quickly applied to such a setting.

BIBLIOGRAPHY

- [1] “Climate change and nuclear power,” *CLIMATE CHANGE AND NUCLEAR POWER 2020 INTERNATIONAL ATOMIC ENERGY AGENCY*, vol. STI/PUB/1911, 2020.
- [2] I. Pioro, R. Duffey, P. Kirillov, and R. Pioro, “Pros and cons of commercial reactor designs: Part 2—current status and future trends in the world nuclear-power industry and technical considerations of nuclear-power reactors,” in *Encyclopedia of Nuclear Energy* (E. Greenspan, ed.), pp. 288–303, Oxford: Elsevier, 2021.
- [3] World Nuclear Association, *Plans For New Reactors Worldwide*.
Online available at <https://www.world-nuclear.org/information-library/current-and-future-generation/plans-for-new-reactors-worldwide.aspx>, 2020.
Accessed: 21/12/2020.
- [4] H. Nam, S. Konishi, and K.-W. Nam, “Comparative analysis of decision making regarding nuclear policy after the fukushima dai-ichi nuclear power plant accident: Case study in germany and japan,” *Technology in Society*, vol. 67, p. 101735, 2021.
- [5] M. Takahashi, G. Shaw, and F. Coppin, “Special issue: Radioactive contamination in forest ecosystems: From chernobyl to fukushima,” *Journal of Environmental Radioactivity*, vol. 161, p. 1, 2016.
Special Issue: Radioactive contamination in forest ecosystems: From Chernobyl to Fukushima.
- [6] W. Isard, “Some Economic Implications of Atomic Energy¹,” *The Quarterly Journal of Economics*, vol. 62, pp. 202–228, 02 1948.
- [7] P. Lappi and J. Lintunen, “From cradle to grave? on optimal nuclear waste disposal,” *Energy Economics*, vol. 103, p. 105556, 2021.
- [8] K. Ray and M. Stick, “Chapter 32 - radiation and health effects,” in *Handbook of Toxicology of Chemical Warfare Agents (Second Edition)* (R. C. Gupta, ed.), pp. 431–446, Boston: Academic Press, second edition ed., 2015.

BIBLIOGRAPHY

- [9] Nuclear Decommissioning Authority, “Geological Disposal Waste Package Evolution Status Report,” tech. rep., Nuclear Decommissioning Authority, 3 2016.
accessed: 06/01/2021.
- [10] “The management of higher activity radioactive waste on nuclear licensed sites,” *Joint guidance from the Office for Nuclear Regulation, the Environment Agency, the Scottish Environment Protection Agency and Natural Resources Wales to nuclear licensees*, 2021.
- [11] UK Government, *Sort and segregate nuclear waste: phase 1 (SBRI competition)*.
Online available at <https://apply-for-innovation-funding.service.gov.uk/competition/685/overview#supporting-information>, 2020.
Accessed: 14/08/2021.
- [12] B. Busby, “Chapter 44 - radiation,” in *Information Resources in Toxicology (Fourth Edition)* (P. Wexler, S. G. Gilbert, P. J. Hakkinen, and A. Mohapatra, eds.), pp. 395–400, San Diego: Academic Press, fourth edition ed., 2009.
- [13] S. Savage and J. Schüz, “Environmental chemicals and childhood cancer,” in *Encyclopedia of Environmental Health* (J. Nriagu, ed.), pp. 336–346, Burlington: Elsevier, 2011.
- [14] O. Desouky, N. Ding, and G. Zhou, “Targeted and non-targeted effects of ionizing radiation,” *Journal of Radiation Research and Applied Sciences*, vol. 8, no. 2, pp. 247–254, 2015.
- [15] J. J. Peirce, R. F. Weiner, and P. A. Vesilind, “Chapter 16 - radioactive waste,” in *Environmental Pollution and Control (Fourth Edition)* (J. J. Peirce, R. F. Weiner, and P. A. Vesilind, eds.), pp. 211–231, Woburn: Butterworth-Heinemann, fourth edition ed., 1998.
- [16] G. R. CHOPPIN, J.-O. LILJENZIN, and J. RYDBERG, “Chapter 4 - unstable nuclei and radioactive decay,” in *Radiochemistry and Nuclear Chemistry (Third Edition)* (G. R. CHOPPIN, J.-O. LILJENZIN, and J. RYDBERG, eds.), pp. 58–93, Woburn: Butterworth-Heinemann, third edition ed., 2002.
- [17] B. Collum, “2 - radiation,” in *Nuclear Facilities* (B. Collum, ed.), pp. 45–60, Woodhead Publishing, 2017.
- [18] N. Jamal AbuAlRoos, M. N. Azman, N. A. Baharul Amin, and R. Zainon, “Tungsten-based material as promising new lead-free gamma radiation shielding material in nuclear medicine,” *Physica Medica*, vol. 78, pp. 48–57, 2020.
- [19] M. F. L’ANNUNZIATA, “1 - nuclear radiation, its interaction with matter and radioisotope decay,” in *Handbook of Radioactivity Analysis (Second Edition)* (M. F. L’Annunziata, ed.), pp. 1–121, San Diego: Academic Press, second edition ed., 2003.

- [20] K. Al Nabhani, "1 - history of the atom and the emergence of nuclear energy," in *Applications of Nuclear and Radioisotope Technology* (K. Al Nabhani, ed.), pp. 1–52, Academic Press, 2021.
- [21] P. Breeze, "Chapter 3 - the basics of nuclear power," in *Nuclear Power* (P. Breeze, ed.), pp. 21–31, Academic Press, 2017.
- [22] R. A. Knief, "Nuclear power reactors," in *Encyclopedia of Physical Science and Technology (Third Edition)* (R. A. Meyers, ed.), pp. 739–761, New York: Academic Press, third edition ed., 2003.
- [23] M. Mourad, H. Saudi, M. Eissa, M. Hassaan, and A. Abdel-Latif M, "Modified austenitic stainless-steel alloys for sheilding nuclear reactors," *Progress in Nuclear Energy*, vol. 142, p. 104009, 2021.
- [24] K. Mehboob, K. Park, and R. Khan, "Quantification of in-containment fission products source term for 1000mwe pwr under loss of coolant accident," *Annals of Nuclear Energy*, vol. 75, pp. 365–376, 2015.
- [25] W. Zhang, Z. Jiao, C. Zhang, linfeng He, G. Xu, X. Chen, and B. Liu, "Diffusion of fission products in nuclear graphite: A review," *Nuclear Materials and Energy*, vol. 29, p. 101100, 2021.
- [26] M. H. Piro, J.-C. Dumas, B. J. Lewis, W. T. Thompson, and F. C. Iglesias, "2.07 - fission product chemistry in oxide fuels," in *Comprehensive Nuclear Materials (Second Edition)* (R. J. Konings and R. E. Stoller, eds.), pp. 173–199, Oxford: Elsevier, second edition ed., 2020.
- [27] World Nuclear Association, *Radioactive Waste Management*.
Online available at <https://world-nuclear.org/information-library/nuclear-fuel-cycle/nuclear-wastes/radioactive-waste-management.aspx>, 2022.
Accessed: 02/02/2022.
- [28] B. Metcalfe and I. Donald, "25 - management of radioactive waste (raw) from nuclear weapons programmes," in *Radioactive Waste Management and Contaminated Site Clean-Up* (W. E. Lee, M. I. Ojovan, and C. M. Jantzen, eds.), Woodhead Publishing Series in Energy, pp. 775–800, Woodhead Publishing, 2013.
- [29] L. Al Attar, B. Safia, B. A. Ghani, and J. Al Abdulah, "Recovery of norm from scales generated by oil extraction," *Journal of Environmental Radioactivity*, vol. 153, pp. 149–155, 2016.

BIBLIOGRAPHY

- [30] International Atomic Energy Authority, “Strategy and methodology for radioactive waste characterization.” https://www-pub.iaea.org/MTCD/publications/PDF/te_1537_web.pdf, 2007.
Accessed: 31/01/2022.
- [31] Nuclear Decommissioning Authority, *Integrated Waste Management: Radioactive Waste Strategy*.
Online available at https://assets.publishing.service.gov.uk/government/uploads/system/uploads/attachment_data/file/838828/Radioactive_Waste_Strategy_September_2019.pdf, 2019.
Accessed: 24/07/2020.
- [32] UK Government, *About us - Sellafield Ltd*.
Online available at <https://www.gov.uk/government/organisations/sellafield-ltd/about>, 2022.
Accessed: 24/02/2022.
- [33] N. D. Authority, *Spent Fuel Management: Life Cycle Analysis Model. Final Report*.
Online available at https://assets.publishing.service.gov.uk/government/uploads/system/uploads/attachment_data/file/457785/Spent_Fuel_Management__Life_Cycle_Analysis_Model_Report_September_2007.pdf, 2007.
Accessed: 24/03/2022.
- [34] HM Government UK, *The UK's Nuclear Future*.
Online available at https://assets.publishing.service.gov.uk/government/uploads/system/uploads/attachment_data/file/168048/bis-13-627-nuclear-industrial-strategy-the-uks-nuclear-future.pdf, 2013.
Accessed: 22/03/2021.
- [35] S. Wallbridge, A. Banford, and A. Azapagic, “Life cycle environmental impacts of decommissioning magnox nuclear power plants in the uk,” *The International Journal of Life Cycle Assessment*, vol. 18, pp. 990–1008, Jun 2013.
- [36] Nuclear Decommissioning Authority, “Nuclear Decommissioning Authority Strategy,” tech. rep., Nuclear Decommissioning Authority, 4 2016.
accessed: 12/04/2021.
- [37] A. Paulillo, J. M. Dodds, A. Milliken, S. J. Palethorpe, and P. Lettieri, “The environmental impacts of reprocessing used nuclear fuels: A uk case study,” *Sustainable Materials and Technologies*, vol. 25, p. e00186, 9 2020.

- [38] K. W. J. Barnham, J. Nelson, and R. A. Stevens, "Did civil reactors supply plutonium for weapons?," *Nature*, vol. 407, pp. 833–834, Oct 2000.
- [39] D. Horsley and P. Hallington, "Nuclear power and the management of the radioactive waste legacy," *Chemical Engineering Research and Design*, vol. 83, no. 7, pp. 773–776, 2005. 7th World Congress of Chemical Engineering.
- [40] R. Meservey, "25 - decommissioning of legacy nuclear waste sites: Idaho national laboratory, usa," in *Nuclear Decommissioning* (M. Laraia, ed.), Woodhead Publishing Series in Energy, pp. 745–776, Woodhead Publishing, 2012.
- [41] M. Sneve, M. Kiselev, and N. Shandala, "Radio-ecological characterization and radiological assessment in support of regulatory supervision of legacy sites in northwest russia," *Journal of Environmental Radioactivity*, vol. 131, pp. 110–118, 2014.
SPECIAL ISSUE: Environmental Radioactivity: Legacy Sites, Chernobyl and Fukushima; selected papers from the 12th International Conference on the Biogeochemistry of Trace Elements (ICOBTE).
- [42] Étienne Vernaz and J. Bruezière, "History of nuclear waste glass in france," *Procedia Materials Science*, vol. 7, pp. 3–9, 2014.
2nd International Summer School on Nuclear Glass Wasteform: Structure, Properties and Long-Term Behavior, SumGLASS 2013.
- [43] Nuclear Decommissioning Authority, "Integrated Waste Management Radioactive Waste Strategy," tech. rep., Nuclear Decommissioning Authority, 9 2019.
accessed: 19/10/2021.
- [44] K. Fujiwara, J. Tani, M. Hironaga, and Y. Tanaka, "Corrosion behaviour of aluminium under simulated environmental conditions of low-level waste," *Corrosion Engineering, Science and Technology*, vol. 52, no. sup1, pp. 162–165, 2017.
- [45] Sellafield Ltd, *Sort and Segregate Nuclear Waste: specification* .
Online available at <https://www.gov.uk/government/publications/sort-and-segregate-\protect\@normalcr\relaxnuclear-waste-specification/sort-and-segregate-nuclear-waste-specification>, 2020.
Accessed: 21/12/2020.
- [46] R. Orr, H. Godfrey, C. Broan, D. Goddard, G. Woodhouse, P. Durham, A. Diggle, and J. Bradshaw, "Formation and physical properties of uranium hydride under conditions relevant to metallic fuel and nuclear waste storage," *Journal of Nuclear Materials*, vol. 477, pp. 236–245, 8 2016.

BIBLIOGRAPHY

- [47] A. Averill, J. Ingram, P. Holborn, P. Battersby, and C. Benson, "Ignition of flammable hydrogen/air mixtures by high mass mechanical impact of magnox contaminated surfaces," *International Journal of Hydrogen Energy*, vol. 45, no. 4, pp. 3372–3380, 2020.
- [48] M. I. O. R. O. A. Rahman, R. Z. Rakhimov and N. R. Rakhimov, *Cementitious Materials for Nuclear Waste Immobilization*. John Wiley & sons, 2015.
- [49] DEFRA, "Policy for the long term management of solid low level radioactive waste in the United Kingdom." https://assets.publishing.service.gov.uk/government/uploads/system/uploads/attachment_data/file/254393/Low_level_waste_policy.pdf, 2007.
Accessed: 01/06/2020.
- [50] Nuclear Decommissioning Authority, "Uk strategy for the management of solid low level waste from the nuclear industry," tech. rep., Nuclear Decommissioning Authority, 2016.
- [51] A. Basso, V. Hlaváč, J. Hůlka, M. Jilich, P. Krsek, S. Malassiotis, R. Molfino, V. Smutný, L. Wagner, and M. Zoppi, "Towards intelligent autonomous sorting of unclassified nuclear wastes," *Procedia Manufacturing*, vol. 11, pp. 389 – 396, 2017.
27th International Conference on Flexible Automation and Intelligent Manufacturing, FAIM2017, 27-30 June 2017, Modena, Italy.
- [52] Nuclear Decommissioning Authority, "Ukrwi inventory report, 2019," tech. rep., Nuclear Decommissioning Authority, 2019.
- [53] International Atomic Energy Authority, "National waste programme: International approaches to radioactive waste classification." https://assets.publishing.service.gov.uk/government/uploads/system/uploads/attachment_data/file/697667/NWP-REP-134-International-Approaches-to-RW-Classification-Oct-2016.pdf.
Accessed: 06/07/2019.
- [54] F. Livens and J. Wilson, "Update on higher activity waste management," tech. rep., Nuclear Decommissioning Authority, 2014.
- [55] G. Black, A. N. Jones, and B. J. Marsden, "Development of an experimental and simulation process to determine the end of life radionuclide inventory of uk irradiated graphite waste," in *Modelling and Measuring Reactor Core Graphite Properties and Performance*, pp. 39–43, The Royal Society of Chemistry, 2013.
- [56] Nuclear Decommissioning Authority, "The long-term management of reactor core graphite waste credible options(gate a)," tech. rep., Nuclear Decommissioning Authority, 2013.

- [57] Nuclear Decommissioning Authority, *Radioactive Wastes in the UK: Context and Methodology Report*.
Online available at <https://ukinventory.nda.gov.uk/>, 2016.
Accessed: 30/12/2020.
- [58] “Status and trends in spent fuel and radioactive waste management,” *IAEA Nuclear Energy Series*, vol. No. NW-T-1.14, 2018.
- [59] I. A. E. Authority, *METHODS FOR THE MINIMIZATION OF RADIOACTIVE WASTE FROM DECONTAMINATION AND DECOMMISSIONING OF NUCLEAR FACILITIES*.
Online available at https://www-pub.iaea.org/MTCD/Publications/PDF/TRS401_scr.pdf, 2001.
Accessed: 21/05/2022.
- [60] D. Bradbury and B. Rottner, “Treatment of magnesium radioactive waste - 13011,” in *Treatment of magnesium radioactive waste - 13011*, 5 International Conference and Exhibition on Decommissioning Challenges - Industrial Reality and Prospects, (France), 2013.
- [61] C. A. Stitt, C. Paraskevoulakos, A. Banos, N. J. Harker, K. R. Hallam, H. Pullin, A. Davenport, S. Street, and T. B. Scott, “In-situ, time resolved monitoring of uranium in bfs:opc grout. part 2: Corrosion in water,” *Scientific Reports*, vol. 8, p. 9282, Jun 2018.
- [62] Nuclear Decommissioning Authority, *NDA Report: NDA interactions with Waste Producers on plans for packaging radioactive wastes. NDA Report no. NDA/RWMD/008*.
Online available at <https://www.rwm.nda.gov.uk>, 2008.
Accessed: 31/01/2022.
- [63] NDA and RWM, “Guidance on the application of the specification for stillages for use in the transport and disposal of 500 litre drum waste packages,” tech. rep., NDA and RWM, 10 2015.
- [64] Nuclear Decommissioning Authority, “2019 UK Radioactive Waste Inventory,” tech. rep., UK Radioactive Waste Inventory, 12 2019.
- [65] R. Waste Management, *Geological Disposal Generic Transport Safety Case-Main Report*. Nuclear Decommissioning Authority, 2016.
- [66] S. P.K.J. Smith and G. Ruloff, “Berkeley vault decommissioning – in a commercial environment,” in *Waste Management Symposia*, Waste Management Symposia, 1999.
- [67] BBC, *Nuclear waste removal begins 30 years after power station closure*.

BIBLIOGRAPHY

- Online available at <https://www.bbc.co.uk/news/uk-england-somerset-50866867>, 2021.
Accessed: 25/03/2021.
- [68] Nuclear Decommissioning Authority, “Industry guidance interim storage of higher activity waste packages – integrated approach,” tech. rep., Nuclear Decommissioning Authority, 2017.
- [69] Nuclear Decommissioning Authority, *Geological Disposal*.
Online available at <https://www.gov.uk/guidance/geological-disposal>, 2020.
Accessed: 18/02/2021.
- [70] Nuclear Decommissioning Authority, *Geological Disposal*.
Online available at <https://www.gov.uk/guidance/gdf-geological-disposal-facility>, 2020.
Accessed: 18/02/2021.
- [71] Gov.uk, *LLW Repository Ltd*.
Online available at <https://www.gov.uk/government/organisations/low-level-waste-repository-ltd/about>, 2022.
Accessed: 24/05/2022.
- [72] International Atomic Energy Authority, “Status and trends in spent fuel and radioactive waste management.” <https://www.iaea.org/publications/11173/status-and-trends-in-spent-fuel-and-radioactive-waste-management>.
Accessed: 07/06/2019.
- [73] I. A. E. Authority, *IAEA Power Reactor Information System (PRIS)*.
Online available at <https://pris.iaea.org/PRIS/WorldStatistics/ShutdownReactorsByCountry.aspx>, 2020.
Accessed: 21/12/2020.
- [74] TECH BRIEFS, *Tech Briefs: Robots Bring Airplane Production Up to Speed*.
<https://www.techbriefs.com/component/content/article/tb/supplements/md/features/applications/33714>, 2021.
Accessed: 25/01/2021.
- [75] Fanuc, *Fanuc: Robotics in food processing*.
<https://www.fanuc.eu/uk/en/customer-cases/food-processing-robot>, 2021.
Accessed: 25/01/2021.
- [76] KUKA AG., *KUKA AG*.
Online available at <https://www.kuka.com/>, 2022.

Accessed: 24/02/2022.

- [77] FANUC, *FANUC*.
Online available at <https://www.fanuc.eu/uk/en>, 2022.
Accessed: 24/02/2022.
- [78] ABB, *ABB*.
Online available at <https://global.abb/group/en>, 2022.
Accessed: 24/02/2022.
- [79] Kinova, *Kinova*.
Online available at <https://www.kinovarobotics.com/>, 2022.
Accessed: 24/02/2022.
- [80] Association for Advanced Automation, “The Art of Industrial Painting with Robots,” 2013.
Accessed: 05/07/2021.
- [81] Qinetiq, “Multi-Mission Explosive Ordnance Disposal Robot,” 2021.
Accessed: 05/07/2021.
- [82] K. Zhang, C. Hutson, J. Knighton, G. Herrmann, and T. Scott, “Radiation tolerance testing methodology of robotic manipulator prior to nuclear waste handling,” *Frontiers in Robotics and AI*, vol. 7, p. 6, 2020.
- [83] O. Tokatli, P. Das, R. Nath, L. Pangione, A. Altobelli, G. Burroughes, E. T. Jonasson, M. F. Turner, and R. Skilton, “Robot-assisted glovebox teleoperation for nuclear industry,” *Robotics*, vol. 10, no. 3, 2021.
- [84] L. Pérez, Rodríguez, N. Rodríguez, R. Usamentiaga, and D. F. García, “Robot guidance using machine vision techniques in industrial environments: A comparative review,” *Sensors*, vol. 16, no. 3, 2016.
- [85] B. Chappell, A. Pramanik, A. Basak, P. Sarker, C. Prakash, S. Debnath, and S. Shankar, “Processing household plastics for recycling – a review,” *Cleaner Materials*, vol. 6, p. 100158, 2022.
- [86] J. Lim, Y. Ahn, and J. Kim, “Optimal sorting and recycling of plastic waste as a renewable energy resource considering economic feasibility and environmental pollution,” *Process Safety and Environmental Protection*, vol. 169, pp. 685–696, 2023.
- [87] E. Strollo, G. Sansonetti, M. C. Mayer, C. Limongelli, and A. Micarelli, “An ai-based approach to automatic waste sorting,” in *HCI International 2020 - Posters* (C. Stephanidis and M. Antona, eds.), (Cham), pp. 662–669, Springer International Publishing, 2020.

BIBLIOGRAPHY

- [88] P. L. R. M. J. C. J. Hastings, C. Zimmerman, “Preparation of waste fingerprints for the miscellaneous beta gamma waste feeds to the box encapsulation plant at sellafield,” in *Waste Management Symposia*, Waste Management Symposia, 12016.
- [89] J. Harken, “Remote retrieval, disruption and processing of legacy nuclear waste,” in *Waste Management Symposia*, Waste Management Symposia, 12016.
- [90] R. Smith, E. Cucco, and C. Fairbairn, “Robotic development for the nuclear environment: Challenges and strategy,” *Robotics*, vol. 9, no. 4, 2020.
- [91] Nuclear Decommissioning Authority, “Radioactive wastes in the uk:a summary of the 2016 inventory.” <http://ukinventory.nda.gov.uk/wp-content/uploads/sites/18/2017/03/High-Level-Summary-UK-Radwaste-Inventory-2016.pdf>. Accessed: 06/07/2019.
- [92] B. Tondu, S. Ippolito, J. Guiochet, and A. Daidié, “A seven-degrees-of-freedom robot-arm driven by pneumatic artificial muscles for humanoid robots,” *International Journal of Robotics Research*, vol. 24, 01 2005.
- [93] J. Denavit and R. S. Hartenberg, “A kinematic notation for lower-pair mechanisms based on matrices,” *Trans. ASME E, Journal of Applied Mechanics*, vol. 22, pp. 215–221, June 1955.
- [94] H. Wang, H. Qi, M. Xu, Y. Tang, J. Yao, X. Yan, and M. Li, “Research on the relationship between classic denavit-hartenberg and modified denavit-hartenberg,” in *2014 Seventh International Symposium on Computational Intelligence and Design*, vol. 2, pp. 26–29, 2014.
- [95] I. A. Vasilyev and A. M. Lyashin, “Analytical solution to inverse kinematic problem for 6-dof robot-manipulator,” *Automation and Remote Control*, vol. 71, pp. 2195–2199, Oct 2010.
- [96] N. Liqing and H. Qingjiu, “Inverse kinematics for 6-dof manipulator by the method of sequential retrieval,” in *Proceedings of the 1st International Conference on Mechanical Engineering and Material Science (MEMS 2012)*, pp. 600–603, Atlantis Press, 2012/12.
- [97] M. Safeea, *Safe Collaborative Robotic Manipulators*. PhD thesis, 10 2020.
- [98] S. Mokaram, J. M. Aitken, U. Martinez-Hernandez, I. Eimontaite, D. Cameron, J. Rolph, I. Gwilt, O. McAree, and J. Law, “A ros-integrated api for the kuka lbr iiwa collaborative robot**the authors acknowledge support from the epsrc centre for innovative manufacturing in intelligent automation, in undertaking this research work under grant

reference number ep/i033467/1, and the university of sheffield impact, innovation and knowledge exchange grant "human robot interaction development". equipment has been provided under the epsrc great technologies capital call: Robotics and autonomous systems.,” *IFAC-PapersOnLine*, vol. 50, no. 1, pp. 15859–15864, 2017.

20th IFAC World Congress.

- [99] KUKA, *KUKA LBR iiwa*.
<https://www.kuka.com/en-gb/products/robotics-systems/industrial-robots/lbr-iiwa>, 2021.
Accessed: 10/02/2021.
- [100] X. Chen, Y. Chen, X. Song, W. Liang, and Y. Wang, “Calibration of stereo cameras with a marked-crossed fringe pattern,” *Optics and Lasers in Engineering*, vol. 147, p. 106733, 2021.
- [101] Intel, *RealSense L515 Specifications*.
<https://www.intelrealsense.com/depth-camera-d435/>, 2021.
Accessed: 10/10/2021.
- [102] Intel, *RealSense L515 Specifications*.
<https://www.intelrealsense.com/lidar-camera-l515/>, 2021.
Accessed: 10/10/2021.
- [103] E. W. Weisstein, “Affine transformation.”
- [104] G. Bradski, “The OpenCV Library,” *Dr. Dobb’s Journal of Software Tools*, 2000.
- [105] B. Shirinzadeh, P. L. Teoh, Y. Tian, M. M. Dalvand, Y. Zhong, and H. C. Liaw, “Laser interferometry-based guidance methodology for high precision positioning of mechanisms and robots,” *Robot. Comput.-Integr. Manuf.*, vol. 26, p. 74–82, feb 2010.
- [106] Blue Robotics, *Blue Robotics*.
Online available at <https://bluerobotics.com/store/thrusters/grippers/newton-gripper-asm-r2-rp/>, 2022.
Accessed: 06/06/2022.
- [107] X.-Y. Gong, H. Su, D. Xu, Z. Zhang, F. Shen, and H.-B. Yang, “An overview of contour detection approaches,” *International Journal of Automation and Computing*, vol. 15, pp. 1–17, 06 2018.
- [108] M. MD, S. MS, P. MPH, M. MD, M. MD, M. Mikulski, S. Leonard, W. Sanderson, P. Hartley, N. Sprince, and L. Fuortes, “Risk of beryllium sensitization in a low-exposed former nuclear weapons cohort from the cold war era,” *American Journal of Industrial Medicine*, vol. 54, pp. 194 – 204, 03 2011.

BIBLIOGRAPHY

- [109] G. B. Kim, S. T. P. Boyd, R. H. Cantor, A. S. Voyles, J. T. Morrell, L. A. Bernstein, and S. Friedrich, “A new measurement of the 60 keV emission from am-241 using metallic magnetic calorimeters,” in *A New Measurement of the 60 keV Emission from Am-241 Using Metallic Magnetic Calorimeters*, vol. 199, pp. 1055–1061, Springer, May 2020.
- [110] S. J. S. Ryde, “Practical gamma-ray spectrometry g. gilmore and j. d. hemingway published by john wiley & sons, chichester, 1995 isbn 0-471-95150-1 price £60.00; 314 pp,” *Rapid Communications in Mass Spectrometry*, vol. 9, no. 12, pp. 1225–1225, 1995.
- [111] G. Knoll, *Radiation Detection and Measurement*. Wiley, 2000.
- [112] K. Buchtela, “Radiochemical methods | gamma-ray spectrometry,” in *Encyclopedia of Analytical Science (Third Edition)* (P. Worsfold, C. Poole, A. Townshend, and M. Miró, eds.), pp. 15–22, Oxford: Academic Press, third edition ed., 2019.
- [113] B. Akça, B. Gürbulak, and S. Zeki Erzeneoğlu, “Effect of voltages on ray linear attenuation coefficients for some semiconductors,” *Radiation Physics and Chemistry*, vol. 179, p. 109208, 2021.
- [114] J. BIRKS, “Chapter 2 - absorption of the incident radiation,” in *The Theory and Practice of Scintillation Counting* (J. BIRKS, ed.), International Series of Monographs in Electronics and Instrumentation, pp. 15–38, Pergamon, 1964.
- [115] G. R. CHOPPIN, J.-O. LILJENZIN, and J. RYDBERG, “Chapter 6 - absorption of nuclear radiation,” in *Radiochemistry and Nuclear Chemistry (Third Edition)* (G. R. CHOPPIN, J.-O. LILJENZIN, and J. RYDBERG, eds.), pp. 123–165, Woburn: Butterworth-Heinemann, third edition ed., 2002.
- [116] S. N. Ahmed, “3 - gas-filled detectors,” in *Physics and Engineering of Radiation Detection (Second Edition)* (S. N. Ahmed, ed.), pp. 157 – 231, Elsevier, second edition ed., 2015.
- [117] F. A. Mettler and M. J. Guiberteau, “2 - instrumentation and quality control,” in *Essentials of Nuclear Medicine and Molecular Imaging (Seventh Edition)* (F. A. Mettler and M. J. Guiberteau, eds.), pp. 19–59, Philadelphia: Elsevier, seventh edition ed., 2019.
- [118] F. A. Mettler and M. J. Guiberteau, “2 - instrumentation and quality control,” in *Essentials of Nuclear Medicine and Molecular Imaging (Seventh Edition)* (F. A. Mettler and M. J. Guiberteau, eds.), pp. 19–59, Philadelphia: Elsevier, seventh edition ed., 2019.
- [119] S. Usman and A. Patil, “Radiation detector deadtime and pile up: A review of the status of science,” *Nuclear Engineering and Technology*, vol. 50, no. 7, pp. 1006 – 1016, 2018.

- [120] D. Grey, R. Sood, and R. Manchanda, “Resolution and spectral characteristics of ultra high pressure proportional counters using various quench gases,” *Nuclear Instruments and Methods in Physics Research Section A: Accelerators, Spectrometers, Detectors and Associated Equipment*, vol. 527, no. 3, pp. 493 – 511, 2004.
- [121] P. Lecoq, “Scintillation detectors for charged particles and photons,” *Particle Physics Reference Library*, pp. 45–89, 2020.
- [122] M. Kobayashi, Y. Usuki, M. Ishii, and M. Nikl, “Doping pbwo4 with different ions to increase the light yield,” *Nuclear Instruments and Methods in Physics Research Section A: Accelerators, Spectrometers, Detectors and Associated Equipment*, vol. 486, no. 1, pp. 170–175, 2002.
- Proceedings of the 6th International Conference on Inorganic Scintillators and their Use in Scientific and Industrial Applications.
- [123] Z. Lin, B. Hautefeuille, S.-H. Jung, J. Moon, and J.-G. Park, “The design of a scintillation system based on sipms integrated with gain correction functionality,” *Nuclear Engineering and Technology*, vol. 52, no. 1, pp. 164 – 169, 2020.
- [124] R. yuan Zhu, “Radiation damage in scintillating crystals,” *Nuclear Instruments and Methods in Physics Research Section A: Accelerators, Spectrometers, Detectors and Associated Equipment*, vol. 413, no. 2, pp. 297–311, 1998.
- [125] R. yuan Zhu, “Radiation damage in scintillating crystals,” *Nuclear Instruments and Methods in Physics Research Section A: Accelerators, Spectrometers, Detectors and Associated Equipment*, vol. 413, no. 2, pp. 297–311, 1998.
- [126] L. A. Franks, B. A. Brunett, R. W. Olsen, D. S. Walsh, G. Vizkelethy, J. I. Trombka, B. L. Doyle, and R. B. James, “Radiation damage measurements in room-temperature semiconductor radiation detectors,” *Nuclear Instruments and Methods in Physics Research Section A: Accelerators, Spectrometers, Detectors and Associated Equipment*, vol. 428, no. 1, pp. 95–101, 1999.
- [127] P. Martin, O. Payton, Y. Yamashiki, D. Richards, and T. Scott, “High-resolution radiation mapping to investigate fdnpp derived contaminant migration,” *Journal of Environmental Radioactivity*, vol. 164, pp. 26 – 35, 2016.
- [128] D. Connor, P. Martin, N. Smith, L. Payne, C. Hutson, O. Payton, Y. Yamashiki, and T. Scott, “Application of airborne photogrammetry for the visualisation and assessment of contamination migration arising from a fukushima waste storage facility,” *Environmental Pollution*, vol. 234, pp. 610 – 619, 2018.

BIBLIOGRAPHY

- [129] B. Bird, M. Nancekievill, A. West, J. Hayman, C. Ballard, W. Jones, S. Ross, T. Wild, T. Scott, and B. Lennox, “Vega—a small, low cost, ground robot for nuclear decommissioning,” *Journal of Field Robotics*, 11 2021.
- [130] G. F. Knoll, “Nuclear radiation detection devices,” in *Encyclopedia of Physical Science and Technology (Third Edition)* (R. A. Meyers, ed.), pp. 763 – 773, New York: Academic Press, third edition ed., 2003.
- [131] A. Syntfeld-Każuch, P. Sibczyński, M. Moszyński, A. Gektin, W. Czarnacki, M. Grodzicka, J. Iwanowska, M. Szawłowski, T. Szczęśniak, and L. Świdorski, “Energy resolution of csi(na) scintillators,” *Radiation Measurements*, vol. 45, no. 3, pp. 377–379, 2010.
Proceedings of the 7th European Conference on Luminescent Detectors and Transformers of Ionizing Radiation (LUMDETR 2009).
- [132] Saint-Gobain, *CsI(Tl), CsI(Na) Cesium Iodide Scintillation Material Data Sheet*.
Online available at <https://www.crystals.saint-gobain.com/sites/imdf.crystals.com/files/documents/csitl-and-na-material-data-sheet.pdf>, 2021.
Accessed: 23/02/2021.
- [133] N. Balamurugan, A. Arulchakkaravarthi, S. Selvakumar, M. Lenin, R. Kumar, S. Muralithar, K. Sivaji, and P. Ramasamy, “Growth and characterization of undoped and thallium doped cesium iodide single crystals,” *Journal of Crystal Growth*, vol. 286, no. 2, pp. 294–299, 2006.
- [134] Kromek, *SIGMA Compact CsI Scintillation Spectrometer Specification Sheet*.
Online available at <https://www.kromek.com/product/sigma-scintillator-detectors/>, 2020.
Accessed: 24/11/2020.
- [135] H. V. Piltingsrud, “The low-temperature scintillation properties of bismuth germanate and its application to high-energy gamma radiation imaging devices,” *Journal of Nuclear Medicine*, vol. 20, no. 12, pp. 1279–1285, 1979.
- [136] S. Ra, S. Kim, H. J. Kim, H. Park, S. Lee, H. Kang, and S. Doh, “Luminescence and scintillation properties of a cbr₃ single crystal,” *IEEE Transactions on Nuclear Science*, vol. 55, no. 3, pp. 1221–1224, 2008.
- [137] R. Billnert, S. Oberstedt, E. Andreotti, M. Hult, G. Marissens, and A. Oberstedt, “New information on the characteristics of 1in.×1in. cerium bromide scintillation detectors,” *Nuclear Instruments and Methods in Physics Research Section A: Accelerators, Spectrometers, Detectors and Associated Equipment*, vol. 647, no. 1, pp. 94–99, 2011.

- [138] Saint-Gobain, *Lanthanum Bromide and Enhanced Lanthanum Bromide Data Sheet*.
Online available at <https://www.crystals.saint-gobain.com/sites/imdf.crystals.com/files/documents/lanthanum-material-data-sheet.pdf>, 2021.
Accessed: 23/02/2021.
- [139] R. Nicolini, F. Camera, N. Blasi, S. Brambilla, R. Bassini, C. Boiano, A. Bracco, F. Crespi, O. Wieland, G. Benzoni, S. Leoni, B. Million, D. Montanari, and A. Zalite, “Investigation of the properties of a 1”×1” labr3:ce scintillator,” *Nuclear Instruments and Methods in Physics Research Section A: Accelerators, Spectrometers, Detectors and Associated Equipment*, vol. 582, no. 2, pp. 554 – 561, 2007.
- [140] A. Phunpueok, W. Chewpraditkul, P. Limsuwan, and C. Wanarak, “Light output and energy resolution of lu0.7y0.3alo3:ce and lu1.95y0.05sio5:ce scintillators,” *Procedia Engineering*, vol. 32, pp. 564 – 570, 2012.
ISEEC.
- [141] I. Mouhti, A. Elanique, M. Messous, A. Benahmed, J. McFee, Y. Elgoub, and P. Griffith, “Characterization of csi(tl) and lyso(ce) scintillator detectors by measurements and monte carlo simulations,” *Applied Radiation and Isotopes*, vol. 154, p. 108878, 2019.
- [142] Nuclear Decommissioning Authority, “Waste package specification and guidance documentation: Specification for waste packages containing low heat generating waste: Part c – fundamental requirements,” tech. rep., Nuclear Decommissioning Authority, 2020.
https://assets.publishing.service.gov.uk/government/uploads/system/uploads/attachment_data/file/935717/WPS_220_01_Part_C_-_Specification_for_Waste_Packages_Containing_Low_Heat_Generating_Waste.pdf.
- [143] J. Zieba-Palus, R. Borusiewicz, and M. Kunicki, “Praxis—combined μ -raman and μ -xrf spectrometers in the examination of forensic samples,” *Forensic Science International*, vol. 175, no. 1, pp. 1–10, 2008.
- [144] I. W. Croudace, L. Löwemark, R. Tjallingii, and B. Zolitschka, “High resolution xrf core scanners: A key tool for the environmental and palaeoclimate sciences,” *Quaternary International*, vol. 514, pp. 1–4, 2019.
Advances in Data Quantification and Application of high resolution XRF Core Scanners.
- [145] G. Balasubramanian and S. A. Muthukumaraswamy, “Element analysis with fundamental parameters using an xrf spectrum analysis matlab algorithm,” in *Element Analysis with Fundamental Parameters using an XRF Spectrum Analysis MATLAB Algorithm*, 2016.
- [146] A. Girão, G. Caputo, and M. Ferro, *Application of Scanning Electron Microscopy-Energy Dispersive X-ray Spectroscopy (SEM-EDS)*, ch. 6, pp. 153–166.

BIBLIOGRAPHY

Elsevier, 06 2017.

- [147] L. V. Godfrey and J. B. Glass, "Chapter twenty-two - the geochemical record of the ancient nitrogen cycle, nitrogen isotopes, and metal cofactors," in *Research on Nitrification and Related Processes, Part A* (M. G. Klotz, ed.), vol. 486 of *Methods in Enzymology*, pp. 483–506, Academic Press, 2011.
- [148] K. Wilkinson, J. Lundkvist, G. Seisenbaeva, and V. Kessler, "New tabletop sem-eds-based approach for cost-efficient monitoring of airborne particulate matter," *Environmental Pollution*, vol. 159, no. 1, pp. 311–318, 2011.
- [149] S. C. Wilschefski and M. R. Baxter, "Inductively coupled plasma mass spectrometry: Introduction to analytical aspects," *The Clinical biochemist. Reviews*, vol. 40, pp. 115–133, Aug 2019.
- [150] C. Streli, P. Wobrauschek, and P. Kregsamer, "X-ray fluorescence spectroscopy, applications," in *Encyclopedia of Spectroscopy and Spectrometry* (J. C. Lindon, ed.), pp. 2478–2487, Oxford: Elsevier, 1999.
- [151] T. A. Callcott, "13 - soft x-ray fluorescence spectroscopy," in *Vacuum Ultraviolet Spectroscopy* (J. Samson and D. Ederer, eds.), pp. 279 – 300, Burlington: Academic Press, 1999.
- [152] F. J. A. Rebollo, *XRF: X-Ray Fluorescence Spectroscopy | Hi Rel Parts*.
Online available at <https://wpo-altertechnology.com/xrf-x-ray-fluorescence-spectroscopy-hi-rel-parts/>, 2022.
Accessed: 11/06/2022.
- [153] K. Janssens, G. Vittiglio, I. Deraedt, A. Aerts, B. Vekemans, L. Vincze, F. Wei, I. De Ryck, O. Schalm, F. Adams, A. Rindby, A. Knöchel, A. Simionovici, and A. Snigirev, "Use of microscopic xrf for non-destructive analysis in art and archaeometry," *X-Ray Spectrometry*, vol. 29, no. 1, pp. 73–91, 2000.
- [154] K. Janssens, M. Alfeld, G. Van der Snickt, W. De Nolf, F. Vanmeert, M. Radepont, L. Monico, J. Dik, M. Cotte, G. Falkenberg, C. Miliani, and B. G. Brunetti, "The use of synchrotron radiation for the characterization of artists' pigments and paintings," *Annual Review of Analytical Chemistry*, vol. 6, no. 1, pp. 399–425, 2013.
PMID: 23772661.
- [155] V. Thomsen and D. Schatzlein, "Advances in field-portable xrf," *Spectroscopy -Springfield then Eugene then Duluth-*, vol. 17, 07 2002.
- [156] P. Lechner, C. Fiorini, R. Hartmann, J. Kemmer, N. Krause, P. Leutenegger, A. Longoni, H. Soltau, D. Stötter, R. Stötter, L. Strüder, and U. Weber, "Silicon drift detectors for

- high count rate x-ray spectroscopy at room temperature,” *Nuclear Instruments and Methods in Physics Research Section A: Accelerators, Spectrometers, Detectors and Associated Equipment*, vol. 458, no. 1, pp. 281–287, 2001.
- Proc. 11th Int. Workshop on Room Temperature Semiconductor X- and Gamma-Ray Detectors and Associated Electronics.
- [157] A. Longoni, C. Fiorini, P. Leutenegger, S. Sciuti, G. Fronterotta, L. Strüder, and P. Lechner, “A portable xrf spectrometer for non-destructive analyses in archaeometry,” *Nuclear Instruments and Methods in Physics Research Section A: Accelerators, Spectrometers, Detectors and Associated Equipment*, vol. 409, no. 1, pp. 407–409, 1998.
- [158] A. Turner and A. Taylor, “On site determination of trace metals in estuarine sediments by field-portable-xrf,” *Talanta*, vol. 190, pp. 498 – 506, 2018.
- [159] A. Turner, “In situ elemental characterisation of marine microplastics by portable xrf,” *Marine Pollution Bulletin*, vol. 124, no. 1, pp. 286 – 291, 2017.
- [160] A. Turner, H. Poon, A. Taylor, and M. T. Brown, “In situ determination of trace elements in fucus spp. by field-portable-xrf,” *Science of The Total Environment*, vol. 593-594, pp. 227 – 235, 2017.
- [161] J. Qin, M. S. Kim, K. Chao, S. Dhakal, B.-K. Cho, S. Lohumi, C. Mo, Y. Peng, and M. Huang, “Advances in raman spectroscopy and imaging techniques for quality and safety inspection of horticultural products,” *Postharvest Biology and Technology*, vol. 149, pp. 101 – 117, 2019.
- [162] J. R. Ferraro, K. Nakamoto, and C. W. Brown, “Acknowledgments,” in *Introductory Raman Spectroscopy (Second Edition)*, p. xi, San Diego: Academic Press, second edition ed., 2003.
- [163] E. Izake, “Forensic and homeland security applications of modern portable raman spectroscopy,” *Forensic Science International*, vol. 202, no. 1-3, pp. 1–8, 2010.
cited By 114.
- [164] E. Instruments, *What is Raman Spectroscopy?*
Online available at <https://www.edinst.com/blog/what-is-raman-spectroscopy/>,
2022.
Accessed: 11/06/2022.
- [165] G. S. Bumbrah and R. M. Sharma, “Raman spectroscopy – basic principle, instrumentation and selected applications for the characterization of drugs of abuse,” *Egyptian Journal of Forensic Sciences*, vol. 6, no. 3, pp. 209 – 215, 2016.

BIBLIOGRAPHY

- [166] A. Braz, M. López-López, and C. García-Ruiz, “Raman spectroscopy for forensic analysis of inks in questioned documents,” *Forensic Science International*, vol. 232, no. 1, pp. 206 – 212, 2013.
- [167] F. Li, Z. Li, S. Wang, S. Li, Z. Men, S. Ouyang, and C. Sun, “Structure of water molecules from raman measurements of cooling different concentrations of naoh solutions,” *Spectrochimica Acta Part A: Molecular and Biomolecular Spectroscopy*, vol. 183, pp. 425 – 430, 2017.
- [168] R. H. Atalla, U. P. Agarwal, and J. S. Bond, *Raman Spectroscopy*. Berlin, Heidelberg: Springer Berlin Heidelberg, 1992.
- [169] T. H. Sebastian Wachsmann-Hogiu, Tyler Weeks, *Chemical analysis in vivo and in vitro by Raman spectroscopy-from single cells to humans*, vol. 20, pp. 63–73. Elsevier Limited, Feb. 2009.
- [170] D. W. Shipp, F. Sinjab, and I. Notingher, “Raman spectroscopy: techniques and applications in the life sciences,” *Adv. Opt. Photon.*, vol. 9, pp. 315–428, Jun 2017.
- [171] E. Smith and G. Dent, *Modern Raman Spectroscopy: A Practical Approach*. 08 2005.
- [172] D. Le Pevelen, “Nir ft-raman,” in *Encyclopedia of Spectroscopy and Spectrometry (Third Edition)* (J. C. Lindon, G. E. Tranter, and D. W. Koppenaal, eds.), pp. 98–109, Oxford: Academic Press, third edition ed., 2017.
- [173] A. Gilbert, “Vibrational, rotational and raman spectroscopy, historical perspective,” in *Encyclopedia of Spectroscopy and Spectrometry (Third Edition)* (J. C. Lindon, G. E. Tranter, and D. W. Koppenaal, eds.), pp. 600–609, Oxford: Academic Press, third edition ed., 2017.
- [174] S. White, “Nuclear waste drum scanning: An investigation into scanning procedures and techniques,” Master’s thesis, 09 2018.
- [175] IAEA, “Minimization and segregation of radioactive wastes,” *IAEA-TECDOC-652*, no. July 1992, 1992.
- [176] A. Shaukat, Y. Gao, J. A. Kuo, B. A. Bowen, and P. E. Mort, “Visual classification of waste material for nuclear decommissioning,” *Robotics and Autonomous Systems*, vol. 75, pp. 365 – 378, 2016.
- [177] Nuclear Decommissioning Authority, *Geological Disposal: Waste Package Data and Information Recording Requirements: Explanatory Material and Guidance*. Online available at <https://www.gov.uk/guidance/all-guidance-documents>, 2015.

Accessed: 24/11/2020.

- [178] Z. Wang, B. He, W. Ma, Z. Yao, S. Huang, M. Liu, and J. Sheng, "Evaluation of the degradation on a cots linear ccd induced by total ionizing dose radiation damage," *Journal of Sensors*, vol. 2016, p. 9604042, Jul 2016.
- [179] S. Chesnevskaya, C. Via, B. Utting, H. Hughes, and S. Watts, "Radiation testing of robotic systems – lidar as a case study - abstract," 05 2019.
- [180] S. R. White, D. A. Megson-Smith, K. Zhang, D. T. Connor, P. G. Martin, C. Hutson, G. Herrmann, J. Dilworth, and T. B. Scott, "Radiation mapping and laser profiling using a robotic manipulator," *Frontiers in Robotics and AI*, vol. 7, p. 141, 2020.
- [181] J. M. Gutierrez-Villalobos, T. Dimas, and J. C. Mora-Vazquez, "Simple and low cost scanner 3d system based on a time-of-flight ranging sensor," in *2017 XIII International Engineering Congress (CONIIN), Santiago de Queretaro, Mexico*, pp. 1–5, May 2017.
- [182] D. T. Connor, K. Wood, P. G. Martin, S. Goren, D. Megson-Smith, Y. Verbelen, I. Chyzhevskiy, S. Kirieiev, N. T. Smith, T. Richardson, and T. B. Scott, "Radiological mapping of post-disaster nuclear environments using fixed-wing unmanned aerial systems: A study from chornobyl," *Frontiers in Robotics and AI*, vol. 6, p. 149, 2020.
- [183] IAEA, "International atomic energy agency (iaea) in the general safety guide gsg-1," tech. rep., International Atomic Energy Authority, 2009.
https://www-pub.iaea.org/MTCD/Publications/PDF/Pub1419_web.pdf.
- [184] S. Monk, C. West, M. Bandala, N. Dixon, A. Montazeri, C. J. Taylor, and D. Cheneler, "A low-cost and semi-autonomous robotic scanning system for characterising radiological waste," *Robotics*, vol. 10, p. 119, 11 2021.
- [185] D. McAlister, "Gamma ray attenuation properties of common shielding materials," 10 2021.
- [186] J. Kennedy and R. Eberhart, "Particle swarm optimization," in *Proceedings of ICNN'95 - International Conference on Neural Networks*, vol. 4, pp. 1942–1948 vol.4, 1995.
- [187] M. Clerc, "Standard Particle Swarm Optimisation." 15 pages, Sept. 2012.
- [188] H.-P. Dai, D.-D. Chen, and Z.-S. Zheng, "Effects of random values for particle swarm optimization algorithm," *Algorithms*, vol. 11, no. 2, 2018.
- [189] P. Virtanen, R. Gommers, T. E. Oliphant, M. Haberland, T. Reddy, D. Cournapeau, E. Burovski, P. Peterson, W. Weckesser, J. Bright, S. J. van der Walt, M. Brett, J. Wilson, K. J. Millman, N. Mayorov, A. R. J. Nelson, E. Jones, R. Kern, E. Larson, C. J. Carey, Í. Polat, Y. Feng, E. W. Moore, J. VanderPlas, D. Laxalde, J. Perktold, R. Cimrman,

- I. Henriksen, E. A. Quintero, C. R. Harris, A. M. Archibald, A. H. Ribeiro, F. Pedregosa, P. van Mulbregt, and SciPy 1.0 Contributors, “SciPy 1.0: Fundamental Algorithms for Scientific Computing in Python,” *Nature Methods*, vol. 17, pp. 261–272, 2020.
- [190] N. R. Syambas, S. Salsabila, and G. M. Suranegara, “Fast heuristic algorithm for traveling salesman problem,” in *2017 11th International Conference on Telecommunication Systems Services and Applications (TSSA)*, pp. 1–5, 2017.
- [191] S. Endres, C. Sandrock, and W. Focke, “A simplicial homology algorithm for lipschitz optimisation,” *Journal of Global Optimization*, vol. 72, 10 2018.
- [192] E. Sperner, “Neuer beweis für die invarianz der dimensionszahl und des gebietes,” *Abhandlungen aus dem Mathematischen Seminar der Universität Hamburg*, vol. 6, pp. 265–272, Dec 1928.
- [193] D. J. Wales and J. P. K. Doye, “Global optimization by basin-hopping and the lowest energy structures of lennard-jones clusters containing up to 110 atoms,” *The Journal of Physical Chemistry A*, vol. 101, pp. 5111–5116, Jul 1997.
- [194] B. Olson, I. Hashmi, K. Molloy, and A. Shehu, “Basin hopping as a general and versatile optimization framework for the characterization of biological macromolecules,” *Advances in Artificial Intelligence*, vol. 2012, p. 674832, Dec 2012.
- [195] R. Storn and K. Price, “Differential evolution – a simple and efficient heuristic for global optimization over continuous spaces,” *Journal of Global Optimization*, vol. 11, pp. 341–359, Dec 1997.
- [196] M. Georgioudakis and V. Plevris, “A comparative study of differential evolution variants in constrained structural optimization,” *Frontiers in Built Environment*, vol. 6, p. 102, 2020.
- [197] Y. Xiang, S. Gubian, B. Suomela, and J. Hoeng, “Generalized Simulated Annealing for Global Optimization: The GenSA Package,” *The R Journal*, vol. 5, no. 1, pp. 13–28, 2013.
- [198] P. Shanmughasundaram and A. K. Dahle, “Heat treatment of aluminum alloys,” in *Reference Module in Materials Science and Materials Engineering*, Elsevier, 2018.
- [199] S. Kirkpatrick, C. D. Gelatt, and M. P. Vecchi, “Optimization by simulated annealing,” *Science*, vol. 220, no. 4598, pp. 671–680, 1983.
- [200] Y. Li, T. Kong, R. Chu, Y. Li, P. Wang, and L. Li, “Simultaneous semantic and collision learning for 6-dof grasp pose estimation,” in *2021 IEEE/RSJ International Conference on Intelligent Robots and Systems (IROS)*, pp. 3571–3578, 2021.

- [201] H. Yu and R. Bro, “Parafac2 and local minima,” *Chemometrics and Intelligent Laboratory Systems*, vol. 219, p. 104446, 2021.
- [202] D. Connor, P. Martin, H. Pullin, K. Hallam, O. Payton, Y. Yamashiki, N. Smith, and T. Scott, “Radiological comparison of a fdnpp waste storage site during and after construction,” *Environmental Pollution*, vol. 243, pp. 582 – 590, 2018.
- [203] A. Selivanova, J. Hůlka, D. Seifert, V. Hlaváč, P. Krsek, V. Smutný, L. Wagner, J. Voltr, P. Rubovič, I. Češpírová, and L. Gryc, “The use of a cztdetector with robotic systems,” *Applied Radiation and Isotopes*, vol. 166, p. 109395, 2020.
- [204] W. A. Westall and B. L. Tawton, “Radiological Characterisation Experience with Magnox Reactors,” in *Radiological Characterisation Experience with Magnox Reactors*, 2012.
- [205] Nuclear Decommissioning Authority, “Intermediate level waste (ilw) storage and fuel element debris (fed) treatment optimisation study,” in *Intermediate Level Waste (ILW) Storage and Fuel Element Debris (FED) Treatment Optimisation Study*, 2013.
- [206] Nuclear Decommissioning Authority, “Waste stream 9g40, fed nimonic,” in *WASTE STREAM 9G40, FED Nimonic*, 2019.
- [207] T. Kawasaki, S. Naito, Y. Sano, T. Hayakawa, T. Shizuma, R. Hajima, and S. Miyamoto, “Measurement of deflection on germanium and gold prisms using 1.7 mev laser compton scattering γ -rays,” *Physics Letters A*, vol. 381, no. 36, pp. 3129 – 3133, 2017.
- [208] S. Frangos, E. Giannoula, P. Exadaktylou, K. Michael, and I. Iakovou, “Collimators for γ cameras,” in *Reference Module in Biomedical Sciences*, Elsevier, 2021.
- [209] S. Gopal and B. Sanjeevaiah, “A method to determine the γ -ray attenuation coefficients,” *Nuclear Instruments and Methods*, vol. 107, no. 2, pp. 221–225, 1973.
- [210] H. O. ANGER, “Use of a gamma-ray pinhole camera for in vivo studies,” *Nature*, vol. 170, pp. 200–201, Aug 1952.
- [211] F. Carrel, R. A. Khalil, S. Colas, D. de Toro, G. Ferrand, E. Gaillard-Lecanu, M. Gmar, D. Hameau, S. Jahan, F. Lainé, *et al.*, “Gampix: A new gamma imaging system for radiological safety and homeland security purposes,” in *2011 IEEE Nuclear Science Symposium Conference Record*, pp. 4739–4744, IEEE, 2011.
- [212] H. Lemaire, R. A. Khalil, K. Amgarou, J.-C. Angélique, F. Bonnet, D. D. Toro, F. Carrel, O. Giarmana, M. Gmar, N. Mena, Y. Menesguen, S. Normand, A. Patoz, V. Schoepff, P. Talent, and T. Timi, “Implementation of an imaging spectrometer for localization and identification of radioactive sources,” *Nuclear Instruments and Methods in Physics*

BIBLIOGRAPHY

- Research Section A: Accelerators, Spectrometers, Detectors and Associated Equipment*, vol. 763, pp. 97 – 103, 2014.
- [213] G. Amoyal, V. Schoepff, F. Carrel, V. Lourenco, D. Lacour, and T. Branger, “Metrological characterization of the gampix gamma camera,” *Nuclear Instruments and Methods in Physics Research Section A: Accelerators, Spectrometers, Detectors and Associated Equipment*, vol. 944, p. 162568, 2019.
- [214] S. Kaczmarz, “Angentihrtte auflosung von systemen linearer gleichungen,” *Bull. Int. Acad. Pol. Sei. Lett., A*, vol. 35, pp. 355–357, 1937.
- [215] R. Gordon, R. Bender, and G. T. Herman, “Algebraic reconstruction techniques (art) for three-dimensional electron microscopy and x-ray photography,” *Journal of Theoretical Biology*, vol. 29, no. 3, pp. 471–481, 1970.
- [216] A. Leitao and J. Zubelli, “Iterative regularization methods for a discrete inverse problem in mri,” 2020.
- [217] R. Gordon, R. Bender, and G. Herman, “Algebraic reconstruction technique (art) for three-dimensional electron microscopy and x-ray photography,” *Journal of theoretical biology*, vol. 29, pp. 471–81, 01 1971.
- [218] M. Meribout and M. Kalra, “A portable system for two dimensional magnetic particle imaging,” *Measurement*, vol. 152, p. 107281, 2020.
- [219] X. Chen, “The kaczmarz algorithm, row action methods, and statistical learning algorithms,” *Contemporary mathematics*, pp. 115–127, 2018.
- [220] T. Strohmer and R. Vershynin, “A randomized kaczmarz algorithm with exponential convergence,” *Journal of Fourier Analysis and Applications*, vol. 15, no. 2, p. 262, 2008.
- [221] D. Needell, “Randomized kaczmarz solver for noisy linear systems,” *BIT Numerical Mathematics*, vol. 50, p. 395–403, Apr 2010.
- [222] S. Chevillard, “The functions erf and erfc computed with arbitrary precision and explicit error bounds,” *Information and Computation*, vol. 216, pp. 72 – 95, 2012.
Special Issue: 8th Conference on Real Numbers and Computers.
- [223] A. C. Allwood, J. A. Hurowitz, B. C. Clark, L. Cinquini, S. Davidoff, R. W. Denise, W. T. Elam, M. C. Foote, D. T. Flannery, J. H. Gerhard, J. P. Grotzinger, C. M. Heirwegh, C. Hernandez, R. P. Hodyss, M. W. Jones, J. L. Jorgensen, J. Henneke, P. R. Lawson, Y. Liu, H. MacDonald, S. M. McLennan, K. R. Moore, M. Nachon, P. Nemere, L. O’Neil, D. A. K. Pedersen, K. P. Sinclair, M. E. Sondheim, E. Song, N. R. Tallarida, M. M. Tice,

- A. Treiman, K. Uckert, L. A. Wade, J. D. Young, and P. Zamani, “The pixl instrument on the mars 2020 perseverance rover,” 2021.
- [224] P. Campos, C. Appoloni, M. Rizzutto, A. Leite, R. Assis, H. Santos, T. Silva, C. Rodrigues, M. Tabacniks, and N. Added, “A low-cost portable system for elemental mapping by xrf aiming in situ analyses,” *Applied Radiation and Isotopes*, vol. 152, pp. 78 – 85, 2019.
- [225] M. Panalytical, *Malvern Panalytical Zetium Datasheet*.
Online available at <https://www.malvernpanalytical.com/en/products/product-range/zetium>, 2020.
Accessed: 10/12/2020.
- [226] Nuclear Decommissioning Authority, “Geological Disposal Generic Disposal Facility Design December 2016,” tech. rep., Nuclear Decommissioning Authority, 3 2016.
accessed: 18/02/2021.
- [227] Nuclear Decommissioning Authority, “Waste Package Specification And Guidance Documentation: WPS/640: Guidance on the Monitoring of Waste Packages during Storage,” tech. rep., Nuclear Decommissioning Authority, 3 2008.
accessed: 17/12/2020.
- [228] Nuclear Decommissioning Authority, “Industry Guidance Interim Storage of Higher Activity Waste Packages – Integrated Approach,” tech. rep., Nuclear Decommissioning Authority, 11 2012.
accessed: 19/10/2021.
- [229] T. A. Callcott, “13 - soft x-ray fluorescence spectroscopy,” in *Vacuum Ultraviolet Spectroscopy* (J. Samson and D. Ederer, eds.), pp. 279 – 300, Burlington: Academic Press, 1999.
- [230] Olympus, *Olympus Vanta Specifications*.
<https://www.olympus-ims.com/en/vanta/>, 2021.
Accessed: 25/01/2021.
- [231] Nuclear Decommissioning Authority, “Inventory for geological disposal main report.”
https://assets.publishing.service.gov.uk/government/uploads/system/uploads/attachment_data/file/997521/RWM_REPORT_DSSC_403_03_Inventory_for_Geological_Disposal_MAIN_REPORT.pdf.
Accessed: 02/02/2021.
- [232] S. Sutherland-Harper, C. Pearce, C. Campbell, M. Carrott, H. Colledge, C. Gregson, J. Hobbs, F. Livens, N. Kaltsoyannis, R. Orr, M. Sarsfield, H. Sims, H. Steele, I. Vatter, L. Walton, K. Webb, and R. Taylor, “Characterisation and heat treatment of chloride-contaminated

BIBLIOGRAPHY

- and humidified puo2 samples,” *Journal of Nuclear Materials*, vol. 509, pp. 654 – 666, 2018.
- [233] P. I. Pavlova-Schmitz, J. A. La Verne, and S. M. Pimblott, “Production and postirradiation release of hcl and h2 in the radiolysis of pvc,” 12 'Tihany' symposium on radiation chemistry Program and abstracts, (Hungary), p. 168, 2011.
- RADIATION CHEMISTRY, RADIOCHEMISTRY AND NUCLEAR CHEMISTRY.
- [234] E. Pira, F. Donato, L. Maida, and G. Discalzi, “Exposure to asbestos: past, present and future,” *Journal of thoracic disease*, vol. 10, pp. S237–S245, Jan 2018. 29507791[pmid].
- [235] V. Zholobenko, F. Rutten, A. Zholobenko, and A. Holmes, “In situ spectroscopic identification of the six types of asbestos,” *Journal of Hazardous Materials*, vol. 403, p. 123951, 2021.
- [236] A. J. Hobro and B. Lendl, “Stand-off raman spectroscopy,” *TrAC Trends in Analytical Chemistry*, vol. 28, no. 11, pp. 1235–1242, 2009.
- [237] P. Coffey, N. Smith, B. Lennox, G. Kijne, B. Bowen, A. Davis-Johnston, and P. A. Martin, “Robotic arm material characterisation using libs and raman in a nuclear hot cell decommissioning environment,” *Journal of Hazardous Materials*, vol. 412, p. 125193, 2021.
- [238] Clifton Photonics, *Portable Raman Spectrometer*.
Online available at <https://cliftonphotonics.com/spectrometers/#probes>, 2021.
Accessed: 24/11/2021.
- [239] H. P. Ng, S. H. Ong, K. W. C. Foong, P.-S. Goh, and W. L. Nowinski, “Medical image segmentation using k-means clustering and improved watershed algorithm,” *2006 IEEE Southwest Symposium on Image Analysis and Interpretation*, pp. 61–65, 2006.
- [240] F. Pedregosa, G. Varoquaux, A. Gramfort, V. Michel, B. Thirion, O. Grisel, M. Blondel, P. Prettenhofer, R. Weiss, V. Dubourg, J. Vanderplas, A. Passos, D. Cournapeau, M. Brucher, M. Perrot, and E. Duchesnay, “Scikit-learn: Machine learning in Python,” *Journal of Machine Learning Research*, vol. 12, pp. 2825–2830, 2011.
- [241] V. Satopaa, J. Albrecht, D. Irwin, and B. Raghavan, “Finding a "kneedle" in a haystack: Detecting knee points in system behavior,” in *2011 31st International Conference on Distributed Computing Systems Workshops*, pp. 166–171, 2011.
- [242] T. Roliński, S. Gawinkowski, A. Kamińska, and J. Waluk, *Raman Spectra of Solid Amino Acids: Spectral Correlation Analysis as the First Step Towards Identification by Raman Spectroscopy*, pp. 329–354.
12 2014.

- [243] PySimpleGUI, *PySimpleGUI Documentation*.
<https://pysimplegui.readthedocs.io/en/latest/>, 2022.
Accessed: 10/01/2022.
- [244] K. Prokhorov, D. Aleksandrova, E. Sagitova, G. Nikolaeva, T. Vlasova, P. Pashinin, C. Jones, and S. Shilton, “Raman spectroscopy evaluation of polyvinylchloride structure,” *Journal of Physics: Conference Series*, vol. 691, p. 012001, 02 2016.
- [245] M. KINNO, K. ichi KIMURA, and T. NAKAMURA, “Raw materials for low-activation concrete neutron shields,” *Journal of Nuclear Science and Technology*, vol. 39, no. 12, pp. 1275–1280, 2002.
- [246] M.-A. Berton, D. Estivie, E. Cantrel, J. Moeller, M. Ondaro, B. Ooms, S. Wittenauer, and B. Burton, “The nea co-operative programme on decommissioning decontamination and demolition of concrete structures,” tech. rep., Nuclear Energy Agency of the OECD (NEA), Sep 2011.
NEA-RWM-R-2011-1.
- [247] J. Lipka, V. Slugen, I. Toth, J. Hascik, and M. Lehota, “Phase analysis of corrosion products from nuclear power plants,” *Hyperfine Interactions*, vol. 139, pp. 501–511, Mar 2002.
- [248] K. A. Habib, M. S. Damra, J. J. Saura, I. Cervera, and J. Bellés, “Breakdown and evolution of the protective oxide scales of aisi 304 and aisi 316 stainless steels under high-temperature oxidation,” *International Journal of Corrosion*, vol. 2011, p. 824676, Aug 2011.
- [249] C. T. e. a. Kim S, Chen J *PubChem in 2021: new data content and improved web interfaces*, 2021.
- [250] J. Zhao, S. Xu, R. Wang, B. Zhang, G. Guo, D. Doermann, and D. Sun, “Data-adaptive binary neural networks for efficient object detection and recognition,” *Pattern Recognition Letters*, vol. 153, pp. 239–245, 2022.
- [251] F. Padilla Cabal, N. Lopez-Pino, J. Luis Bernal-Castillo, Y. Martinez-Palenzuela, J. Aguilar-Mena, K. D’Alessandro, Y. Arbelo, Y. Corrales, and O. Diaz, “Monte carlo based geometrical model for efficiency calculation of an n-type hpge detector,” *Applied Radiation and Isotopes*, vol. 68, no. 12, pp. 2403–2408, 2010.
- [252] D. Connor, *Advancing the Development of Lightweight Unoccupied Aerial Systems (UAS) for Environmental Radiation Mapping*.
PhD thesis, 1 2021.
- [253] Eckert Ziegler, “Recommended nuclear decay data co-60.” website, Jan. 2010.

BIBLIOGRAPHY

- [254] I. Akkurt, K. Gunoglu, and S. S. Arda, "Detection efficiency of nai(tl) detector in 511–1332 keV energy range," *Science and Technology of Nuclear Installations*, vol. 2014, p. 186798, Mar 2014.
- [255] L. K. Herold and R. T. Kouzes, "Intrinsic germanium detector efficiency calculations," *IEEE Transactions on Nuclear Science (Institute of Electrical and Electronics Engineers); (United States)*, vol. 38:2, 4 1991.
- [256] R. C. McFarland, "Behavior of several germanium detector full-energy-peak efficiency curve-fitting functions," 1991.
- [257] S. J. Fearn, S. Kaluvan, T. B. Scott, and P. G. Martin, "An open-source iterative python module for the automated identification of photopeaks in photon spectra," *Radiation*, vol. 2, no. 2, pp. 193–214, 2022.
- [258] J. M. M. W. Tao, T.-C. Wang and R. Ramamoorthi, "Depth estimation for glossy surfaces with light-field cameras." *Lecture Notes in Computer Science*, 2014.